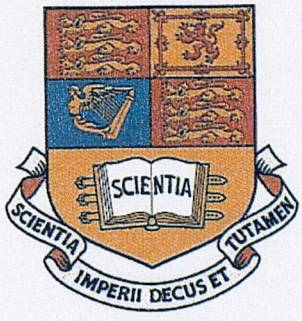
Topographic Modelling from SAR Imagery of Impact Craters on Venus

Christopher Gordon Cochrane

Department of Earth Science and Engineering

Imperial College of Science, Technology and Medicine

University of London



Submitted for the degree of Doctor of Philosophy

and

Diploma of Imperial College

Submitted: August 2004

Corrected: February 2005

ABSTRACT

The main output of the work is a new crater depth-diameter characteristic for Venus, a geologically active planet with a dense atmosphere. This characteristic shows that small craters on Venus are unusually shallow, compared to scaled versions of those on the Moon, Mars and Mercury.

This study concerns 75 craters (8% of the planetary population) located in an area astride western Ovda Regio, chosen for its good stereo coverage by the Magellan Synthetic Aperture Radar (SAR). A Digital Elevation Model (DEM) is produced for each of 62 craters, using NASA's Magellan Stereo Toolkit (MST) to match same-side image pairs at the level of about one SAR resolution cell. Sufficient DEMs are validated by use of a third, opposite-side image to validate the set of 62, which is shown to be broadly representative of the planetary population.

Most small craters on Venus have been classified as "Knobby Base", a class that constitutes more than half the planetary population. The work reported herein shows that these Knobby Base craters are the result of the impact of well-distributed bolide fragments produced by the disintegration in the atmosphere of a single parent bolide. Such "Compound" craters exhibit a depth:diameter trend that is parallel to that of Simple craters, an indication that the impulse at impact was insufficient to fluidise target material and form a Complex crater.

The DEMs are shown to have vertical accuracy in a range from ± 118 to ± 128 m. This is rather more than estimated elsewhere but includes the effect of data compression on the downlink. The DEMs also show that:

- Most crater diameters have previously been underestimated by about 10%, implying an increase of ~20% in the estimated age of the Venus surface.
- Large craters, i.e., > 38 km in diameter, all have a depth of about 1 km, irrespective of diameter.
- Central Peak craters tend to be deeper than expected from theory.

Some detailed observations of the geology within the Sample Area are made:

- Manzolini lies on an arcuate ridge, not unlike those surrounding two coronae to its east. The crater is not horizontally deformed but is inclined, perhaps due to differential uplift, and radar-dark material lies only in the lower half of the crater floor.
- Beyond the 510 km diameter radar-dark halo around Mead crater, a grey arc to the South and West may be evidence of a pyroclastic-like ejecta surge following its formation.
- The long (~1000 km), radar-dark scar that apparently emanates from Joliot-Curie, is probably a thin layer of radar-absorbent ejecta lying on smooth, grey lava from Verdandi Corona. These ejecta were carried preferentially westwards by prevailing winds but only in sufficient quantity to alter radar return of the valley floor and not the surrounding tessera. This observation may explain the relative absence, in tessera, of craters with dark halos.
- Three craters, each about 6 km in diameter, are located along a > 100 km ground track and were perhaps formed during a single event. This observation either indicates a disruptive effect by the initial impact(s) on the arrival of later fragments, or implies that some fragments can become well-separated during their descent through the atmosphere.

Further use of MST to study geological features on Venus is suggested. A new tool to analyse radar layover, e.g., on central peaks, is proposed for application on the Huygens-Cassini Mission. Some trade-offs for the next spacecraft to explore key areas of the geology of Venus are identified.

Acknowledgements

I would like to acknowledge my huge debt to Professor Mike Warner and Dr Richard Ghail for guiding my interest to this topic, and then my research of it.

I also wish to thank: Dr Robert Herrick of the Lunar and Planetary Institute (LPI) in Huston for providing access to his data and describing his processes, Dr Hoonyol Lee for teaching me to use MST, and Tim Bond for help on cratering density.

I also thank Graham Davison, formerly of Farnborough Space Department, and Dick Harris, formerly of Malvern Knowledge Information Systems, for their sponsorship.

And I am indebted to Victoria Petersen for her moral support.

Contents

Abstract 1

Acknowledgements 3

List of Figures 7

List of Tables 13

1. Impact Craters on the Terrestrial Planets 14

1.1. Role of Impacts in the later Evolution of the Terrestrial Planets 16

1.2. Comparison of Earth and Venus as Impact Targets 23

1.3. Comparison of Earth and Venus as Terrestrial Planets 32

1.4. The Surface Geology of Venus 37

1.5. The Crater Population of Venus 43

1.6. Crater Topography 48

1.7. Chapter Summary 54

2. The Magellan Mission and its Data Products 55

2.1. Magellan Mission Description 57

2.2. Magellan Operations at Venus 61

2.3. The Magellan Synthetic Aperture Radar 63

2.4. Magellan Downlink Data Compression 67

2.5. Magellan Product Generation 70

2.6. Crater Depth from one Image 72

2.7. The Magellan Stereo Toolkit 74

2.8. Opposite Side Stereo 78

2.9. Chapter Summary 79

3. Crater Sample Selection, Model Generation and Results 81

3.1. Sample Area Definition and Description 82

3.2. Craters in the Sample 85

3.3. Crater Diameters 92

3.4. Crater Depth/Diameter Ratios 94

3.5. Comparison of Sample Craters with the planetary Population 109

3.6. Chapter Summary 115

4. Model Validation 116

4.1 Validation of the smaller crater DEMs 118

4.2 Validation of the deepest crater DEMs 135

4.3 Validation of the largest crater DEMs 143

4.4 Chapter Summary 154

5. Errors and Artifacts in the Models 156

5.1 DEM Error Analysis 157

5.2 Errors due to Block Adaptive Quantisation 160

5.3 Effects of Multi-looking 165

5.4 Effects of Resampling and Mosaicking 169

5.5 Effects of Subsurface Scattering 172

5.6 Effects of Radar Layover 177

5.7 Chapter Summary 182

6. Geological Implications of the Models **183**

6.1 Crater Morphology 184

6.2 Age of the Cratered Surface 187

6.3 The Shape of Manzolini 190

6.4 Radar-bright Arc around Mead 194

6.5 Dark Flow past Joliot-Curie 201

6.6 New Crater Field 203

6.7 Chapter Summary 205

7. Proposals for Further Work **207**

7.1 Reuse of MST and these Processes 208

7.2 Modelling of Central Peaks 210

7.3 Further investigation of Venus 212

7.4 Chapter Summary 216

References **217**

Acronyms used in this Thesis **228**

Contents of the accompanying Compact Disc **229**

List of Figures

1.1: Morphological type vs diameter for Venusian Craters. 15

1.2: Barringer Meteor Crater in Arizona, USA. 16

1.3: Dione. 17

1.4: Identified terrestrial impact structures. 18

1.5: Vredefort Crater. 19

1.6: Map of the Horizontal Gravity Gradient near Chicxulub. 20

1.7: Multile-flooredCrater. 25

1.8: Crater Field Formation Diagrams for Earth and Venus. 26

1.9: Markham Crater. 29

1.10: A sphere pancaking in the atmosphere of Venus. 30

1.11: A comparison of Venus and Earth. 32

1.12: Hypsometric curves for Venus and Earth 37

1.13: Venera Landing Sites. 38

1.14 Venera Image of the surface of Venus. 39

1.15: Synthetic perspective view of highlands in Ovda Regio. 40

1.16: Approximate crater densities as a function of crater diameter. 43

1.17: Crater density distribution 46

1.18: Trends of crater depth and diameter for the terrestrial planets, 49

1.19: Depth versus diameter for craters on the terrestrial planets. 50

1.20: 'Transitional' crater. 51

1.21: Illustrations of the rounded shoulders of a crater. 53

2.1: Magellan operations in Venus orbit. 57

2.2: Earth and Venus orbit geometry for Magellan Cycle 1. 58

2.3: Magellan Cycle 1 coverage. 59

2.4: Magellan mapping orbit profile. 60

2.5: Timelines for Magellan Microwave Instruments. 64

2.6: Bright feature used for Magellan SAR sidelobe characterisation. 66

2.7: a. BAQ Step Response. 68

2.7: b. West-East DN plot acrosss Helvi. 68

2.8: Crater Depth from a Single Image 72

2.9: Radar Backscatter of representative surfaces 73

2.10: Same Side Parallax-to-Height Ratio. 77

2.11: Opposite Side Parallax-to-Height Ratio. 78

3.1: Location of the Sample Area on the planet. 81

3.2: Coverage of all 3 Cycles astride western Ovda Regio. 82

3.3: Definition of the Sample Area. 83

3.4: Visualisation of Carter crater. 89

3.5: Diameters of craters compared to those in the LPI database. 92

3.6: Azimuthly averaged topography of the largest craters. 93

3.7: Depth/diameter trend for 72 craters. 94

3.8: Two depth/diameter trends for 72 craters, for < and > 10 km. 95

3.9: Two depth/diameter trends for 62 DEMs, for < and > 12 km. 96

3.10: Effect of pancaking within the D:d domain. 99

3.11: Effect of pancaking on a simulation of Venus craters. 101

3.12: Release wave forming during the Excavation Stage of an impact. 102

3.13: Cross-section of a typical Impact. 102

3.14: Comparison of Single and Multiple Impacts. 103

3.15: Depth/diameter trends for 29 "Knobby Base" and 19 "Central Peak" DEMs in a set of 57. 106

3.16: The only SAR image of the central feature of Voynich. 107

3.19: SAR images of Parra. 107

3.17: DEM and SAR image of Naomi. 108

3.18: DEM and SAR image of Doris. 108

3.19: Distribution of Crater Diameters. 109

3.20: Distribution of Crater Altitudes. 110

3.21: Distribution of Crater Morphologies. 111

3.22: Areal Distribution of Craters within the Sample Area. 112

4.1: Depth/diameter trends for 29 Knobby Base DEMs in a set of 57. 117

4.2: Percentages of Morphological Types. 117

4.3: Parameter differences for small crater DEMs. 119

4.4: SAR Images of Elma from Cycles 1, 2 and 3. 120

4.5: Contours and features of the DEM of Elma. 120

4.6: Herrick & Sharpton's pick points for Elma. 121

4.7: Images of Elma's Central Peak from Cycle 1, 2 and 3. 123

4.8: Cycle 2 points on the floor of Elma derived from Herrick & Sharpton's offsets. 124

4.9: Corrected Cycle 2 points on the floor of Elma. 125

4.10: Images of Nsele from Cycles 1, 2 and 3. 126

4.11: Contours and features of the SFS DEM of Nsele. 127

4.12: Herrick & Sharpton's pick points and Rim for Nsele. 127

4.13: Images of Crater B from Cycles 1, 2 and 3. 128

4.14: Contours, rim and bottom of the SFS DEM of Crater B. 128

4.15: Matched points within Crater B. 129

4.16: Image-J version of Crater B IDL DEM, Rim and Floor marked. 130

4.17: ERDAS visualisation of Crater B SFS DEM. 130

4.18: Images of Crater A from Cycles 1, 2 and 3. 131

4.19: SFS DEM of Crater A. 131

4.20: Image-J version of Crater A DEM, with Rim and Floor marked. 132

4.21: Maximum Diameter of Crater A DEM. 132

4.22: Minimum Diameter of Crater A DEM. 132

4.23: Matched points within Crater A. 133

4.24: Images of Deloria from Cycles 1, 2 and 3. 136

4.25: Visualisation of Deloria Crater. 136

4.26: Validation points for Deloria Crater. 138

4.27: SAR Images of Samintang. 139

4.28: Samintang Crater. 139

4.29: Samintang Rim Profile. 140

4.30: Validation points for Samintang Crater. 141

4.31: West-East profile of Samintang Crater. 141

4.32: SAR Coverage of Mead. 143

4.33: Mosaicking of the eastern half of Mead. 144

4.34: Checking the depth of the inner floor of Mead. 145

4.35: Altimetry profiles of Mead. 146

4.36: Image-J assessment of Mead. 147

4.37: Coverage of Joliot-Curie. 148

4.38: Visualization of the 2 DEM elements of Joliot-Curie. 149

4.39: Cross-section across the western half of Joliot-Curie. 150

4.40: Cross-section across the western Rim of Joliot-Curie. 151

4.41: Coverage of Potanina. 152

4.42: DEM mosaic of Potanina. 152

4.43: Points chosen to determine the depth of Potanina. 153

5.1: Effect of limited range resolution on surface terrain accuracy. 158

5.2: Effect of BAQ threshold on detected image transition position. 160

5.3: Errors on a DEM of Teumere, for transitions equal to I. 161

5.4: Histogram of Height Errors in a DEM of Teumere. 161

5.5: Errors on a DEM of Teumere, for transitions of I, 2I & 4I. 162

5.6: Errors on a DEM of Helvi, for transitions of I, 2I & 4I. 162

5.7: Type 1 Errors on DEMs. 163

5.8: Spacecraft motion approaching Helvi during Cycle 1. 166

5.9: Ridges near Amanda. 168

5.10: DEMs of Langtry. 169

5.11: Parameters of the 3 swaths over Langtry during Cycles 1 and 3. 170

5.12: Ghail's DEM with swath overlaps superimposed. 171

5.13: Comparison of Landsat and SIR-A images of hyper-arid desert. 172

5.14: Landsat and SIR-A radar images of Egyptian Desert. 173

5.15: Radar penetration depths in fine sediment lying in a crater. 174

5.16: Scar adjacent to Florence. 174

5.17: Overlaid images of Lullin. 175

5.18: DEM of Cori crater showing dark material on the escarpment. 176

5.19: Domes with Pits near Ruit crater. 178

5.20: Radar layover artefacts in 3 images of Pits near Ruit crater. 178

5.21: Probable cross-section of the Larger Pit. 178

5.22: Projections of the layover of a Central Peak in a Cycle 1 image. 179

5.23: Projections of the layover of a Central Peak in 3 images. 180

5.24: Examples of the layover of a Central Peak (Lullin). 181

6.1: Depth/diameter trends for the 55 DEMs with significant depth. 185

6.2: Trend for terrestrial impact frequency. 187

6.3: Effect of pancaking on the simulated age of the cratered surface of Venus. 189

6.4: Vicinity of Manzolini. 190

6.5: The Rim of Manzolini. 191

6.6: Visualisation of the DEM for Manzolini. 191

6.7: Topography in the Region of Manzolini and adjacent Coronae. 192

6.8: East-West profile through the DEM of Manzolini. 193

6.9: Radar-bright Arc southwest of Mead. 194

6.10: Images of Kuro. 195

6.11: Images of Florence. 195

6.12: Region of Romola. 196

6.13: Image of Romola. 197

6.14: Region of Jasmin. 197

6.15: Image of Jasmin. 198

6.16: Images of Amenardes. 199

6.17: Images of Adivar. 199

6.18: Sketch of bow shock propagation and interaction with the planetary surface. 200

6.19: Region of Joliot-Curie. 201

6.20: Altimetry near Joliot-Curie. 202

6.21: Map of the locality of Craters A and B. 203

7.1: Cycle 3 coverage of Ishtar Terra. 209

7.2: Ground traces for planned SAR passes over Titan. 211

List of Tables

1.1: Some coefficients for the Terrestrial planets. 41

2.1. MST Parameters for Helvi. 75

2.2. MST Stereo Matching Settings. 76

3.1: The 33 Craters in the Sample Area with 3 images. 87

3.2: The 29 Craters in the Sample Area with 2 same-side images. 88

3.3: The 10 Craters in the Sample Area with 2 opposite-side images. 90

3.4: The 3 Craters in the Sample Area with only one image. 91

3.5: Depth and Diameter of the largest craters. 93

3.6: Parameters of the "Knobby Base" DEM set. 104

3.7: Parameters of the "Central Peak" DEM set. 105

4.1: Matching offsets defining the floor of Elma. 122

4.2: Parameters for Elma "Y" Feature. 123

4.3: Herrick and Sharpton's offsets on the western floor of Elma. 124

4.4: Spreadsheet for Crater A. 133

4.5: Parameters for the deepest DEMs. 135

4.6: Validation points for Deloria. 137

4.7: Validation points for Samintang. 140

5.1: Elevation (height) error due to finite range resolution. 159

5.2: Multi-looking parameters. 165

6.1: Shallow Crater Parameters. 184

7.1: SAR passes on Titan. 210

7.2: Main parameters of Venus Surface Imaging Missions. 212

Chapter 1

Impact Craters on the Terrestrial Planets

This Thesis concerns Venus, and especially the data set returned, between 1990 and 1993, from the Synthetic Aperture Radar (SAR) on NASA's Magellan mission. This Chapter is a literature review that shows the relevance, to impact craters on the terrestrial planets, of that mission and the SAR instrument. Both mission and instrument are described in more detail in Chapter 2.

Phillips *et al.* (1991) characterise craters as having ejecta deposits, raised rims and terraced walls. Melosh (1989), French (1998) and Shoemaker & Shoemaker (1999) describe how comets and asteroids arrive in the region of the terrestrial planets at velocities of several tens of kilometers per second. What happens to them during the few seconds they take to pass through an atmosphere is not well understood but is one of the topics addressed herein. Study of the large numbers of craters on the Moon, Mars and Mercury has led to the following sequence of crater formation:

Shock. On arrival of the impactor at the surface, its kinetic energy couples to the surface in a hemispherical shock wave, which propagates downwards and outwards.

Ejection. The outward development of the shock at shallow depths is almost unconstrained; rocks are shocked into shatter cones, and plate-like elements are sputtered off.

Displacement. Underneath the developing shock wave, its pressure fluidizes the rock; material is displaced downwards, outwards and eventually upwards.

Melting. The kinetic energy of the impactor generates heat which vaporises and then expands the fluid, ejecting more finely divided material upwards and outwards from what is now described as a transient crater.

Collapse. After energy transfer comes to an end, material in various forms settles back into the transient crater. Some of this material arrives as projectiles in

very steep trajectories, some is fluidised material that flows under gravity, and some is material from beyond the transient crater but fractured by it.

The classical taxonomy of crater shape is: Simple, Central Peak, Peak Ring and Multi-ring, with a sharp transition in the depth~diameter trend line between the "Simple" group and the other classes, called collectively "Complex craters". Like craters on the Moon, the larger craters on Venus have more complex interiors. As illustrated in Fig 1.1, the transition from one form to the next occurs at increasing diameter in fairly broad bands, which are primarily a function of gravitational constant and material density. The atmosphere of Venus has been thought to completely prevent simple craters, because smaller bolides are eliminated by ablation or explosion before they can reach the surface – see Melosh (1989), Herrick *et al.* (1997), and MacKinnon *et al.* (1997). For Venus, the LPI database uses a more pragmatic categorisation of morphology from planform images (since the altimetry data points are at least 7 km apart): Bowl, Knobby Base, Central Peak, Several Peaks, Peak Ring, Multi-ring, and Flat Floor. Although there are only 6 bowl-shaped craters, they would appear they should be categorised as "Simple" craters. An important aspect of this Thesis is that the knobby base craters on Venus are shown to be equivalent to an overlapping series of "Simple" craters.

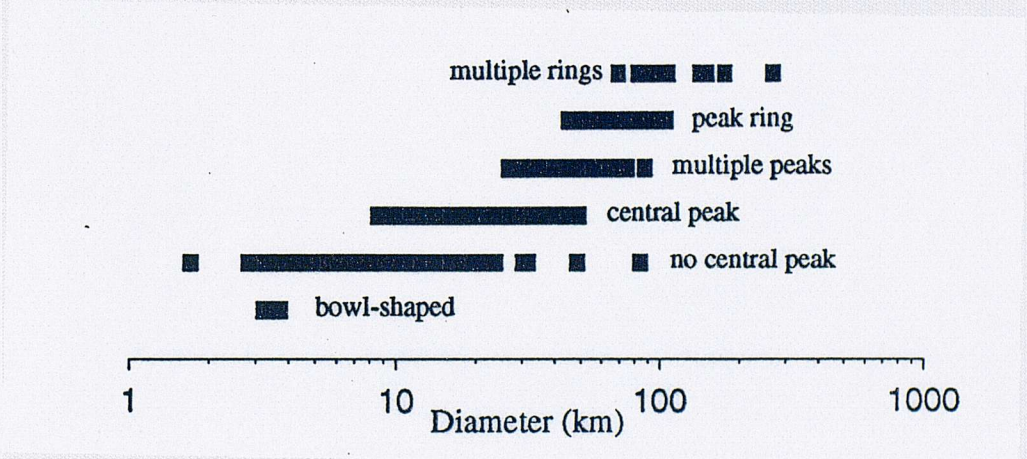


Figure 1.1: Morphological type vs diameter for Venusian Craters. The LPI database identifies only 6 bowl-shaped craters, and all are under 4 km diameter. The most populous group, here called "no central peak" are described in the LPI database as "knobby base". From Herrick *et al.* (1997) and based on analysis of Magellan data.

1.1. The Role of Impacts in the later Evolution of the Terrestrial Planets

Shoemaker (1977) said that the impact of solid bodies is the most fundamental of all processes that have taken place on the terrestrial planets. Barringer Crater is a typical impact crater (See Fig. 1.2).



Figure 1.2: Barringer Meteor Crater in Arizona, USA. Barringer is a young, well-preserved crater, of 1.2km in diameter and 217 m deep, formed by impact of an iron meteorite of ~ 50 m diameter, about 0.05 Ma ago. Above is an aerial photograph from the south, from McNab & Younger (1999). The lower image, including Diablo Canyon to the west, is by ERS spaceborne SAR at 25 m nominal resolution, from ESA SP-1275 (2003).

Improving our understanding of structures such as these craters is worthwhile because they provide evidence not only of planetary development but also of mineral and hydrocarbon deposits of considerable economic value. As Fig. 1.3 illustrates, cratering is evident on many planets.

As French (1998) points out, exploration of the solar system and terrestrial impact structures confirm that impacts by extraterrestrial objects in geologically recent times significantly shaped Earth's surface, disturbing its crust and altering its evolution. French (1998) identified some 145 separate geological structures. See Fig. 1.4. More than 20 new candidates have been found since French (1998) was published.

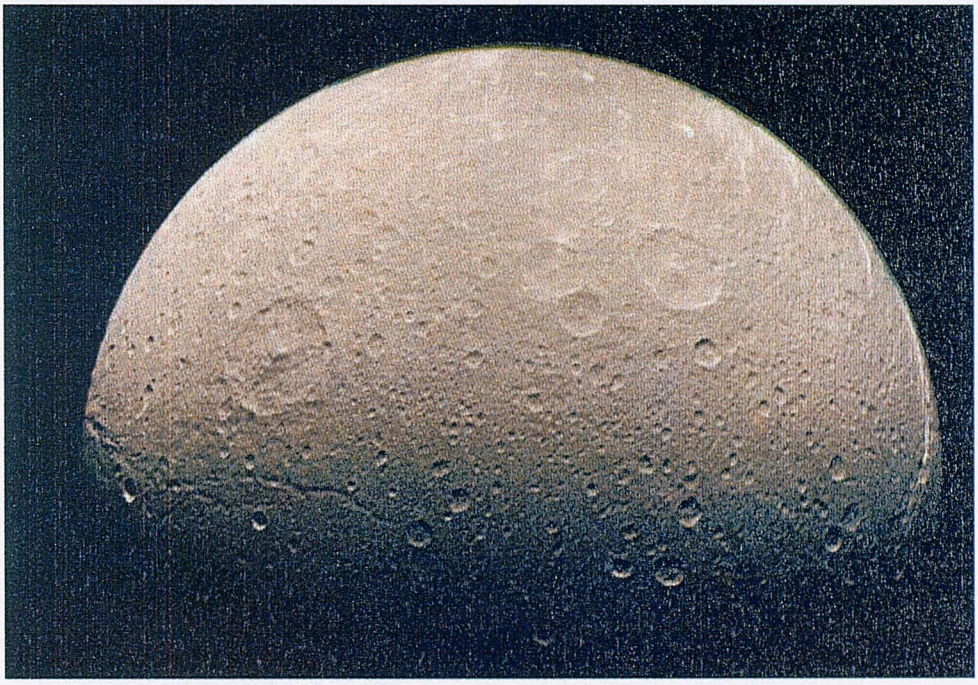


Figure 1.3: Dione. The densest (1400 kg m^{-3}) moon of Saturn, Dione is of 1100 km diameter, half ice and half silicate rock. Its surface is saturated with impact craters that are much shallower than those on the terrestrial planets, probably due to slumping. Many craters have well-developed central rebound peaks, e.g.Aeneas (155 km diameter) at centre left and Dido (120 km diameter) at upper right. Crater counts indicate that Dione has undergone periods of resurfacing. Voyager 1 image from Norton (2002).

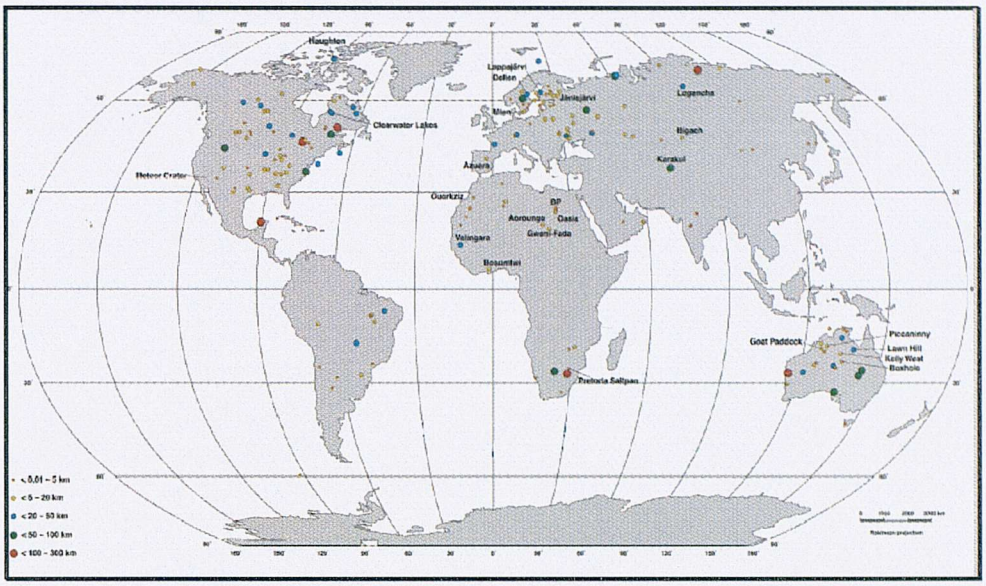


Figure 1.4: Identified terrestrial impact structures. The non-random distribution reflects geological and social factors rather than the original bombardment flux, i.e.: a. better preservation on continental shields; b. few systematic searches for submarine impacts; c. strong geological research activity in Canada, Russia, Ukraine and Australia; d. post-impact geological processes, affecting almost all structures < 200 Ma old; e. small structures (0 – 5 km) greatly under-represented. From French ((1998).

Most identified impact sites lie on continental shields. Grieve & Shoemaker (1994) showed that, at least on the European and American shields, an average of 5 craters larger than 20 km diameter are created per 10^6 square km per 10^6 yrs. These craters range from uneroded, circular bowls of 20 m diameter to complex structures more than 200 km diameter and 2 billion years old covered by layers of younger sedimentary rock, e.g.Sudbury and Vredefort (illustrated in Fig. 1.5).

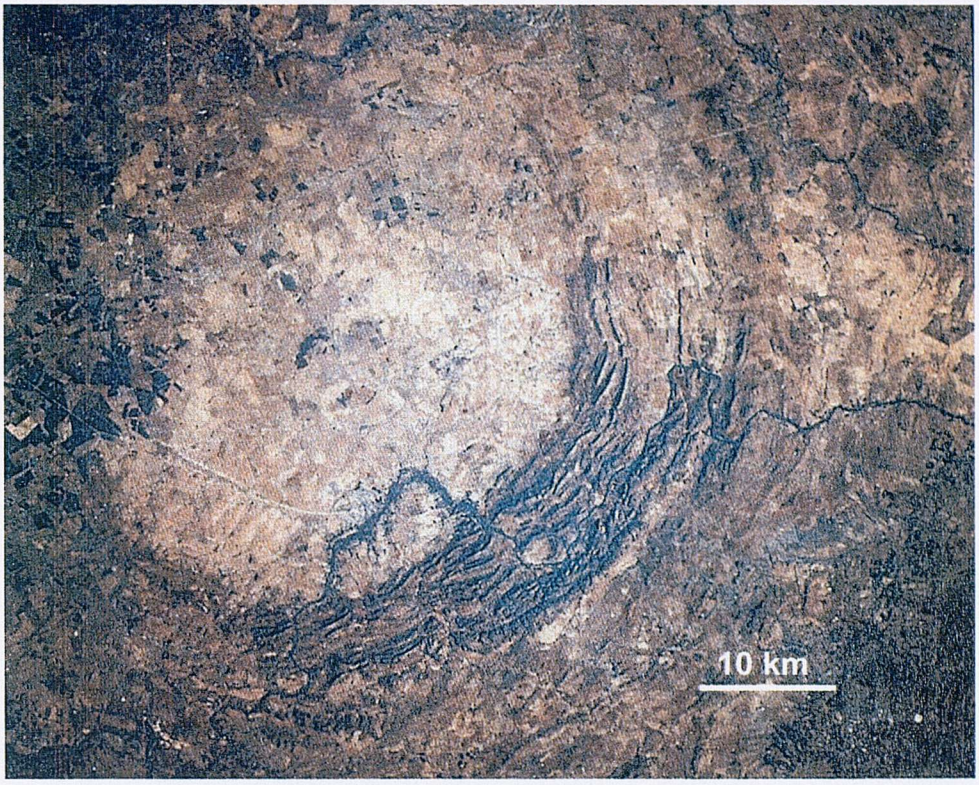


Figure 1.5: Vredefort. Landsat panchromatic image of the 40 km diameter, uplifted central core of Vredefort, one of the oldest terrestrial impact structures. Shock metamorphism effects have been found out to 70 km, suggesting an original diameter of at least 140 km. From Norton (2002)[1].

In 1956, a palaeontologist, M.W. de Laubenfels, proposed the extinction of the dinosaurs might have been caused by heat associated with the impact of a large meteorite, but this hypothesis was almost completely ignored. Urey (1973) proposed that several extinction events in the last 50 million years were caused by the impact of comets. Alvarez *et al.* (1980) reported the first physical evidence of such a pervasive extinction event: an unusually narrow sediment containing concentrated iridium at the so-called the K-T boundary. The K-T boundary, 65 Ma ago, is where rock strata show 15 % of the families of marine animals and 50% of the genera on Earth became extinct. Alvarez *et al.* (1980) offered 2 hypotheses that:

1. Earth had been the subject of a large impact at the K-T Boundary, and

2. this impact was the direct cause of the mass extinctions at that time.

[1] Bevan (1998) includes a greyscale image of this structure and suggests an original diameter of ~ 200 to 300 km.

Both hypotheses were controversial when proposed. The first is now widely accepted but the debate about the second continues. Turekian & Luck (1982) found osmium isotope ratios in the distinctive clay layer at the K-T boundary to be more similar to those found in meteorites than to those found anywhere else on Earth. Abundance of microtektites and shocked quartz, also taken as markers of impact events, were evident. In 1990, a 180 km diameter crater of the right age was identified in at Chixculub, in the Yucatan Peninsula of Mexico. See Fig. 1.6.

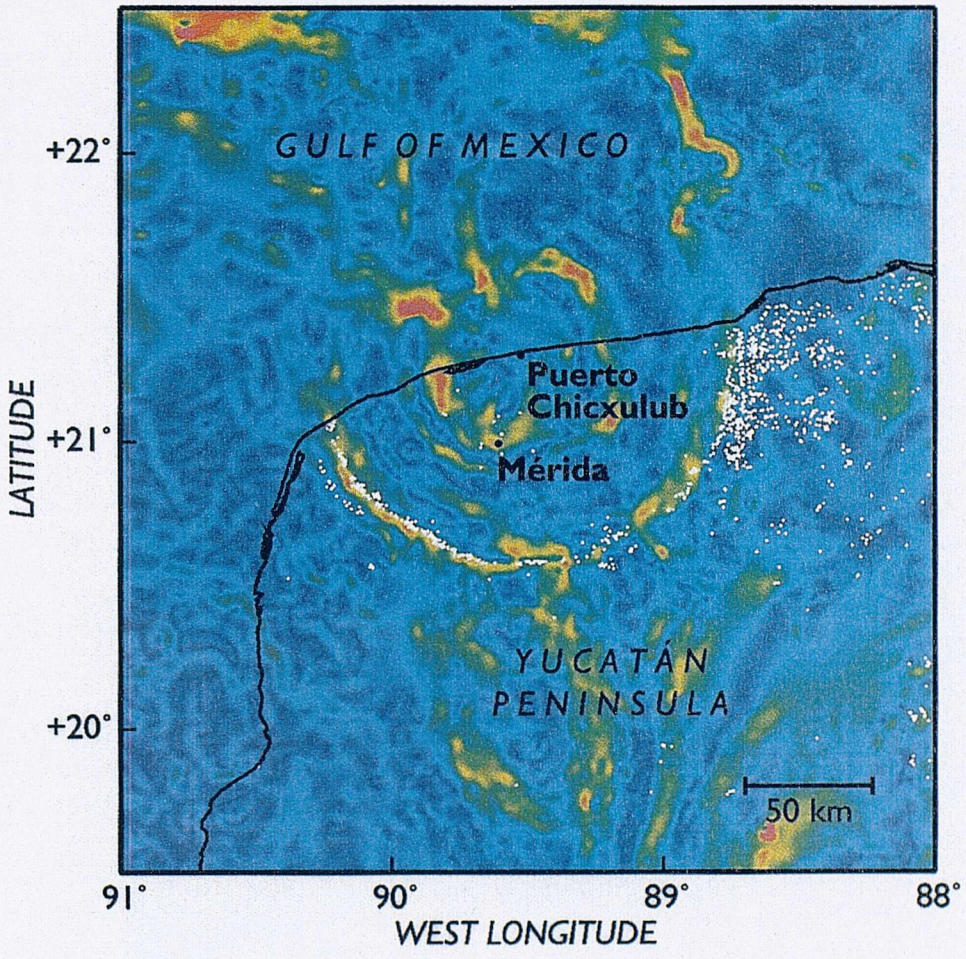


Figure 1.6: Map of the Horizontal Gravity Gradient near Chicxulub. Warmer colours denote a high rate of change of gravity,i.e.a symptom of a subsurface discontinuity or boundary. Data processed to show shallow subsurface structure under younger limestone, not evident in surface topography. Data are incomplete, especially for area under water. White dots represent locations of water-filled sinkholes indicating that the ancient crater topography somehow still governs ground water flows 600m above it. From Shoemaker & Shoemaker (1999) but attributed to Hildebrand.

Alvarez *et al.* (1995) is one of several papers showing that Chicxulub was the source of the iridium and, hence, may be assumed to be the site of the impact that caused the extinction event. The impact apparently occurred in shallow water off what was then the coast, and the crater was covered with sediment before becoming part of the peninsula. See Gehrels (1994), Palmer (1994) and Steel (1995).

O'Keefe & Ahrens (1982) considered the case that an asteroid, comet or meteoroid swarm of objects ~ 10 km diameter arrives at 15 to 45 km s^{-1}, to impact a silicate Earth covered by an atmosphere and an ocean. They showed that only ~ 5 to 15% of bolide energy couples into atmosphere and ocean but ~ 10 to 100 times the bolide mass of water and rock is ejected into the stratosphere.

Alvarez & Muller (1984) proposed 3 hypotheses for a periodicity of about 28 Ma in a series of major terrestrial extinctions, which Raup (1999) surveyed as follows:

- Oscillation of the solar system through the galactic plane. Rampino & Stothers (1984) presented extinction statistics, deduced a period of 30 Ma and proposed that this was due to the Sun's motion perpendicular to the galactic plane, with comets perturbed from the Oort cloud as it approached interstellar clouds.
- A companion star to the Sun. Whitmire & Jackson (1985) proposed a period of 26 Ma due to an as-yet-unidentified star. Davis *et al* (1984) proposed the same period and the same cause, which they named Nemesis. Both papers conclude that the star must be small,i.e.less than 10% of the Sun's mass, in a highly eccentric orbit passing through the Oort cloud, and currently about 2 light years (0.6 parsec) from the solar system.
- An unseen planet. Whitmire & Matese (1985) proposed a tenth planet, in an out-of-the-ecliptic and eccentric orbit to explain why it has not yet been detected.

To derive the periodicity in the ages of terrestrial craters, Jetsu & Pelt (2000) applied 5 different mathematical methods to 6 different subsamples of the crater record and one sample of extinction epochs. They showed interference of

rounding errors, and detected no periodicity in crater ages nor in mass extinction epochs.

A current view is provided by Ward (2002), as follows:

"Paleontologists have identified five "major" mass extinctions (>50 species die-off in less than a million years) and more than 20 other minor events over the past 550 million years. Earlier major extinction events undoubtedly also occurred, but we have no fossil record; these were probably associated with, for example, the early heavy bombardment that cleared out the solar system, the advent of oxygen in the atmosphere, and various "snowball Earth" events. Mass extinctions are viewed as both destructive (species death) and constructive, in that they allow evolutionary innovation in the wake of species disappearances. From an astrobiological perspective, mass extinctions must be considered as able both to reduce biodiversity and even potentially end life on any planet. Of the five major mass extinctions identified on Earth, only one (the Cretaceous/Tertiary event 65 million years ago that famously killed off the dinosaurs) is unambiguously related to the impact of an asteroid or comet (~10 km diameter). The Permian/Triassic (250 Ma ago) and Triassic/Jurassic (202 Ma ago) events are now the center of debate between those favoring impact and those suggesting large volume flooding by basaltic lavas. The final two events, Ordovician (440 Ma ago) and Devonian (370 Ma ago) have no accepted causal mechanisms."

This introduction has shown that impacts have been important in the later evolution of the Earth. Attempts have been made to demonstrate that several mass species extinctions have been triggered by impacts, and that their apparent periodicity provides some clues to impactor origin.

1.2. *Comparison of Earth and Venus as Impact Targets*

There are only a few rocky planets close enough to study for comparison with Earth; a modest sample considering the scale of the Universe. Of these, Venus is closest in size (95% of the radius, 81.5% of the mass) to Earth. Venus is Earth's nearest neighbour, at 72.3% of the Earth's mean distance from the sun. Shoemaker & Shoemaker (1999) show that the cratering rates of asteroids at Earth and Venus are approximately the same, taking account of the above differences and the likely existence of as-yet-undiscovered objects that remain entirely within the orbit of the Earth. Shoemaker & Shoemaker (1999) also show that the arrival rates of comets at Earth and Venus are also approximately the same. So, it may be anticipated that Venus and Earth present similar targets to approaching impactors. As the masses and compositions of the 2 planets are similar, the development of impact craters on them might also be expected to be similar. Therefore, crater topology on Venus is interesting not only in itself, but also for the understanding of terrestrial impacts - because of the similarities of the two planets, the extent to which original crater forms have been preserved and their accessibility to remote sensing. But some differences must be expected between craters on these two planets.

Impact Velocities. Grieve & Cintala (1999) give the mean arrival velocities of asteroids as 18 km s^{-1} at Earth but 21 km s^{-1} at Venus. For comets, Grieve & Cintala (1999) give the mean arrival velocities at Earth of ~ 40 to 55 km s^{-1}. Because of their proximity to the sun, any given comet will cross the orbit of Venus faster than the orbit of Earth. Compared to long period comets with their high eccentricity, short period comets will be travelling slower at perihelion but be proportionally faster at Venus than at Earth because Venus is closer to the sun. The momentum, or energy, of impact scales as the square of the impactor arrival velocity. It is therefore reasonable to assume that the spread of arrival velocity differences between the 2 planets will be smaller than the range of the mean arrival velocities given by Grieve & Cintala (1999) for Earth. In all cases, impact momentum will be higher at Venus, and any given impactor might therefore be expected to do relatively more damage than on Earth.

Atmospheric protection. However, the surface of Venus is protected by a denser atmosphere, with a mean surface pressure of 94 bar. Many authors, e.g.Hartmann (1972), Melosh (1989), and MacKinnon *et al.* (1997), attribute the complete absence of impact craters smaller than 1km to the efficient screening of small impactors by the dense atmosphere of Venus. Brackett & McKinnon (1992) point out that the mass per unit area of the Venusian atmosphere is ~10^6 kg m^{-2} and that an equivalent mass per unit area of water is 1 km deep. They show, for a carbonaceous chondrite arriving at 20 km s^{-1}, the dense atmosphere of Venus exerts a pressure against the incoming impactor of ~ 40% of the pressure due to an impact into a basalt surface. McKinnon et al (1997) follow Passey & Melosh (1980) to note the absence of small craters on Venus and propose that small impactors will encounter sufficient pressure to cause fracture, and possibly brittle failure, before impact.

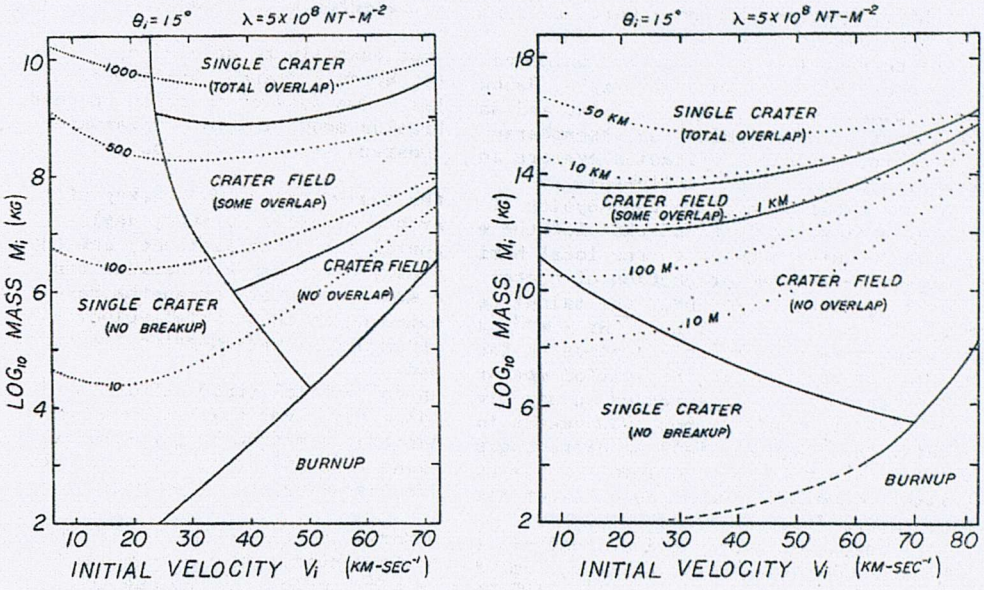
Surface composition. Venus is very dry, and different results should be expected from such an impact into a real terrestrial ocean 1 km deep. The physics of the impact excavation will be different: Matsui *et al.* (2000) model the tsunami wave induced by the Chicxulub impact, assuming it occurred in an ocean 200 m deep. Also, the geology of the impact products will be different, e.g.Jones *et al.* (2002) propose that komatiite may have formed following impacts into oceanic lithosphere. They show that the delicate crystals that characterise komatiite could not have been transported in a flow but must have been formed rapidly in situ, i.e. by rapid quenching of hot basaltic magma by surface water.

Multiple impacts. Passey & Melosh (1980) observed that features of many craters were consistent with having been caused by several impactors, rather than a single one (see Fig. 1.7). They produced Fig. 1.8a as a summary diagram for Earth by measuring the crater distribution within terrestrial crater fields, and deriving formulae for down range and across track dispersion. Fig. 1.8a is broadly consistent with Grigoryan (1979), which showed the Tunguska event could have been caused by an icy meteorite, of 10 to 100m diameter arriving at 30 km s^{-1} and exploding at ~ 4 to 10 km altitude. Chyba *et al* (1993) based similar calculations and conclusions on visual sightings recorded 20 years after the event and a contemporary seismic record in Ben-Menahem (1975).



Figure 1.7: Multile-flooredCrater. Magellan SAR image of a cluster of 4 craters in rim contact at 21.4^{0}S, 335.2^{0}E. The non-circular rim, and multiple, hummocky floors are probably the result of the break up of a single meteroid into several large fragments. The group, of approximately 14 km overall diameter, is illuminated here from the left at 38^0 incidence. From Ford et al (1993).

Svetsov (1996) explains the absence of meteoritic material at Tunguska by modelling the arrival of an asteroid-like impactor at 15 km s^{-1} and 45^0 incidence, showing that it could have been completely reduced by Earth's atmosphere into small fragments at ~ 6 to 10 km altitude, by the release of 6 x 10^{16} joules, which is equivalent to the explosion of 15 megatons of TNT. Passey (1980) produced Fig. 1.8b, an equivalent summary diagram for Venus, and expected crater fields an order of magnitude larger than on Earth. Fig. 1.8 indicates that, whereas an iron bolide of any size entering Earth atmosphere at the most likely asteroidal velocity (20 km s^{-1}) will not break-up, impactors at that velocity and of initial mass > 10^{10} kg will do so in the atmosphere of Venus. Also, the diagrams show that larger iron impactors, i.e.of initial mass < 10^{14} kg, should cause single craters. The dotted contours are a guide to final crater diameter; they suggest that most of the crater population of Venus should be crater fields, since all crater diameters are in the range: 2 to 300 km. The diagrams also imply that only small impactors with high velocity burn up, and are more likely to do so on Earth than Venus – a conclusion that seems counter-intuitive.



a. Earth b. Venus

Figure 1.8: Crater Field Formation Diagrams. Schematic illustrations of the fate of iron impactors, with a yield strength of 500 Mpa and an arrival entry angle of 15^0 into the atmospheres of Earth and Venus. Iron meteoroids are relatively rare, and the dotted contours are only a guide to the diameter of the largest crater in a crater field. Fig. 1.8a from Melosh & Passey (1980) and Fig. 1.8b from McKinnon *et al.* (1997).

For Venus, Ivanov & Yu (1991b) explored the case that all bolides above a critical diameter survive atmospheric deceleration without any damage, whereas larger ones completely disperse. They found such a critical diameter for Venus of 900 m but this does not lead to the correct crater size-frequency model. Hence, they concluded that all bolides giving rise to craters of 8 to 50 km diameter must retain some strength. In another paper, Ivanov & Yu (1991a) use a simplified model to estimate the effect of atmospheric break-up of meteoroids. Their results show that, if the projectile is regarded as a deformable fluid, its shape is a function of altitude, independent of initial projectile size, and results in aspect ratios in the range of 1.5 – 7 prior to impact. Furthermore, for a 2.5 km diameter, icy (100 kg m^{-3}) impactor, they show the crater diameter on Venus will be half that on an atmosphere-free planet.

Zahnle (1992) estimated that a meteoroid should flatten in the Venusian atmosphere into a pancake-like swarm with a cross-sectional area (orthogonal to its velocity vector) at least 20 times greater than that of the original meteoroid,

i.e. before ablation, any cross-section of the swarm containing its velocity vector will have an aspect ratio of at least 90:1 (diameter: depth).

Hills & Goda (1993) address atmospheric protection against the smaller asteroids like at Tunguska, which they show to have been caused by a bolide with a minimum diameter of 80m. Following Melosh (1989), they assume the bolide typicaly fragments into a "meteoroid debris cloud" that remains behind a single bow shock. As its diameter expands, they found to perhaps twice the diameter of the original asteroid, voids began to appear in the cloud and fragments develop their own bow shocks with a rapid increase in aerodynamic drag. They show that the dissipation of energy into the atmosphere is significant, protecting the surface from direct damage, i.e. by impact cratering, but giving rise to a blast wave that damages twice the area.

After considering Zahnle (1992), Herrick & Phillips (1994b) prefer to constrain the size of crater fields and multiple crater floors following Melosh (1981), i.e. for the atmosphere of Venus, to a maximum of twice the initial radius of the impactor. They then find that bolide flattening (ie pancaking) or atmospheric explosion must be included to prevent formation of craters smaller than those observed on Venus. Their simulations show that lower-density meteroids must be less likely to survive atmospheric passage than simple density differences account for in their model. They offer two candidate explanations: more bolide flattening or an explosion occurs after less kinetic energy loss. They favour the latter, on the grounds that Shultz (1992) and Ivanov *et al.* (1992) report that low-density fragmented material may assume a more streamlined shape, and find that 75% of the crater fields on Venus involve only 2 craters.

Ivanov *et al.* (1992) specifically deduce that a sphere of 2 km initial diameter, D_i , will create a 22 km diameter crater, D_m,i.e.

$$D_m = 11\ D_i \quad \text{.....(1)}$$

where: D_i = initial impactor diameter

D_m = measured crater diameter

O'Keefe *et al.* (1994) developed a Smooth Particle Hydrodynamic (SPH) model that included 2 forms of instability at the boundaries of the impactor:

- Kelvin-Helmholtz instabilities due to the bow shock. Here, the high temperature of the shock melts and ablates micron-sized particles from the bolide, into the flow past its sides. Also, where the dynamic pressure due to passage through the atmosphere exceeds the local strength of the bolide, the front of the latter is compressed and flattened.
- Rayleigh-Taylor instabilities driven by aerodynamic forces, i.e. lift and drag. These cause, for Venus, the relative diameter of the bolide to increase from unity to ~ 4 for a 1 km radius impactor, and ~ 1.7 for a 5 km impactor.

O'Keefe *et al.* (1994) find that these two instabilities together constrain distortion of the bolide such that its diameter, orthogonal to the velocity vector, does not expand more than ~ 20 times (and the thickness of the bolide does not reduce more than 400 fold).

Takata *et al.* (1995) used the scaling law of Schmitt (1980) to show that a stony (density of 2700 kg m^{-3}) sphere of 2 km diameter that impacts the surface of Venus at 20 km s^{-1} would give rise to a crater diameter of 7.5 to 5 times the impactor diameter, as impact angle varies from 90^0 to 15^0. Outside the crater itself, they found that an atmospheric shock front must disturb a "halo" area of 10 to 17 times the diameter of the crater.

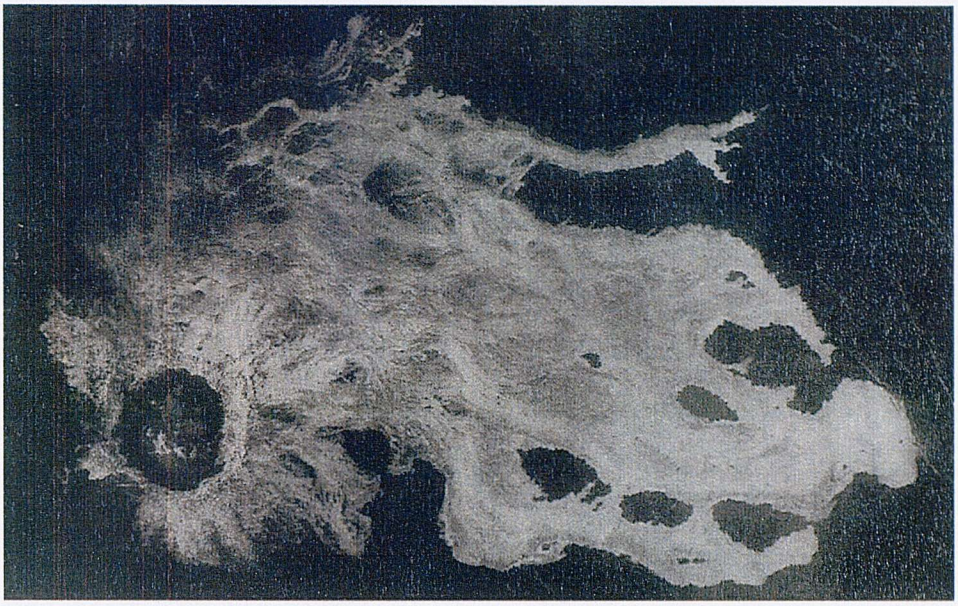


Figure 1.9: Markham Crater. Located at 4.1^{0}S, 155.6^{0}E on Venus, Markham has a partial peak ring and a radar dark floor, which might help to obscure the rest of the peak ring. Compared to its rim diameter of 69 km, the extensive outflows from this crater (out to 330 km) probably show that the impact released lava as well as created melt. From Head & Basilevsky (1999).

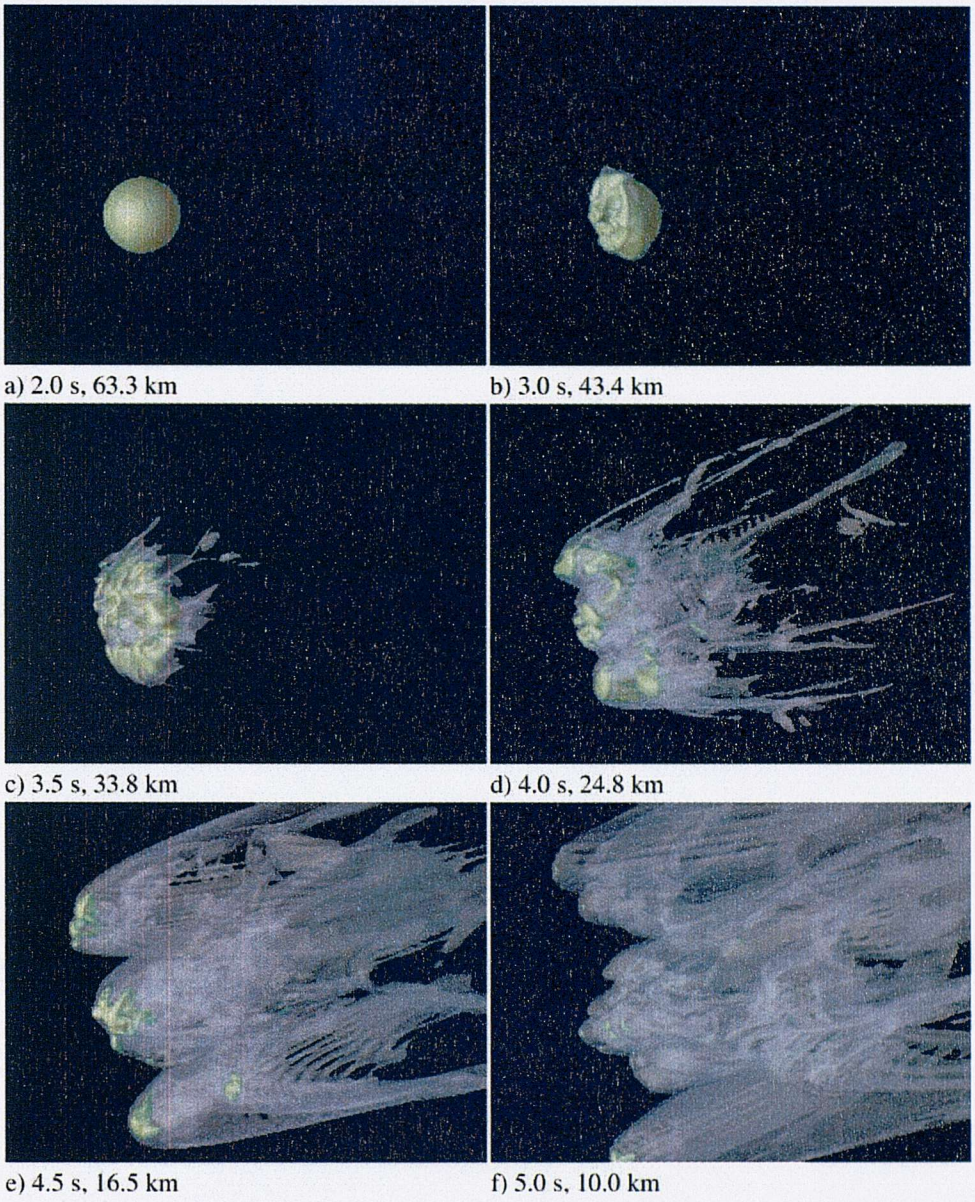
McKinnon *et al.* (1997) address peak-ring formation and the extensive run-out ejecta flows on Venus, e.g.from Markham (see Fig. 1.9), noting that these are:

- Correlated with larger crater sizes,
- Correlated with more oblique impact trajectories[2],
- Radar-bright compared to surrounding terrain, i.e. rough-textured at the radar wavelength (0.12 m).

Korycansky *et al.* (2000) introduced the term "pancaking" to describe how the smaller impactors, i.e. initially < 1 to 2 km diameter, are compressed and distorted during their passage through a dense atmosphere (eg of Venus). They addressed the deceleration of asteroids, using a high resolution model which included the effects of Rayleigh-Taylor and Kelvin-Helmholtz instabilities. They found that pancaking, illustrated in Fig. 1.10, occurs when compression waves

[2] as determined by the asymmetry of their ejecta distributions.

travel back through the body of the impactor before it falls through a Scale height ~15km on Venus) and, typically, this applies to impactors smaller than 2 km diameter. They show 1 km impactors are the smallest that survive to the surface.



a) 2.0 s, 63.3 km b) 3.0 s, 43.4 km

c) 3.5 s, 33.8 km d) 4.0 s, 24.8 km

e) 4.5 s, 16.5 km f) 5.0 s, 10.0 km

Figure 1.10: A sphere pancaking in the atmosphere of Venus. To illustrate the boundary of the pancake, 3 nested isosurfaces (blue, green and yellow: ρ = 100, 1000 and 2000 kg m^{-3}) are shown. In this example, the sphere has a diameter of 1.08 km and a density of 2400 kg m^{-3}, i.e. equivalent to the asteroid Castalia, when it first strikes the atmosphere at normal incidence. Under each image, the time after first striking the atmosphere, and the altitude to which it has descended, are shown. From *Korycansky et al.* (2002).

Most of their simulations of 1 km diameter impactors pancake, as do 2 km diameter impactors at 60^0 incidence. For 3 km diameter cases, they consider pancaking is not significant because ablation dominates. They do not model the impact itself but they do make use of a concept of an equivalent crater diameter, i.e. that of a crater due to a virtual impact if the surface of Venus were at that point in the atmosphere. In particular, they show that the descent of a 2 km diameter, normally-incident, bolide creates a 14 km diameter crater on the real surface of Venus, and it would create a 20 km crater if there were no atmosphere. Their best-fit case for pancaking has a drag coefficient of 1.4, but it is not possible [3] to deduce the aspect ratio from this coefficient.

Herrick *et al.* (1997) discuss crater morphometry and degradation on Venus more fully. McKinnon *et al.* (1997) and Grady *et al.* (1998) derive the likely impactor population statistics for Venus and Earth. Melosh & Ivanov (1999) address the later phases of crater formation on Venus and the importance of acoustic fluidisation. Jones *et al.* (2002) show a large iron bolide of 20 km diameter might induce a large igneous province (~ 10^6 km^3) on Earth, and obliterate its own impact crater.

This section has shown that study of the crater population of Venus can help inform understanding of impact processes on terrestrial continents. However, the smallest impactors, in a diameter range of 1 to 3 km, suffer more severe distortion during their decent through the atmosphere of Venus than would apply in Earth atmosphere. Also the mass of such impactors will be reduced by ablation to a different extent on the two planets. So, a study of the topography of smaller craters on Venus might help validate these aspects of current models of atmospheric penetration.

[3] Personal communication: K Kelleher, 25 Nov 2003

1.3. Comparison of Earth and Venus as Terrestrial Planets

An understanding of the geology of the two planets, shown in Fig. 1.11, is an essential prerequisite to any comparison of crater topography.

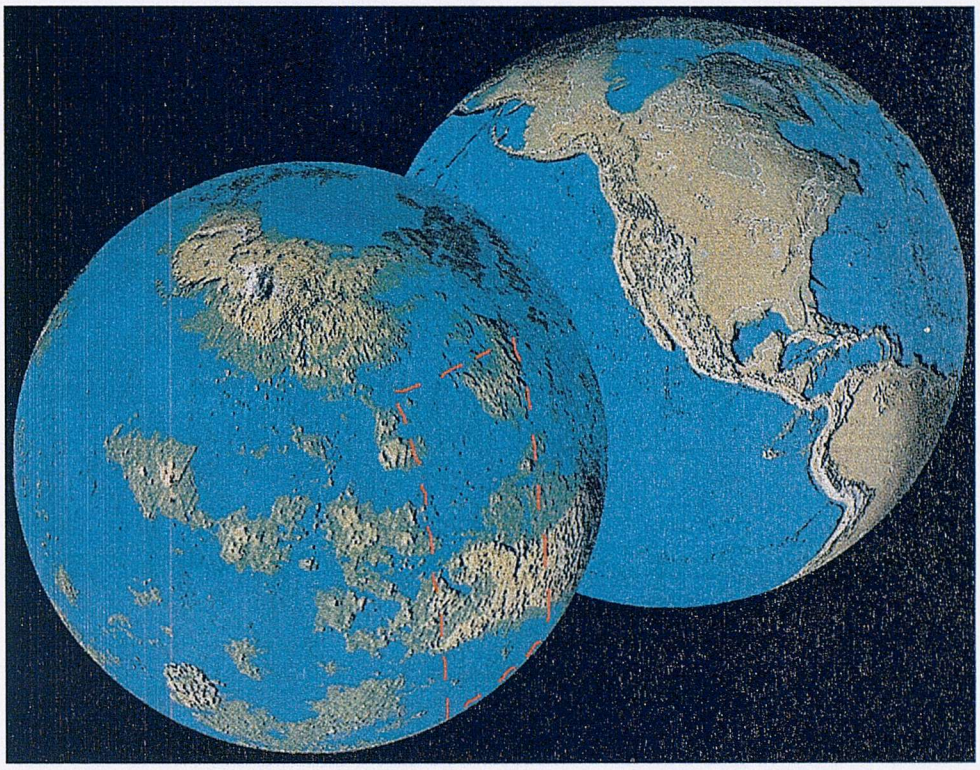


Figure 1.11: A comparison of Venus and Earth. Earth and Venus are of similar size. The landscape of Venus is dominated by vast plains and lowlands, here all coloured in a uniform blue to illustrate the similarities of highlands on Venus to continents on Earth. From Saunders(1999).

Formation and composition. Czechowski *et al.* (1992) describe the terrestrial planets as material formed by condensation and accretion processes about 5 billion years ago (Ga). They, and the sun, were formed in the same epoch, given by Wood (1999) as 4.55 Ga. For comparison, the oldest lunar rocks have been dated by Rb-Sr radiochronometry between 4.45 and 4.48 Ga (Cassen & Woolum, 1999). Kaula (1990) points out that Venus differs from Earth by only 18.5% in mass and 2% in mean density, when corrected to a mean pressure of 10^9 Pa and on the assumption that all Fe and FeS are in a central core. All the other bodies in the Solar System differ from Earth by more than 89% in mass and 8% in mean

density. Hence, Venus and Earth are by far the most similar of the planets in their primary properties, yet they differ markedly in secondary properties. Kaula (1990) identifies only 2 differences that must be a consequence of the planetary formation process:

- Earth has a large moon and a rapid prograde rotation; Venus rotates slowly retrograde.
- Venus currently has a greater abundance of atmospheric, non-radiogenic inert gases than Earth. If these gasses were of primordial origin, Venus should also have retained more water, which is not evident on the surface but may have been retained in the interior.

Bakun-Czubarow (1992) notes the small difference in mean density, and offers 4 conditions that would have to be true if Venus had the same composition and structure as the Earth:

- Most iron would have to be in the core, so the mantle would have a molar ratio Mg/(Mg+Fe) of about 0.88, and
- Almost all sulphur should be in the core, and
- The crust should be about 0.6% of the total planet mass, and
- The thermal gradient down to about 100km depth should be defined by solid-state convection and not be affected by the higher surface temperature.

Bakun-Czubarow (1992) advances the following possible causes for the lower mean density of Venus:

- Venus has less iron than Earth, mainly because adjacent planets captured more iron but perhaps also because the accretion of Venus ended later than the Earth and is relatively richer in low-temperature condensates.
- Venus has less sulphur than Earth, because temperatures in the solar nebula where the proto-Venus formed exceeded the condensation temperature of FeS, namely 700^0K, so iron in this form escaped. NB: de Pater & Lissauer (2001) suggest a lack of FeS may have since caused the core of Venus to solidify, and hence the planet's lack of a magnetic field.

- Venus has more oxygen than Earth,i.e.more oxidation of surface materials. This follows Ringwood & Anderson (1977): being smaller, Venus had a lower accretion temperature so was more oxidised, giving different Fe/(FeO + MgO) ratios in the mantle (Venus: 0.24, Earth: 0.12) and planetary mass fraction of core (Venus: 0.23, Earth: 0.325).
- High surface temperatures on Venus shifted the basalt-eclogite phase transition boundary, reducing the density of the basaltic crust.

Crustal characteristics. Kaula (1990) deduces that "*at pressures of 1.5 to 2 Gpa, basalt (or gabbro) undergoes a phase transition to eclogite, which is denser than the ferromagnesian rocks expected to constitute the mantle. This transition would thus set a limit to the mean crustal thickness of 100 km, depending on temperature.*" Bakun-Czubarow (1992) estimates that the crust of Venus is at least 21 km thick, and considers that its morphology shows signs of thermo-tectonic activity and isostasis. Noting the transition to radial, rather than concentric and/or polygonal, fracture patterns in craters of 80 - 100km diameter, Wichman (1993), following both Baldwin (1968) and Brotchie & Silvester (1969), derived a lithospheric thickness for Venus of 48 - 72 km. Moores & Twiss (1995) consider that the high surface temperature of Venus argues against the existence of thick, relatively dense lithospheric slabs. They concede that, whilst Mars, Mercury and the Moon appear to have a single global plate, only on Venus "*is there a suggestion of anything like plate tectonic processes.... and these are apparently subordinate, or at least episodic*". Also, they consider "*theoretical models of the structures on Venus argue for a thinner boundary layer (lithosphere) than that common on Earth*". Head (1999) quotes estimates "from spacecraft data[4] " that crustal thickness averages 40 to 60 km, with local variations – particularly in tessera regions – that probably exceed 50 to 60 km. This is not unlike the thickest parts of the Earth's continental crust (60 - 70 km), where most identified impact craters are located. De Pater and Lissauer (2001) consider that Venus' higher surface temperature suggests the lithosphere to be half as thick as that on Earth. Nimmo[5] considered the lithosphere of Venus might be thicker, e.g. ~ 150 to 200 km.

[4] Presumably, Magellan's orbit parameters for Cycles1-3, when atmospheric drag was minimal.
[5] Personal communication, F Nimmo, Mar 2002

Previous measurements of the depth of large craters on Venus show a mean depth of about 1 km, irrespective of diameter, i.e. Sharpton (1994), for 3 craters > 100 km, and Herrick & Sharpton (2000), for 3 craters > 90 km. Wichman (1993) might explain such separation from the accepted scaling laws for the largest craters as due to post-impact isostatic equilibration rather than igneous modification. Wichman (1996) analyses rim, floor and central peak diameters, and notes that tectonism accompanies an increased floor size in bright-floored craters, possibly due to central uplift. Wichman (1996, 1999) favour post-impact volcanism as the explanation of dark-floored craters. Herrick & Sharpton (1996) find evidence that Mead has an updomed floor and low relief at the floor margins. They observe the up-doming of the central floor cannot be due simply to viscous relaxation[6] indicative of the bulk mechanical properties of the lithosphere; they concede that subsurface structure must be postulated in order to derive credible values for lithospheric properties. They also observe post impact volcanism, especially in the crater field. Brown & Grimm (1996) assessed all 19 craters on the planet >75 km diameter and produced azimuthly averaged profiles for 12 craters (including Mead, Joliot-Curie and Potanina), which are all concave. They do not address the relatively shallow topography of these craters, ascribing depression of the central floor (and the associated fractures) to subsidence. They model sub-solidus thermal contraction below the crater as due to conductive cooling of impact-induced heat over a time period of 100 Ma. Their results fit the actual altimetry of Stanton (23^0S, 199^0E) well. They conclude 3 bright-floored craters (Stanton, Greenaway and Stowe) give no indication of rebound[7]. They exclude consideration of 7 dark-floored craters because the dark material might mask any rebound.

Tectonics. Head (1999) observes that, prior to Magellan, Venus was expected to display evidence of earth-like plate tectonics. Tectonics recycles the Earth's crust on timescales of 100 to 1,000 million years (de Pater & Lissauer, 2001), modifying and eventually removing craters. The data returned by

[6] "Viscous relaxation" is not defined by these authors but is said to result in doming of the central floor,i.e.it is taken here to be synonymous with Wichman's "isostatic equilibration".

[7] "Rebound" is taken here to mean modification towards a state of "Isostatic Equilibrium" as defined in de Pater and Lissauer (2001). Melosh and Ivanov (1999) use "Elastic Rebound" to describe the tendency of rock, that is not crushed due to its proximity to an impact, to experience only elastic distortion and return to the pre-event state.

Magellan shows evidence of Venus having experienced periods of contraction and extension but no sign of plate tectonism.

Weathering. Both weathering and volcanism give rise to sedimentation and modify terrestrial landscapes. No author reports similar effects on Venus. There is now no water on the surface of Venus to cut channels through sediments of any kind. Surface wind speeds on Venus were reported by Greeley (1992) as 0.3 to 1 m s^{-1} and shown to have minimal effect on landscapes. Although volcanism is very prevalent on Venus, this wind speed is insufficient to expose geological strata.

Hence, this survey shows that these two planets have similar composition but, perhaps because of the lack of water, different tectonics and weathering. Attempts to derive the thickness of the crust of Venus from crater characteristics have not succeeded. The planets present different problems for crater assessment. On Earth, craters are difficult to locate but their original form can be derived from seismic surveys, etc. On Venus, Magellan has provided comprehensive surface coverage but its topography cannot be fully understood without more data on surface composition and underlying geology.

No evidence emerges from this survey to suggest that impact crater forms on Venus are different to those on Earth, so study of one should inform the other. However, better use could be made of the Magellan data to more accurately characterise the craters on Venus by using a more rigorously selected sample and the existing tools but to better resolution.

1.4. The Surface Geology of Venus

The distribution of the topography of Venus is unimodal and, as illustrated in Fig. 1.12, quite unlike the bimodal topography of the Earth.

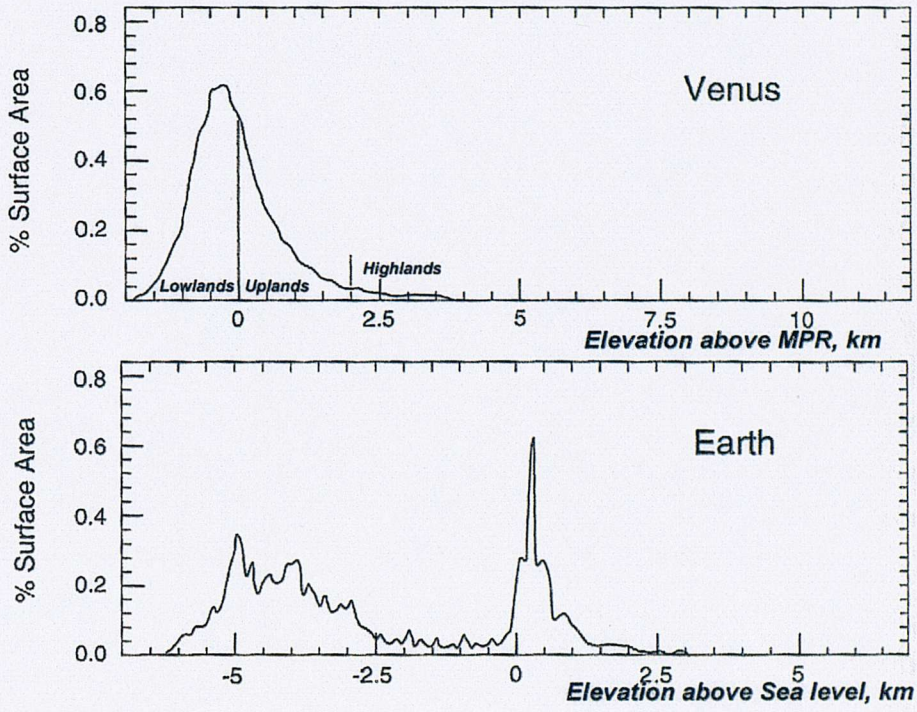


Figure 1.12: Hypsometric curves for Venus and Earth. Altitude frequency distribution of the topography of each planet. From Head & Basilevsky (1999).

Christiansen & Hamblin (1995) describe 60% of the surface of Venus as lowland plains lying below the Mean Planetary Radius (MPR), which Ford & Pettengill (1992) quote from Magellan altimetry as 6051.84 km. These lowland plains have up to 500 m local relief and compressional deformations similar to terrestrial mountain belts. The extent and smoothness of the plains, and sample analysis by Venera and Vega landers (see Marov & Grinspoon, 1998), indicate they are formed from volcanic basalt. Few volcanoes lie on plains. However, plains are crossed by lava flow fronts and long sinuous rilles, which might be associated with more recent volcanism. The plains include basins as deep as 2 km, which Christiansen & Hamblin (1995) consider are due to downward bending of the lithosphere rather than impact cratering. They note the near

absence of craters on the plains and date them as between a few 100 to 1,000 Ma old. Wrinkle ridges[8] are prevalent. Christiansen & Hamblin (1995) summarise the plains as resembling terrestrial ocean basins, the northern plains of Mars and the Lunar mare basins. The largest, Atalanta Planitia, is about the size of the Gulf of Mexico.

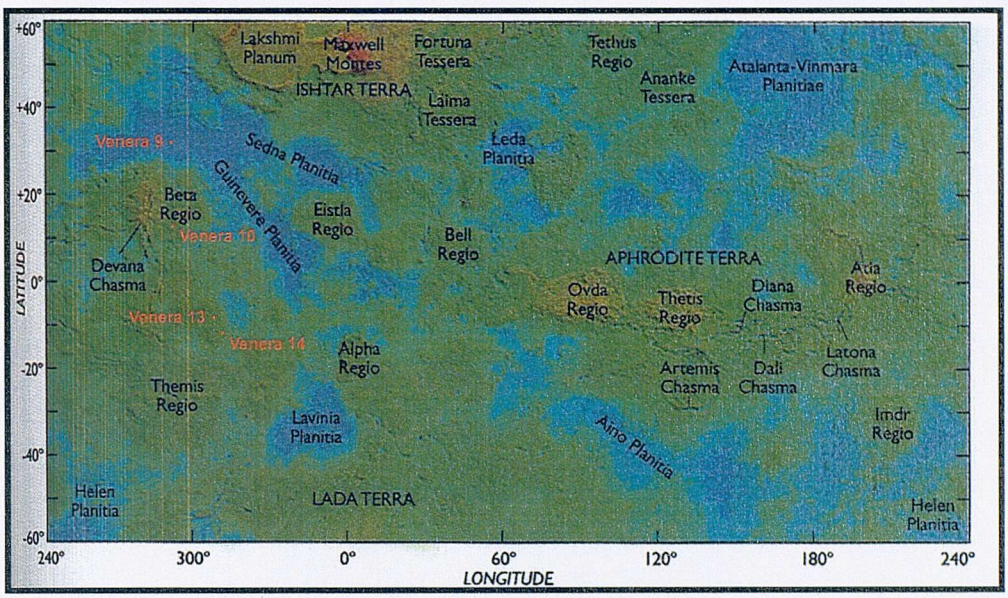


Figure 1.13: Venera Landing Sites. Mercator projection of Magellan altimeter data, showing landing sites of Venera imaging missions. Highest elevations in red; lowest in blue. From de Pater & Lissauer (2001), courtesy of Ford, NASA.

The only available imagery from the surface of Venus is of the immediate surroundings of 4 Venera landers, all on plains. See Fig 1.13. Marov & Grinspoon (1998) note the first image of the surface of Venus showed Venera 9 landed on a 30° slope, perhaps of talus from a nearby cliff. It was close to Beta Regio where plains embay the higher ground and have high reflectivity at radio frequencies. The image shows the horizon is only a few 10s of metres away. The largest rocks were found to be 0.5 to 0.7 m wide and 0.15 to 0.2 m high. Fragments are seen to have broken off these plate-like rocks and some fine-grained sediment is present, but some material from the fissures between the rocks may have been carried away by the, presumably light, surface winds. Some rocks have dark splotches, which may be due to erosion. Venera 10 landed on a wrinkle-ridged plain 2,000 km from Venera 9 and at a similar altitude. It rests on

[8] Defined by Head (1999) as 10 to 50 km long, narrow (1 km), sinuous and occurring in parallel sets

a large rock, no less than 3 m in diameter, it returned a landscape characteristic of magmatic bedrock , and the horizon is distant. That large rock and others nearby show some signs of erosion, and are embedded in dark sediment. Other cameras on Venera 13 and 14 returned similar images, respectively from radar-dark plains (see Fig 1.13) and the slopes of a 75km diameter volcano. They show also signs of unconsolidated sediment or debris a few centimetres deep, with rocks bedding into it. All the Venera and Vega landers conducted geochemical and physical tests of surface composition.



Figure 1.14: Venera 13 Image. One of the panoramas near Phoebe Regio. The wide-angle camera was tilted to scan from horizon to horizon, via notched photometric marks on the base of the spacecraft. Note the dominance of slabby or platy rocks, interspersed with little sediment. These rocks were found to be similar in composition to terrestrial basalts. Personal communication R Ghail, Jan 2004.

Christiansen & Hamblin (1995) describe volcanic domes and broad swells, rising as much as 2 km above the mean planetary radius, as uplands. They have extensional features: fracture belts, troughs and rifts. Many volcanoes have summit craters and flow features. Low-relief calderas, fissure-fed lavas and central volcanoes are common. Also, common on uplands are coronae[9]. The most prominent upland dome, Beta Regio, contains a shield volcano flanked by the Devana Chasma rift, and is several thousand kilometers across. Christiansen & Hamblin (1995) propose that these uplands are similar to Tharsis and Elysium on Mars and may be the result of up-welling mantle plumes.

[9] thought to be of volcanic origin and unique to Venus.

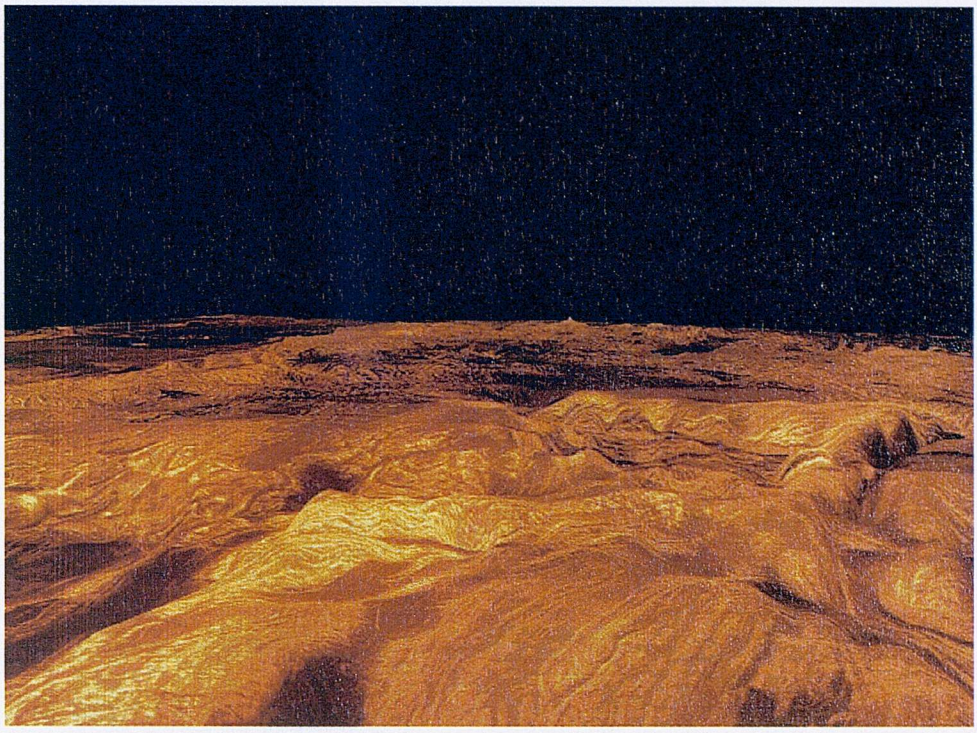


Figure 1.15: Synthetic perspective view of highlands in Ovda Regio. SAR data superimposed on altimetry. Simulated colour, based on images from Venera landers, is used to enhance small-scale structure. The view is from the NE looking to the SW; x22.5 vertical exaggeration. The complex ridge terrain, also know as tessera, are interpreted to have formed by compression. In several places the ridges are flooded by radar-dark (smooth) lava flows, after ridge formation. From JPL website (1993), P42392 MGN-118.

Head & Basilevsky (1995) define the highlands as the tessera[10], which cover only 8% of the surface of Venus and might appear as illustrated in Fig. 1.15. Christiansen & Hamblin (1995) describe *"flat plateaus at 3 to 5 km elevation, peaking to 11 km above the planetary mean"* as highlands, covering *"less than 15%"* of the surface. These highlands include sinuous valleys and ridges interpreted as compressional, and grade out into lower regions of complex disruption called tesserae. For comparison, Earth's continents cover 30% of the planet and Everest peaks at 12 km above the planetary mean. The highest highland massif on Venus, Ishtar Terra, is similar in size to Australia, and includes Maxwell Montes, the highest mountain on the planet. The largest highland, Aphrodite Terra, extends more than 9500 km and is approximately the size of Africa. It is dominated by 3 tessera plateaus separated by saddle-like depressions. The focus of this thesis is the most westerly of these tessera, Ovda Regio, and the plains to the north and south of it. Christiansen & Hamblin (1995)

conclude that the highlands are due to crustal thickening over regions of mantle down-welling. Head (1999) finds that tessera have up to 40% higher crater densities than the global average, suggesting they are oldest geological units.

Marov & Grinspoon (1998) present the data given in Table 1.1 for the surface characteristics for the terrestrial planets. Note that the radar reflection, *k*, from the surface of Venus is less narrowly confined than from Mars, and approximately twice that of the mean value for the Moon, Mercury and Mars. The Relative[11] Permittivity, ε , values for Venus are typical of dry silicate rock, like basalt or granite (see Kuzmin & Marov, 1974), and are consistent with the extremely low values of radio-thermal emissivity, typical of dry basalts. Also note that the mean value of permittivity for Venus leads to a density estimate of 2,500 kg m^{-3}, much higher than the Moon and parts of Mars.

Planet	Reflection	Relative Permittivity	Density	Scattering Angle
	k, %	ε	ρ, kg m^{-3}	θ, degrees
Moon	5.7 – 6.3	2.6 –2.8	1200 – 1300	6 - 7
Mercury	5.8 – 8.3	2.7 – 3.3	1300 – 1600	5 - 8
Venus	11 - 18	4 – 6	2000 – 3000	2.5 - 5
Mars	3 - 14	1.4 – 4.8		

Table 1.1: Some coefficients for the Terrestrial planets. Density calculated from Krotikov, (1962) ie: $\rho = (\sqrt{\varepsilon} - 1)/a$, for dry terrestrial rocks at a few wavelengths depth, where: ρ is the planet's sediment density, ε = permittivity, and a is usually ~ 0.5. Mean Scattering Angle, θ, is as due to surface roughness. From Marov & Grinspoon (1998).

Hence, Marov & Grinspoon (1998) suggest an absence of porous or finely granulated rock on the surface of Venus. Penttengill et al (1982,1988) deduce that the surface density on Venus is unusually high at 2,500 to 5,000 kg m^{-3}, which argues against the presence of large areas of sediment on Venus. At the time of Magellan's arrival at Venus, Garvin (1990), extrapolating from lunar conditions, estimated that the impact-generated regolith on Venus would be between 2 and 12 m deep if spread uniformly over the entire surface. However, the Magellan data shows this is almost certainly an over-estimate, because it ignored important conditions at Venus, e.g. atmospheric screening, lithospheric turnover, etc.

[10] Form latin for a tile.
[11] Relative to the dielectric constant of free space

Crumper *et al.* (1993) observed a distribution of volcanic and tectonic activity over broad zones, and some symmetry in the rifting on Ovda Regio on a scale of 1000s of km. They suggest that Venus might have a larger number of less rigid lithospheric plates than the Earth.

Marov & Grinspoon (1998) describe only 8% of the surface of Venus as highlands, and point out that much of this uplift may be due to spreading over hot spots. For example, the western section of Aphrodite Terra (i.e. Ovda Regio) is shown by Crumper & Head (1987) and Head & Crumper (1987) to contain many features similar to those characteristic of diverging lithospheric plate boundaries in terrestrial mid-ocean ridges, especially mutually symmetric topographic elements (oriented from northwest to southeast). Solomon & Head (1982) proposed planetary heat loss occurs through the creation and separation of plates rather than scattered volcanism. The correlation of the topography of Aphrodite Terra and the gravitational field could point to a more direct connection on Venus than on Earth between large scale convection in the mantle and the divergence of tectonic plates. See Sjorgren *et al.* (1980)

Arvidson *et al.* (1994) found a gradual increase in dielectric constant around and over Ovda Regio. From rock-like values (4 to 5) at 6054 km above planet centre, it increases to approximately 50 at 6056 km, and then returns to rock-like values over the next 500 m. They suggest this indicates a ferro-electric surface layer in the highlands. Campbell (1994) proposes that the high permittivity and low emissivity of highland regions may be due to high electrical conductivity in the surface. This may be associated with mineral deposits, at high altitude, e.g. iron pyrite (Pettengill *et al.*, 1988; Klose *et al.*, 1992).

The surface of Venus is much more homogenous than that of Earth; it is very arid, and its landscape is made up of barren basaltic rock with little sediment. The local topography of the surface is not unlike that of an Earth without its oceans. The highlands have some unusual electrical properties, which may affect SAR imagery.

1.5. The Crater Population of Venus

Magellan provided the first imagery that resolved all craters down to the smallest size possible, which is 1.3 km diameter. Hartmann (1999) shows that the distribution of crater diameters on Venus is similar to that on continental shields on Earth (see Fig. 1.16). The mode for Venus (16 km diameter) is no more than twice that in Europe and North America. Phillips *et al.* (1991 and 1992), Price & Suppe (1994), and MacKinnon *et al.* (1997) use the small crater population and its size distribution to derive an approximate surface age for Venus of 800 - 500 Ma, and associate this with turnover of the crust. This finding also explains the sharp upper cut-off of the distribution. Gentler slopes at the extremes of terrestrial distributions reflect difficulties in recognising very large and very small craters.

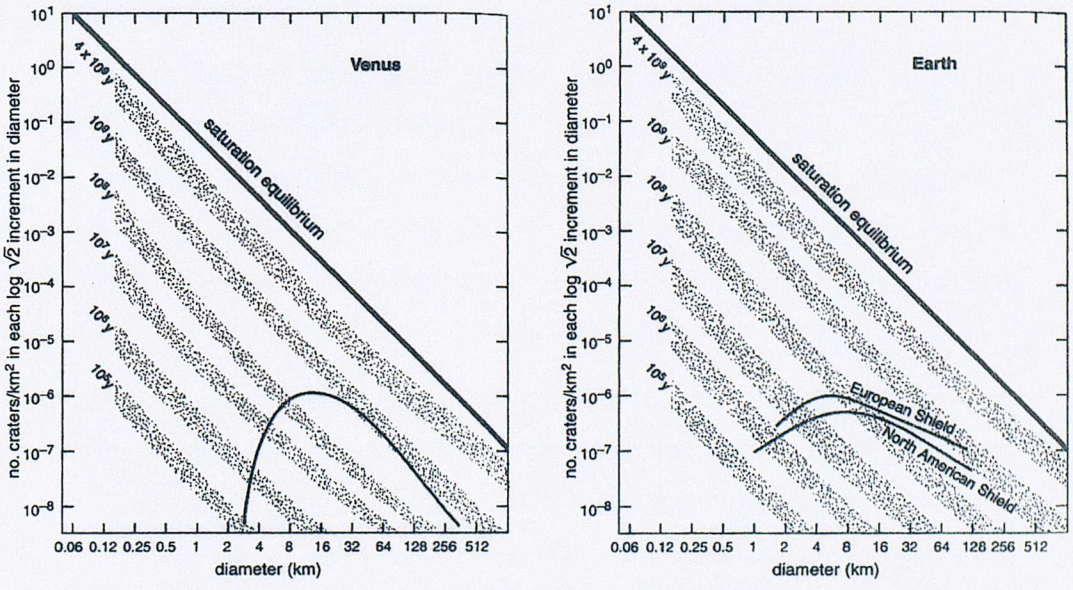


Figure 1.16: Approximate crater densities as a function of crater diameter. Using Moon rocks for ground truth and a model for the density and size distribution of impactors over time and throughout the solar system to estimate surface age. Small craters are screened out by any atmosphere and geologic processes remove the largest and oldest. From Hartmann (1999).

There are two published databases of craters on Venus:

- The US Geological Survey (USGS) database[12], March 1999 version, lists 967 craters: from the largest, Mead (270 km diameter), to the smallest (1.3 km).
- The Lunar and Planetary Institute (LPI) database[13], updated in 2002, lists a population of 941 after elimination of some contentious candidates. This database has a more comprehensive set of parameters.

Neither database provides estimates of crater depth. This Thesis prefers the LPI version as the more comprehensive and better maintained source.

Phillips *et al.* (1991) analysed 763 craters as Magellan data was coming in, noting that they showed no evidence of weathering, erosion or burial. They calculated, by 4 methods, the mean surface age as 400 – 500 Ma. Phillips *et al.* (1992) observed that the craters on Venus:

- Number less than 1000.
- Cannot be distinguished from a random distribution, and
- Are almost always pristine.

Arvidson *et al.* (1992) suggested the degree of degradation of radar-dark deposits associated with craters could be used for estimating their age, and the neighbouring geologic units. Phillips *et al* (1992) offered 2 simple, end member, planetary resurfacing models of a spectrum of possible explanations:

- Catastrophic Resurfacing Model (CRM). In this model, the entire surface of the planet is of a single age. They note that both the small percentage of craters being removed due to volcanic embayment or tectonic deformation, and the geological surface age, correlate with local crater density. In particular, they show a correlation of embayed craters with low crater density, implying the removal of craters by volcanism rather than tectonics. They also show a correlation of crater density and radar cross-section, confirming that crater elimination is associated with certain geological terrain. They conclude the youngest geological units show recent activity, the Aphrodite volcano-tectonic zone being dominant.

[12] GG Schaber, RL Kirk & RG. Strom, Mar 1999, available on-line by USGS at websites: wwwflag.wr.usgs.gov/USGSFlag/Space/venus/ & astrogeology.usgs.gov/Projects/VenusImpactCraters/
[13] In 2002, Herrick placed this database on website: http://www.lpi.usra.edu/research/vc/vchome.html

- Equilibrium Resurfacing Model (ERM). In this model, resurfacing occurs in patches of area, a, at frequency, ω, due to spatially non-random volcanism (see Head *et al.*, 1997). The small number of partially removed craters is shown to be a function of patch size. The areas that give this small value are, as a fraction of the planet area: $0.0003 < a < 0.1$, or, in terms of the subtended solid angle, $4^0 < a < 74^0$. This implies that the resurfacing events can either be of 150 thousand km^2 mean size at intervals of about 150 thousand yrs, or of 45 million km^2 every 50 million years. However, the areas of the craters themselves constitute a larger fraction of the area of the smaller patches, so these craters are less likely to be completely removed by them. Hence, the observed proportions of embayed and modified craters are shown to be most consistent with a value of a just below 0.0003 but the authors concede there is some evidence to reject all values of a.

Phillips *et al.* (1992) find both models unsatisfactory, and modify their ERM to apply in a limited number of small patches in any geological period, with the remainder of the planet in crater production. Hence they postulate a two-stage model with mantle-scale and lithospheric-scale processes interacting.

Strom *et al.* (1994) summarise early Magellan results to propose that:

- the crater population is spatially and hypsometrically[14] random;
- a global resurfacing occurred 300 Ma ago, and then ended abruptly (in < 10 Ma); and
- the area bounded by 30°N and S, and 60° - 300°E, containing significantly more heavily fractured and lava-embayed craters than the planetary average, is subject to a continuing low level of activity.

Herrick & Phillips (1994a) is perhaps the most comprehensive analysis of crater density, see Fig 1.17. They point out that low crater density is "*associated with a long, primarily equatorial, band of rifts and large volcanoes*". They note an excess of craters from 0 to 1 km below MPR and a deficit from 0.5 km to 1 km above it. They give a production age of the venusian crater population as 400 Ma.

[14] i.e. by altitude

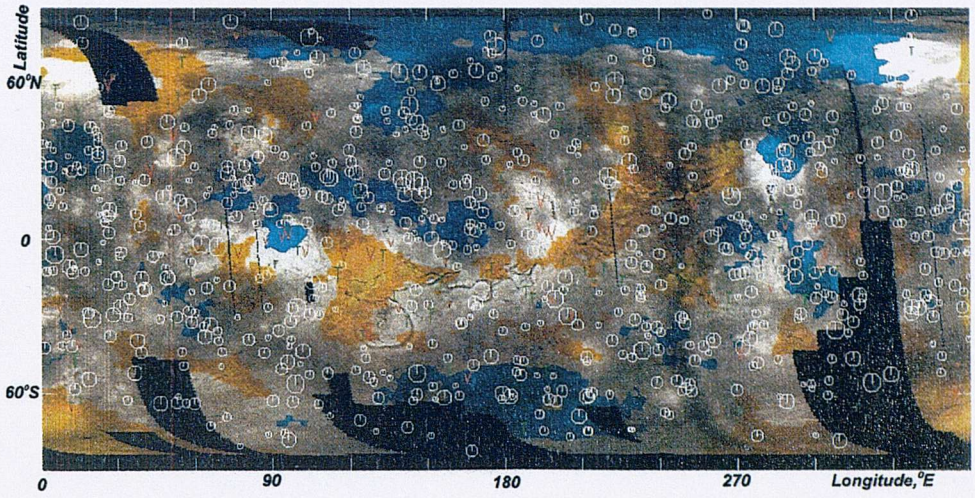


Figure 1.17: Crater density distribution. Cylindrical projection of areal distribution of crater density over greyscale topography, with dark denoting lowlands and bright denoting highlands. For a counting circle of 1200 km radius, orange and yellow areas represent regions where crater densities are 1Φ and 2Φ lower than the mean; blue regions have densities 1Φ and 2Φ higher than the mean. White octogons are the locations of pristine craters, red Vs are volcanically embayed craters, and green Ts are tectonically deformed craters. From Herrick & Phillips (1994a).

Namiki & Solomon (1994) argued that large volcanoes have half the average crater density, and are still evolving. Price & Suppe (1994) found significant areal differences in crater density for different geologic units. Herrick *et al.* (1995) argued that the original resurfacing process was less dramatic and is still evolving throughout the planet; and Strom *et al.* (1995) then extended the resurfacing period to 300 - 500 Ma ago. Hauck *et al.* (1998) concluded that complete spatial randomness cannot be used to constrain resurfacing models because observed crater distribution can be matched several ways and the strong indication of a significant spread of ages within the plains. Basilevsky & Head (2001a) dated sub-populations of craters ∃30 km on regional plains and on post-regional-plains units, showing the results to be independent of crater size and latitude.

Marov & Grinspoon (1998) question the uniformitarian assumption implicit in many early papers on Venus tectonics. They consider that the distribution, numbers and modification spectrum of impact craters imply that resurfacing rates have declined rapidly since an episode, or epoch, of lava flooding that produced the globally distributed plains. The area addressed in this Thesis includes parts of

2 such plains: Lada and Lakshmi Planitiae. Arkani-Hamed *et al.* (1993) propose a single transition, due to a rapid thermal evolution of Venus associated with its higher surface temperature. Parmentier & Hess (1992) proposed episodic plate tectonics due to chemical differentiation in a one-plate planet. Turcotte (1993) suggests that, for the last 500 ± 200 Ma, the lithosphere of Venus has been cooling and thickening as a one-plate planet. Marov & Grinspoon (1998) also quote model results as showing a periodicity of about 300 to 500 Ma.

McKinnon *et al.* (1997) assume that the impactor population is composed of six categories of asteroid or comet, and calculate the flux of each sub-population from first principles, estimate the effects of the atmosphere on each, and sum them to produce a close fit to the observed crater population.

In summary, the crater population of Venus have been classified, and found to be similar to that of continental shields on Earth. It indicates a mean surface age of Venus between 500 and 800 Ma, but its distribution is near random and cannot provide clues as to the nature or cause of the resurfacing event(s) that removed earlier craters. The sub-populations of crater-forming impactors have been characterised. Two databases of crater plan-form parameters are available; this Thesis primarily uses that published by LPI.

1.6. Crater Topography

On Earth, all post-impact structures become subject to erosion and sedimentation over the aeons following their formation. The surface of Venus shows few signs of Earth-like weathering, and most impact craters appear "pristine". The topography of the largest craters can be derived directly from Magellan altimeter or SAR data products. Hence, early research focussed on the larger craters:

- Schaber *et al.* (1992) first assessed the depth of 78 craters, with diameters of 2 to 100 km, from single SAR images,i.e.following the monoscopic method presented in Leberl *et al.* (1991). Then, using Magellan altimetry, depths were derived for 18 craters with a diameter > 50 km and found to be consistently shallower than found previously, typically by 500 m.
- Ivanov *et al.* (1992) took, from Ivanov (1989), depths of 76 craters with a diameter between 8 and 64 km. These had been derived by floor-offset from Venera 15 and 16 imagery. Ivanov *et al.* (1992) present these in 6 diameter bins, with a standard deviation bar of several 100m for each bin. Their trend line is validated against altimetry of Aurelia crater, and compared to the depths of the best preserved terrestrial craters.
- Sharpton (1994) measured the depths of 94 craters > 18 km by the floor-offset in Full-Resolution Image Data Records (F-MIDR) pairs, and derived a single trend line by regression analysis. Using Leberl *et al.* (1991), height uncertainties were estimated to be $\forall$ 220m.
- Alexopoulos & McKinnon (1994) characterised all 76 craters > 30 km, but presented only representative altimetry profiles of Mead and Isabella.

Ford & Pettengill (1992) showed that the Magellan altimeter achieved its design goal of a range resolution of 50 m. Because of the elliptical orbit, it's horizontal resolution varied with latitude; see Ford *et al.* (1993). The best resolution, 12 km east-west and 8 km north-south, was achieved near periapsis at 10^0N; towards the edges of cover at 80^0N and 60^0S, it deteriorated to 27 km east-west and 15 km north-south. Sharpton (1994) first summarises earlier work in

the form of the diagram reproduced as Fig. 1.18, and then provides analysis, by the floor-offset method, of all craters on Venus above 20km diameter. This technique, fully described by Ford *et al* (1993), rests on assumptions that:

- the floor is flat, and
- the eastern and western rim heights are the same.

Noting that two thirds of all craters on Venus are 20km diameter or less, Sharpton (1994) proposed a clear distinction for the craters larger than 20km:

$$\text{depth} = 0.4(\text{diameter})^{0.4} \quad \text{for 'Fresh' (radar bright}^{15}\text{)} \quad \ldots\ldots\ldots\ldots\ldots\ldots(2)$$

and

$$\text{depth} = 0.3(\text{diameter})^{0.28} \quad \text{for 'Modified' (radar dark}^{16}\text{)} \ldots\ldots\ldots\ldots\ldots\ldots(3)$$

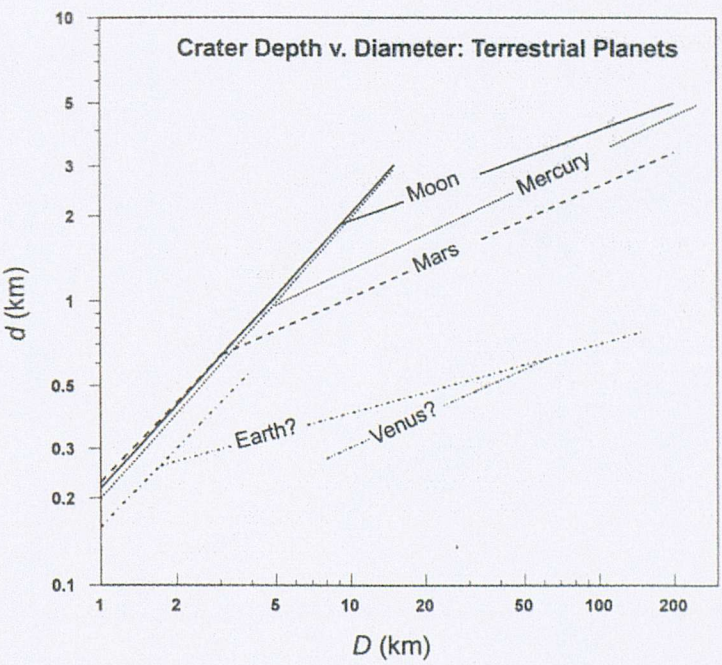


Figure 1.18: Trends for the depths, d, and diameters, D, of craters on the terrestrial planets. Expectations prior to Magellan, based on earlier work for the Moon (Pike, 1974), for Mars (Pike, 1980), for Mercury (Pike, 1988), by scaling lunar dimensions according to the inverse gravity law (Grieve et al, 1981), for Earth (Grieve & Robertson, 1979), and for Venus (Ivanov *et al.*, 1986 and Basilevsky *et al.*, 1987). The key parameter controlling scaling is target surface gravity but target and impactor densities also have influence. The surface gravity of Mars, Mercury and Moon are

[15] Here, radar bright means a strong backscatter signal, typically either because the surface is orthogonal to the received signal, or rough at the radar wavelength, or both.
[16] Radar dark means a weak backscatter signal, e.g. because the surface reflects the signal away from the receiver because it is non-orthogonal, and/or smooth at the radar wavelength.

within a factor of ~2. Assessment of craters on Earth has tended to confirm 1/g scaling but results from Venus are important confirmation. From Sharpton (1994)

Leberl *et al.* (1992) set out formulae to derive elevation from SAR distortion in 2 stereo images, and provided a method to estimate the errors. Connors (1995) also provides the relevant equations. McKinnon *et al.* (1997) identify some inconsistencies between floor-offset and altimeter depth measurements, but show a fundamental similarity of depth-diameter relationships on Venus, Mercury and the Moon, when scaled by g^{-1}, or rather less.

Grieve & Cintala (1999) provide the most recent analysis of crater depth:diameter ratio, primarily from their terrestrial database and reproduced here as Fig. 1.19. Their work on Venus relies on Sharpton (1994) and predates Herrick & Sharpton (2002).

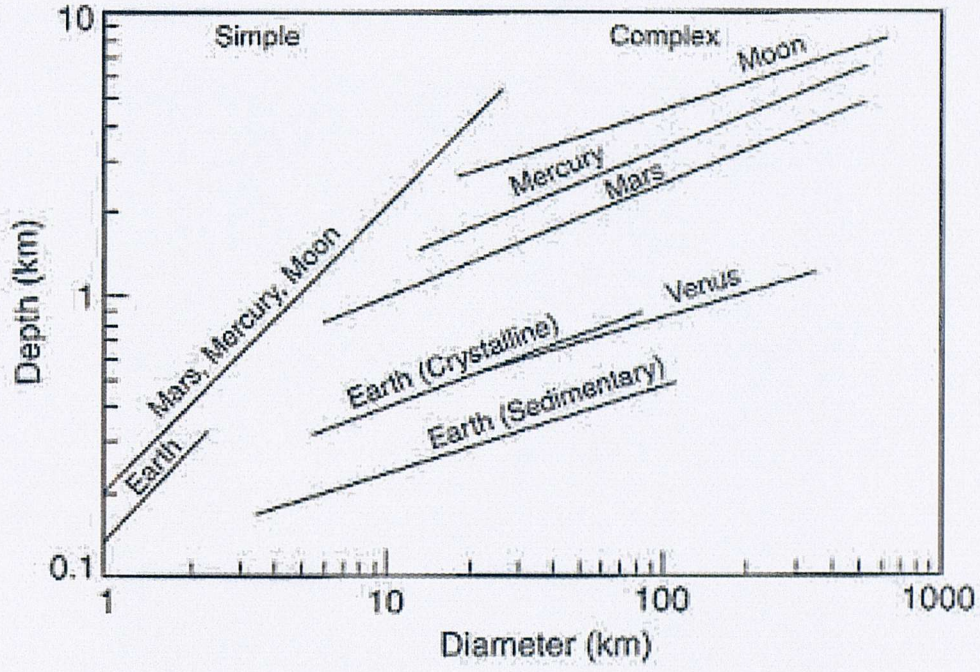


Figure 1.19: Apparent depth versus diameter for craters on the terrestrial planets. The depth-diameter relationship for simple craters is believed to be the same on all planets, the different values on Earth being attributed to rim erosion. The trend is shallower for complex craters than for simple craters. Differences in transition diameter between these 2 forms on different planets, are ascribed to gravity. The trends for Crystalline and Sedimentary rock on Earth shows the significance of target strength. From Grieve and Cintala (1999).

For complex craters, McKinnon *et al* (2003) summarise the alternative scaling laws as:

- Croft (1985) $D = D_c^{!0.18 \forall 0.05} D_{tr}^{1.18 \forall 0.06}$ .....(4)
- McKinnon & Schenk (1985) $D = 1.17 D_c^{!0.13} D_{tr}^{1.13}$ .....(5)
- Holsapple (1993) $D = 1.02 D_c^{!0.085} D_{tr}^{1.086}$ .....(6)

where: D = final crater diameter,
D_c = diameter at the transition from simple to complex form,
D_{tr} = transient crater diameter,

These equations cannot all be right but, since no simple craters have been found on Venus, D_c is unknown for this Thesis. On their website, JPL identify a transition diameter for craters on Venus, between multiple (or 'irregular'), like that illustrated in Fig. 1.20, and complex crater forms.

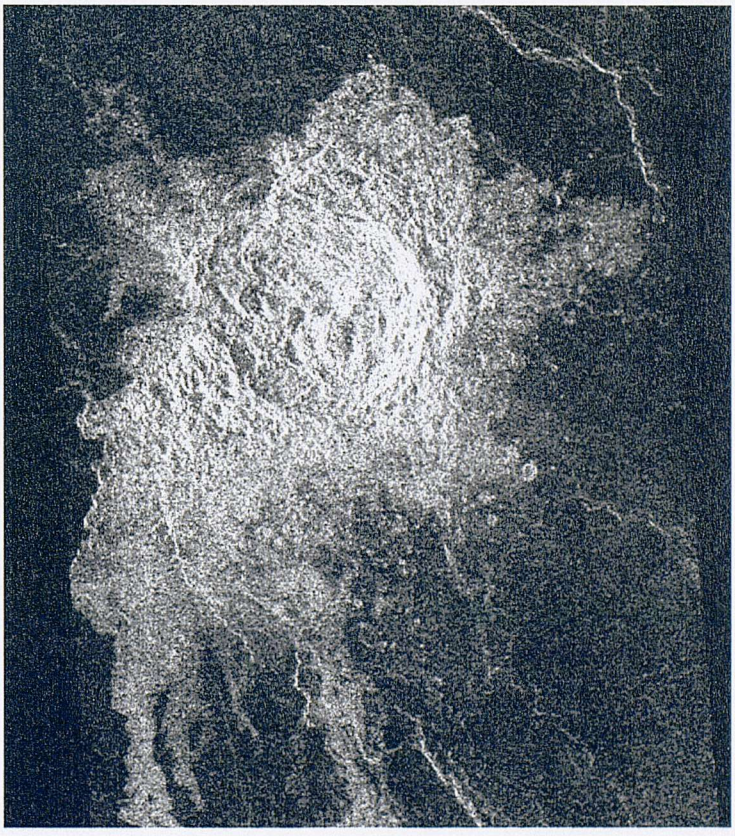


Figure 1.20: 'Transitional' crater. A 15km diameter crater, at 10.7^0E, 340.7^0E, with a somewhat circular rim but a hummocky floor and asymmetric ejecta field. Irregular craters may result from aerodynamic forces crushing and fragmenting a bolide before its impact with the surface of a planet. From JPL PIA 00468, (1999).

Melosh and Ivanov (1999) show that the transition from simple to complex form depends on the inverse of the gravitational constant for the planet, and suggest that collapse occurs when a strength threshold is exceeded. In particular, they drew out two points to which we will return in later Chapters:

- Shock pressures during contact and compression are of the order of the stagnation pressure, ρv^2, where ρ is the smaller of either the impactor or the target density and v is the impactor velocity. For solid impactors, these will exceed the strength of all known materials for velocities of a few km s^{-1}.
- The strength response of rock to a large impact is not well understood. However, models show that the outward displacement of target material just behind the shock wave can produce sufficient hoop tension to shatter rock during the excavation phase, which then readily slumps under gravity during the modification phase.

Herrick & Sharpton (2000) published the first topographic assessments based on 79 Digital Elevation Models (DEMs) produced with the Magellan Stereo Toolkit (MST)[17], which Vexcel Corporation developed for NASA. These DEMs were of all craters at least partially imaged twice down to 12 km diameter, and 20 smaller craters down to 3.6 km diameter. Using FMAP[18] images and MST v.1, they matched points at 900m pitch. Furthermore, in order to remove artifacts, they manually edited some matched points. Because of this editing and the large matching pitch, they do not claim to have accurately determined the elevation of narrow features, such as crater rims. However, they noted that their DEM rim diameters were frequently different from crater diameters given in the databases; they do not quantify the effect but illustrate it, as in Fig. 1.21. They state the vertical resolution of their DEMs is potentially "*a few tens of metres but realistically is ~ 100 m*". They also measure the height of identified central peaks, and confirm the pattern of crater forms found in the LPI and USGS databases.

[17] described in Chapter 2

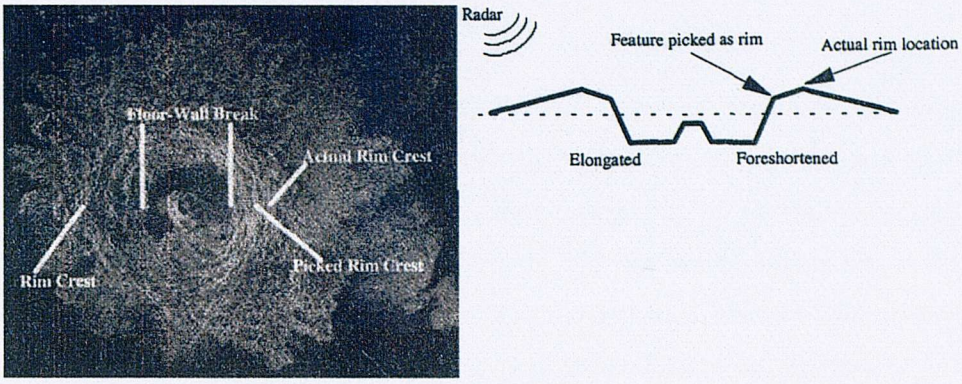


Figure 1.21: Illustrations of the rounded shoulders of a crater. The eye tends to find the rim in one image at the top of the bright escarpment, whereas a DEM usually shows it to be rounded with a peak lying somewhat further out. The elongation and foreshortening of the escarpments, due to their different radar illumination geometry, further complicates rim identification. From Herrick & Sharpton (2000).

In comparison to the level of effort on other aspects of the geology of Venus, very little has been directed towards producing or assessing the topography of its craters. Yet only small-scale experiments may be used to confirm theory. The most recent summary of crater depth vs diameter trends for the terrestrial planets is due to Grieve & Cintala (1999). Herrick & Sharpton (2002) reported the first effort to produce a set of crater DEMs. They claimed to have substantially improved on the crude depth estimates by earlier authors but no error analysis is provided. Furthermore they identified a systematic error in measuring crater diameters but did not quantify it.

[18] described in Chapter 2

1.7. Chapter Summary

This review has shown that impacts by extraterrestrial objects in geologically recent times significantly shaped Earth's surface, disturbing its crust and altering its evolution. Further study of impact crater topography on Venus is expected to prove complementary to that on the Earth. The surface of Venus seems much more homogenous than that of Earth, and thought to be mostly barren basaltic rock with little sediment. Its topography is unimodal but its topography is not unlike to that of the bi-modal Earth but without its oceans. The crater population of Venus is similar to that on Earth's continents, and it indicates a mean surface age between 500 and 800 Ma. However, small impactors must suffer severe distortion during their descent through the atmosphere of Venus, and their mass will be reduced by ablation to a different extent on the two planets. An important observation is that most of the smaller craters on Venus are of irregular shape. It has also been observed that the depth of the larger craters is about 1 km and independent of their rim diameter. The transition between what may be different crater classes has not been characterised.

Two good databases of crater plan-form parameters and a stereo toolkit, called MST, are available. The most recent summary of crater depth vs diameter trends for the terrestrial planets is due to Grieve & Cintala (1999). For Venus, this rests on the work summarised by Sharpton (1994) and predates Herrick & Sharpton (2002). No research has been done on the accuracy of height estimates since Leberl *et al.* (1992).

Chapter 2

The Magellan Mission and its data products

This Chapter describes NASA's Magellan mission to Venus, and especially the data set returned, between 1990 and 1993, from its SAR. In the interests of brevity, only key aspects are drawn out and discussed only to the extent that they affect topography derived from SAR and radar altimeter data. Also described are the methods and software tools available to derive topography from 2 dimensional images, and specifically how they were applied for this Thesis.

The radar instruments themselves are paramount so a few background notes are offered. RADAR stands for Radar Detection and Ranging. In both applications of interest here, a train of radio pulses is transmitted at the ground, and returned by specular reflection. Because the speed of light is constant, the time of arrival of the backscatter after the transmission of the pulse is an analog of distance to the reflecting surface. The energy received is called the "backscatter" and, since the various facets on the ground reflect versions of the pulse differently, the composite signal at the receiver shows brightness variations called "speckle".

In the case of the radar altimeter, the intent is to measure the distance of the spacecraft above the ground, so the radar pulse is directed downwards. A small supplementary antenna was used on Magellan and its beam illuminated several square kilometres on the surface even when the spacecraft was at its minimum altitude. This "footprint" gives rise to a coarse horizontal resolution and is treated as a function of spacecraft (and target) latitude. The leading edge of the returned radar pulse was relatively sharp and the vertical resolution was 50 m. The surface topography along the spacecraft ground trace was then derived from the spacecraft orbit, essentially as a mean planetary radius for each footprint.

In contrast, the SAR was intended to map the surface with much better horizontal resolution than the altimeter. To do so it used a large antenna to focus the available power into as narrow a beam as possible in order to detect returns as small and area as possible. It looked sideways down a slant range, to spread out

the different across track returns in time. Its slant range resolution is a function of radar bandwidth. To resolve the returns along track, the SAR measured their doppler shift. The effective ground resolution is a function of the viewing geometry, and the spacecraft can look to the right or the left.

Only the across-track data is used for deriving topographic profiles by "matching" a pair of stereo images. The along-track resolution enriches the matching process by providing more independent across-track "slices" to profile. These profiles can then be set alongside each other using altimetry data for the large scale trend. Given the lack of ground truth, a third SAR image is the only validation available for topographic features smaller than the altimeter footprint, ie tens of km.

2.1. Magellan Mission Description

Young (1990) was published just prior to Magellan's Venus Orbit Insertion, and describes the Magellan mission to Venus; see Figs. 2.1 and 2.2. It also details the Science Task Groups for data analysis.

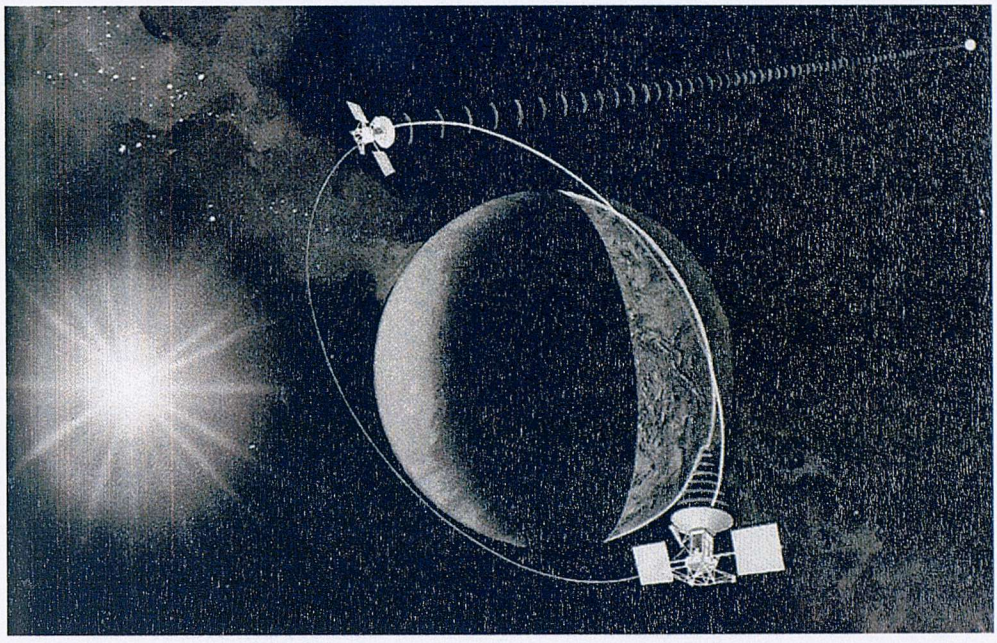


Figure 2.1: Magellan operations in Venus orbit. In this illustration, the spacecraft is shown in both its main operational modes. The orbit was designed so the spacecraft passed low over one side of the planet for radar operations, then downlinked the data back to Earth during the slower, high altitude part of the orbit on the other side of the planet. The bright line indicates one 22 km wide radar swath from which the map of the planet was built up. From Young (1990).

Other sections report on:

- design of the Magellan spacecraft
- application of its radar sensor to radar imaging, altimetry, and radiometry,
- the Venus orbit-insertion manoeuvre, see Fig. 2.2, and
- the in-orbit mapping strategy.

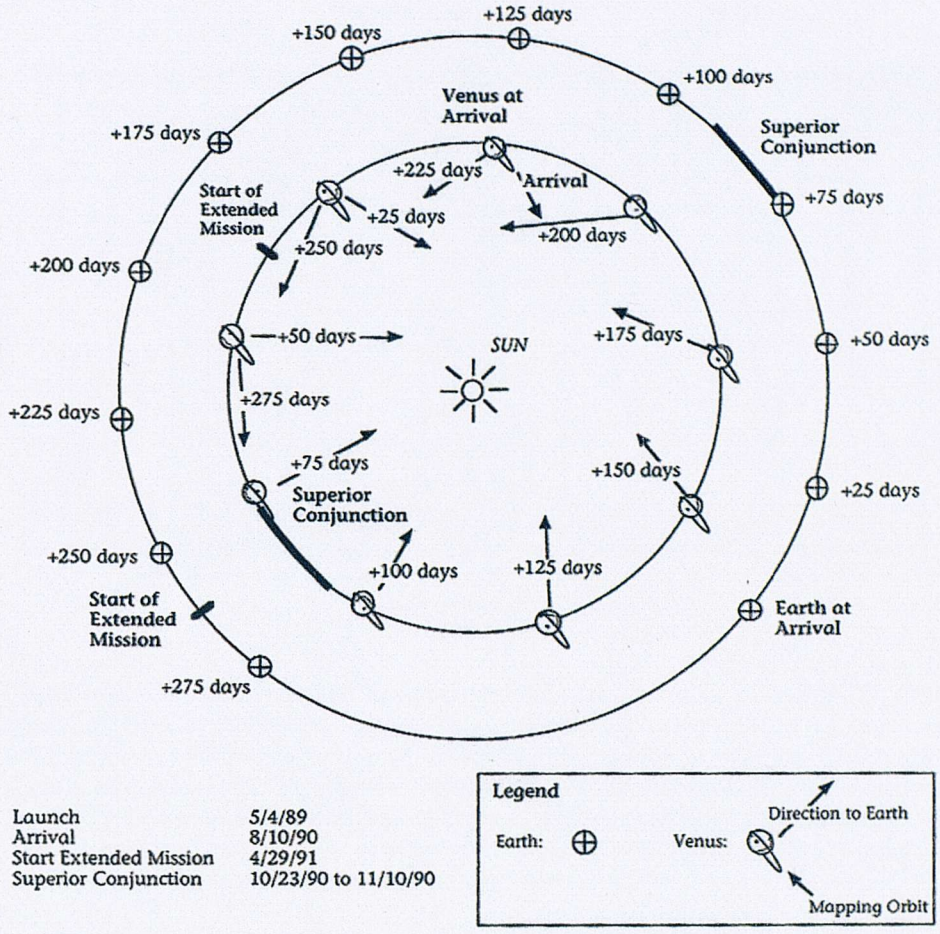


Figure 2.2: Earth and Venus orbit geometry for Magellan Cycle 1. View of the ecliptic plane from the North side, showing that Venus was on the far side of the Sun to Earth when Magellan arrived. There was a conjunction soon after Venus Orbit Insertion (VOI) Propagation conditions were much more favourable at the start of the extended mission. Each Cycle lasted 1 Venus day (243 Earth days). The SAR failed halfway through Cycle 3. From Young (1990).

During 1990-93, the Magellan SAR imaged 98% of the surface of Venus, at least once. Figs. 2.3 and 2.4 illustrate how the planned coverage was achieved. There have been no other missions to Venus since Magellan.

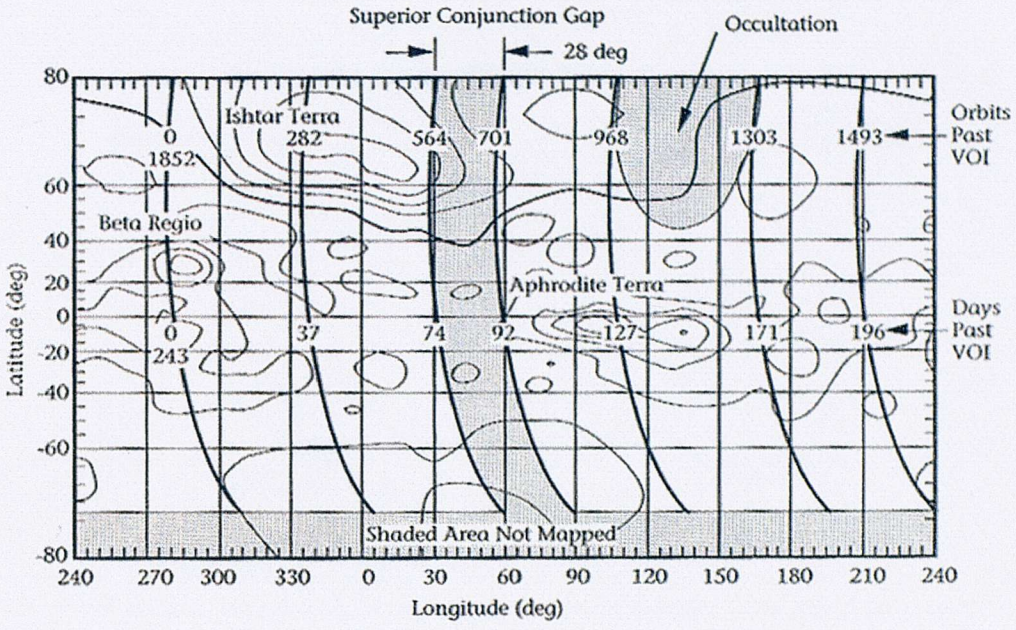


Figure 2.3: Magellan Cycle 1 coverage. Mapping started on Orbit No 376, with the spacecraft moving southwards and looking left, i.e. to the East. During the conjunction, the Sun obstructed the downlink; as Venus itself did during occultation. The south pole could not be imaged during Cycle 1 because of the spacecraft orbit inclination and its left looking radar orientation. Cycle 2 filled in these gaps and provided right looking imagery. Cycle 3 provided left looking coverage at lower incidence for stereo data products until the radar failed mid way through it. From Ford *et al.* (1989).

Saunders et al (1990) show the SAR was designed to operate from altitudes of 225 to 3500 km, imaging the planet in swaths, each 20 to 25 km wide and up to 16,000 km long. Two types of radar mapping pass were interleaved to optimize coverage of the globe. An "Immediate" pass started near the north pole at about 2,150 km altitude, continued through periapsis, and finished at about 1,400 km altitude near 52^0S. A "Delayed" pass started near 66^0 N at about 1,200 km altitude, continued through periapsis, and finished at about 2,400 km altitude near 72^0S. Actual parameters for each pass can be found in one of the 4 Orbitpointinfo files[19] and Pointinfotab file in the Magellan Experimenter's Notebook. These files are included as Excel spreadsheets in the enclosed CD.

[19] The file name contains the starting orbit number.

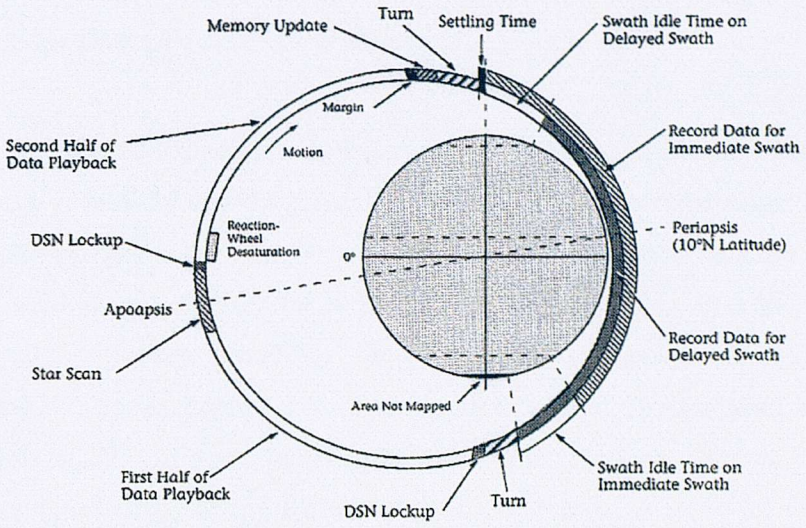


Figure 2.4: Magellan mapping orbit profile. The spacecraft moves clockwise in this view. It rotated throughout radar mapping to minimise range variation in spite of orbit ellipticity, then pointed at Earth for data downlinking; the 1,852 orbits of Cycle 1 involved 7,408 major attitude changes. "Immediate" and "Delayed" swaths alternated to minimise mapping overlaps at high latitudes. From Young (1990).

2.2. *Magellan Operations at Venus.*

The Magellan mission was constrained by the interplanetary transfer and available delta-V to map the planet from an elliptical, near-polar orbit. This orbit was sized and inclined so that Venus would rotate beneath the spacecraft by 0.201^0 per revolution, or some 20 km at the equator. As its design matured and plans unfolded into actual operations, the Magellan orbit parameters migrated, as reported by various authors at the time. In his textbook, Elachi (1988) assumed a periapsis of 250 km and a period of 3.2 hrs. In their design analysis, Kwok and Johnson (1989) expected an altitude of periapsis of 250 km, and a 3.15 hr period. Ford *et al* (1989), the JPL handbook, gives a periapsis of 250km at 10^oN and a period of 3.15 hrs. Before Venus Orbit Insertion (VOI), Saunders & Pettengill (1991) described an expected orbit with periapsis at 9.9^0N, altitudes of 294km (periapsis) and 2225 km (N pole), inclination of 85.5^0N, and a period of 3.26 hrs (compared to design parameters of: 10^0N, 275 km, 2145km, 85.3^0N and 3.186 hrs respectively). Well into the extended mission, Saunders et al (1992) quoted a 290 km periapsis altitude at 10^oN, and a period of 3.25 hrs, whereas Johnson reported 290 km and 3.26 hrs. Ford *et al.* (1993), an updated JPL handbook, gives a periapsis at 9.5^0N with an altitude of 289 km, an inclination of 85.5^0 and a period of 3.259 hrs.

Cycle 1 imaged about 84% of the planet from the north pole to about 74^0 S. During Cycle 2, the spacecraft looked left during Orbits 2465 - 2587 to replace imaging lost during Cycle 1 due to a sun conjunction, and right to cover the South Pole. Cycle 3 provided distinctly patchy coverage until the radar final failed at around 180^0E. An analysis[20] of files contained in the Magellan Experimenter's Notebook[21] showed that commands were sent to image about half (488) of all craters, including 138 craters (i.e. 1 in 7 of the total population) that were to be imaged during all 3 Cycles. However, the relevant data products include many

[20] See spreadsheet Venus_Triangulated_Craters9.2.xls on the enclosed CD

[21] The Magellan Experimenter's Notebook is an informal name given to a set of tables that record the commands uploaded to the spacecraft. Personal Communication: E-mail 22 Feb 2002 from S Slaveny, SMTP:slavney@wunder.wustl.edu,

missing swaths and other nulls, some of which are explained in Wall *et al.* (1995), e.g., due to spacecraft, ground station or other anomalies.

The effect of the missing data is, for example, that only 78 (ie 1 in 12) craters were actually imaged 3 times, and some of these images do not cover all of the crater and its ejecta blanket. A third image for 5 more craters, from Cycle 2 coverage detailed in Wall *et al.* (1995), should have been available but the USGS were unable to provide them. Overall, Cycles 1 and 2 between them covered 97% of the planet, and included a test of complementary, same-side imagery for stereogrammetry, reported by Leberl (1992).

This test, Cycle 3 was planned to provide a second set of left-looking images at about 20^0 lower incidence than that of Cycle 1. For many reasons detailed by Wall *et al.* (1995), Cycle 3 provided distinctly patchy coverage until the radar failed completely at around 180°E, after providing stereo coverage of some 17% of the planet. Analysis of the Magellan Experimenter's Notebook[22] shows that data from Orbits 5164 - 5280 should have provided stereo coverage of 14 more craters but the USGS have confirmed they are now unable to provide it. The best stereo coverage was of an area asride western Ovda Regio centred on the equator around 75 °E, which is the area selected for detailed study, and described in Chapter 3.

The SAR achieved ~ 10 times better resolution than earlier mapping missions and Magellan altimeter. This was better than NASA planned: the primary mission aim was *"to map at least 70% of the surface to an accuracy of at least 300m"*. Johnson (1991) shows that the horizontal resolution achieved by this SAR was:

- Along track: 120 m, and
- Across track: 120 to 400 m, depending on Incidence Angle[23].

All topography from a SAR is derived from across-track image distortions. This means that the smallest crater on Venus, which has diameter of 1.7 km, subtends 14 to 4 SAR pixels, depending on its latitude. MST is therefore close to its performance limit when generating the topography of the smallest craters.

[22] Most command uploads were executed over several orbits. These data tables were obtained from the USGS and appear in the enclosed CD.

[23] For the actual across-track resolution at any feature, this Thesis takes the relevant value of "sargrdistres - SAR ground distance resolution" in the Pointinfo Table. It is zero for 63 of the 8760 lines in the Table, less than 119.2 m for another 28, and more than 400 m for 112.

During Cycle 4, from September 1992, the spacecraft transmitted constantly to Earth whilst the Deep Space Network measured doppler frequency to build up a detailed gravity map of Venus. The Magellan orbit was then reduced, in part by aerobraking, to collect better gravity data in the higher latitudes. In August 1993, the orbit period was 94 mins, periapsis was 180 km, and apoapsis 541 km. In September 1994, the orbit was lowered once more for a "windmill experiment" to measure the torque due to upper atmospheric drag. Magellan was de-orbited in October 1994 and broke up in the atmosphere; some sections of it were expected to hit the planet's surface intact but no data is available.

2.3. *The Magellan Synthetic Aperture Radar*

Most SARs are operated at constant altitude. Johnson (1991) explains that a precursor to Magellan, called Venus Orbiting Imaging Radar (VOIR), was designed to operate in a 400km altitude, circular orbit. VOIR proved too expensive, so a modified mission was started in 1983; it was initially called Venus Radar Mapper (VRM) and is described in Johnson & Edgerton (1985). VRM was renamed Magellan in 1986. Johnson (1991) reports that its SAR was designed to achieve nearly constant speckle performance from an elliptical orbit by operating at variable look angle and in burst mode, as per Fig. 2.5. This led to the variation of range resolution with latitude described in Section 2.2.

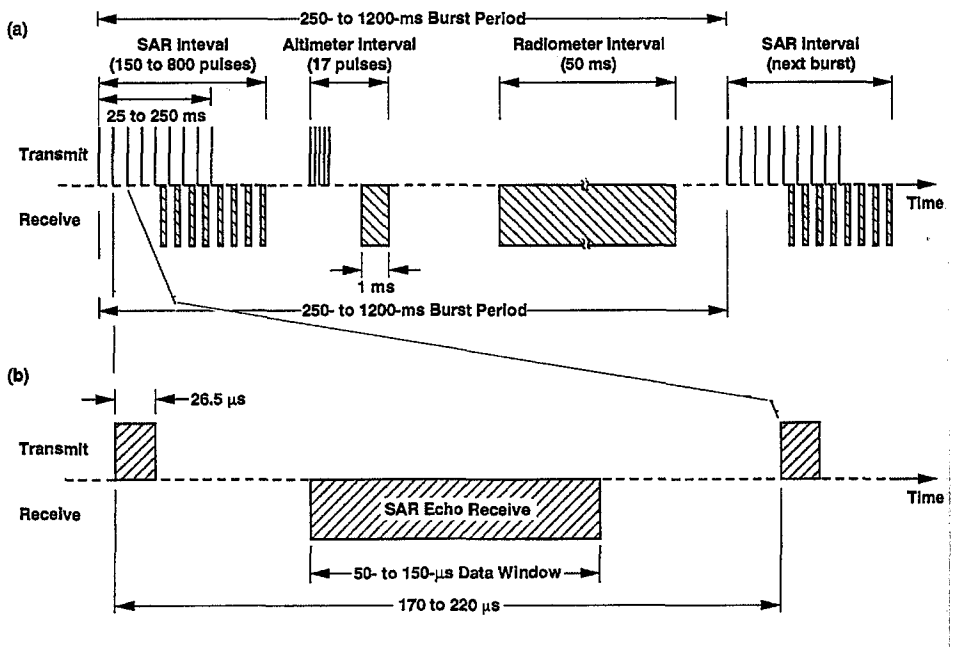


Figure 2.5: Timelines for Magellan Microwave Instruments. (a) The radar transmitted a variable number of SAR pulses with a variable pulse separation time. The number of pulses were set to minimise variations in receiver signal-to-noise ratio and the data volume to be downlinked. The SAR burst period was set to compensate for variations of target range, due to the elliptical orbit. Altimeter and Radiometer were operated between SAR bursts. (b) Between each SAR pulse, the radar received echo returns through a variable window. From Ford *et al.* (1993)

The first mapping orbit, No 376, started down the 330°E Meridian at 16.23 hrs UT on 15 Sept 1990. Ford *et al.* (1993) summarise the duty cycles and coverage patterns. The latter contain many overlaps, especially near the Poles and at the latitudes where Immediate and Delayed coverage begins or ends. Saunders et al (1992) report that the best frame was selected from these overlaps as they were extracted from the raw radar data, ie most probably on the basis of data, rather than image, quality tests. Calculation of the command vectors to control the radar was a significant task and initially led to some inconsistencies in the imagery. Certainly, the early Cycle 1 coverage, e.g. of Mead crater, has both a characteristic "Venetian Blind" pattern and some sharp transitions in the level of greyscale recorded for radar-dark plains. Comparative analysis of the two sets of imagery returned during these coverage overlaps showed an across-track radiometric difference of less than ± 1 dB between adjacent orbits and a mean difference between Cycles 1 and 2 of 0.14 dB. Overall, results indicated an end-to-end absolute calibration within ± 2 dB.

Saunders *et al.* (1992) report on radiometric tests using a "jagged bright feature at 27.4°N on Orbit 1661, 22 dB above its surrounding plains". This feature is shown in Fig. 2.6 and the tests validated the sidelobe level in the range dimension as better than !18.8 dB. Unfortunately, this jagged feature was not imaged again during either Cycle 2 or 3. Using a bright target of small extent to the north of the jagged feature[24], the 3 dB resolution was found to be ~ 120 m, in both the along-track and across-track directions.

[24] At this latitude, the *effective* multi-look resolution may be calculated from Johnson (1989) as 130 m, i.e. consistent with the SAR pixel resolution given in the Command Upload. Saunders *et al.* (1992) expected an across-track resolution of 118 m, presumably as this was a single look test.

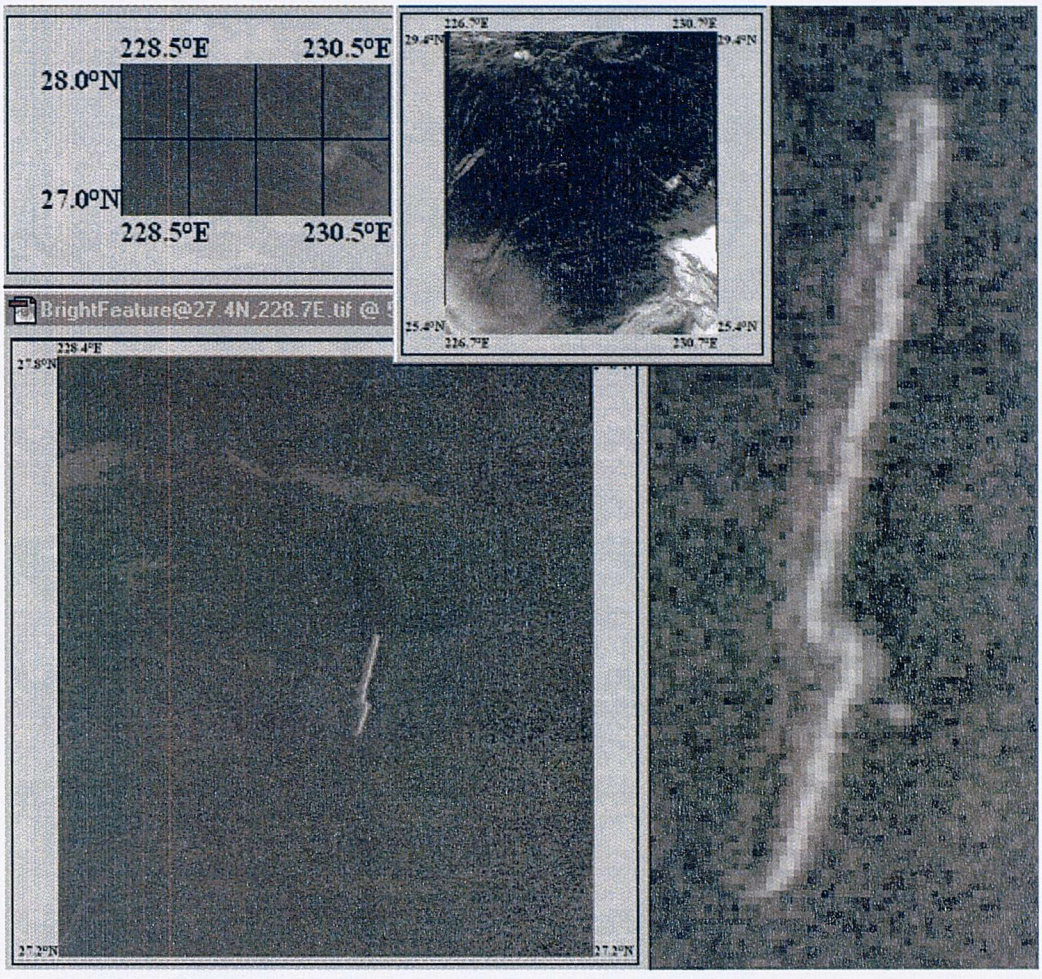


Figure 2.6: Bright feature used for Magellan SAR sidelobe characterisation. Located by use of the Magellan Experimenter's Notebook at 228.7^{0}E, this download from PDS shows the feature lies on a radar-dark plain, 1.4^0 west of an unnamed, 9 km diameter crater at 27.4^{0}N, 230.1^{0}E, Serial No ganiki 230. It is interpreted as a trench, 8.7 km long, with a down-range cliff 2 - 3 pixels wide. Saunders *et al.* (1992) print a similar image upside down, as Fig. 9. They interpreted what is most probably the raised lip of the up-range cliff as a down-range ghost.

2.4. Magellan Downlink Data Compression

The planned 189 minute orbit dictated that the SAR image the surface for about 37 mins, ie, at the required ground resolution, an instantaneous output rate of 36 Mbps and a total data volume of some 18 Gbytes per orbit. Tape recorders were the only available volume storage devices when Magellan was designed, and the best tape recording rate available was 0.8 Mbps.

The compressed image data from each radar swath had to be transmitted to Earth at 268.8 kbps, over 114 minutes before, during, and after apoapsis. Kwok & Johnson (1989) considered that the necessary data compression factor of about 45 might be achieved by a combination of three techniques:

- Inter-pulse buffering (a factor of 1.25),
- Burst mode operation (a factor of 9), and
- A specially designed Block Adaptive Quantization (BAQ) code.

Johnson & Edgerton (1989) report trade-offs of radar pulse bandwidth and quantization noise favouring a 2-bit quantizer, with a compression factor of 4. Such a quantizer would bring the total compression to 45, making a system design feasible. Kwok & Johnson (1989) describe the BAQ coder design as first adding the average signal magnitude of the radar output on both I and Q channels, over 8 pulses, for each group of 16 range samples. Such outputs are generally assumed to be Gaussian with zero mean and unknown variance, so each can be characterised by a single "statistic". Edge effects were removed by arranging that the last data group was the last 16 samples, even if some of them were also part of the previous group. Each statistic was transposed in a look-up table into a 8-bit control word that set the quantizer threshold. It was also downlinked for reconstruction of the data using weightings of 0.52 for "0" and 1.73 for "1". Hence, one bit in the quantizer output (the "signal level" bit) indicated that the original signal sample was larger or smaller than the current threshold setting, and the latter was adjusted so that the reconstituted signal would have minimum mean-square error. The other bit of the quantizer output was the "sign" of the original signal sample.

Thus, the BAQ scheme maps onto the surface in patches 8 pulses wide and 16 range bins deep, measuring the data returned from each patch by reference to a threshold setting derived from the signal characteristics of the previous patch. The actual size of these patches on the surface varies. To understand the dimensions of the smallest patches, consider the inter-pulse period was between 170 and 220 μsecs, and a range bin was equivalent to 88m slant range, or 120 - 360 m on the surface, depending on incidence angle. At Helvi, a 11.2 km diameter crater at 12.4^0N, 87.2^0E and close to periapsis, the inter-pulse period would have been 170μsecs. During Cycle 1, Magellan imaged Helvi travelling at 8.77 km s^{-1} so covered only 12 m along track during 8 pulses; across track, it imaged at 45.8^0 Incidence so the 16 range bins extended 2km on the surface. Hence, the patches had an aspect ratio of 167:1, so they are best visualised as across-track strips.

Kwok & Johnson (1989) claim a dynamic range of approximately 39.5 dB for their design. They simulated the radar response to a 30 dB step in average input power, with and without the BAQ coding; see Fig 2.7.a. Kwok & Johnson (1989) also tested the visual effects of the BAQ coder by simulation using 150 m SAR resolution cells and 75m pixels.

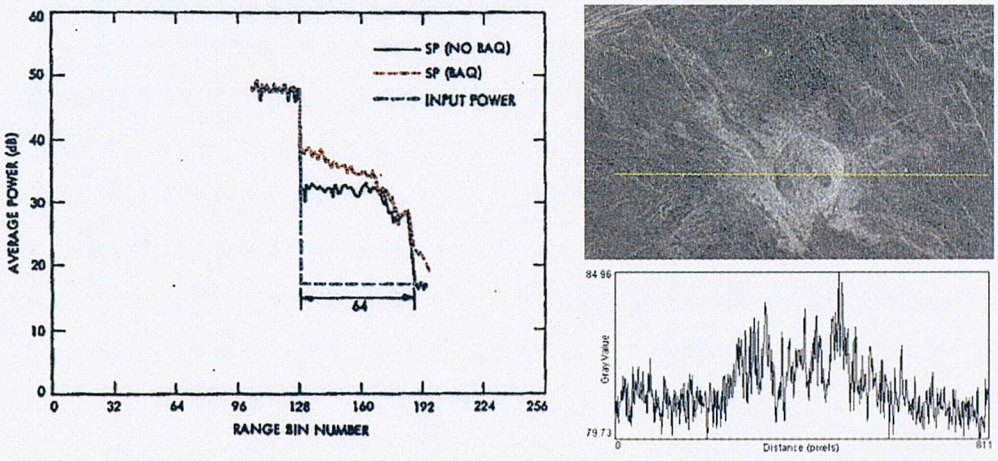


Figure 2.7: a. BAQ Step Response. A 30db step in the input, broken blue line, gives only about 15db in the output, the solid black line, until after the subsequent 64 range bins. The effect of the BAQ (the red line) is to slug the response by a few more dBs, and a few more range bins. From Kwok & Johnson (1989).
b. West-East DN plot acrosss Helvi. A down-range plot illustrates such smoothing in the delayed rise of brightness in the western ejecta field compared to its persistence in the east. N.B.: Helvi, a 11.2 km diameter crater, lies close to periapsis at 12.5^0N, 82.7^0E.

Such smoothing should not directly effect DEM generation, which matches brightness transitions, not absolute brightnesses. Also, the logarithmic conversion of signal strength to imagery grey scale, given in Ford *et al.* (1993), enhances the significance of small changes. This conversion is given by equation:

$$\sigma^0 = 0.2 \text{ (pixel DN} - 101) \text{ dB} \quad \text{.....(7)}$$

where: σ^0 = relative backscatter coefficient, measured in deciBels (dB), and

pixel DN = Digital Number, the greyscale code value in the image.

So the 30 dB, or 251 DN, step change in Fig. 2.7(a) is equivalent to almost the full range of the imagery greyscale of 1 DN to 256 DN. However, in spite of the BAQ coding and other leakage effects, the conversion equation ensures that the radar data processor will give a significant (141 DN) initial change in the image even though the signal strength is at first only 8 dB. However, the downlink will continue to include remnants of the pre-step signal, and only achieve the full 251 DN after 64 range bins. In the case of Helvi, this will be 8 km in Cycle 1 and 14 km in Cycle 3. Such remnants might be removed by matching up-range feature edges rather than groups of pixels. The first derivatives of the 2 images will have sharper edges, and might be matchable, but this has not been investigated.

To consider how stereo-matching is affected, note the BAQ code suppresses the brightness transitions on both sides of a feature, eg a bright crater in a dark plain, using threashold settings that are not geo-referenced. Also, absolute SAR performance was not good enough to ensure that 2 images from different cycles are directly comparable at pixel level. Pettengill *et al.* (1992) report an absolute pixel accuracy of about a factor of 2, and a relative accuracy among pixels in a given swath of about 25%. Furthermore, the across track resolution is different for the 2 cycles because of the different incidence angles. Chapter 5 addresses how these effect DEM errors.

2.5. *Magellan Product Generation.*

Saunders *et al* (1992) and Ford *et al.* (1995) describe how the Deep Space Control Center (DSCC) recorded the downlink data stream as Original Data Records (ODRs), on magnetic tape. Most of the engineering data were relayed electronically to the Space Flight Operations Center (SFOC), at JPL, where data were permanently archived by the Data Management and Archive Team (DMAT). The radar imaging, altimetry, and radiometry ODRs were shipped to JPL because adequate datalinks were not available. The raw radar data were time-ordered and formatted by the Magellan High-Rate Processor (MHRP) and returned to the DMAT in the form of an Experiment Data Record (EDR). The EDRs were fed into the SAR Data Processing Subsystem (SDPS), where they were BAQ decoded into the original format, SAR correlated, resampled in 75m by 75 m pixels aligned to the local latitude, and output as an image strip. The Image Data Processing Subsystem (IDPS) mosaicked the image strips into large area maps of Venus.

The primary image data product created from each orbit's data was the long, narrow image swath, about 25 km wide by approximately 16,000 km long, termed a Full-Resolution Basic Image Data Record (F-BIDR). Some 1,852 such image strips were produced during a 243-day mapping cycle. These were mosaicked to produce Mosaicked Image Data Records (MIDRs) for ease of interpretation and comparison with the altimetry and radiometry data. Saunders *et al.* (1990) reports that sinusoidal, equal area projections were used to form the BIDRs.

In the early 1990s, full-resolution mosaics for the 90 percent of the planet covered by F-BIDRs constituted an enormous data set, so the main dissemination products were compressed strips, in the following forms:

- C1-MIDRs, compressed once to cover 15^0 latitude by 15^0 longitude;
- C2-MIDRs, compressed twice to cover 45^0 latitude by 45^0 longitude; or
- C3-MIDR, compressed three times to cover 80^0 latitude by 120^0 longitude.

The mosaics were not evenly shaped; 1 degree equals approximately 100 km.

Also, approximately 15 percent of the F-BIDRs were processed into full-resolution mosaics (F-MIDRs) for key regions on the planet's surface.

Up to the end-of-Project transfer, DMAT had managed about 100,000 data products. Many of these products were provided to NASA's Regional Planetary Facilities worldwide. Then NASA Goddard became the principal archive and distribution centre, and distributed Magellan's image products in CD form, called F-Maps. NASA Goddard also distributed the altimeter/radiometer data as CDs. Most of the work undertaken for this Thesis was based on data held by the UK Planetary Information Facility (PIF) at University College London. This data set can now be accessed on line at the Planetary Data Service (PDS) "Map a Planet" website[25].

SAR imagery can suffer from several types of aberration and it is normal to use tie points to correct the consequent distortions. Davies & Rogers (1991) show the Magellan data was mosaicked to closure round the planet, and used to improve the ephemeris. Saunders *et al.* (1992) report that the final ephemeris for Cycle 1 met the requirements: 150 m radial and 1 km across track, except for orbits close to the solar conjunction.

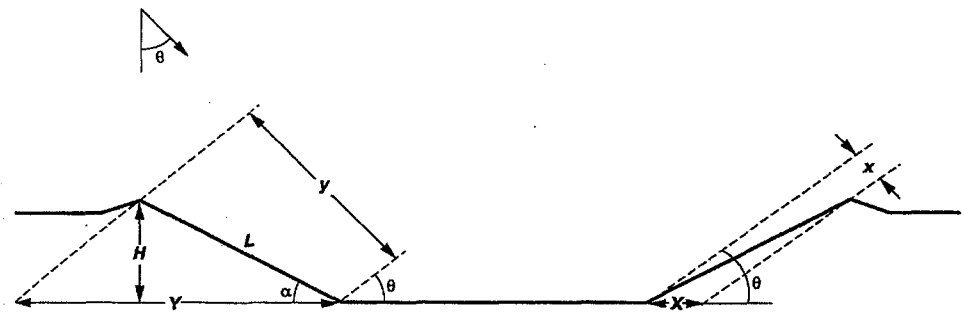
Ford et al (1993) describes an implementation error of an empirically derived formula for radar backscatter from Muhleman (1964). As a result, all F-BIDR images, and all data products derived from them, are about 10 DN too dark. A single, constant equivalent noise temperature was used, ie no corrections for changes in the noise due to the temperature of the atmosphere and the surface. No corrections were made for changes in atmospheric attenuation, eg due to incidence angle and terrain elevation.

JPL D-2300 (1991) recommended JPL Topographic Model, Version 4.1, which took samples only every 0.125° of latitude and longitude (ie about 6.6km at the equator), and quantized elevation in only 32-bit samples.

[25] http://pdsmaps.wr.usgs.gov/PDS/public/explorer/html/fmapadvc.htm

2.6. Crater Depth from one Image

It is possible to derive crater depth from a single image by comparing the image widths of the eastern and western escarpments, or colloquially the apparent "floor-offset", as shown in Fig. 2.8.



$L = H/\sin\alpha$

$y = L\sin(\theta + \alpha)$

$Y = y/\sin\theta$

$Y = L\sin(\theta + \alpha)/\sin\theta$

$Y = H\sin(\theta + \alpha)/\sin\theta\sin\alpha$

$H = \frac{Y - X}{2}\tan\theta$

$\tan\alpha = \frac{1 - (X/Y)}{1 + (X/Y)}\tan\theta$

$x = L\sin(\theta - \alpha)$

$X = x/\sin\theta$

$X = H\sin(\theta - \alpha)/\sin\theta\sin\alpha$

Figure 2.8: Crater Depth from a Single Image. For a crater with escarpment length *L*, rim height above the floor, *H*, and slope, ∀, a radar with Incidence Angle, *2*, will find the facing escarpment to have range extent, x. The near side escarpment will be found to have range extent, *y*. Hence, *x* and *y* may be projected into the horizontal plane as *X* and *Y* respectively. Provided *H* and ∀ are the same on each side of the crater, they may be derived as shown. These equations do not apply if there is radar layover in the image(s). From Ford *et al.* (1993).

Ford *et al.* (1993) also show that the radar backscatter from surfaces of given texture is approximately an inverse function of incidence angle, as illustrated in Fig. 2.9. Connors and Suppe (2001) show how the two effects in the Magellan data can be used as the basis for geological assessments of homogenous terrain. Because craters are considered heterogeneous features, this method is not used in this Thesis.

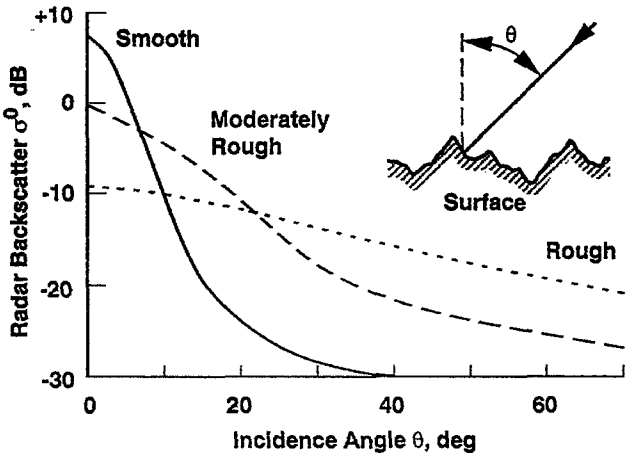


Figure 2.9: Radar Backscatter of representative surfaces. For Incidence Angle, *2*, less than about 25^0, smoother surfaces have greater backscatter than rougher surfaces. From Ford *et al.* (1993).

2.7. The Magellan Stereo Toolkit

Leberl *et al.* (1992) made the case for a third Cycle of SAR imaging of Venus, and detailed stereo radargrammetric mapping of the planet. The Magellan Stereo Toolkit (MST) was provided for that purpose. In the event, the radar's operational availablility deteriorated and MST was delivered much later than originally intended. Nevertheless it was the first toolkit of its kind and can be used with the F-Maps to produce detailed models of surface features with horizontal dimensions of a few hundreds of km.

Maurice (1997) shows MST V2.0 was the final release of the NASA-funded project awarded to Vexcel Corp against a system specification issued in 1993. Imperial College obtained a copy, under a single user license, on an Exabyte tape with releases for the following platforms:

- GSI/Irix 5.x and 6.x series, and
- Sun/Solaris 2.x series computers.

It requires the following minimum host environment:

- ~200MB of disc space,
- X Windows R5/6 up, and
- Motif 1.2/2.x up.

Also, Vexcel recommend the use of Image Display Language (IDL) for displaying the basic DEM output. For this Thesis, MST V2.0 was installed on the Ultra F Server and accessed via the College Intranet. MST V2.0 includes the *vxdisp* viewer for displaying images without IDL, which was not available for this Thesis. Programme listings are provided in the enclosed CD. Prior to DEM generation, the necessary co-ordinates for MST were obtained using the spread sheet[26] with embedded macros, illustrated in Table 2.1.

[26] Provided by Richard Ghail, personal communication 21 March 2002.

Frame Latitude	13	N
Frame Longitude	83	E
Frame Lines	2830	pixels
Frame Samples	2814	pixels
FMAP Latitude	18	N
FMAP Longitude	78	E
Image Resolution	75	m
Subframe Start x	386	
Subframe Start y	1749	
Subframe Lines	1024	pixels
Subframe Samples	1024	pixels

	left	stereo
look-angle	43.128735	24.489220
hgt	597638.554690	352033.324922
srange	818885.421816	386833.111971
grange	638008.821740	772851.923778
Stereo Start x	343	
Stereo Start y	1750	
Separation	3226	m
Height Offset	2860	m

LL lat	12.030724
LL lon	82.211442
UL lat	12.757929
UL lon	82.281061
UR lat	12.757929
UR lon	83.026674
LR lat	12.030724
LR lon	82.954978
Specline	-7382
Projsamp	5879
C1	-7383
C2	-5879
UL lon	4.281061
centre lat	12.394326

Table 2.1. MST Parameters for Helvi. The data required for MST appear in the yellow cells, having been computed by macros from data entered in the blue cells.

Both the spreadsheet illustrated in Table 2.1 and the procedure for DEM Generation are included in the enclosed CD. The procedure for DEM generation, uses the following MST capabilities in sequence:

- Automated Image Matching,
- Image Orthorectification (or Stereo Matching),
- DEM Generation
- Shape from Shading (SFS) DEM Enhancement, and
- Quality Control.

Important aspects of these capabilities are described in the following paragraphs:

Automated Image Matching. The input images, of exactly 1024 by 1024 pixels, were cut from the Cycle 1 and 3 data using Photoshop. DEM generation often failed if the input images were not accurately matched in their top left hand corners. Key settings were as shown in Table 2.2. The numbers in red[27] were manually edited from the default settings supplied with the software. Maurice (1997) recommends the default number of iterations (5) of stereo matching should

[27] Recommended by Richard Ghail, personal communication 10 April 2002.

not be changed, even though the interface design implied the possibility of increasing these to 8.

Level	Ref Window Size	Ref Window Spacing	Y Dir Search B'nd'ry	X Dir Search B'nd'ry	Pixel Av'ging Factor	Y Search Dist	Pk Val Filter Factor	X Disp'ty Filter Factor	Y Disp'ty Filter Factor	XX Covar Filter Factor	YY Covar Filter Factor	Estimate Weight'g Factor	Previous Weight'g Factor
1	64	64	8	48	4	1	0.1	0.5	0.5	4	4	0.5	0.5
2	32	32	4	24	2	1	0.1	0.5	0.5	4	4	0.5	0.5
3	16	16	2	12	1	1	0.1	0.5	0.5	4	4	0.5	0.5
4	8	8	1	6	1	1	0.1	0.5	0.5	4	4	0.5	0.5
5	4	4	1	3	1	1	0.1	0.5	0.5	4	4	0.5	0.5
6	any	any	any	any	any	any	any	any	any	any	any	any	any
7	any	any	any	any	any	any	any	any	any	any	any	any	any
8	any	any	any	any	any	any	any	any	any	any	any	any	any

Table 2.2. MST Stereo Matching Settings. The settings show that the input images were initially processed as 64 by 64 pixel sub-images, within an across-track range of 48 and an along-track range of 8, etc.

Image Orthorectification. Orthorectification of an oblique viewed image is the removal of horizontal offsets due to vertical height differences to produce a proper plan image. Maurice (1997) shows the MST Stereo Processing sub-system can be used with or without IDL, which was not available for this Thesis. Grid Spacing was always set to "2" so that the DEM would have a resolution in both horizontal axes of 2 pixels (ie 150 m).

DEM Generation. Fig. 2.10, from Ford *et al.* (1993), gives the formulae in for offsets due to feature height in a stereo pair of images, for same-side geometry.

Shape from Shading. Shape from Shading (SFS) treats changes in greyscale as due to changes in slope, so as to improve the detailed topography along the lines described in Connors and Suppe (2001). MST provides for enhancement of the initial DEM produced by IDL with an SFS process. At the settings specified in Table 2.2, the SFS function was found to make little difference to the crater parameters being measured for this Thesis, and made the contour display in the QC mode more difficult to read.

Quality Control. The function was used for initial evaluation of the outputs, which were: ortho-rectified versions of the 2 images, a basic DEM and an SFS version of it.

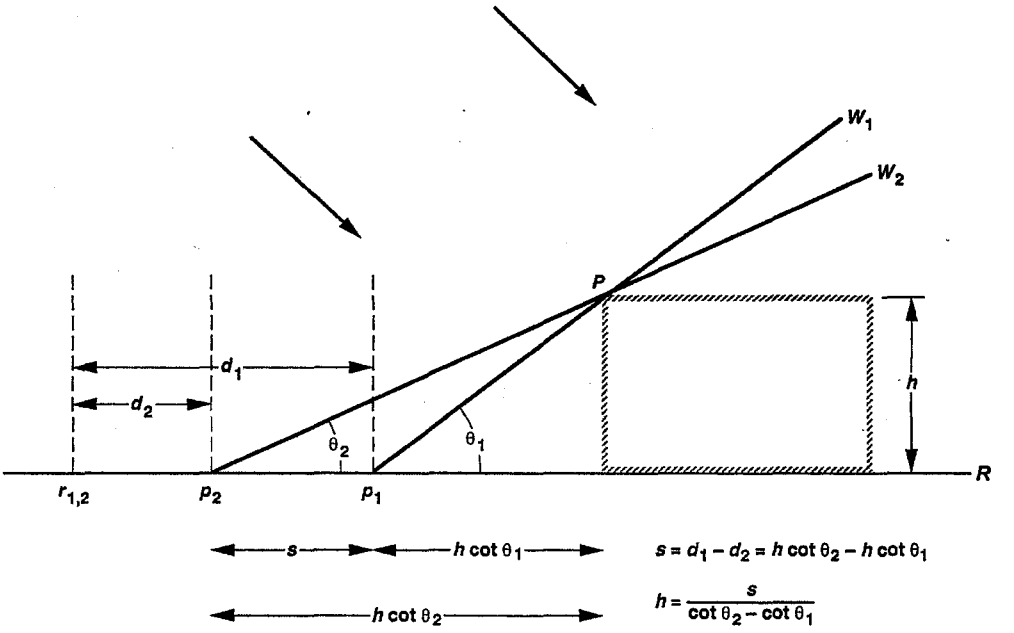


Figure 2.10: Same Side Parallax-to-Height Ratio. If h is the height of a feature and P is its upper, radar-facing edge, then the wavefront, W_1, at Incidence Angle, 2_1, will project P onto position P_1 on R, the reference plane for SAR processing. Also, W_2, at Incidence Angle, 2_2, will project P onto position P_2. By trigonometry, the difference, s, in the distances, d, from reference points, r, give a term for the parallax-to-height ratio: ($\cot 2_2$! $\cot 2_1$). From Ford *et al.* (1993).

The MST output files were transferred into ERDAS Imagine for visualisation for detailed assessment with the procedure included in the enclosed CD. Later on, a crater measurement procedure was defined using Image-J, and is described in Section 3.2. This programme was originally included in the F-Map CDs, and updated via the internet. The version used is included in the accompanying CD.

2.8. Opposite Side Stereo

Ford *et al.* (1993) also give equations for the offsets due to feature height in a pair of opposite-side stereo images. These equations are the basis of the software produced by Hoonyol Lee whilst he was at Imperial College.

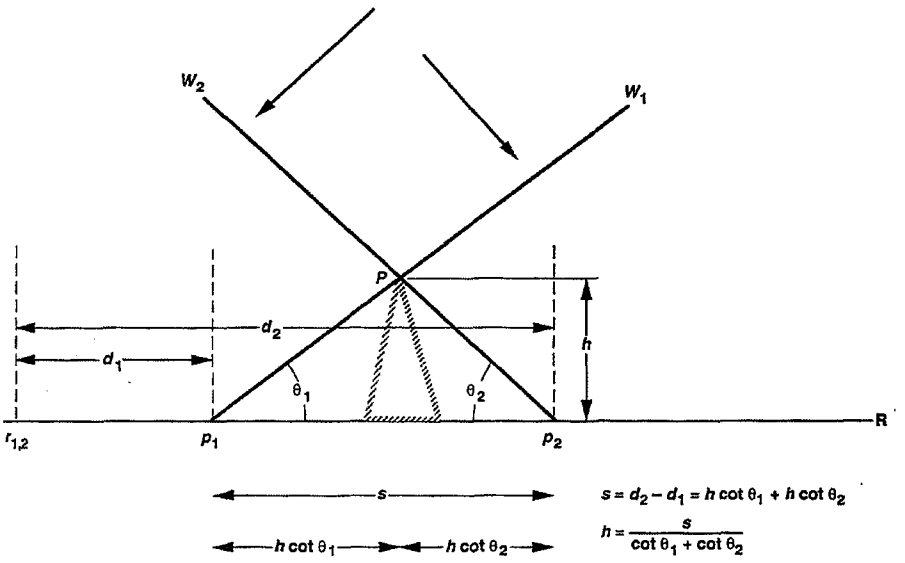


Figure 2.11: Opposite Side Parallax-to-Height Ratio. If h is the height of a feature and *P* is its top edge, then the wave front, W_1, at Incidence Angle, 2_1, will project *P* onto position P_1 on *R*, the reference plane for SAR processing. Also, W_2, at Incidence Angle, 2_2, will project *P* onto position P_2, now on the opposite side of the feature (i.e. the image of the feature top is distorted towards the radar). The difference, s, in the distances, *d*, from reference points, *r*, may be found by trigonometry. The parallax-to-height ratio is the term: ($\cot 2_2 + \cot 2_1$). From Ford *et al.* (1993).

They were also used for manual calculation of feature topography. The opposite side parallax-to-height ratio includes a sum of cotangents of incidence, whereas the same side parallax-to-height ratio has a difference of cotangents of incidence. For estimating feature height from Magellan data at low latitudes, this makes matching opposite side image pairs potentially more accurate than in same side pairs by about a factor of four. However, to achieve this improvement, features must be unambiguously recognised to one pixel in spite of the viewing geometry and SAR range resolution differences between the 2 images.

2.9. Chapter Summary

This Chapter has reviewed the availability of relevant data, methods and software tools.

During 1990-93, the Magellan SAR imaged 98% of the surface of Venus, at least once, in swaths some 20km wide. Ground resolution was 120 by 120 m, at best. Raw data was multi-looked and resampled, in 75 by 75 m pixels aligned with the local lines of latitude, to produce a basic data product called F-BIDR, which were mosaicked to provide a range of different image products.

Sharp features were shown to be resolved to approximately 2 resampled pixels. Downlink compression was used but its direst effect within images was minimised by logarithmic conversion of signal strength to greyscale (DN) values.

A basis for estimating crater depth from a single image was available for use where a stereo pair is not available. Where a stereo pair was available, MST can be used to generate DEMs from 75 by 75 km matched images cut from the F-Maps for Cycles 1 and 3. Some of these can be validated by use of a Cycle 2 image.

Chapter 3

Crater Sample Selection, Model Generation and Results

This Chapter describes why the craters in a particular area of Venus were selected for study, presents the DEMs produced of them in the course of this Thesis, and the extent to which these craters and their DEMs form a set that can be regarded as representative of all craters on Venus.

For the reasons given in Section 3.1, the area shown in Fig.3.1 was chosen as a sample area. All craters within it are treated as a sample set for this Thesis but, for various exigencies described in the following text, the set is progressively reduced in size.

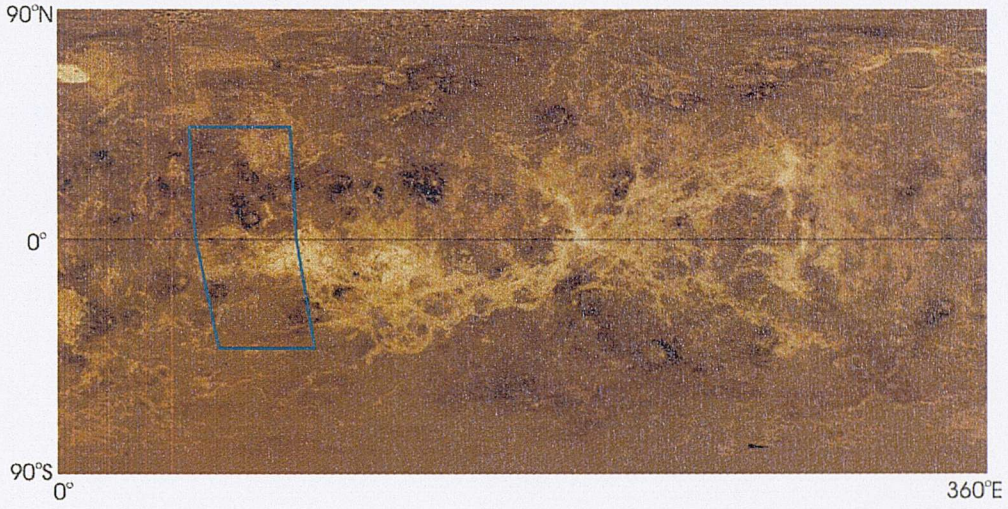


Figure 3.1: Location of the Sample Area on the planet. The sample area of 32.33 million km^2 (7% of the planetary surface), is outlined in blue on a map of Magellan radar reflectivity from the Solar System Visualization project at JPL Multimission Image Processing Laboratory. Comprised of JPL PIA 00255 and 00256 images, in cylindrical projection and coloured with the hue found by Venera 13/14. Images downloaded from http://photojournal.jpl.nasa.gov/targetFamily/Venus.

3.1. Sample Area Definition and Description

The contiguous area of the planet that was best covered in all 3 Magellan Cycles lies astride western Ovda Regio, centred on the equator and around longitude 75^0E. Fig. 3.2 shows the actual coverage during the 3 Cycles. This area, called the "Sample Area", is defined by the co-ordinates and dimensions given in Fig. 3.3. It is located on the planet as shown in Fig. 3.1.

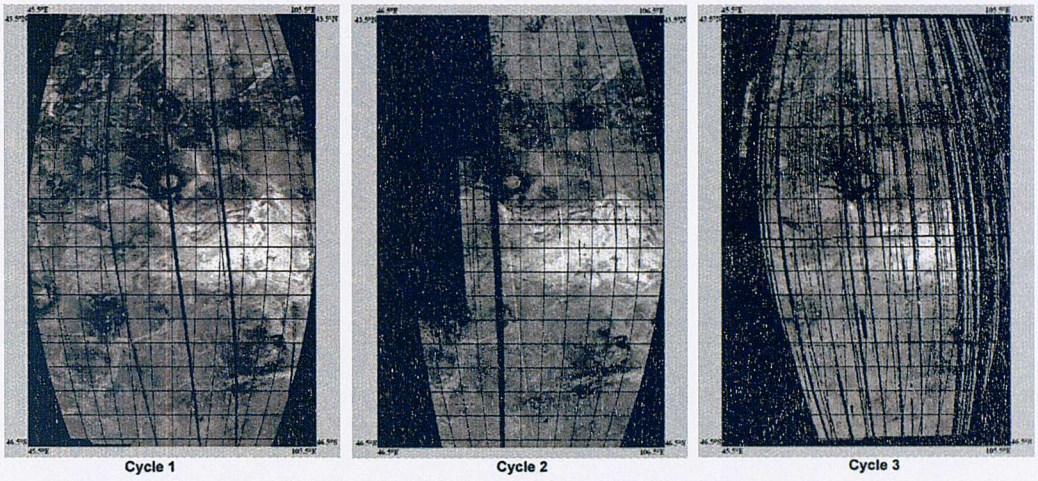


Figure 3.2: Coverage of all 3 Cycles astride western Ovda Regio. There are missing swaths, and the occasional hiatus, in all 3 diagrams. Cycle 2 coverage of the northern hemisphere did not start until 60^0E; Cycle 3 coverage was beginning to become spasmodic before 100^0E. The gridlines are at 5^o intervals. The images are screenshots of PDS downloads in sinusoidal projection.

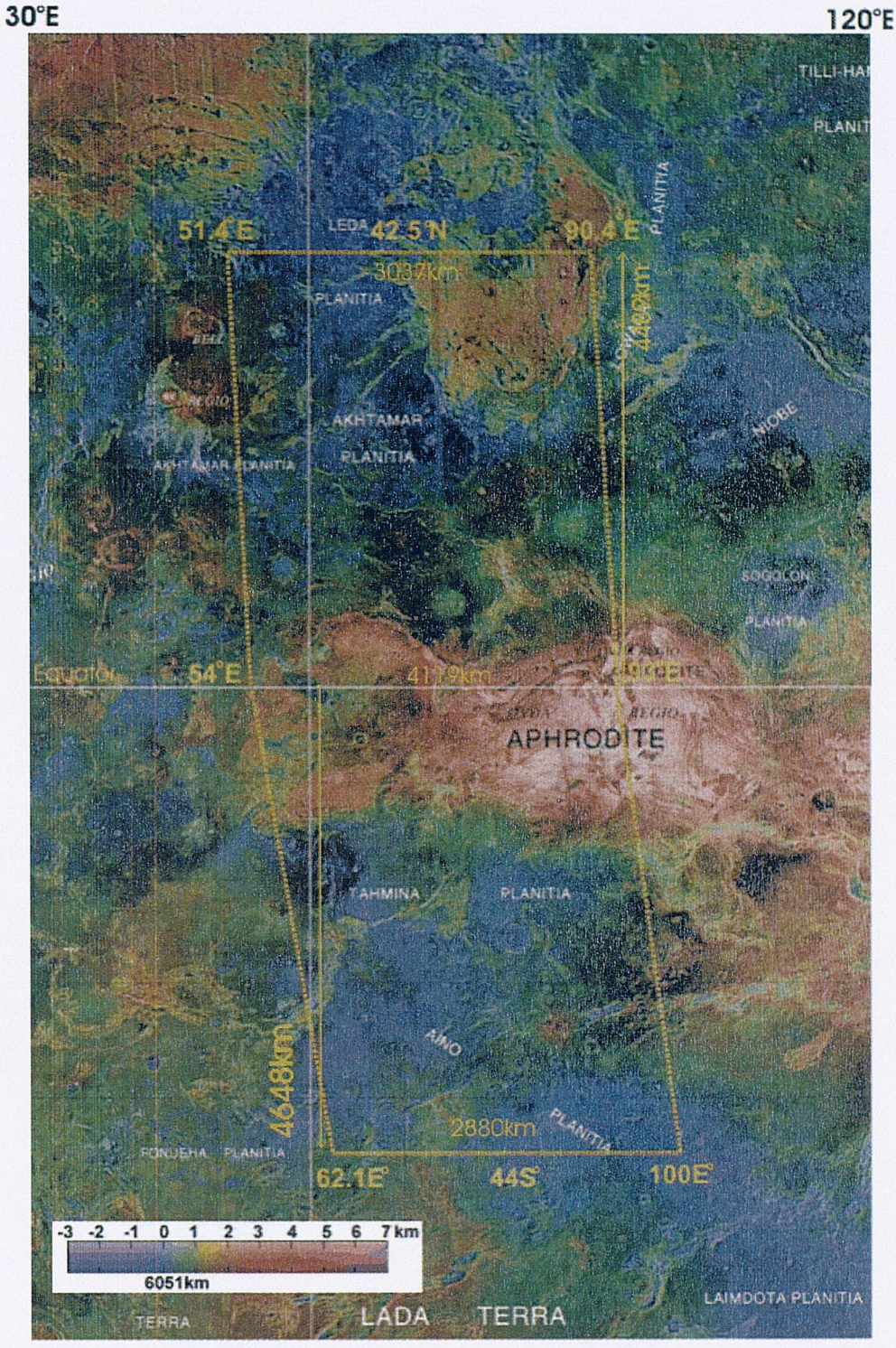


Figure 3.3: Definition of the Sample Area. Defined by 3 lines of constant latitude at 42.5°N, 0° and 44°S, the ends of which are joined by lines that are straight on a cylindrical projection. Key dimensions and the longitudes at the ends of each line are also given. The backdrop is from a mosaic of Magellan radar reflectivity, coloured for elevation taken from Magellan, Venera and Pioneer Venus altimetry. The effective resolution of this image is about 3 km. From NASA Planetary Photo Journal.

The selected area extends from parts of Leda Planitia and Tellus Tessera in the north, over the western half of Ovda Regio and across a large part of Aino Planitia almost to Lada Terra in the south. It therefore contains approximately equal areas of lowlands, uplands and highlands.

Cycle 1 coverage is almost 100%, and Cycle 2 right-looking coverage is about 70%. Cycle 3 coverage suffers from some missing swaths but is still about 90%, including several poor swaths.

A comparable area on Earth, and similarly placed across the equator, is in the Americas, extending from Chicago in the north to central Patagonia in the south, and is as wide as the distance from Charleston to Los Angeles, or Salvador to Lima.

3.2. *Craters in the Sample*

The Magellan Experimenter's Notebook was used to identify all the craters in the larger (USGS) database that were due to be imaged during each Cycle. The USGS-12 page of the Venus_Sample_Craters2.xls spreadsheet in the data CD shows that Magellan was intended to SAR image about half (488) of all craters at least twice, and 138 of these craters 3 times. Largely because of the intermittent nature of Cycle 3 coverage, actual achievement was little better than 50%. Inspection of the imagery reveals that there are 3 usable images of only 78 craters, and hence perhaps only a further 198 craters have stereo image pairs.

The Sample Area constitutes 7.02% of the surface of the planet whereas there are 942 craters listed in Revision 2 of the LPI database for maps covering 98% of that surface. If the planetary cratering density applies to the Sample Area, there should be 65 craters in it, with a standard deviation of 8.06. Taking Herrick's advice [28] to exclude Jasmin, Kyen and an unnamed crater called herein Crater F [29], the Sample Area was found to include 75 craters. This is 7.96% of the 942 listed by the LPI, and denser than the planetary mean by 1.12 standard deviations. The Magellan Experimenter's Notebook shows that 42 were to be imaged during all 3 Cycles, and another 21 were to be imaged during Cycles 1 and 3. Inspection shows there are 3 images of 33 of these craters, same-side image pairs of a further 29, and opposite-side image pairs of another 10. These 75 craters are listed in Tables 3.1 to 3.4. Venus_Sample_Craters2.xls, included on the enclosed CD, shows all the relevant orbit and radar parameters for each image of each crater. Unnamed craters are identified by their latitude and longitude and, in this research, a unique letter (A-E) in descending order of diameter given in the USGS database.

DEMs were produced for 62 craters (83% of the 75 craters listed in Tables 3.1 to 3.4, and 6.6% of the 942 listed by the LPI), using MSTv2 with a standardised process which matched 75 by 75 km, same-side image pairs down to groups of 2 by 4 pixels which is approximately one SAR resolution cell. Some

[28] Personal Communication: E-mail from Herrick 17 Apr 02

[29] Listed in the USGS database as a 3.85 km crater at 27.5°N, 86.0°E. A DEM of this crater shows it to be 181 m deep, ie the smallest in the Sample but not the shallowest.

DEMs of the larger craters were produced by Bierer and Silverthorne, in parallel with this work and to the same procedure. This is called "Procedure for generating DEMs7.doc" and a copy provided in the enclosed CD. As Tables 3.1 and 3.2 show, all DEMs were at least usable but some could not be improved with the Shape from Shading function in MST. DEMs for 3 large craters (Khatun, Agrippina and Deloria) have at least one missing swath, and 2 more craters (Adivar and Aisha) are only half covered in one image.

In spite of several attempts, the procedure would not produce a standard sized DEM for one of the smallest craters (Crater B), and the results for several craters were poor. DEMs of the 4 largest craters covered in Cycles 1 & 3 (Mead, Potanina, Joliot-Curie and Andreanova) were produced in 75 x 75 km sections, called here "mosaics" because the intention was to merge them. No way could be found to do so in 3 dimensions to the accuracy required, and they were used in isolation to support assessment of the entire crater taken from altimetry.

Name	Lat	Long	D	d	Eval	DEM	Notes on DEM
	deg	deg	(km)	(m)	in	by	
Cori	25.4	72.9	57.9	764	A,E,J	C,S	IDL. Missing swath & E rim
Amaya	11.3	89.3	40.4	1094	J,R	S	SFS. West half only & poor
Manzolini	25.7	91.3	53.85	456	E,J	C,S	SFS
Mu Guiying	41.2	81.0	37.9	810	E,J	C,S	SFS
Adivar	8.9	76.2	28.7	893	J,R	C,S	SFS. West half only ok
Tseraskaya	28.6	79.2	33.2	907	E,J	C,S	SFS
Samintang	-39.0	80.7	27.8	1586	J	C	SFS. CP not detected
Christie	28.3	72.7	26.3	522	J	C	SFS. Central black swath
Quimby	-5.7	76.7	24.8	864	M	C	1st DEM poor; CP connected to E rim
Lullin	23.0	81.3	25.98	622	E,F,J,M	C,S	SFS.
Bernhardt	31.6	84.4	23.1	863	J,M	C	SFS. Central black swath
Riley	14.1	72.5	21	725	J,M,R	C,S	SFS.
Carter	5.3	67.3	18.5	693	E,J	C	SFS. Central ridge to E
Doris	2.3	90.0	17.5	482	E,J	C	SFS.
Anush	14.9	86.5	15.2	429	E,J	C	SFS.
Kastusha	-28.6	60.0	14.5	632	E,J	C	SFS.
Amanda	-29.2	94.5	15	445	M	C	DEM poor. IDL of south rim only.
Helvi	-15.2	82.7	12.6	608	E,J	C	SFS.
Hadisha	-39.0	97.2	13.2	283	E,J	C	SFS. Triple crater, D = equiv diam
Florence	12.5	85.0	13.3	534	E,J	C	SFS. Central ridge to N
Jodi	-35.7	68.7	12.2	755	E,J	C	SFS.
Elma	-10.1	91.1	11.3	524	E,J	C	SFS.
Tekarohi	21.2	76.5	9.5	599	E,J	C	SFS.
Mosaido	17.3	75.2	8.8	153	E,J	C	SFS.
Ailar	-15.8	68.4	8.6	213	E,J	C	SFS. Ridge fm SE cuts into crater
Altana	1.4	69.9	8.3	272	E,J	C	SFS.
Eini	-41.6	96.4	7.9	581	E,J	C	SFS.
Georgina	-20.4	58.8	7.3	74	E,M	C	IDL. Central ridge
Teumere	-38.3	88.1	7	383	E,J	C	SFS.
Mbul'di	23.8	74.7	6.9	279	E,J	C	SFS.
CraterA	5.8	84.3	6.6	299	E,J	C	256x256 SFS. One of a doublet crater.
CraterB	6.4	83.4	6.4	250	E,J	C	192x192 SFS
Nsele	6.7	64.2	4.9	247	E,J	C	SFS. Central ridge

Key:			
A	Crater depth from Altimetry	H flipped	DEM from horizontally flipped images
B	DEM produced by Bierer	IDL	Basic form of MST DEM
C	DEM produced by Cochrane	J	DEM measured in Image-J
CP	Central Peak	M	DEM measured directly in MST
E	DEM visualised in ERDAS Imagine	R	DEM visualised in ER Mapper
Eval	Evaluated	S	DEM produced by Silverthorne
F	Crater depth from floor offset	SFS	DEM improved by Shape from Shading
		192x192	Non-standard image size, in pixels

Table 3.1: The 33 Craters in the Sample Area with 3 images. All DEMs were produced in MST v2.0, and enhanced with Shape from Shading, if possible. First, spot heights on rim, central peak, and floor were measured with MST's contour function. Then the DEM was visualised in ERDAS Imagine. The crater parameters of good quality DEMs were measured in Image-J, by picking 20 – 30 peaks and saddles on the rim, fitting a circle to them and finding the floor contour that contained 10% of the area contained by the rim. Where texture was adequate, the third image was used for validation.

Name	Lat	Long	D	d	Eval	DEM	Notes
	deg	deg	(km)	(m)	in	by	
Mead	12.5	57.2	296	1066	A,J	B,C	9 mosaics
Potanina	31.6	53.1	112.8	925	A,E,J	C	4 mosaics; only West 2 good
Joliot-Curie	-1.6	62.4	120	605	A,E,J	S	West half only; 2 mosaics
Andreianova	-3.0	68.8	77.3	1185	A,E,J	C	4 mosaics; little floor
Voynich	35.4	56.1	54.1	893	A,E,J	C,S	SFS, H flipped. Centre only
Agrippina	-33.2	65.7	40.5	928	E,J	C,S	SFS. Central black swath
Heloise	42.0	51.9	39.7	440	M	C	SFS. Centre only. Doublet, D = equiv diam
Khatun	40.3	87.2	43.2	1372	E,M	S	SFS. Central black swath
Deloria	-32.0	97.1	38.1	1248	E,J	S	SFS.Central black swath
Germain	-37.9	63.7	36.2	1074	E,J	C	SFS. CP missing; ridge on s floor
Bassi	-19.0	64.7	32.8	1058	J	C,S	SFS.
Amenardes	15.0	54.3	29.8	743	J	C,S	SFS.
Recamier	-12.6	58.1	28.6	1391	J	C	SFS.
Merian	34.5	76.3	21.9	486	M	C	IDL of W rim only
MaShouzhen	-35.7	92.5	20.1	864	E,J	C	SFS. Rim low in E and W
Naomi	6.0	70.3	18.6	768	E,J	C	SFS.
Kylli	41.1	67.0	13.9	563	E,J	C	SFS.
Kuro	7.8	57.6	13	617	E,J	C	SFS.
Dado	-14.0	87.7	12.3	420	E,J	C	SFS. Central ridge to ENE
Aisha	39.3	53.3	12	243	E,J	C	SFS. E half only, H flipped.
Loan	28.3	60.0	11.2	512	E,J	C	SFS. Doublet crater, D = equiv. diam.
Fava	-0.8	87.4	10.9	695	E,J	C	SFS.
Puhioia	20.6	69.4	10	327	E,M	C	IDL
Ndella	-15.9	60.7	6.1	303	E,J	C	SFS. Doublet crater, D = equiv. diam.
Marere	19.6	65.8	6.6	291	E,J	C	SFS.
Tehina	-30.4	76.4	5.9	121	E,J	C	SFS.
Nyai'ga	17.0	64.5	5.6	306	E,J	C	SFS.
CraterD	40.6	65.3	5.1	289	E,J	C	SFS.
CraterE	39.2	53.2	4.4	75	E,J	C	SFS.

Key:			
A	Crater depth from Altimetry	H flipped	DEM from horizontally flipped images
B	DEM produced by Bierer	IDL	Basic form of MST DEM
C	DEM produced by Cochrane	J	DEM measured in Image-J
CP	Central Peak	M	DEM measured directly in MST
E	DEM visualised in ERDAS Imagine	R	DEM visualised in ER Mapper
Eval	Evaluated	S	DEM produced by Silverthorne
F	Crater depth from floor offset	SFS	DEM improved by Shape from Shading
		Equiv. diam.	Diameter of one circle of same area

Table 3.2: The 29 Craters in the Sample Area with 2 same-side images. All DEMs were produced in MST v2.0, and enhanced with Shape from Shading, if possible. First, spot heights on rim, central peak, and floor were measured with MST's contour function. Then the DEM was visualised in ERDAS Imagine. The crater parameters of good quality DEMs were measured in Image-J, by picking 20 – 30 peaks and saddles on the rim, fitting a circle to them and finding the floor contour that contained 10% of the area contained by the rim. DEM mosaicks of larger craters could not be matched satisfactorily so were used to supplement altimetry.

The DEMs craters listed in Tables 3.1 and 3.2 were first evaluated in MST, with the "QC" function, which allows the rim peaks and the deepest point on the floor to be identified and measured. Where possible, the DEM file from MST was imported into ERDAS Imagine for visualisation with the "Procedure for transferring MST Files to ERDAS Imagine2.doc" included in the accompanying CD. The ERDAS Image files were then imported into Image-J for measurement using the variable threshold function. First the threshold was reduced to identify the peaks in the rim, and the saddles between them. Each was marked so a listing of the spot heights could be output and the mean rim height derived. Three attempts were made to fit a circle to the marks, and the mean rim diameter derived. The threshold was then reduced to the floor and 3 attempts made to find a contour that contained 10% of the area contained by the rim. The average height within this contour was taken as the floor height, and a rim-floor depth derived as the mean of the 3 attempts. Surrounding terrain was measured as the mean of 3 attempts to adjust the threshold so that it bisected the area outside the crater. Central features were measured in similar ways.

MST frequently failed to generate a DEM if the two image frames had not first been closely matched in their top left corners. The first DEMs produced of Amanda, Carter (see Fig. 3.4) and Quimby contained a central ridge, joining east

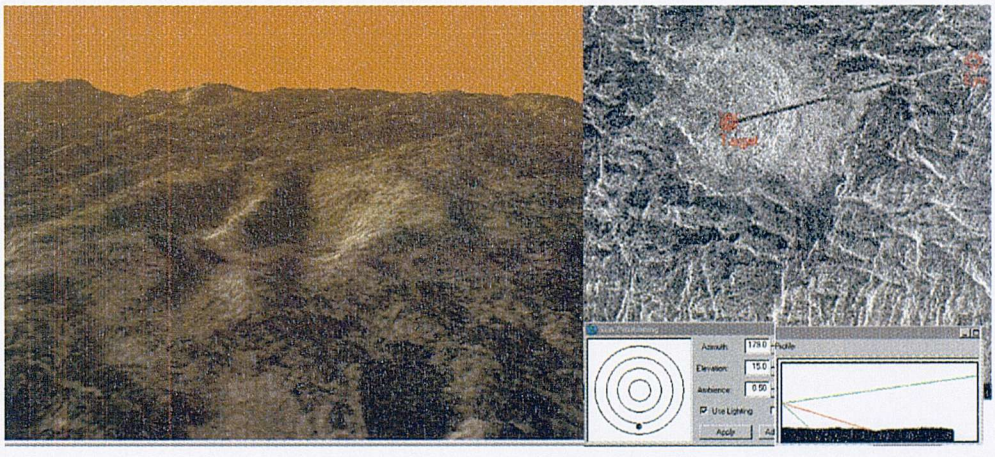


Figure 3.4: Visualisation of artefact in Carter crater. The prominent East-West ridge is due to failure of image matching to track down the central section of the western escarpment of the crater. Visualisation in ERDAS Imagine of my DEM, from the position indicated on the right, shows that the matching has found a flat floor either side of the ridge artifact.

and west rims. This was attributed to the matching failing to track down the central section of the western escarpment, and hence did not render the DEM unusable. More careful selection of the matching image frames produced more acceptable results; the residual artifacts are discussed more fully in Chapter 4. In one case, Aisha, the top left corners of the matching frames were featureless so it was necessary to match the bottom left corner of the two frames and flip the images horizontally prior to matching. In another, Merian, only a very small part of the eastern rim appeared in the left side of the frames. The images were therefore matched on their eastern sides and flipped vertically so that the matching process would proceed from the surrounding terrain down into the crater rather than try to start up the escarpment. Two of the mosaics for Voynich were similarly manipulated. In all cases, the resulting DEM must be flipped to restore its correct geographic orientation.

OSMATCH software was being developed at Imperial College, as described in Lee *et al* (unpublished). It was used to generate DEMs from the 10 opposite-side image pairs; they were then assessed with ER-Mapper. Like MST, his software used the y-excursion, or "Y Disparity" as a check of matching validity; in all cases this showed that matching was unacceptably poor. Hence these craters were measured either by feature parallax or by floor offset, where it was distinct.

Name	Lat	Long	D	d	Eval	Notes
	deg	deg	(km)	(m)	in	
Parra	20.5	78.5	44.5	900	F	Cycles 1 & 2
Elena	-18.3	73.4	18.6	532	P	Cycles 1 & 2
Emilia	-26.5	88.2	13.7	1000	P	Cycles 1 & 2
Temou	-10.0	83.4	10.5	460	P	Cycles 1 & 2
Maurea	-39.5	69.1	10.4	455	F	Cycles 2 & 3
Teura	-12.3	90.2	10.0	308	P	West rim only in cycle 3
Shushan	-43.8	70.2	9.1	340	F	Cycles 2 & 3; E escarpment missing
Madina	22.7	58.1	7.5	602	F	
Ruit	-25.6	73.0	7.1	318	P	Cycles 1 & 2
CraterC	8.0	74.2	4.9	140	P	Cycles 1 & 2

Key:	
F	Crater depth from floor offset
P	Crater depth from opposite-side parallax

Table 3.3: The 10 Craters in the Sample Area with 2 opposite-side images. Attempts were made to produce DEMs with a preliminary version of OSMATCH, but Y-disparities were too high for any part of the DEMs to be considered reliable. Also, radar shadowing restricted coverage of the crater rim escarpments to the East and West. Hence, crater depths were estimated by floor offset or feature parallax. Diameters and depths are as found in this study.

The 3 craters in the Sample Area that could not be measured with any confidence are listed in Table 3.4. There is also a spreadsheet of general crater parameters on the CD called "Venus Sample Craters2.xls".

Name	Long	Lat	D	Notes
	deg	deg	(km)	
Romola	54.3	9.3	19.1	W half of Cycle 1 only; irregular crater
Mansa	63.4	-33.9	8.2	Cycle 1; irregular crater
Rae	58.4	-8.9	5.6	Cycle 1; W rim indistinct, floor irregular

Table 3.4: The 3 Craters in the Sample Area with only one image. Diameters are taken from the LPI database. None of the rims are sufficiently clear to allow depth estimation of these craters by floor offset.

To confirm their validity, Lullin was measured by both methods separately. The results, described in the Crater Notes, were reasonably consistent but the results from the two methods were not sufficiently consistent and indicate that there is some merit in presenting all the depth~diameter results to show the consistency of their broad pattern.

Also, the checks with Lullin indicate that the depths given in a DEM may be validated by "spot checks" from a third image. Given the lack of ground truth and limitations of other instruments, a third SAR image is the only validation available for features smaller than the altimeter footprint, ie about < 12 km across-track. Of the 33 crater DEMs with a Cycle 2 image, only 17 were found to be useful for validation.

3.3. Crater Diameters

This research first explored an effect reported in Herrick & Sharpton (2000). Using the techniques described in the previous section, the diameters of 59 DEMs, from the smallest to Andreanova, were established. As Fig. 3.5 shows, typically the rim diameter found in the DEM produced for this study is 10% ± 15% larger than that published by the LPI database. A comparison with the USGS data is similar.

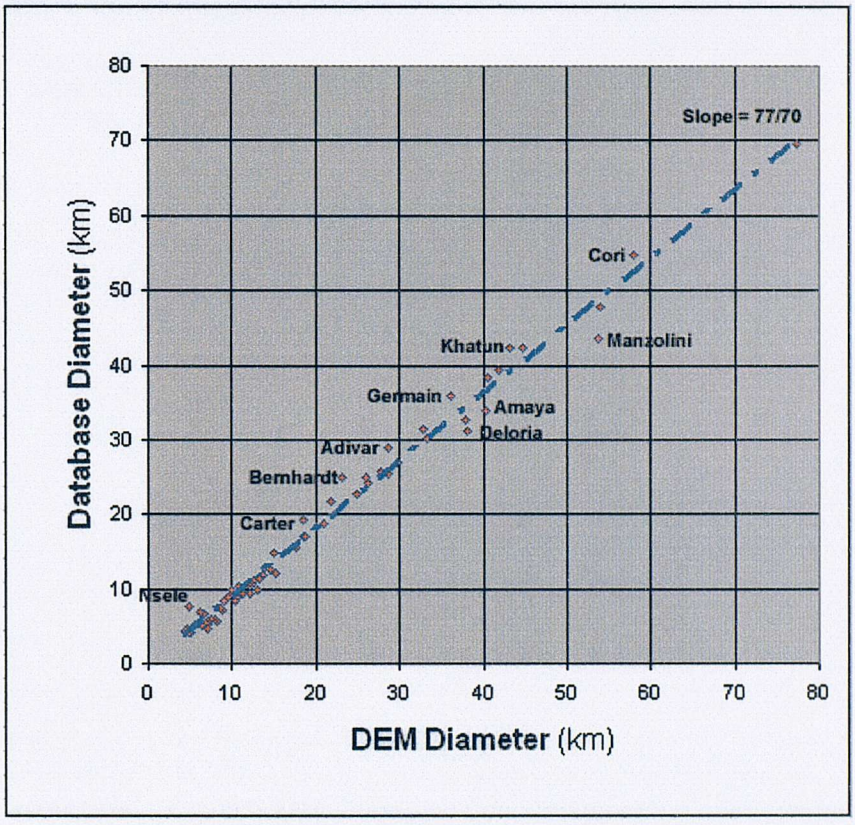


Figure 3.5: Diameters of craters compared to those in the LPI database. Trend for all 62 DEMs, less the 3 largest craters, Mead, Potanina and Joliot-Curie. The slope indicates that the diameter of all craters has been underestimated by 10%. Manzolini is the most significant variation, the other craters which significantly depart from the trend, in both senses, are named. The diameters given in the USGS database are also found to be similarly under-estimated.

The three larger craters (Mead, Potanina and Joliot-Curie) were excluded from this analysis on the grounds that they are much larger than the other craters

and that their rims were established primarily on the basis of altimetry profiles from Brown & Grimm (1996) given in Fig. 3.6.

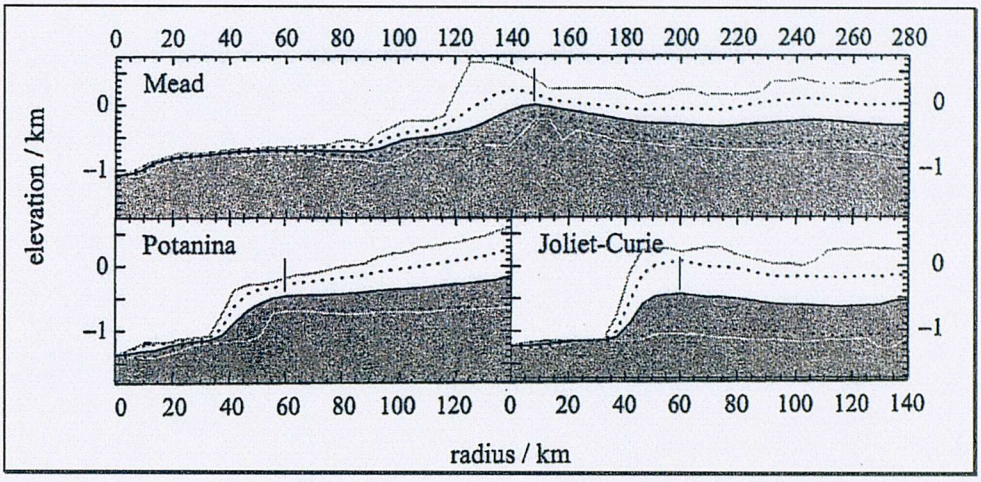


Figure 3.6: Azimuthly averaged topography of the largest craters. Elevations are referenced to a mean planetary radius of 6051.85 km (6051.84 is more generally accepted). The solid curves mark the mean elevations; grey curves indicate the maximum and minimum elevations recorded at each radius. The dotted curves show the mean plus and minus one standard deviation at each radius. Solid vertical lines show the rim as defined in this study for measuring depth. Taken from Brown & Grimm (1996).

Name	°Latitude	°Longitude	Diameter km	depth m	Altimeter Resolution EW x NS km	Data points inside crater
Mead	12.5	57.0	296	1080	13 x 9	1176
Joliot-Curie	-1.7	62.4	120	725	13 x 9	193
Potanina	31.7	53.0	112	900	14 x 9	159

Table 3.5: Depth and Diameter of the largest craters. The points defined in Fig. 4.27 give the crater rims. Diameter and depth are taken directly from the curves. Depth estimates are from crater rim-floor to absolute floor bottom and all were revised as discussed in Chapter 4. For these numbers of data points inside the crater concerned, the technique should provide reliable rim averaging but all profiles converge to a single central measurement.

These results show a more pronounced trend of diameters found to be larger than published for Mead, Joliot-Curie and Potanina by at least 10%.

3.4. Crater Depth/Diameter Ratios

Fig. 3.7 shows the results of measuring the rim-floor depth and rim diameters, as described above, of 72 craters (7.64% of the population listed by LPI), and compared to the trend lines from earlier research. These data are well distributed about a single trend line, and the new trend line has a slope that is inconsistent with earlier work. The trend is essentially unchanged if all the data on opposite-side image pairs are removed.

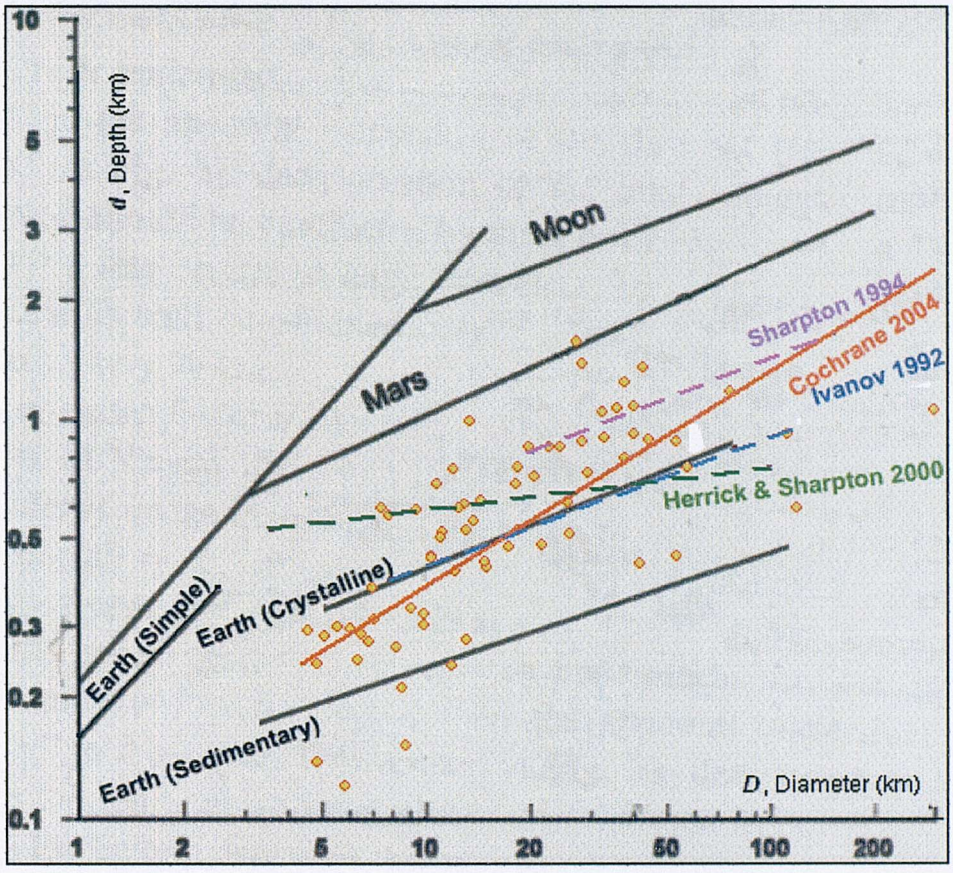


Figure 3.7: Depth/diameter trend for 72 craters, compared to earlier research. Measured by methods as described herein and compared to published trends for Venus [coloured for Sharpton (1994), Ivanov et al (1992) and Herrick & Sharpton (2000); and black for other terrestrial planets from Grieve and Cintala (1999), based on the database of terrestrial craters at Natural Resources Canada and Dressler, Grieve and Sharpton (1994)]. The trend line for all 72 craters is: $d = 2.63\ D^{0.54}$ and, at R2 = 0.51, a poor fit to the data. Removing the data for the opposite side pairs makes no difference to the trend, to 2 decimal places. Note particularly that this trend is inconsistent with earlier work.

Cochrane (2002) showed that the small diameter craters, in a set chosen for coverage in all 3 Cycles, are unusually shallow. As this was presumed to be due to many distributed impactors, he proposed that they might be termed "Compound". The key characteristic of this class of crater was defined as a D:d trend parallel to that for simple craters on Earth-like planets.

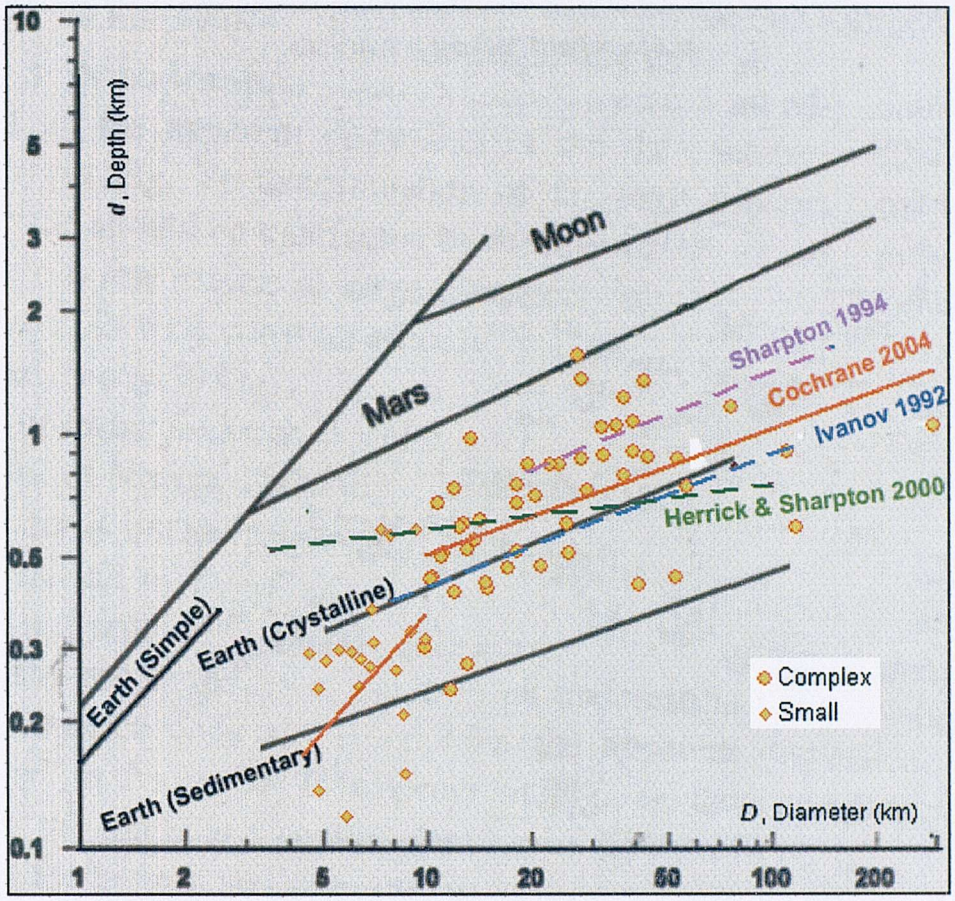


Figure 3.8: Two depth/diameter trends for 72 craters, for < and > 10 km. Measured and compared as described in Fig. 3.7. The trend line for 22 craters < 10 km diameter, d = 0.49 D 0.97, is close to that of Simple craters on Earth (d = 0.27 D 0.93) and, at R2 = 0.16, a better fit than in Fig 3.7. The trend line for "Complex" craters > 10 km diameter is d = 31.6D 0.30 and, at R2 = 0.28, is a better fit than in Fig 3.7 and more consistent with earlier work. Hence, there appears to be a transition on Venus at about D = 10 km that is similar to the transition on Earth at about D = 3 km between Simple craters and Complex craters into Crystalline or Sedimentary strata.

Fig. 3.8 shows that the new results are better represented by 2 trend lines, not unlike those for Simple and Complex craters on the other terrestrial planets. The transition diameter of 10 km was found by trial and error, looking for the best match to the slope for simple craters on Earth. The slope for craters larger than 10

km then lies parallel to and between the results using floor offset in Ivanov *et al.* (1992) (76 craters from 8 to 64 km diameter) and Sharpton (1994) (94 craters > 18 km diameter).

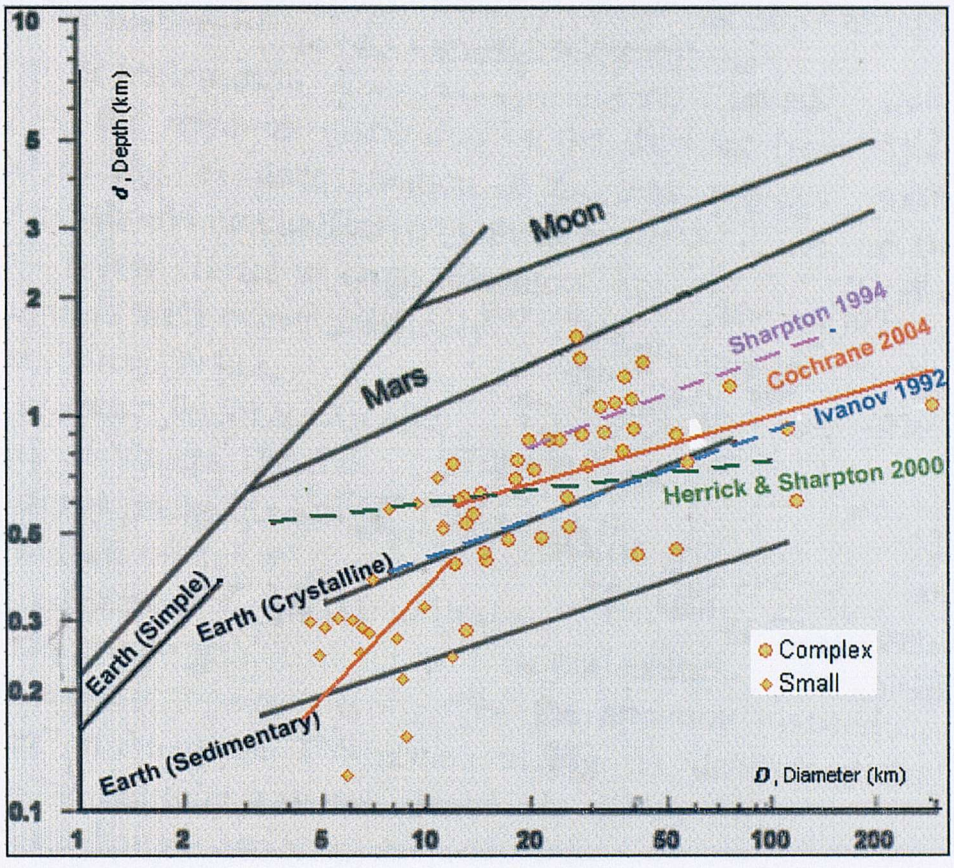


Figure 3.9: Two depth/diameter trends for 62 DEMs, for < and > 12 km. The sample has been reduced by removing those craters measured by floor-offset. These are also compared as described in Fig. 3.7. The trend line for 22 craters < 12.1 km diameter is: $d = 0.065D^{0.94}$, ie closer to that of Simple craters on Earth ($d = 0.27D^{0.93}$) and, at $R^2 = 0.23$, a good fit. The trend line for the 14 craters < 8.5 km diameter is similar. Furthermore, the trend line for "Complex" craters, ie > 12.1 km diameter is: $d = 63D^{0.25}$ and, at $R^2 = 0.20$, gives an upper trend line very close to that of Ivanov *et al* (1992). Hence, the DEMs show a transition on Venus somewhere between D = 8.5 and 12.1 km that is similar to the transition on Earth at about D = 3 km between Simple craters and Complex craters into Crystalline or Sedimentary strata.

This trend intersects but does not lie parallel to the results of Herrick & Sharpton (2000) (79 DEMs from 3.6 to 101 km diameter). Removing the measurements by floor-offset method, as in Figs 3.9, did not significantly affect the trend line but 2 transition diameters of 8.5 km and 12.1 km were found. Fig

3.9 illustrates the latter case, where there are 22 craters in the smaller set and the upper trend line lies between those of Herrick & Sharpton (2000), Sharpton (1994) and Ivanov et al (1992).

To understand the offset of the "Compound" from the "Simple" trend line at a depth of 250 m, assume D_E is the diameter of any crater on Earth, and d_E is its depth. The trend for Simple craters on Earth in Fig 3.9, etc. from Grieve and Cintala (1999), gives:

$$d_E = 0.27\, D_E^{0.93} \quad \text{.....(8)}$$

Then, for example, it may be shown that

$$D_E = 1.55 \text{ km} \quad \text{.....(9)}$$

i.e. on Earth, a crater 250 m deep has a diameter of 1.55 km.

If the set of "compound" craters on Venus is called set **C**, which have a depth d_C and a diameter D_C, then from Fig 3.9:

$$d_C = 0.065\, D_C^{0.94} \quad \text{.....(10)}$$

i.e. on Venus, a crater 250 m deep has a diameter of 6.51 km.

Hence, compound craters have about 4.2 times the diameter of a terrestrial crater of the same depth, that is:

$$D_C \cong 4.2\, D_E \quad \text{.....(12)}$$

Hence, if the mean depth of any crater is a fraction, K, of its measured depth and the excavated volume, V_E , of each element of a compound crater of N elements is given by:

$$V_E = \frac{\pi K_E d_E D_E^2}{4} \quad \text{.....(13)}$$

And, the excavated volume, V_E, of a compound crater of N elements will be given by:

$$V_C = N.V_E = \frac{N\pi K_E d_E D_E^2}{4} \quad \text{.....(14)}$$

If: $K_E \cong K_C$ ..... (15)

it can be shown that.

$$V_C \cong 4.2^2 V_E \cong 17.6.V_E \quad \text{.....(16)}$$

Hence, each compound crater must have been formed by at least 18 elements. This may be plausible for all 5 small craters in the Sample classified in the LPI database as multiple: Florence (13.3 km diam), Hadisha (13.2 km diam), Kuro (13.0 km diam), Loan (11.2 km diam) and Temou (10.5 km diam). The only other multiple crater in the Sample is Heloise (33.3km diam), which appears to be a binary impact, subsequently embayed by flood lava. There are also 2 S-type craters in the Sample classified in the LPI database as crater fields: Nsele (4.9 km diam) and Crater A (4 km diam).

Also, the above conjecture implies that a small bolide, of diameter D_B, which would normally cause a crater on Earth of diameter 10 D_B, must fragment in the atmosphere of Venus and disperse to a pancaked diameter, D_P , that is the diameter of the final crater less the diameter of an element of it. So, D_P must be given by:

$$D_P = (4.2-1).10.D_B = 32.D_B \quad \text{.....(17)}$$

And its thickness, t_P , at impact, i.e. after mass wasting due to an ablation factor of L_V, is given by:

$$t_P = \frac{1.33.\pi.L_V.D_B^3}{\pi.32^2.D_B^2} = 0.0013\,L_V.D_B \quad \text{.....(18)}$$

This aspect ratio (800:1) is higher than other research supports and may be unreasonable. The assumption that excavated volumes are equivalent is not supported by any evidence, eg from numerical modelling. This Thesis retains the conjecture as a plausible explanation of the DEM data, and this aspect ratio as, at best, an upper bound for the spreading of bolides of initially about 1 km diameter.

Numerical modelling to date, e.g. Korycansky *et al.* (2000), has integrated total mass and momentum over all heights to find that a normally-incident, 2 km diameter, spherical bolide looses sufficient momentum in the atmosphere of Venus to cause a 14 km diameter crater, instead of a 20 km diameter crater if there were no atmosphere. This diameter reduction by a factor of 0.7, is illustrated in Fig. 3.10 as point **A** moving down a fixed D:d trend line to point **A'**. Korycansky *et al.* (2000) find that in only 2 of 10 cases such a bolide pancakes.

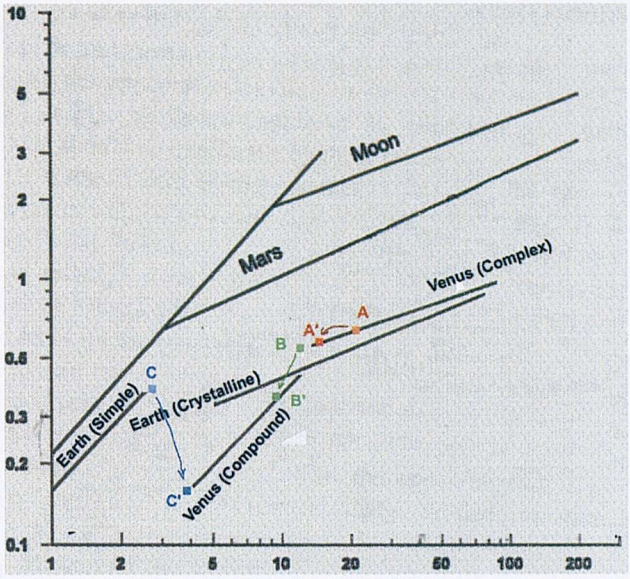


Figure 3.10: Effect of pancaking within the D:d domain. The background is from key elements of Fig. 3.9. Case A is an example, from Korycansky *et al* (2000), of a 2 km bolide causing a 14 km crater, that would have been 20 km but for the atmosphere. Case B illustrates how a 1.2 km m bolide might pancake to some extent and give rise to a shallower but smaller diameter crater. In Case C, a 270 m bolide might disperse sufficiently to cause a 4 km diameter crater, larger than would have been caused without the atmosphere but very much shallower.

Korycansky *et al.* (2002) confirms that their crater diameters were derived from lumped mass and momentum scaling according to Schmitt and Housen (1987), and their final crater diameter in the above case is beyond the range of the DEM data. Consider, instead, a bolide of 1.2 km diameter, which would be expected to lead to crater of 12 km diameter in the absence of an atmosphere, i.e. a case that falls within the range of the DEM data. The conjecture proposes that here the bolide pancakes, so the effective crater diameter reduction is less, and ablates more so that crater depth is reduced. This case is illustrated in Fig. 3.11 as point **B** departing from the D:d trend line for Complex craters on Venus to point **B'** on the DEM trend, labelled Venus (Compound). In the limit, the conjecture

may imply that a very small initial bolide, could pancake to give rise to a diameter crater, point **C**, larger than would have been the case, point **C'**, because its mass and momentum is delivered to the surface over the whole area of the pancake. In fact, Korycansky *et al.* (2002) find that such small impacts are enhanced by entrained atmospheric shock.

Finally, craters < 12 km diameter constitute 44% of the crater population. The extent to which that part of the population has been affected will depend on the ablation and drag acting on the bolides in the atmosphere of Venus as well as their cohesion, and none of these parameters are well characterised. MacKinnon *et al.* (1997) is most probably the best attempt to model the relevant factors so as to assess the age of the cratered surface. McKinnon *et al.* (1997) assume that the impactor population is composed of the following six categories:

- Asteroids[30]: S type,
  C type,
  Irons,
- Comets: Long Period,
  Short Period, Jupiter family,
  Short Period, Halley family.

It should be noted that they assume all craters are complex and treat them as due to point impacts of distorted bolides, not their distributed fragments. In particular, they estimate that the atmosphere can totally prevent impact of about 25,000 incoming bolides yet allow about 1,000 through to impact normally after deceleration and ablation. Fig. 3.11 shows (in black) the results of one of their simulations, and how the conjecture might help explain the poor fit they find in the smallest 3 bins (blue arrow).

[30] This is a simplified taxonomy. See Norton (2002).

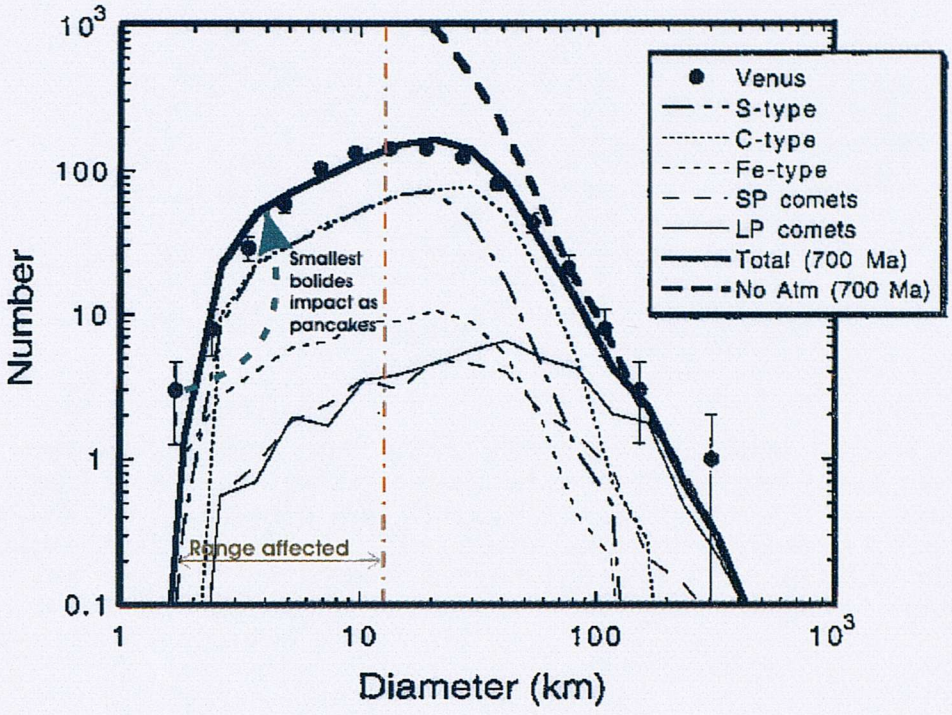


Figure 3.11: Effect of pancaking on a simulation of Venus craters. Results from MacKinnon *et al.* (1997) in black, concerning a population of 940 craters, a surface age of 700 Ma and using the impactor populations from Shoemaker *et al.* (1990, 1994). Pancaking may affect craters up to 12 km diameter (orange line), about 44% of the population. The pancaking of some small bolides may explain the simulated excess of the smallest craters and an equivalent deficiency of slightly larger craters.

The key feature of the conjecture - a Diameter:depth trend like simple impacts - may be explained if compound impacts create less disruption in the material surrounding the transient crater than complex craters of a similar size. Typically, shock wave geometry for a single impact or element of a multiple impact is as per Fig. 3.12, a cartoon, and Fig. 3.13, a cross-section diagram. In a multiple impact, compression and rarefaction waves from the separate elements must interact, so later compressions suppress the rarefaction due to earlier impacts, as illustrated in Fig. 3.14. This should have the effect that less target material fails in tension, i.e. less of the surrounding rock shatters, preventing the onset of the collapse typical of complex craters in intermediate-sized impacts. According to Melosh (1989), possible indicators of compound impacts are less spallation and rim uplift than following a single impact, for a given crater diameter.

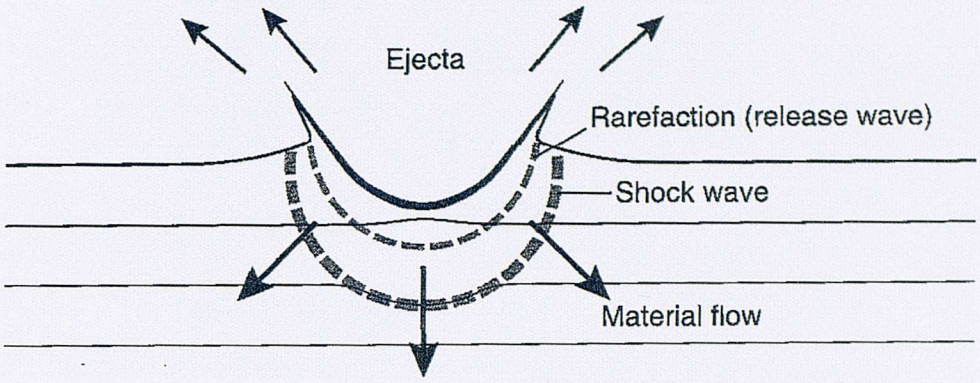


Figure 3.12: Release wave forming during the Excavation Stage of an impact. A release wave starts to form after the end of the Compression stage, which Melosh (1989) estimates to be some 100 msec after the initial contact of a 1 km diameter silicate bolide striking at 10 km s^{-1}. This diagram, from French (1999), shows sufficient rarefraction to lift the strata underling the impact. According to Shoemaker & Shoemaker (1999), the rarefaction creates an expanding cavity, from which decompressed material sprays out as an ejecta sheet.

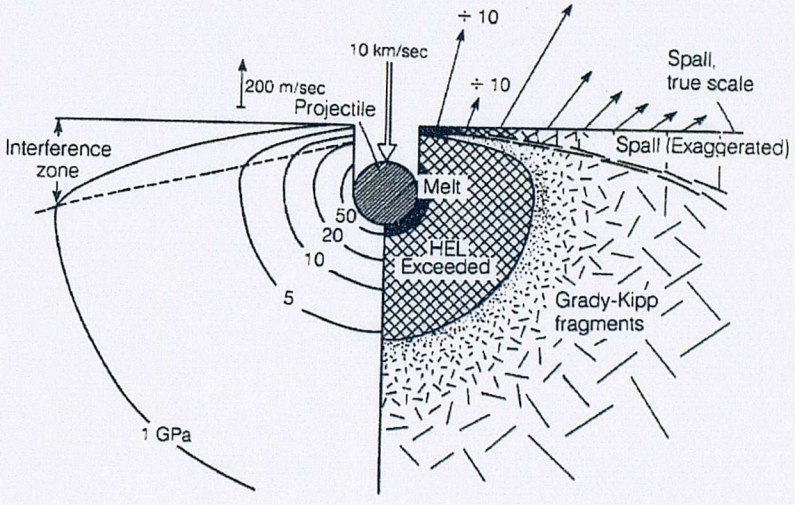


Figure 3.13: Cross-section of a typical Impact. Cartoon from Melosh (1989). The impactor buries itself in the target, causing a hemispherical shock front to expand, shattering the rocks beneath into small fragments characterised by Grady & Kipp (1980). Near the surface, the rarefaction wave interferes with the compression wave, first reducing its effect and then dominating. Cracks begin to nucleate in the surface rock and spall plates are thrown up from the surface at high speed. These spall plates may break up in flight or cause secondary impacts.

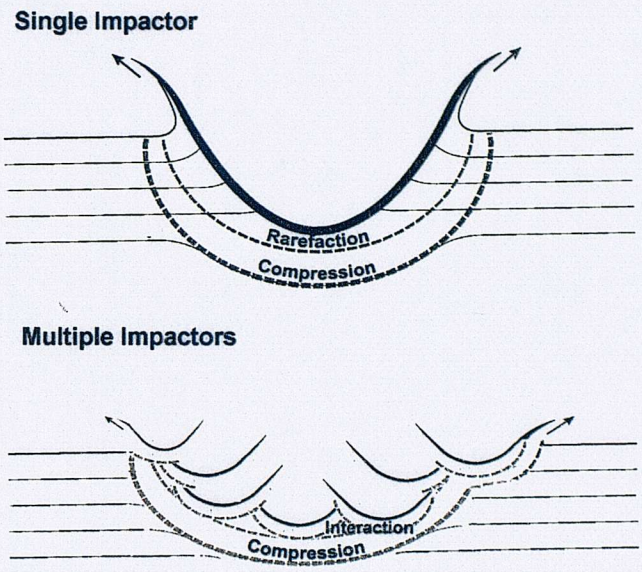


Figure 3.14: Comparison of Single and Multiple Impacts. The top diagram is from French (1999) to represent the transient cavity at the end of the compression stage. In the lower diagram, compression and rarefaction waves from each elemental impact interact. A sequence of such impacts will suppress associated tensional failure of the target rock, excavate a shallower crater, produce less ejecta and cause little rim uplift.

Although there is no theoretical foundation for a class of "Knobby base" crater, it is the most populous in the LPI database. In the Sample set, 41 (54%) are classified as having a "Knobby base", and these range in diameter from Crater A (4 km) to Naomi (18.6 km).

In the Set of 62 DEMs, there are 29 (46.8%) knobby base craters with diameters of 4 to 18.6 km, and these are listed in Table 3.6. There are also 19 (30.6%) central peak craters with diameters of 12.8 to 54.1 km, and these are listed in Table 3. 7. There are similar percentages in the crater population of 942: 496 (52.7%) Knobby Base and 279 (29.6%) Central Peak craters.

Table 3.6 shows that the Knobby Base craters lie at all altitudes above the planetary mean, and on various terrains. They appear to have various ages: 8 have perceptible dark halos and all show a significant range of degradation but none have dark parabolas.

Crater			This Thesis					LPI 2002						
Name in LPI Database or given for this study	Latitude	Longitude	diameter	Rim-Floor Ht	Rim Ht	Terrain-Floor Ht	Central peak Ht	Escarpment Diameter	elevation above planetary mean	dark halo diam	multiple crater	floor reflectivity	Terrain	degradation state
	°Lat	°Long	D					km	km					
Naomi	6.0	70.3	18.6	768	-29	797	n/d	17.1	1229	x	s	i	t	2
Carter	5.3	67.3	18.5	693	2	691	n/d	19.3	2285	55	s	b	t	2
Amanda	-29.1	94.5	15	185	4	325	n/d	14.8	231	x	s	i	v	1
Florence	-15.3	85.0	13.3	534	142	392	n/d	11.6	1050	x	m	i	p	1
Hadisha	-39.1	97.2	13.2	283	66	218	n/d	11.3	-593	60	m	b	p	1
Kuro	7.8	57.6	13	617	164	454	n/d	10.0	-252	30	m	i	pf	2
Helvi	12.4	82.7	12.6	608	2	507	n/d	11.2	510	x	s	b	pf	1
Dado	-14.0	87.7	12.3	420	-	-	n/d	10.7	1218	x	s	i	pf	1
Jodi	-35.7	68.7	12.2	755	79	676	n/d	9.5	-657	x	s	b	p	1
Elma	-10.1	91.1	11.3	524	121	155	n/d	9.7	2775	x	x	i	t	1
Loan	28.2	60.0	11.2	512	69	443	n/d	9.5	-587	x	m	b	p	1
Fava	-0.8	87.4	10.9	695	-27	721	n/d	10.3	3442	x	s	d	t	3
Puhioia	20.6	69.4	10	327	-	-	n/d	6.4	-819	x	s	b	p	1
Tekarohi	21.2	76.5	9.5	599	67	532	n/d	8.9	-149	x	s	b	pf	1
Mosaido	17.3	75.2	8.8	153	104	49	n/d	7.3	-249	x	s	i	pf	1
Ailar	-15.9	68.4	8.6	213	47	166	n/d	7.5	-371	x	s	i	p	1
Altana	1.5	69.9	8.3	272	-	-	n/d	5.7	1632	x	s	i	t	1
Eini	-41.6	96.4	7.9	581	-34	615	n/d	5.9	-930	30	s	i	p	1
Georgina	-20.4	58.8	7.1	74	-	-	n/d	5.2	-600	40	s	i	p	1
Teumere	-38.3	88.1	7.0	83	59	324	n/d	4.7	-751	x	s	i	p	1
Mbul'di	23.8	74.7	6.9	279	56	223	n/d	5.5	-1109	x	s	i	p	1
Marere	19.6	65.8	6.6	291	75	216	n/d	6.7	-686	x	s	i	pf	2
Crater A	5.8	84.3	6.6	299	4	325	n/d	4.8	316	60	f	i	p	1
Crater B	6.4	83.4	6.4	250	2	247	n/d	5.1	160	80	s	d	p	1
Ndella	-15.9	60.7	6.1	303	180	123	n/d	5.0	-618	x	s	b	v	3
Tehina	-30.4	76.4	5.9	121	111	11	n/d	5.4	-764	x	s	i	p	1
Nyal'ga	17.0	64.5	5.6	306	83	224	n/d	5.2	-348	x	s	i	pf	2
CraterD	40.7	65.4	5.1	289	85	204	n/d	4.1	-540	x	s	i	pf	2
Nsele	6.7	64.2	4.9	247	0	247	n/d	4.9	1656	40	f	i	t	1
Key:	n/c = not covered; n/d = not detected													
	Multiple Crater: f = Crater field, m = Multiple crater, s = Single crater													
	Floor reflectivity: d = dark, i = intermediate, b = bright													
	Terrain: p = plains, pf = fractured plains, r = ridge belt, t = tessera													
	Degradation: 1 = pristine, 2 = no ejecta, 3 = degraded													

Table 3.6: Parameters of the "Knobby Base" DEM set. These parameters, some extracted from the LPI (2002) database, show that these 29 knobby base craters lie at altitudes from 1109 m below to 3442 m above the planetary mean, on a variety of terrains, with all classes of floor brightness and degradation (ie age). Seven craters have perceptible dark halos, 5 have a clearly identifiable central prominence, and 4 others are multiple craters. No central feature height is given for multiple craters or where one cannot be detected above matching noise (taken to be 100 m).

In contrast, Table 3.7 shows that this selection of Central Peak craters lie predominantly on plains and halos are more prevalent. Both sets have the full range of floor brightness.

Crater			This Thesis					LPI 2002					
Name in LPI Database or given for this study	Latitude	Longitude	diameter	Rim-Floor Ht	Rim Ht	Terrain-Floor Ht	Central peak Ht	Escarpment Diameter	elevation above planetary mean	dark halo diam	floor reflectivity	Terrain	degradation state
	°Lat	°Long	D	m	m	m	m	km	km	km			
Voynich	35.3	56.1	54.1	893	169	468	121	47.9	-372	190	d	p	1
Agrippina	-33.3	65.7	40.5	928	388	541	273	38.4	-783	x	d	p	1
Amaya	11.3	89.3	40.4	1094	240	437	n/c	34.0	722	120	d	r	1
Germain	-38.0	63.7	36.2	1074	547	527	245	35.9	-750	110	d	p	1
Tseraskaya	28.6	79.3	33.2	907	128	780	560	30.1	-202	x	i	t	2
Bassi	-19.0	64.7	32.8	1058	306	752	760	31.4	-821	110	b	p	1
Amenardes	15.0	54.3	29.8	743	107	67	624	27.0	-323	x	i	pf	2
Adivar	8.9	76.2	28.7	893	74	819	464	29.0	-76	70	i	p	1
Recamier	-12.6	58.1	28.6	1391	336	1055	421	25.5	865	x	b	t	3
Samintang	-39.0	80.7	27.8	1586	85	1201	n/d	25.8	-470	x	d	pf	1
Christie	28.3	72.7	26.3	522	106	416	n/c	24.3	-1004	170	i	p	1
Lullin	23.0	81.3	26.0	622	96	527	553	24.9	-40	160	d	p	1
Quimby	-5.7	76.7	24.8	864	215	649	n/d	22.9	2395	x	b	t	2
Bernhardt	31.6	84.4	24.8	863	n/d	n/d	n/d	22.9	181	x	d	t	1
Riley	14.0	72.5	21	725	167	559	323	18.8	72	80	i	p	1
MaShouzhen	-35.7	92.5	20.1	864	864	215	649	18.3	-40	40	d	p	1
Anush	14.9	86.5	15.2	429	172	265	119	12.2	37	x	d	p	1
Kastusha	-28.6	60.0	14.5	632	280	457	411	12.7	-614	100	i	p	1
Kylii	41.1	67.0	13.9	563	30	534	222	12.8	-378	x	b	pf	1
Key:	n/c = not covered; n/d = not detected												
	Floor reflectivity: d = dark, i = intermediate, b = bright												
	Terrain: p = plains, pf = fractured plains, r = ridge belt, t = tessera												
	Degradation: 1 = pristine, 2 = no ejecta, 3 = degraded												

Table 3.7: Parameters of the "Central Peak" DEM set. Most of these 19 craters lie on lowland plains but this is not typical of all such craters in the LPI database. Those in the Sample area have all classes of floor brightness and degradation; many have perceptible dark halos. Some parameters are from the LPI (2002) database.

Fig. 3.15 shows the trend line for Knobby Base is strikingly similar to that for the "small" set analysed above. Also it merges into the Central Peak set, so as to show a gradual transition from form to the other. Finally, Fig. 3.15 shows how the 9 large craters, classified by the LPI as Multiple Peak, Peak Ring, or Multi-ring basin, tend to have a depth of about 1 km irrespective of diameter. This may support the suggestion, in Herrick & Sharpton (1996), that viscous relaxation has reduced the depth of Mead.

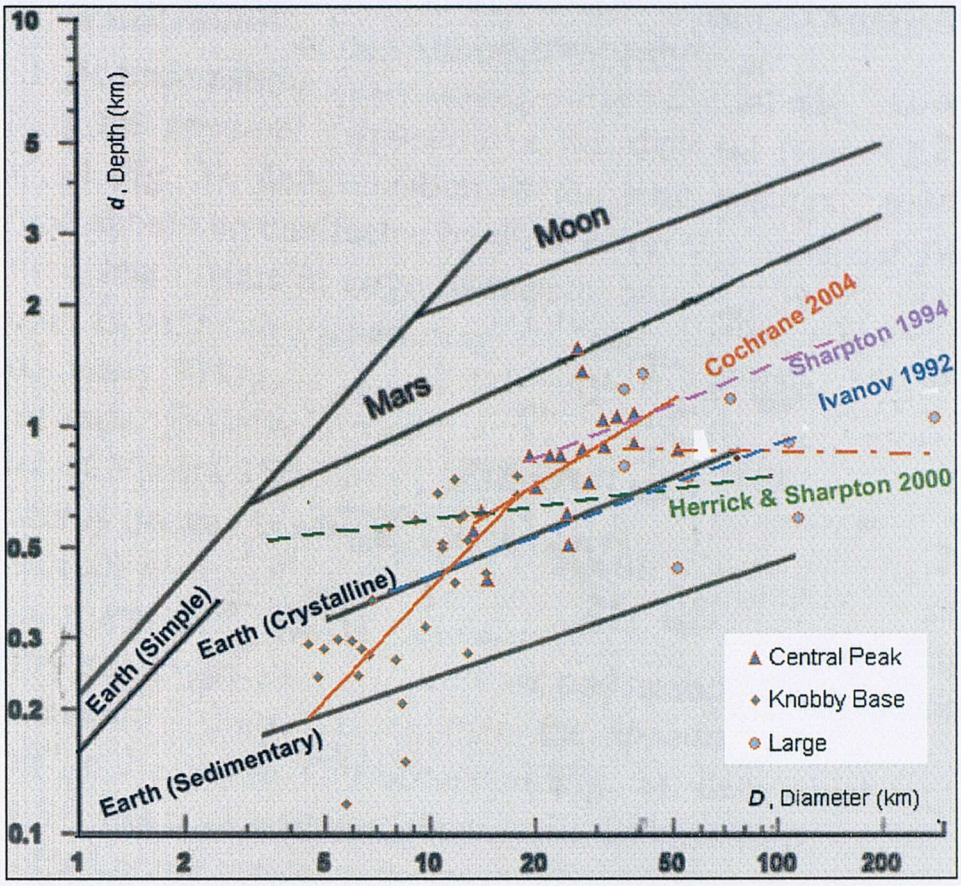


Figure 3.15: Depth/diameter trends for 29 "Knobby Base" and 19 "Central Peak" DEMs in a set of 57. After removing the "flat floor" craters (Heloise, Doris, Merian and Crater E) and a "bowl" crater (Aisha), the remaining set has Central Peak craters with a trend line of $d_{CP} = 3.8D^{0.53}$, with $R^2 = 0.34$. The trend for Knobby base craters, $d_{KB} = 0.1D^{0.89}$ with $R^2 = 0.39$, intersects that for Central Peak craters at 18.5 km, within the overlap of the 2 sets. Hence, the DEMs show a transition between Knobby base and Central Peak craters without a significant difference in crater depth. The other 9 DEMs, classified as "Large", has a depth of about 900 m irrespective of diameter, includes 3 craters with several central peaks, 2 with peak rings and 4 multi-ring basins.

Although they do not materially change the above assessments, some observations on the Knobby Base and the Central Peak sets should be recorded. There is only one image of the central region of Voynich, included as Fig. 3.16, and it shows it has a central peak ring rather than a single central peak.

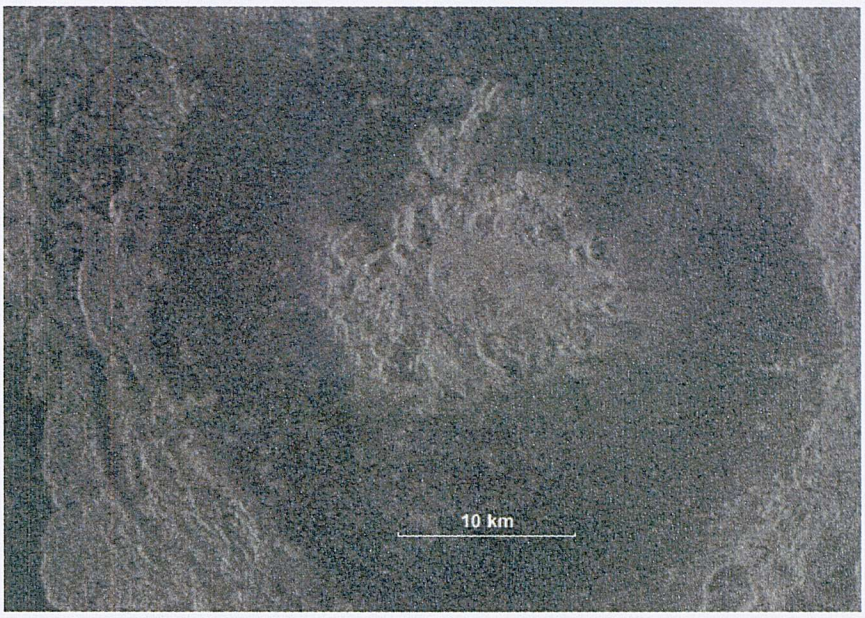
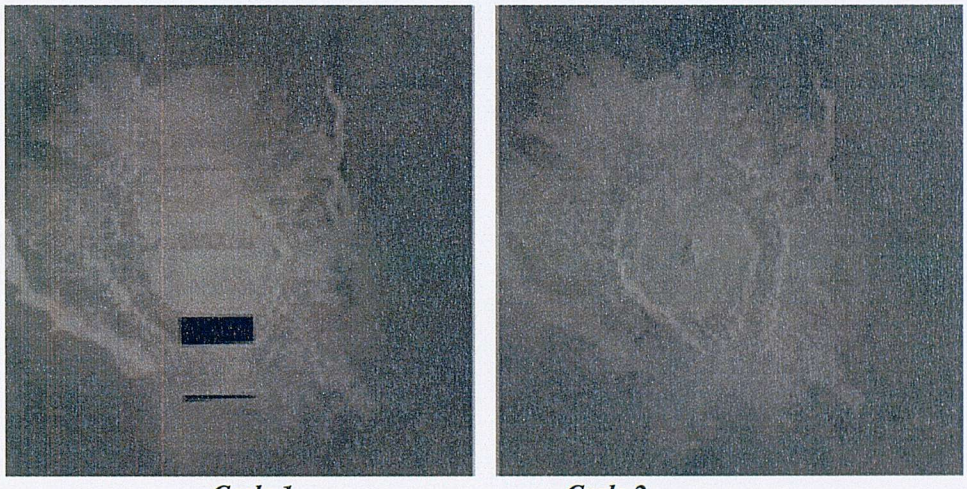


Figure 3.16: The only SAR image of the central feature of Voynich. There appears to be a featureless area in the middle with a ring of hills around it. Voynich should therefore be regarded as in the "Large" set, and at the transition between central peak and peak ring craters. (Cycle 1, PDS Download).

LPI also classifies Parra (44.5 km diameter) as having a Knobby Base, most probably on the basis of its Cycle 1 image, which Fig 3.19 indicates was corrupted. The Cycle 2 image shows it is a well-formed Central Peak crater, so is treated as such in this Thesis, and eliminated from the Knobby base set.



Cycle 1 *Cycle 2*

Figure 3.19: SAR images of Parra. The marked smearing of the swath through the centre of the crater Cycle 1 image may explain why LPI classify Parra as "knobby base". The Cycle 2 image shows it has a central peak, like others of similar diameter (44.5 km), and this thesis treats it as such.

Also, as shown in Figs. 3.17 and 3.18, the DEM of Doris shows it to be similar to Naomi and not "flat floored", ie like Heloise.



Figure 3.17: DEM and SAR image of Naomi. Viewed without vertical exaggeration from the south, at 40 km range and a slant angle of 10^0 with the sun in the west at an elevation of 10^0. The terrain falls away to the northeast, making the rim appear more prominent than it is. Note the low contrast of ejecta.

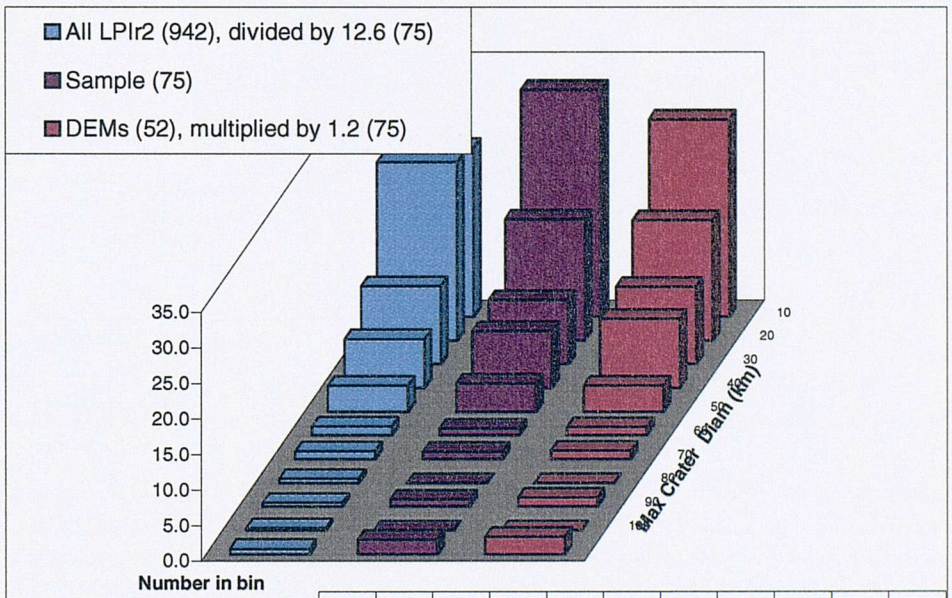


Figure 3.18: DEM and SAR image of Doris. Viewed without vertical exaggeration from the southeast, at 25 km range and a slant angle of $9^0$with the sun in the west at an elevation of 23^0, Doris appears very similar to Naomi and should also be included in the "Knobby Base" set.

3.5. *Comparison of Sample Craters with the planetary population*

Although the craters in the Sample Set illustrated in Fig. 3.15 were not chosen at random, their characteristics seem typical. These results can be applied to the planet as a whole to the extent that the Sample Area is shown to be representative of it.

Diameter Distribution. As has been noted, the DEMs show true diameters of craters in the Sample Area have been underestimated, and this may apply to the entire crater population. To make a like-for-like comparison, Fig 3.19 compares the LPI diameter distribution of the Sample of 75 craters to the Crater Population, factored down to number 75, and the Set of 62 DEMs, factored up to 75.

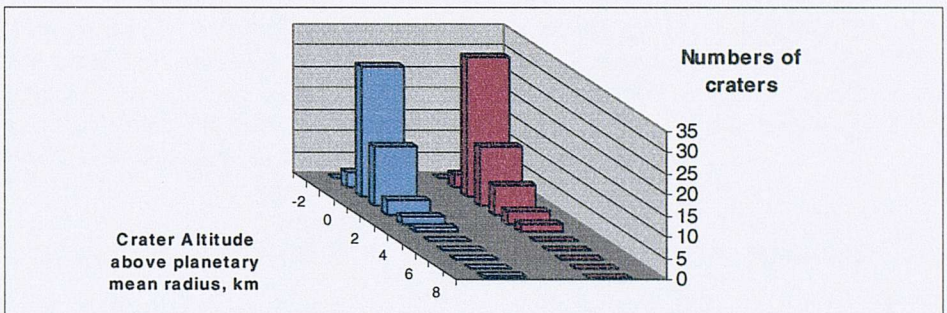


	10	20	30	40	50	60	70	80	90	100	
All LPIr2 (942), divided by 12.6 (75)	23.9	25.2	11.0	6.8	3.7	1.3	1.1	0.6	0.5	0.3	0.7
Sample (75)	32	17	9	8	4	1	1	0	1	0	2
DEMs (52), multiplied by 1.2 (75)	27.8	16.9	10.9	9.7	3.6	1.2	1.2	0.0	1.2	0.0	2.4

Figure 3.19: Distribution of Crater Diameters. Most of the planetary population of 942 craters (65.4%) are of diameter less than 20 km. The original Set of 75 craters and the Set of 62 DEMs in Fig. 3.9 resemble the planetary population in that: Original Sample = 65.3% and Set of DEMs = 59.6% but both are incorrectly distributed above and below 10 km.

Craters between 10 to 20 km are under-represented in the Sample but this is compensated by an excess of small craters so approximately 65% have diameters less than 20 km. Overall, the distribution of crater diameters in the Sample Area is considered to be broadly representative of the whole crater population of the planet. The diameters of the Core Set defined in Fig. 3.9 are found to be representative of all craters in the Sample Area, but with an excess of large craters and a shortfall of craters in the range of 10 to 20 km.

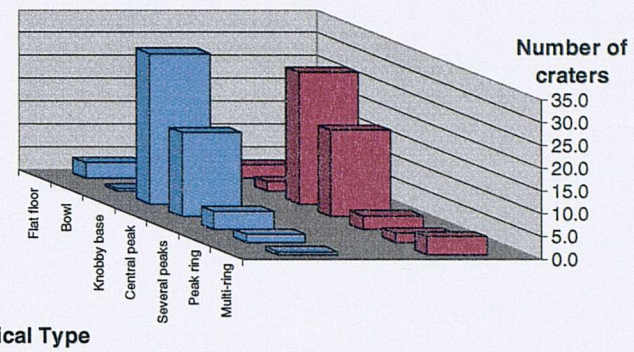
Crater Altitude. No correlation has been found between any crater characteristics and altitude. However, Fig. 3.20 shows that the Core Set and the Population are similarly distributed by altitude above the planetary mean.



	-2	-1	0	1	2	3	5	6	7	8	9
Population (938), divided by 17.4 (54)	0	3.58	30.49	13.92	3.35	1.39	0.17	0.00	0.06	0.00	0.06
DEM Set (62)	0	3	33	14	7	3	0	0	0	0	0

Figure 3.20: Distribution of Crater Altitudes. Most (56.5%) of the planetary population of 938 craters for which an altitude has been determined lie within 500m of the mean planetary radius. The Core Set of 54 craters closely resembles the population hipsometrically except that the Sample Area contains no high altitude craters. All crater parameters from LPI database, rel 2.

Crater Type Distribution. Fig. 3.21 compares the distribution of LPI morphological types in the Core Set with that of the whole population. Overall, the crater type distribution of craters in the Sample Area is considered to be representative of that of the whole population.



	Flat floor	Bowl	Knobby base	Central peak	Several peaks	Peak ring	Multi-ring
Population (929 assessments) factored to 62	3.4	0.4	33.1	18.6	4.0	1.8	0.7
DEM Set (62)	3	2	29	19	3	2	4

Figure 3.21: Distribution of Crater Morphologies. More than half (53.3%) of the planetary population of 928 craters with morphology categorised by the LPI are "Knobby base". This analysis shows that the bowl DEM Set of 62 craters closely resembles the population except that it contains an excess of mult-ring craters. All the crater classifications are taken from LPI database, rel 2.

Crater Density. Herrick & Phillips (1994) provide a topographic map, coloured according to the area distribution of all the then-known craters. Fig. 3.22 is the relevant part of it with the boundaries of the Sample Area superimposed. Herrick [31] has confirmed that they used a 1200 km sampling radius.

In the south of the Sample Area, regions of both significantly sparse and significantly dense cratering appear whereas north of the equator only significantly only areas of dense cratering appear. Tables 3.1 to 3.4 show 42 craters in the 16.062 million km^2 of the Sample Area north of the equator, and 33 craters in the 16.264 million km^2 to the south of it. Hence, there is one crater per 382,429 km^2 in the northern half of the sample area. This is 1.28 times the planetary mean cratering density, and marginally significant. The crater density in the southern half is one crater per 478,351 km^2, and well within 1 σ of the planetary mean.

[31] RR Herrick, E-mail Communication, 3 Apr 2002

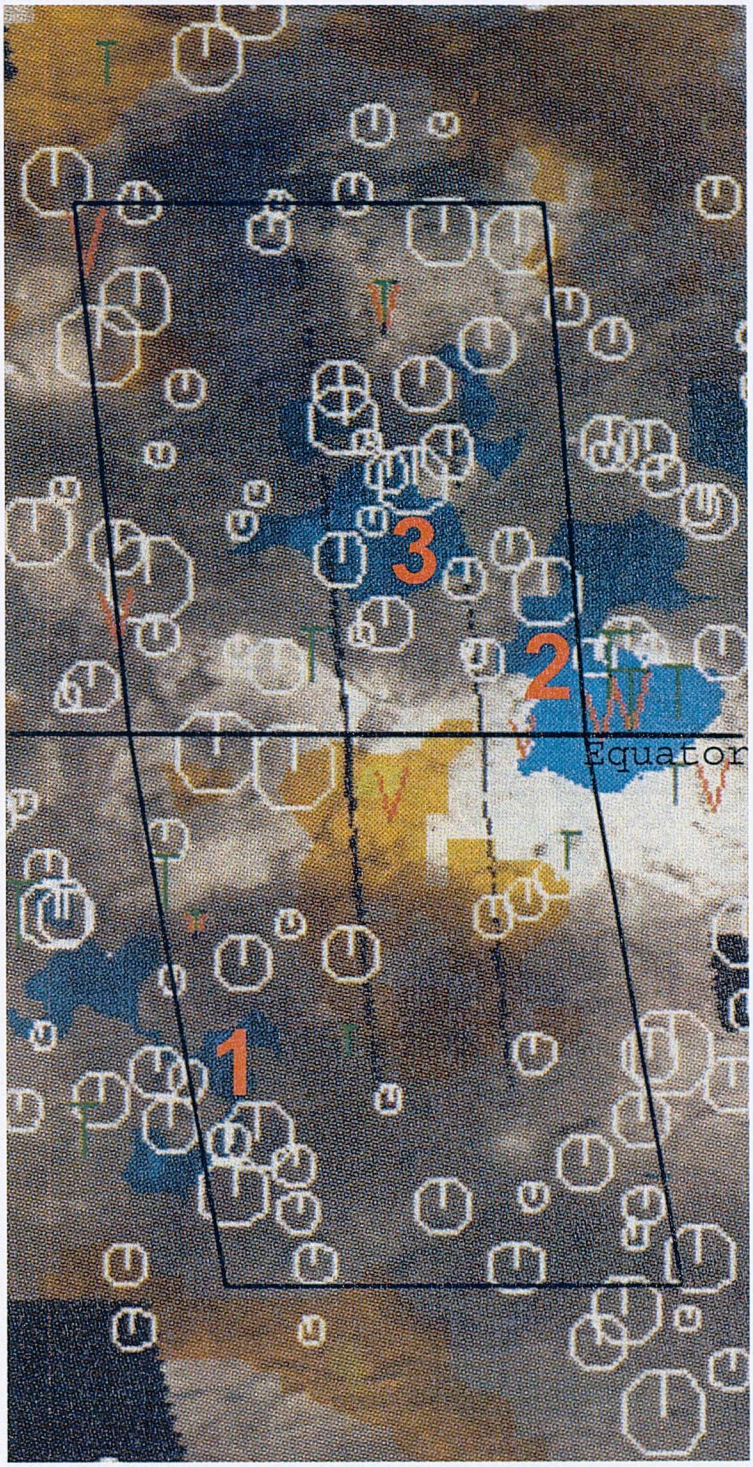


Fig 3.22: Areal Distribution of Craters within the Sample Area. Blue areas are where crater densities are at least 1Φ larger than the mean. Yellow and orange areas are where crater densities are lower by 1Φ and 2Φ respectively. The white circles mark the positions of pristine craters, the red Vs mark the positions of embayed craters, and the green Ts mark the positions of tectonically deformed craters. From Herrick & Phillips (1994) but Sample Area boundaries added and Blue areas numbered.

The Sample Area is 7% of the area of the planet, and should contain 66 of the 942 craters listed by the LPI. Since the Sample Area contains 75 craters, compared to the planetary mean density of cratering, μ, there is an excess of 9 craters in the Sample Area.

For discrete events, the standard deviation, σ, of a distribution is the square root of its mean, ie:

$$\sigma^2 = \mu \quad (19)$$

and, in this case, $\mu = 66$

Hence $\sigma = \sqrt{66} = 8.12$

An excess of 9 craters = 9/8.12 = 1.1σ and marginally significant.

The density distribution of craters in the Sample Area was further explored using a program provided by Bond (2002)[32]. This program takes a sampling radius to define a standard area around each crater of interest in which to count its neighbours. Typically, the sampling radius is set so that an occurrence of a specific number of craters within the sampling area is significant to a specific extent.

To look for concentrations of dense cratering inside the Sample Area, which tapers to less than 3000 km wide at high latitudes, a search radius of 500km was chosen. The population of 942 craters and mean planetary radius of 6051.84 km, give a mean crater separation of 394 km. Hence, a search radius of 500 km is at 1.27 σ, so there is a 90% probability that there will be at least one neighbour within that radius from each crater.

There are 19 craters in the Sample Area with 2 neighbours and 13 craters with 3 neighbours within this search radius. There are no craters with more than 4 Sample Area neighbours within this search radius.

There are 3 dense groups of craters (i.e. with more than 4 neighbours). Two of these are identified by Herrick & Phillips (1992) at their larger search radius and fewer craters. These are numbered in Fig. 3.22 and involve the following craters:

[32] Timothy Bond, E-mail Communication, 27 Feb 2002

1. Jodi and Mansa near 35S 066E, along with Agrippina, Germain, and Maurea inside the Sample Area and Yoshioka outside it.
2. Doris lies on the very edge of the Sample area at 6N 093E, near Suzanna, Hepworth, de Beauvoir, Gregory, Estelle, Abra and Ichenko which all lie outside the Sample Area.

The third group is well to the north west of their high density region in the middle of Ahktamar Planitia, marked in Fig. 3.21 with a "3":

3. Heloise and Aisha near 40N 052E, along with Voynich and Crater A inside the Sample Area, and Miriam and Namiko outside it.

To find the number of singleton craters, Bond[33] set the search radius to 527km so that the minus 1σ test of significance gives exactly one crater. There are 13 craters in the sample with no neighbour within 500km (i.e. that have the planetary mean density): Tseraskaya, Merian, Loan and Madina in the north; Joliot-Curie, Samintang, Quimby, Leila, Elena, Temou, Ruit, Tehina and Kyen in the south.

[33] Timothy Bond, E-mail Communication, 7 Apr 2002

3.6. Chapter Summary

This Chapter records measurement of 72 craters, of 75 in the chosen Sample Area. These 72 craters constitute a set that is 7.6% of all craters on Venus. DEMs have been produced for all 62 craters with adequate same-side image pairs in the F-Map library. Both the original set of 75 and the set of 62 DEMs are not unlike the total crater population in terms of the following parameters[34]: diameter, altitude, morphological type and cratering density.

These craters have rim-floor depths and rim diameters that do not accord with earlier analyses, in that:

a. Most crater diameters have been underestimated by about 10%.

b. There is not a single depth/diameter trend but rather one for each of the 3 main morphological classes:

- Large craters, with diameters greater than 38 km, all tend to have the same depth of about 1 km. This trend may apply to 10% of the planetary population (99 craters).
- Central Peak craters, with diameters from 13.9 to 54.1 km and depths from 429 m to 1586 m, have a trend given by the equation:

$$d_{CP} = 3.8\, D_{CP}^{\,0.53} \quad \text{..... (20)}$$

This characteristic may apply to 283 craters (30% of the population).

- Knobby Base craters, with diameters from 4.6 to 18.6 km and depths from 429 m to 1586 m, have a trend given by the equation:

$$d_{KB} = 0.1 D_{KB}^{\,0.89} \quad \text{..... (21)}$$

This characteristic may apply to 503 craters (53% of the population).

The Knobby Base craters may be due to "Compound" impact of distorted, high aspect ratio bolides. An absence of spallation and rim uplift are possible indicators of such impacts.

[34] as listed in the LPI database

Chapter 4

Model Validation

In the foregoing chapters, the DEMs are assumed to be accurate. In this chapter, their validity will be established, first by comparison to earlier work and then by use of a third image.

Only Herrick & Sharpton (2000) have published results from MST models, and they found an unusually shallow slope to the trend line for rim-floor depth of all the craters they considered. This can be explained by dividing the DEMs in this study as follows:

- 29 craters categorised by the LPI as Knobby base. This set is similar to the set of Compound craters defined in Chapter 3.
- 19 larger craters, which Fig. 4.1 shows have a trend line parallel to that of Herrick & Sharpton (2000) but deeper by about 150 m. This suggests that their method produced a systematically deeper measurement.

The statistics of the craters selected by Herrick & Sharpton (2000) show that Knobby base craters are under-represented but not significantly so, see Fig. 4.2. Herrick[35] advised that they took crater depth to be the difference between the lowest matching point in the floor and the mean of the rim matching points. The technique described in Chapter 3 should give a shallower depth. Therefore, the depths of the smaller diameter craters found by Herrick & Sharpton (2000) are inconsistent with those found in this research. The next 3 Sections explore this inconsistency.

[35] Personal communication Herrick, 24 Februaury 2002.

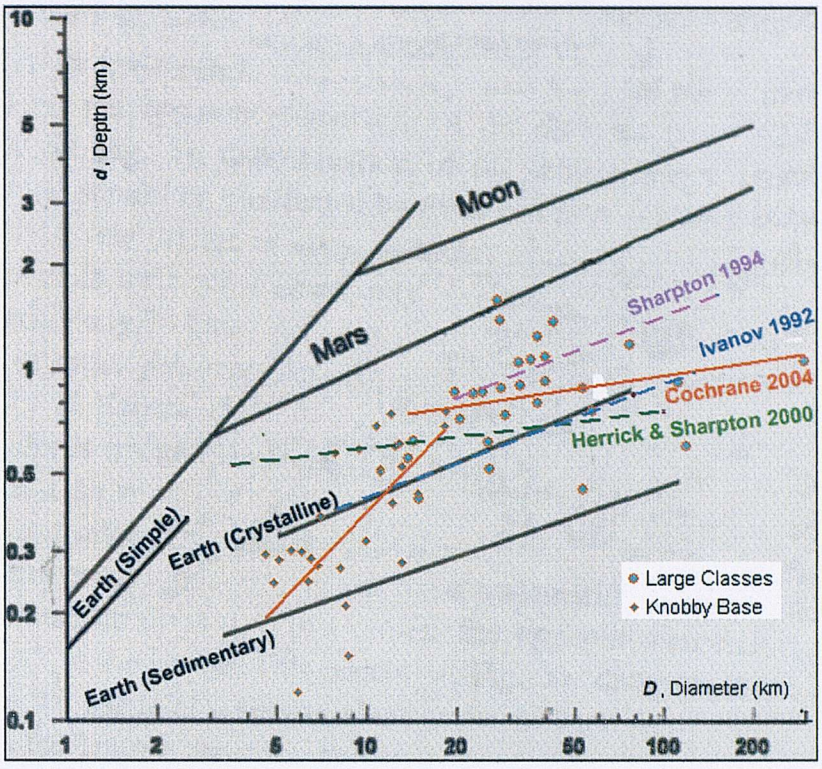
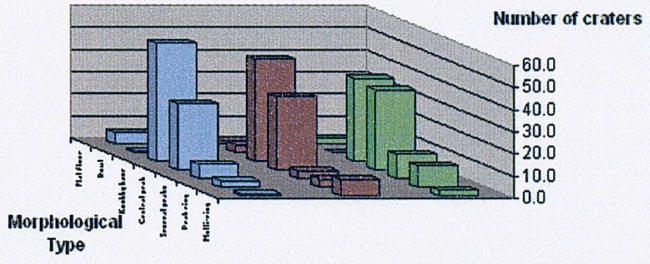


Figure 4.1: Depth/diameter trends for 29 Knobby Base DEMs in a set of 57. The trend for "Large Classes" of crater (including 19 "Central Peak" craters, 3 with several central peaks, 2 with peak rings and 4 multi-ring basins) is virtually parallel to that of Herrick & Sharpton (2000) but about 150 m deeper. Excluded from this analysis are DEMs of: 4 Flat Floored craters (Heloise, Merian Doris and Crater E) and a Bowl crater: Aisha.



	Flat floor	Bowl	Knobby base	Central peak	Several peaks	Peak ring	Multi-ring
Percent in Population (929 assessments)	5.5	0.6	53.4	30.0	6.5	2.9	1.1
Percent in DEM Set (62)	1.9	3.7	46.3	33.3	3.7	3.7	7.4
Percent in H & S Set (72 assessments)	2.8	0.0	37.5	36.1	11.1	9.7	2.8

Figure 4.2: Percentages of Morphological Types. The population of the planet has 53.4% Knobby base craters. Both the DEM set and that in Herrick & Sharpton (2000) under-represent this group. "Large Classes" (ie Central Peak, Multiple Central Peaks, and Peak Ring craters, and Multi-ring Basins) comprise 40.5% of the population and 48.1% of the DEMs but 59.7% of the set chosen by Herrick & Sharpton (2000).

4.1. Validation of the smaller crater DEMs

The most significant difference between the DEMs produced for this study and earlier work is that small diameter craters are significantly shallower. Sharpton (1994) used the floor off-set method on Cycle 1 images and did not attempt to assess any craters < 20 km diameter, so does not conflict in this regard.

Ivanov et al (1992) also used the floor off-set method and measured only 5 craters in the range 8 - 12 km, but these craters are not otherwise identified. They found a depth range from 300 to 600m, and a mean of 450 m. The DEM set includes 9 craters with USGS diameters in the range 8 - 12 km, with depths from 213 to 755 m, and an average depth of 488km. Alternatively, the 10 DEMs with LPI diameters in the range 8 - 12 km have depths from 243 to 755 m, and an average depth of 555 m. So, in both cases, the DEMs produced for this study are rather deeper than Ivanov *et al.* (1992) but consistent, within likely measurement error. Now, as has been shown earlier, this study finds crater diameter errors generally in the order of +10%. So, using diameters found from the DEMs, there are only 8 craters in the range 8 – 12 km, with a mean depth of 393 m over a range of 153 to 695 m. This is rather shallower than the mean depth of 450 m over a range from 300 to 600 m given by Ivanov *et al.* (1992) for 5 craters in the range 8 – 12 km but, again, within likely errors. Hence, the diameter differences noted in Section 3.3 are the source of the slightly shallower depth:diameter trend, compared with Ivanov *et al.* (1992), of the craters in this study.

Herrick & Sharpton (2000) give parameters for 17 MST DEMs of diameter <10 km. The DEM Set includes 16 craters in this size range, the craters common to both lists being: Crater A, Crater B, and Nsele. Herrick & Sharpton (2000) include Elma with a diameter of 9.7 km, whereas the DEM in this study shows its diameter is 11.8 km. Fig 4.3 illustrates how the parameters of these four craters compare in the two assessments, the arrows showing the extent of the change required by this study. There is a third image of all 4 craters, for independent assessment. The following sections show that, for small craters except for Crater B, the set of DEMs in this study are not significantly different to that of Herrick & Sharpton (2000), when error estimates are considered.

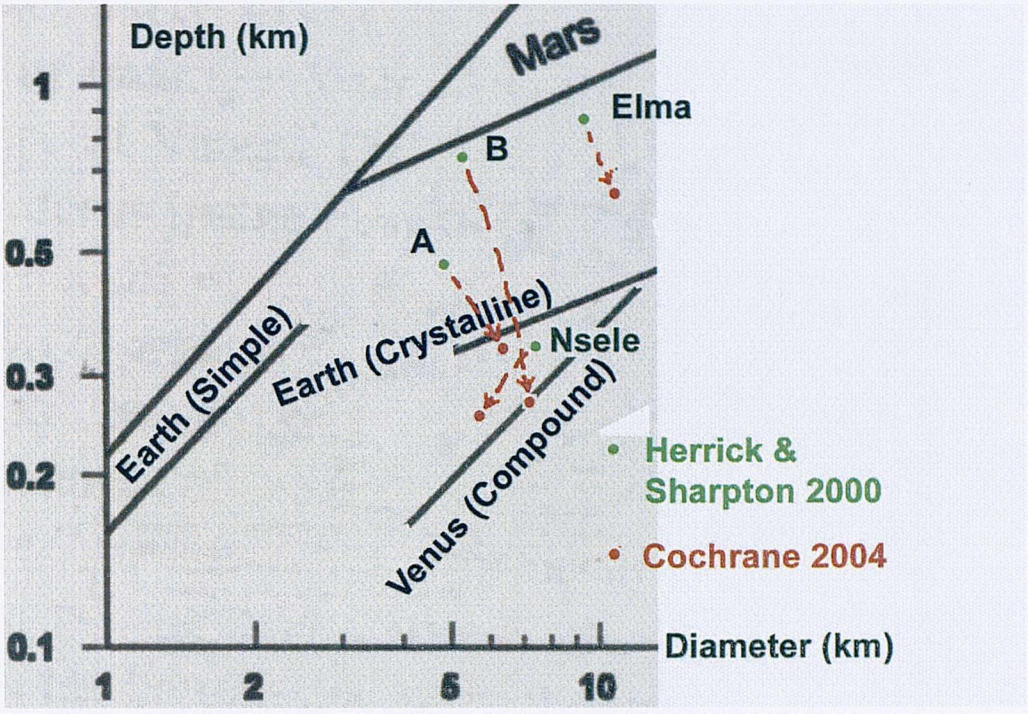
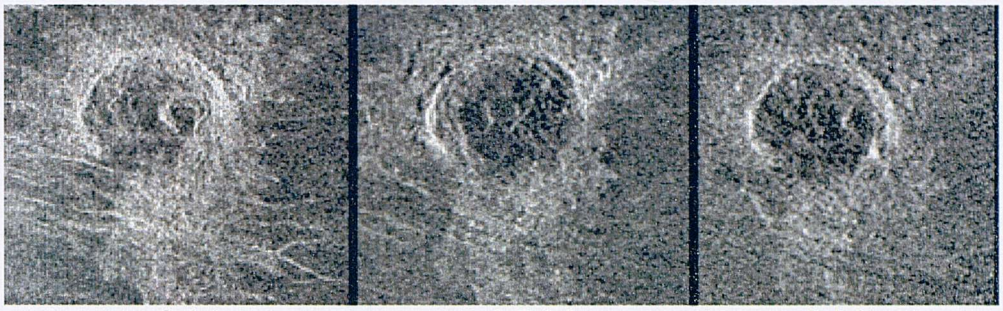


Fig 4.3: Parameter differences for small crater DEMs. This study shows all 4 of these craters are shallower than published in Herrick & Sharpton (2000). In contrast to the general trend in this study, Nsele is found to be of smaller diameter than given in the LPI and USGS databases.

In summary, all 4 are found to be shallower than Herrick & Sharpton (2000). Except in the case of Crater B, the depth differences fall within the errors quoted by Herrick & Sharpton (2000). The diameter differences are more significant: the DEMs in this study show Crater A, Crater B and Elma are larger, and Nsele smaller, than Herrick & Sharpton (2000). In some cases, the diameter differences are much more significant; e.g. for largest changes in each sense, they mean the area of Crater B is twice, and that of Nsele half, that indicated by Herrick & Sharpton (2000). Clearly, the origin of these differences merit examination.

4.1.1. Elma

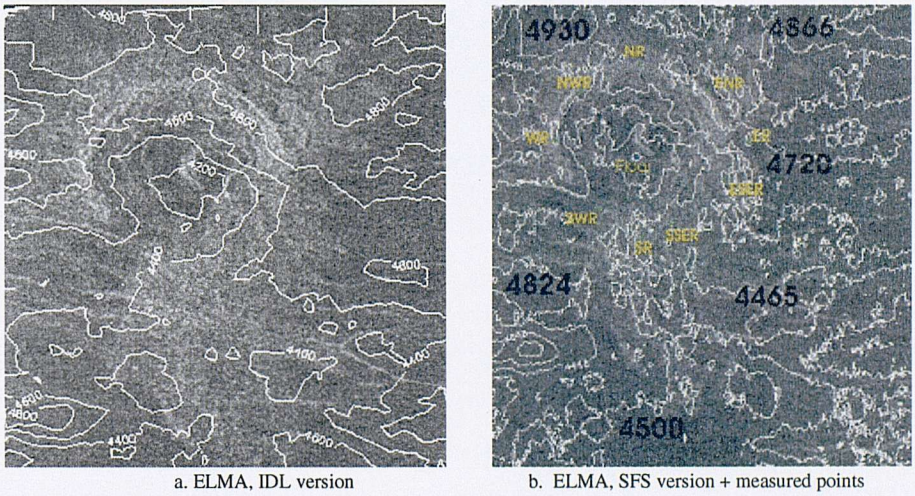
At Elma's latitude (10.1^{0}S), Magellan's altimeter resolution was 14 km by 9 km so altimetry data cannot be used to explore the topography of this ~10 km diameter crater. The 3 images of Elma given in Fig 4.4 show it to be a regular crater with a gap in its rim to the south-west and an asymmetrical ejecta field, suggesting a low impact angle or that the local terrain is uneven.



a. Cycle 1 b. Cycle 2 c. Cycle 3

Figure 4.4: SAR Images of Elma from Cycles 1, 2 and 3. From PDS Downloads.

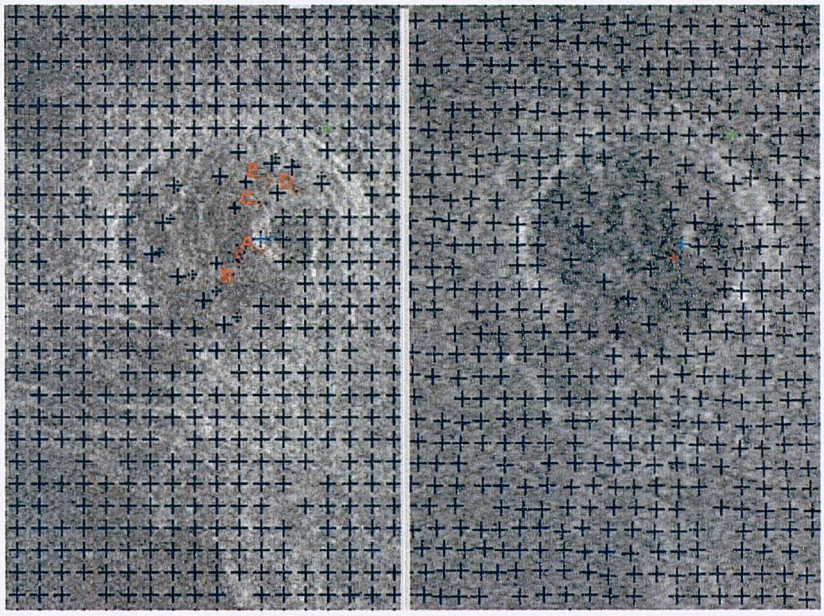
The DEM produced for Elma in this study rests on 2112 matches inside the crater rim, of which 10% (211) are taken to define the floor. Fig. 4.5 shows both versions of the DEM produced in this study. The SFS version includes a ridge to the north of the crater, sloping down from a peak in the north-west by 64 m to the north-east. It does not appear to be an artifact; its peak is 450 m above the south-west corner.



a. ELMA, IDL version b. ELMA, SFS version + measured points

Figure 4.5: Contours and features of the DEM of Elma. The contours on the less detailed IDL version are easier to read than the SFS version, which has the heights of the local terrain marked and the rim peaks identified according to the 32 cardinal points.

Herrick & Sharpton (2000) took the rim peaks as defining its height, and the deepest point of the crater floor as defining it. The DEM for this study has 9 peaks on the rim, as shown in Fig. 4.5. The mean altitude of these peaks is 4709 m, and the last contour line in the centre of the floor is at 4046 m, some 29 m above the deepest point. In this study, the "mean rim to 10% floor depth" is used, which is 524 m for Elma. Following Herrick & Sharpton (2000), the depth from the mean of the rim peaks to the lowest point is 692 m, short of their "Rim-Floor Height" of 850 m by 158 m. The IDL version of the DEM in this study gives a lowest floor depth of 700 m below the highest rim peak (4800 m, and lying to the north east).



a. Cycle 1 + C3 ghosts on floor b. Cycle 3

Figure 4.6: Herrick & Sharpton's matching points for Elma. The process used was to lay down a regular grid of matching point at 12 pixels spacing, then delete those that gave rise to unrealistic matches. The points identified as A to E are all to the west of a central prominence. Ghosts of the 5 Cycle 3 matching points with an offset of 10 or more have been copied onto the Cycle 1 image.

Herrick[36] provided the data files which include the matching points at Elma, shown in Fig. 4.6. The 12 matching-point pitch given by Herrick & Sharpton (2000) would have given 117 matching points inside a crater of 11 km diameter but 38 have been deleted, mostly on the floor and leaving no matching points near where the DEM in this study is deepest. The incidence angles for Cycles 1 & 3 mean that a matching point offset of 12 pixels gives a height difference of 842

[36] Personal communication Herrick, 24 Februaury 2002

m. Table 4.1gives X- and Y- disparities. Disregarding point C because of its high Y-disparity, Herrick & Sharpton (2000)'s floor depth of 770 m below the surrounding terrain rests on only 4 matching points. The datum (marked with a green cross) for this analysis is on the highest point of the rim and 351 m above the terrain. Examination of the texture in the 2 images around these 4 matching points shows that they are not especially good matches.

Elma		
Incidence		
degrees	42.4	24.8
Disparity	**X**	**Y**
A	-13	+1
B	-12	+1
C	-13	+3
D	-10	+1
E	-12	+1

Table 4.1: Matching offsets defining the floor of Elma. A disparity in the X axis gives rise to a height offset; disparities in the Y axis indicate matching inconsistencies. Data measured in the DEM for Elma to support Herrick & Sharpton (2000).

The IDL DEM in this study shows the rim to be 11.1 – 11.4 km, north-south and east-west. The 12 pixel pitch of the matching points in Herrick & Sharpton (2000) gives a quantization of 900 m in their diameter of 9.7 km, i.e. 9.25 – 10.15 km. They delete only 9 of 77 matching points straddling the rim. There is a difference of at least 750m in the 2 estimates of diameter but this study rests on 154 matches whereas Herrick & Sharpton (2000) rests on 68.

Fig 4.7 shows the points chosen to validate the crater depth by matching points in all 3 images, called "triangulation" in Cochrane (2001). The most prominent feature on the floor is a peak[37], marked in the Cycle 1 image by the points A through F and recognisable as a peak by its inversion in the Cycle 2 image. From its offset of 5 pixels, the DEM for Herrick and Sharpton (2000) should show the height of this prominence to be 7 pixels above their floor, viz. 237 m. The SFS DEM for this study shows it to be 190 m above the floor.

A Y-shaped feature on the floor is identifiable in all 3 images in Fig. 4.7, and the dark "furrow" in the fork is marked with a green "Y". Table 4.2 shows a comparison of Cycle 1 and 3 images reflects the floor of Elma is 772 m below a

[37] The LPI database categorizes Elma as being "Knobby Base"; if this peak is a "Central Peak", that categorization must be revised.

reference point to the northeast, at the edge of the ejecta field. Triangulation of the same point in the Cycle 2 image with both C1 and C3 offsets yields the similar offsets (437 or 438 pixels). No offsets could be found between rim features and the reference point so these checks indicate that the crater depth is 772 m, i.e. midway between the results from the SFS DEM in this study and Herrick & Sharpton (2000).

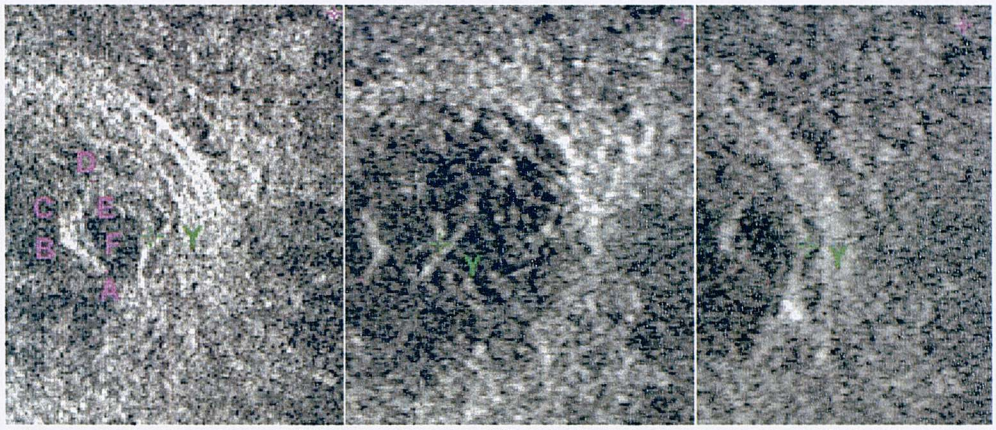


Figure 4.7: Images of Elma's Central Peak from Cycle 1, 2 and 3. The "Y" shaped feature is clearly identifiable in all 3 images. The reference point is marked with a purple cross in the top right corner of each image.

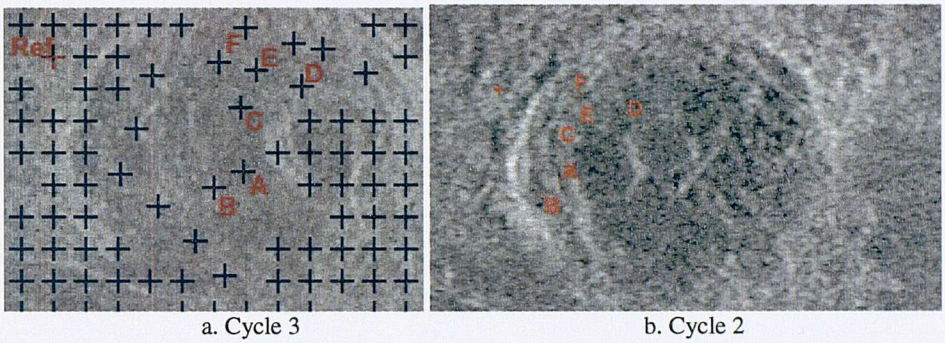
		Cycle 1		Cycle 3										Cycle 2	
Incidence Angle		42.4		24.8										22.6	
								delta	delta	using d_1		using d_3			
Feature	x	y	x	y	d_1	d_3	height	height	offset	x_2	offset	x_2	x	y
Ref	254	32	825	32	pixels	pixels	pixels	m	pixels		pixels	pixels	539	32
Y	177	125	759	124	77	66	-10.3	-772	-25	437	-35	438	437	125

Table 4.2: Parameters for Elma "Y" Feature. From their C1 and C3 offsets, the "Y" shaped feature is found to be 772 m below the reference point, marked with a purple cross in the top right corner of each image. Using this depth and the incidence angle for Cycle 2 gives the same X offset (within 1 pixel) as is found by measurement. A copy of this spreadsheet, with embedded macros, is included in the CD as "ElmaY c1c3drivenparallaxheight calculatorMarkedv2.xls".

Since the Cycle 2 image has a discontinuity in the middle, using a new reference point in the western ejecta field was chosen to check the left-left matches at A through F in Herrick & Sharpton (2000). The depths found are consistent with Herrick and Sharpton's depth of 850 m but the appropriate positions in the Cycle 2 image, illustrated in Fig. 4.8 and listed in Table 4.3, are inconsistent with other features in the Cycle 2 image. For example, B appears in the western rim escarpment and A is too close to it. In other words, the Elma DEM from Herrick & Sharpton (2000) could not be validated by reference to the Cycle 2 image.

	Cycle 1		Cycle 3						Cycle 2					
Incidence		42.4		24.8										22.6
Ref	174	442	457	425	pixels	pixels	pixels	m	pixels	m	pixels	pixels	60	101
							delta	delta	using d_1		using d_3		y_2 using	
Point	x	y	x	y	d_1	d_3	ht	ht	offset	x_2	offset	x_2	d_1	d_2
A	245	485	541	467	71	84	-12.2	-912	-43	88	-56	88	144	143
B	234	491	529	473	60	72	-11.2	-842	-39	81	-51	81	150	149
C	244	461	540	441	70	83	-12.2	-912	-43	87	-56	87	120	117
D	267	453	561	435	93	104	-10.3	-772	-36	117	-47	117	112	111
E	250	447	545	429	76	88	-11.2	-842	-39	97	-51	97	106	105
F	236	444	526	426	62	69	-6.5	-491	-23	99	-30	99	103	102

Table 4.3: Herrick and Sharpton's offsets on the western floor of Elma. From their depths and the appropriate incidence angles the positions in the Cycle 2 image of the points A through to F are predicted.



a. Cycle 3 b. Cycle 2

Figure 4.8: Cycle 2 points on the floor of Elma derived from Herrick & Sharpton's offsets. When plotted on a Cycle 2 image, at least some of the points A through to F are found to be at unreasonable places, suggesting that the depth measurement for Herrick and Sharpton (2000) is too deep.

Using the same technique, the floor depth in the DEM for this study was checked by reducing the Cycle 3 offset for the deepest of Herrick & Sharpton's points, A and C. Fig. 4.9 shows corrected positions in yellow for an offset of 11 rather than 13 pixels. With respect to both the central peak and the escarpment edge, these positions seem more appropriate. Hence, to that extent, the Rim-Floor height of 850 ± 128 m given in Herrick and Sharpton (2000) is too deep by about 140 m. It is concluded that the SFS DEM produced for this study, giving a comparable depth of 663 m, is more reliable than that used for Herrick and Sharpton (2000).

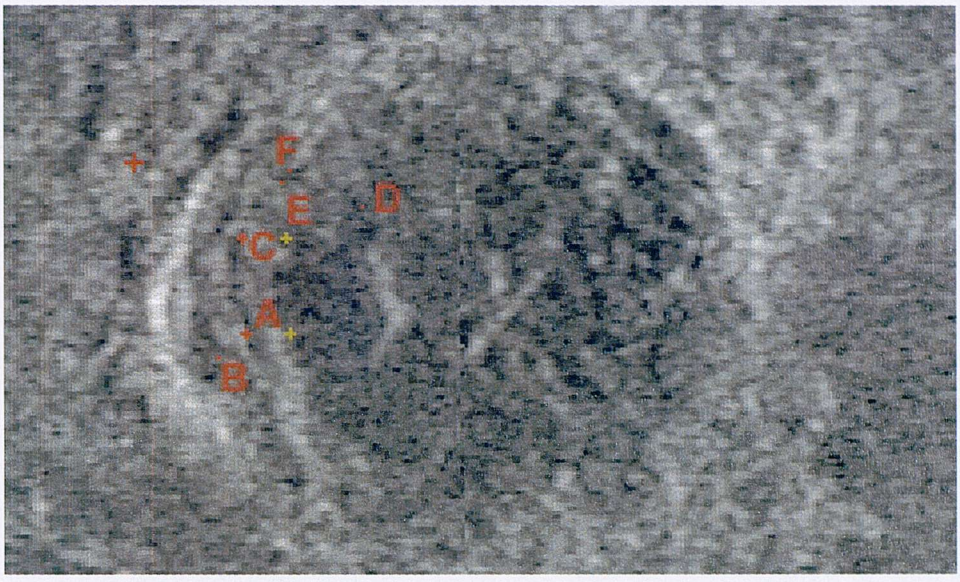
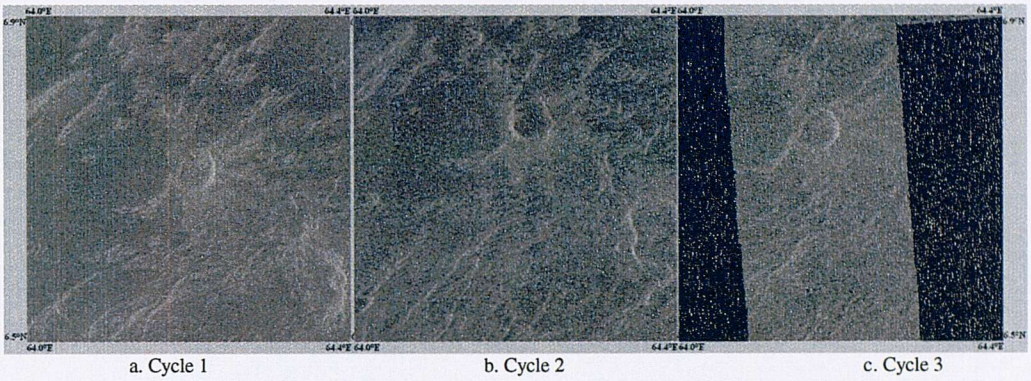


Figure 4.9: Corrected Cycle 2 points on the floor of Elma. When plotted on a Cycle 2 image but at an offset of 12 (vice 13) pixels, the points A and C are found to be at more reasonable places, suggesting that the depth measurement for Herrick and Sharpton (2000) is too deep by about 140 m.

4.1.2. Nsele

The 3 images of Nsele given in Fig. 4.10 show it is irregular, with 3 bright faults joining its rim. At this latitude (6.7^0N), the altimeter resolution is 12 km by 8 km so it cannot resolve a crater that the DEM in this study shows to be 4.9 km in diameter. The LPI lists its diameter as 4.9 km and the USGS as 5.1 km.



a. Cycle 1 b. Cycle 2 c. Cycle 3

Figure 4.10: Images of Nsele from Cycles 1, 2 and 3. Nsele has faults joining its rim from the north, northeast and southwest. The ejecta field is indistinct but only to the southeast. There may be a larger, almost completely embayed, crater immediately to its west but this is not covered in the DEM produced for this study. PDS downloads in sinusoidal projection.

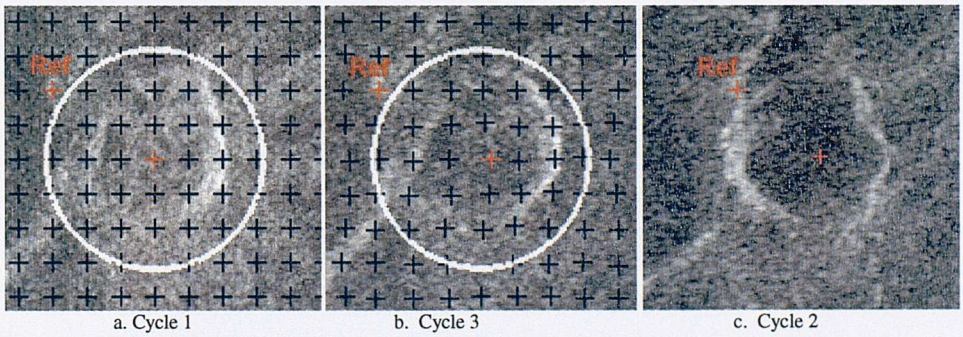
The contours from the SFS DEM of Nsele produced for this study are shown in Fig. 4.11. It is based on about 42 matching points on the floor and about 77 around the rim. The mean of the 4 peaks on the rim is 1858 m, and the lowest point in the centre of the floor is at 1609 m, ie a maximum depth of 249 m. The rim is found to be about 100 m above the local terrain. In comparison, Herrick & Sharpton (2000)'s rim diameter is 7.7 km, and their "Rim-Floor Height" is 300 ± 104 m.

Fig 4.12 shows Herrick & Sharpton's matching points, and that they deleted none. In this case, the matching point array has a pitch of 16 and is aligned with the crater's centre, so the central matching point dominates the depth measurement. It is offset by 5 pixels in the Cycle 3 image, ie a depth of 316 m below the terrain reference. Herrick & Sharpton's rim is illustrated in Figs. 4.12a and b by the white circle, and is too large. They measure the rim height as 50m, ie equivalent to a matching offset of less than one pixel. Fig. 4.12c shows a position for their central point in the Cycle 2 image, computed from their depth. The

depths of the 2 DEMs are within the error range given by Herrick & Sharpton (2000), so the significant difference lies in the diameter measurements.



Figure 4.11: Contours and features of the SFS DEM of Nsele. This DEM shows little variation of altitude. The rim was identified by finding the most prominent peaks, marked here with crosses.

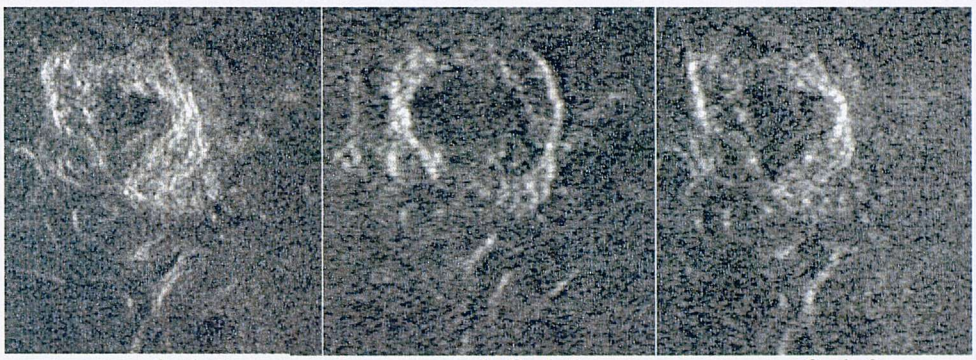


a. Cycle 1 b. Cycle 3 c. Cycle 2

Figure 4.12: Herrick & Sharpton's matching points and Rim for Nsele. The white circles are of 7.7 km diameter, indicating that the LPI diameter is well back from the escarpment, unlike most other craters.

4.1.3. Crater B

This unnamed crater is identified in the LPI database as Serial 849, and in Herrick & Sharpton (2000) by its latitude and longitude (6.4N, 83.4E). Of all craters addressed by both Herrick & Sharpton (2000) and this study, the DEMs of Crater B have the greatest percentage differences, in terms of both diameter and depth. The 3 images of it given in Fig 4.13 show it to be irregular. Herrick & Sharpton find it to be very deep (740 ± 135 m) for its diameter (5.1 km). The contours of the DEM produced for this study are shown in Fig 4.14. The 12 peaks found on the rim have an average height of 3129 m, and the lowest point on the floor is 2939 m, so its mean depth is 190m.



a. Cycle 1 b. Cycle 2 c. Cycle 3

Figure 4.13: Images of Crater B from Cycles 1, 2 and 3. Crater B lies on a largely featureless plain, so MST could only produce small DEMs. These images are the largest (192 x 192 pixels) for which MST generated a DEM.

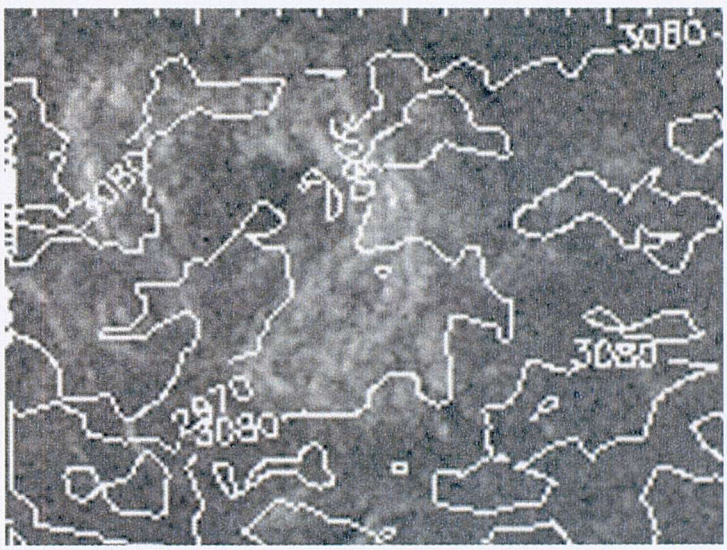
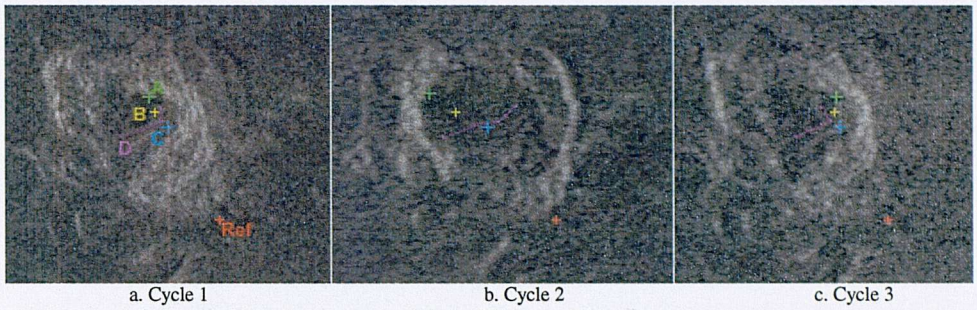


Figure 4.14: Contours, rim and bottom of the SFS DEM of Crater B. The rim was identified by the 12 most prominent peaks, marked here with red crosses, and the floor by the kinked contour.



a. Cycle 1 b. Cycle 2 c. Cycle 3

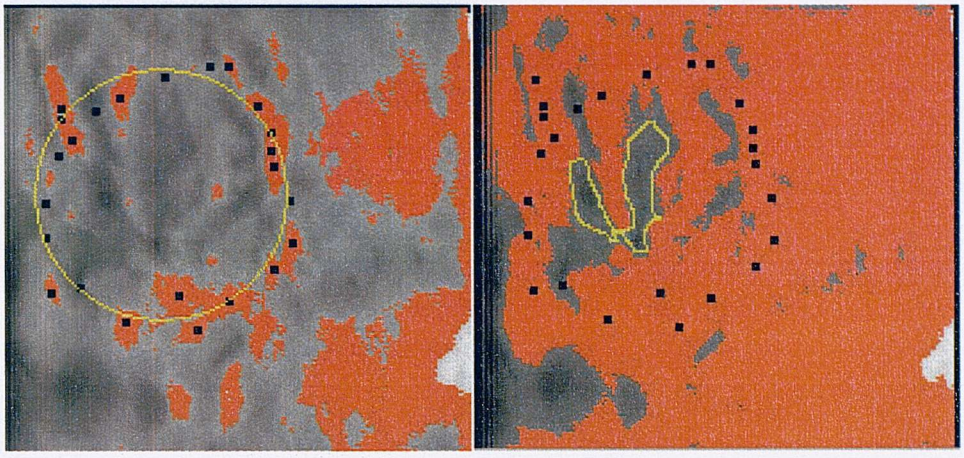
Figure 4.15: Matched points within Crater B. Careful selection and comparison of matched points in all 3 images were used to confirm the depth of the crater as 222 m.

Herrick & Sharpton (2000)'s matching points were not available so only the Cycle 2 image could be used to check the depths from the DEMs produced for this study. As illustrated in Fig. 4.15, several possible matches were computed with reference to a bright return on the southeast edge of the ejecta field:

- A, a point on the end of a promontory on the foot of the north escarpment in the 2 left looking views. It is the most obvious point to select and is computed to be 631 m below the reference, ie consistent with Herrick & Sharpton's depth, but this makes it so deep it merges with the western escarpment in the Cycle 2 image. Hence it cannot be validated.
- B, a point in a notch at the bottom of the east escarpment in the 2 left looking views, which is not detected in the Cycle 2 image. It is 379 m below the reference.
- C, a point where a dark "trough" running southwest-northeast turns north in the 2 left looking views, which may be detectable in the Cycle 2 image. It is 126 m below the reference.
- D, a linear feature in all three images. It starts in the west at the base of the escarpment at 189 m below the reference, rises to the same height close to point C, then turns north to a peak of 252 m above the reference. This may be evidence of a central prominence, or of a compound impact.

In Fig. 4.16a, the positions of the peaks and saddles on the rim are shown on a greyscale of the DEM, with the threshold at 3220 m. In Fig. 4.16b, the threshold had been reduced to 3000 m in order to find the floor, defined as 10% of the area within the rim. This version of the DEM shows the north-west rim to be broken by a sharp ridge that continues across most of the floor. The selections shown in

Fig. 4.16 give a crater diameter of 6.4 km and a depth of 250 m. Herrick & Sharpton (2000) give a diameter of 5.1 km and depth of 740 m



a. Rim b Floor

Figure 4.16: Image-J version of Crater B IDL DEM, Rim and Floor marked. The peaks were found by reducing the threshold and marking the first red area to appear with a black point. The rim was found by fitting the yellow circle by eye.

Close examination of DEM showed it to have some unlikely topography, eg Fig. 4.17 shows ridges in a visualisation of the SFS DEM. In summary, these checks did not confirm either the DEM produced for this study or Herrick & Sharpton (2000)'s depth for Crater B.

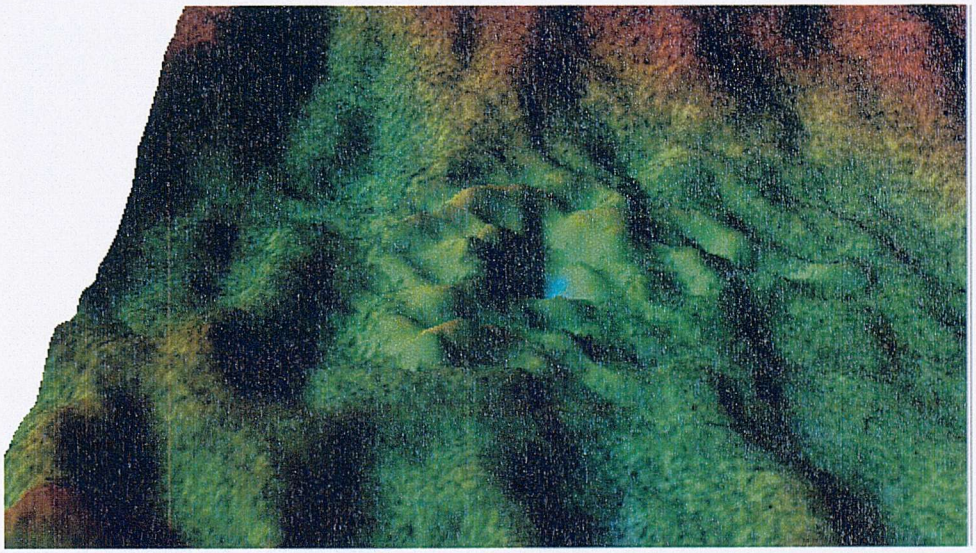
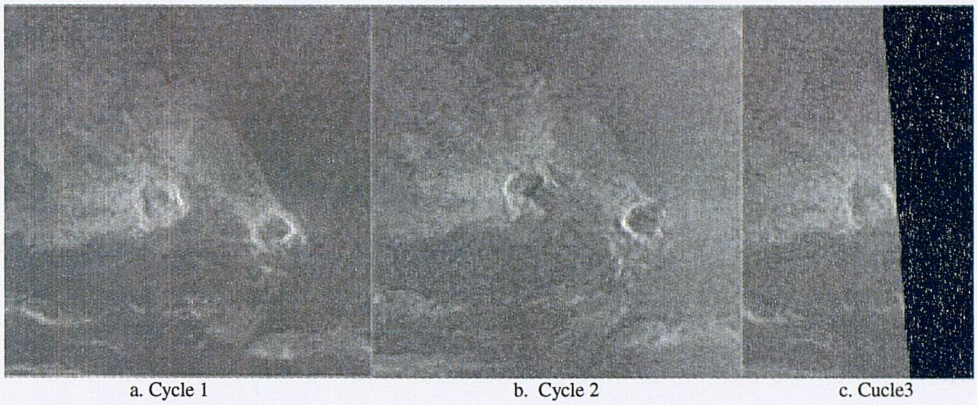


Figure 4.17: ERDAS visualisation of Crater B SFS DEM. The crater is viewed from the west, looking down from an altitude of 7 km. Vertical exaggeration is 5, and the depression angle is 37°, with the sun to the north at an elevation angle of 25.

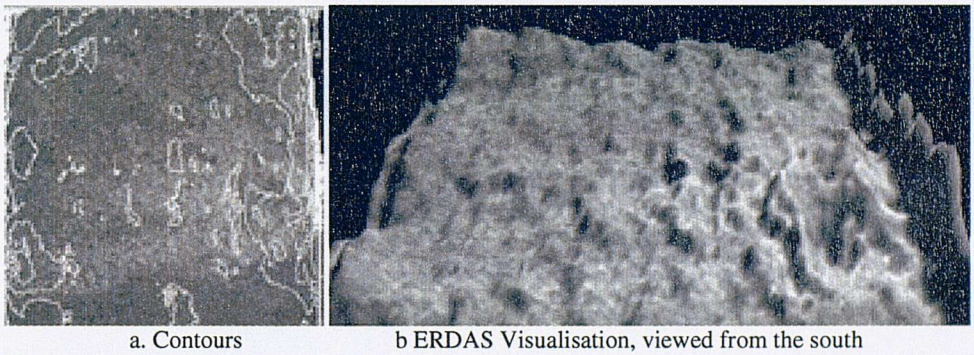
4.1.4. Crater A

This unnamed crater is the smallest in the Sample area and the westerly one of a pair separated by 13.5 km, and only 110km from Crater B. It is identified in the LPI database as Serial 643, and by Herrick & Sharpton (2000) by its latitude and longitude (5.8N, 84.3E). The images of it given in Fig. 4.18 show it to be irregular. Herrick & Sharpton (2000) find it to be 455 ± 104 m deep with a diameter of 4.8 km. The contours of the SFS version of the DEM produced for this study are shown in Fig. 4.19. Given the diameter found of 7.1 km, it is has about 87 matching points on the floor and about 70 around the rim.



a. Cycle 1 b. Cycle 2 c. Cucle3

Figure 4.18: Images of Crater A from Cycles 1, 2 and 3. Crater A lies on a largely featureless plain, so the largest DEM that MST could produce was 256 x 256 pixels.

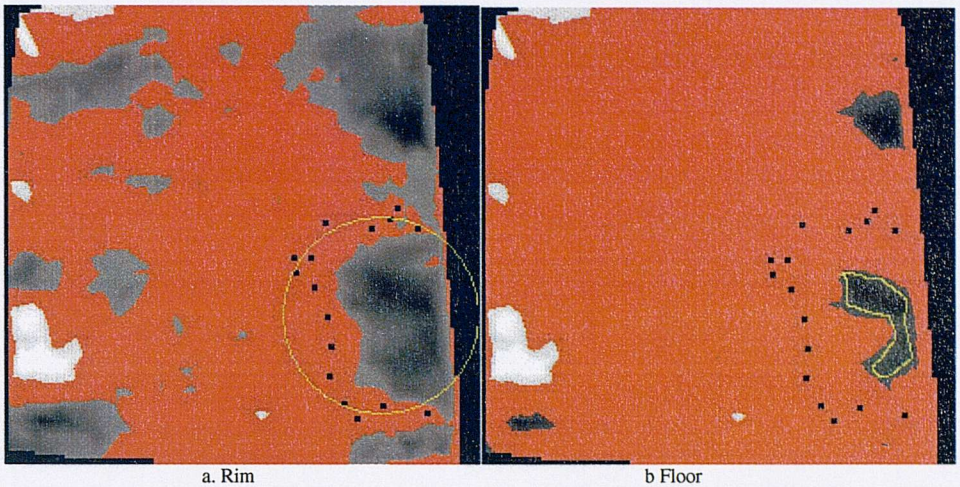


a. Contours b ERDAS Visualisation, viewed from the south

Figure 4.19: SFS DEM of Crater A. The crater is viewed from the south, looking down from an altitude of 3 km. Vertical exaggeration is 5, and the depression angle is 31°, with the sun to the east at an elevation angle of 45.

Measurement of the SFS DEM in MST yielded a depth of 329 m but it was seriously marred by ridges. Hence, the IDL version was preferred for this study. Fig. 4.20a shows the points found in Image-J to define the Rim and Fig. 4.20b

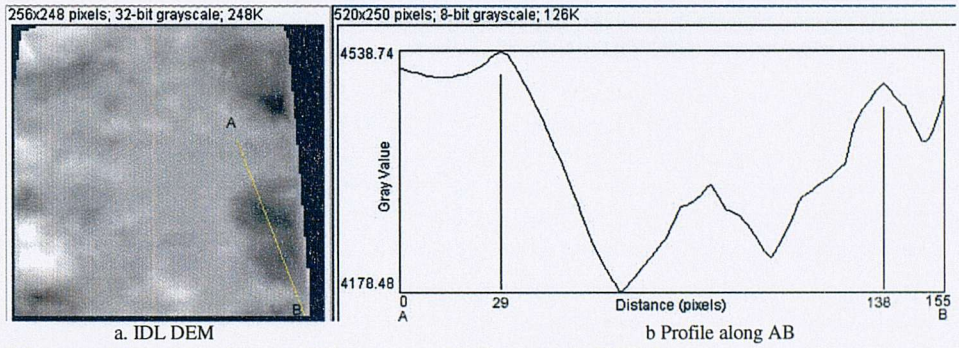
shows the floor contour. Note that no significant saddles could be found through the rim. The rim-floor depth found was 299 m.



a. Rim b Floor

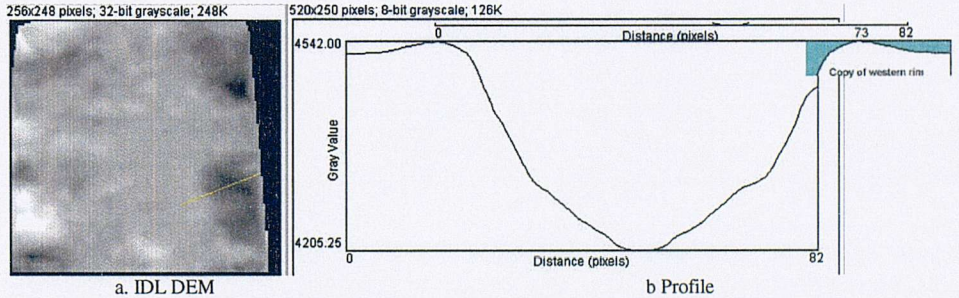
Figure 4.20: Image-J version of Crater A DEM, Rim and Floor marked. The circle, which had to be offset as shown to remain within the image, has a diameter of 7.065km and was originally taken to define the crater diameter.

The crater appeared to be elliptical, so maximum and minimum diameters were measured, as in Image-J as in Figs. 4.21 and 22.



a. IDL DEM b Profile along AB

Figure 4.21: Maximum Diameter of Crater A DEM. Image-J profile along the major axis of ellipse gives a diameter of 109 pixels (8.2 km).

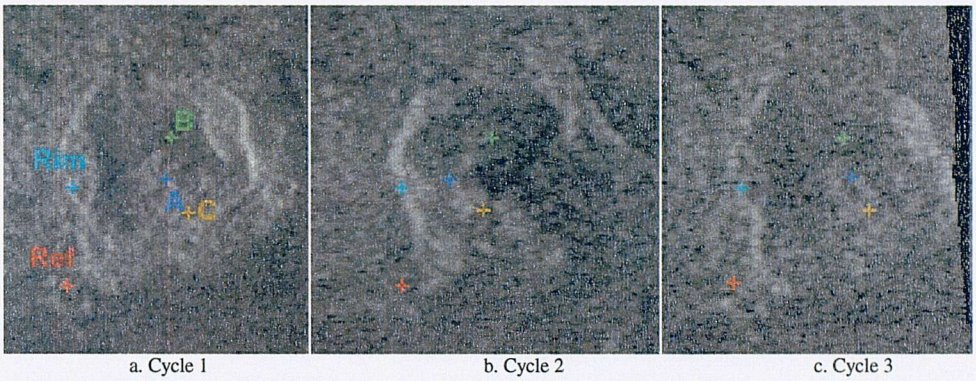


a. IDL DEM b Profile

Figure 4.22: Minimum Diameter of Crater A DEM. Image-J profile along the line shown. A copy of the western rim is used to replace the missing eastern rim and derive a diameter of 73 pixels (5.5 km).

If a copy of the western rim is used to replace the missing eastern rim, the results, 8.2 and 5.5 km respectively, indicate a mean diameter of 6.6 km. This is larger, but hardly significantly so, than the diameters given in the USGS and LPI databases, and Herrick & Sharpton (2000), ie 4.9 km, 5.3 km and 4.8 km respectively.

Herrick & Sharpton's matching points are not available so the Cycle 2 image was used to check crater depth. The spreadsheet used is Table 4.4; it finds the depth at 4 the specific matches in the Cycles 1 and 3 images identified in Fig. 4.23. The equivalent points in the Cycle 2 image were then identified, and checked for consistency.



a. Cycle 1 b. Cycle 2 c. Cycle 3

Figure 4.23: Matched points within Crater A. The chosen points are: A, a point on the northwest end of a bright return in the middle of the floor in both left looking views; B, a dark area in floor in the 2 left looking views, which matches a similar area in the Cycle 2 image; C, a point where a dark "trough" running southwest-northeast turns north in all 3 views; and Rim, at the left-hand tip of a "Y" feature on the rim in all three images. The Reference point is a block on the southwest edge of the ejecta field.

	Cycle 1		Cycle 3						Cycle 2					
Incidence	45.7		24.8											25.2
Ref	22	100	259	99	pixels	pixels	pixels	m	pixels	m	pixels	pixels	141	100
							delta	delta	using d_1		using d_3		y_2 using	
Point	x	y	x	y	d_1	d_3	ht	ht	offset	x_2	offset	x_2	d_1	d_2
A	57	62	301	61	35	42	-5.9	-442	-18	158	-25	158	275	46
B	59	47	298	46	37	39	-1.7	-126	-5	173	-7	173	275	46
C	65	74	307	73	43	48	-4.2	-316	-13	171	-18	171	275	46
Rim	24	65	262	61	2	3	-0.8	-63	-3	140	-4	140	65	62

Table 4.4: Spreadsheet for Crater A. The depth at 4 the specific matches in the Cycles 1 and 3 images are entered, with reference to a bright return of the southern edge of the ejecta field. The equivalent points in the Cycle 2 image are then calculated.

The depth of these points below the reference were:

- A, the most easily recognised point in all 3 images, is 442 m below the reference.
- B is 126 m below the reference.
- C is 316 m below the reference.
- Rim, the only well-defined rim feature in all three images, is 63 m below the reference.

However, the western rim is only a few metres above the surrounding terrain and its vertical cross-section has a radius of about 700 m. Herrick & Sharpton (2000) may not have detected this gentle contour, even at their minimum matching pitch of 12 pixels (900 m). Hence the minimum diameter can be considered to be virtually identical to the published LPI figure and, like so many others in this study, 10% larger than that of USGS. The only difference between this study and earlier work therefore lies in the identification of this crater as elliptical rather than circular. This is consistent with the orientation and shape of the unusual ejecta field, and probably due to a low impactor approach angle.

4.2. Validation of the deepest crater DEMs

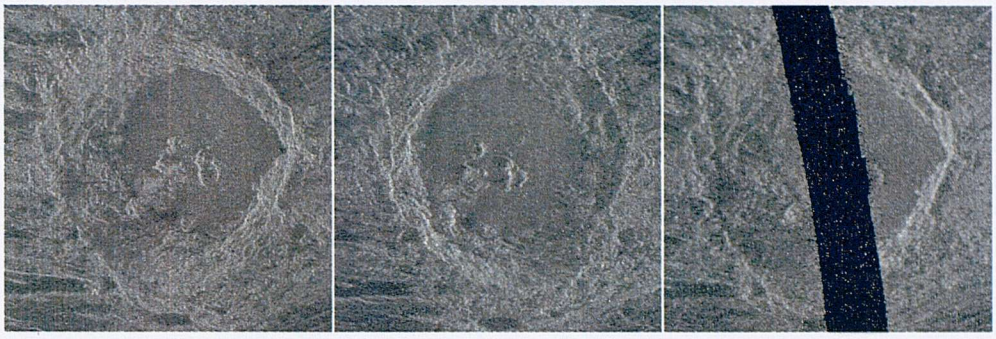
In Chapter 3, some of the deepest craters were found to have intermediate diameters. The 4 craters in the DEM Set that are deeper than 1100 m are listed in Table 4.5; their parameters show they have little in common. Note, though, that as diameter reduces, depth increases.

			This Thesis					LPI2002									USGS		Other	
Colour Key: Green = Cycles 1, 2&3 Blue = Cycles 1 & 3 only	Latitude	Longitude	diameter	Rim-Floor Ht	Rim Ht	Terrain-Floor Ht	Central peak Ht	LPI Diameter	elevation above planetary mean	central structure diam	floor reflectivity	Terrain	interior modification	exterior modification	tectonically deformed	degradation state	USGS Classification	Escarpment Diameter	Basilevsky's Assessment	Herrick & Sharpton (2000)
Name	°Lat	°Long	km	m	m	m	m	km	m	km	Fr	Te	Ie	Ee	T	De		km		
Andreianova	-3.0	68.7	77.3	1185	219	966	-	69.5	1126	38.8	d	t	y	m	n	1	D	66.1	Tt,Pwr	
Deloria	-32.0	97.1	38.1	1248	870	378	-	31.1	290	10.2	i	pf	y	n	n	2	P	31.9	FB,Pwr	o
Recamier	-12.6	58.1	28.6	1391	336	1055	421	25.5	865	4.9	b	t	y	n	y	3	P	25.3		
Samintang	-39.0	80.7	27.8	1586	85	1201	-	25.8	-470	3.6	d	pf	y	n	n	1	P	25.9	Psh2,RT	

Table 4.5: Parameters for the deepest DEMs. These craters are all in the southern half of the Sample Area, at altitudes close to the mean planetary radius, and all have been internally modified. Samintang and Recamier have Central Peaks; Deloria has several Peaks and Andreanova is a Multi-ring Basin. The LPI database also shows they have no haloes or parabolic features.

Only Samintang and Deloria have a third image for validation but both lie well to the south where Cycle 3 Incidence is about 17^0, making radar shadowing prevalent. Of these craters, only Deloria was modelled by Herrick & Sharpton (2000). Andreanova has twice the diameter of the next largest diameter (Deloria). Since there is no possibility of triangulating it and Herrick & Sharpton (2000) do not address it, it was excluded by re-defining the group of deepest craters as deeper than 1200 m depth. Thus the typical deepest crater is 31.6 km diameter and 1408 m deep, with a range of at least ± 12 % on both parameters.

4.2.1. Deloria



a. Cycle 1 b. Cycle 2 c. Cucle3

Figure 4.24: Images of Deloria from Cycles 1, 2 and 3. Coverage of Deloria is marred by a missing swath through the Cycle 3 image just where there are well-separated floor features.

Fig. 4.24 shows 3 images of Deloria, for which Herrick & Sharpton (2000) find a depth of 970 ± 216 m. The DEM of Deloria, produced by Silverthorne is illustrated in Fig. 4.25. Compared to the northern rim, the southern rim is more massive. Analysis of the measurements taken in Image-J showed a mean height difference between north and south rims of about 500 m, depending on how the measurements are taken.

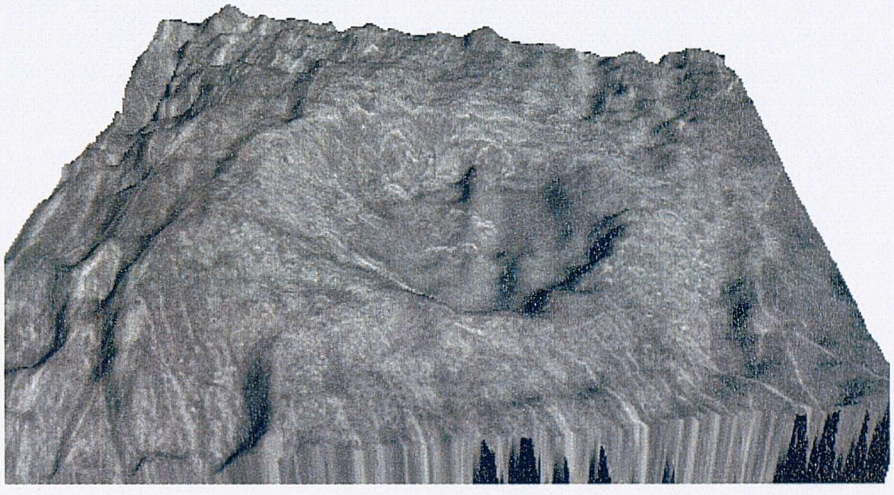


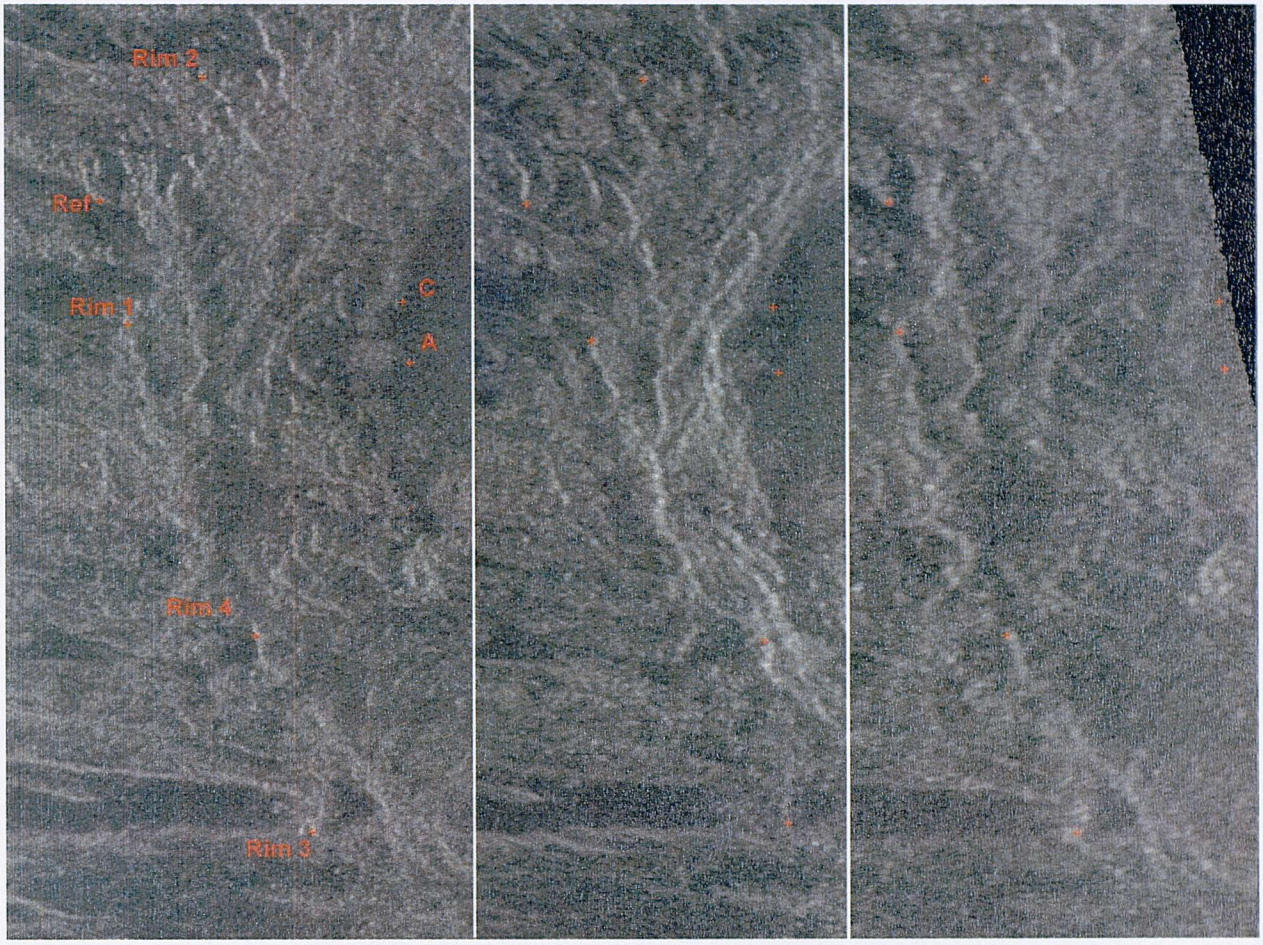
Figure 4.25: Visualisation of Deloria Crater. DEM viewed, in ERDAS Imagine at x5 vertical exaggeration, from the East with the Sun in the Northeast. The southern rim, to the left, is more massive than the northern, a bias in the initial rim sampling measurements was corrected. The bright features on the floor are not detected as prominences in the DEM.

A small difference in sampling the north and south rims for the first analysis in this study gave rise to an error in the mean rim height of 74 m. This bias was removed to give a final rim-floor depth of 1248 m, just deeper than the band quoted by Herrick & Sharpton (2000).

Table 4.6 is the spreadsheet of results for the Western side of the crater, where there are several identifiable features, as marked in Fig. 4.26. The deepest points, A and C, have a Y-disparity of 1 and 2 respectively; the highest rim peak, Rim 4, has a Y-disparity of 2. Hence, taking account of rim and floor shapes, there is good confidence that the peak height above floor bottom, of 1653 m, validates a mean rim-floor depth of 1248 m.

Cycle 1			Cycle 3						Cycle 2							
Incidence:		31.8		16.9										25.2		
Ref	134	163	1036	163	pixels	pixels	pixels	m	pixels	m	pixels	pixels	568	161		
							delta	delta	using d_1		using d_3		y_2 using		Actuals	
Point	x	y	x	y	d_1	d_3	ht	ht	offset	x_2	offset	x_2	d_1	d_2	x_2	y_2
A	315	258	1232	262	181	196	-8.9	-670	-33	716	-48	716	256	260	716	261
B	316	344	1230	346	182	194	-7.1	-536	-27	723	-39	723	342	344	723	345
C	312	222	1229	222	178	193	-8.9	-670	-33	713	-48	713	220	220	713	222
Rim 1	150	235	1042	240	16	6	6.0	447	22	606	32	606	233	238	606	242
Rim 2	194	89	1093	90	60	57	1.8	134	7	635	10	635	87	88	637	87
Rim 3	257	536	1145	537	123	109	8.3	626	31	722	45	722	534	535	721	528
Rim 4	224	420	1104	420	90	68	13.1	983	49	707	71	707	418	418	707	420

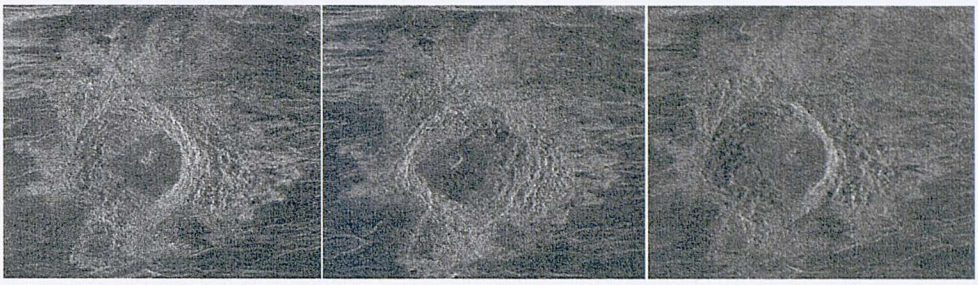
Table 4.6: Validation points for Deloria. The points are defined in Fig 4.24. The spreadsheet uses macros to derive the height of the feature from its Cycle 1 and 3 parameters, then separately define its expected offsets in the Cycle 2 image, from Cycle 1 and 3 data. The DEM is found to be valid if these forecasts are similar to each other and to the actual position chosen by inspection. In this case the poor matches for point A and Rim 1 reflect a poor choices in the Cycle 1 and 3 images. The maximum crater depth is the sum of the height of C below, and the height of Rim 4 above, the reference.



a. Cycle 1 b. Cycle 2 c. Cucle3

Figure 4.26: Validation points for Deloria Crater. These points were selected on the basis of inspection as the same features.

4.2.2. Samintang.



a. Cycle 1 b. Cycle 2 c. Cucle3

Figure 4.27: SAR Images of Samintang. Coverage of Samingtang was complete in all 3 cycles. At 39^{0}S, Incidence Angles were low: 28.2^o, 25.3^o and 15.4^o respectively, and SAR across-track ground resolution high: 188, 209 and 348 m respectively.

Samintang was covered completely in all 3 cycles, as shown in Fig. 3.27. The DEM of Samintang, illustrated in Fig. 4.28, was one of the first to be produced for this study using the standard procedure. With a footprint at 40^0 S of 21 by 8 km, the altimeter cannot be used to reliably validate the DEM of this 27.8 km diameter crater.

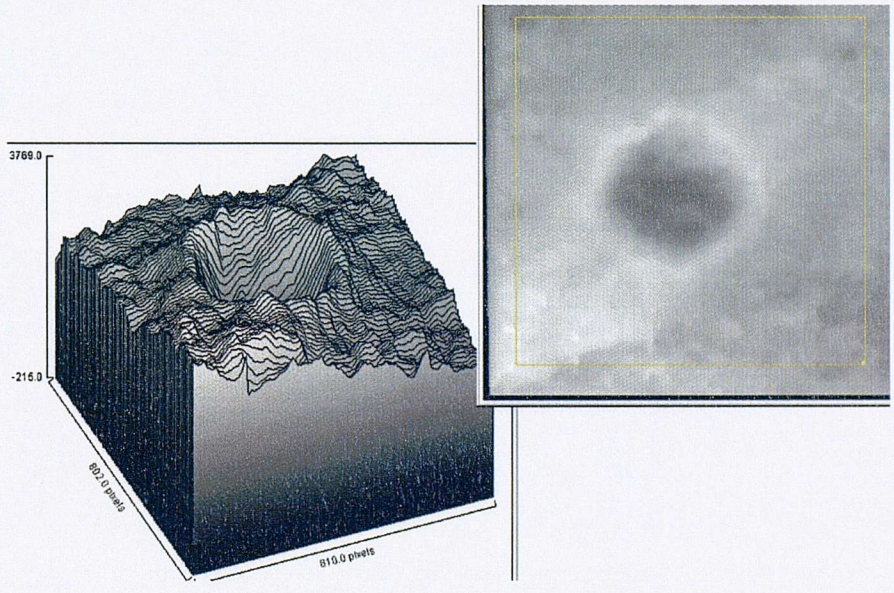


Figure 4.28: Samintang Crater. On the left is a wire grid visualisation of the DEM in Image-J, viewed from the Southwest. On the right is the DEM in greyscale, with the yellow square marking the extent of the wire grid.

Only a vestigial Central Peak was found. Analysis in Image-J gave a rim height of 385 m above the surrounding terrain. The highest rim peak was 1901 m above the lowest point of the floor, ie this is the maximum rim-floor depth. The

defined precedure found a rim-peak depth of 1512 m. Fig. 4.29 is the profile of the rim established in that analysis.

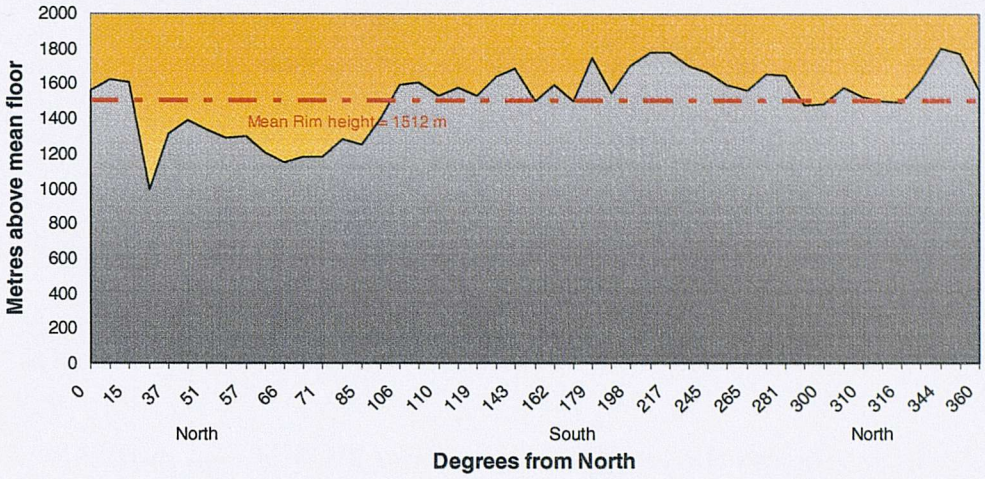
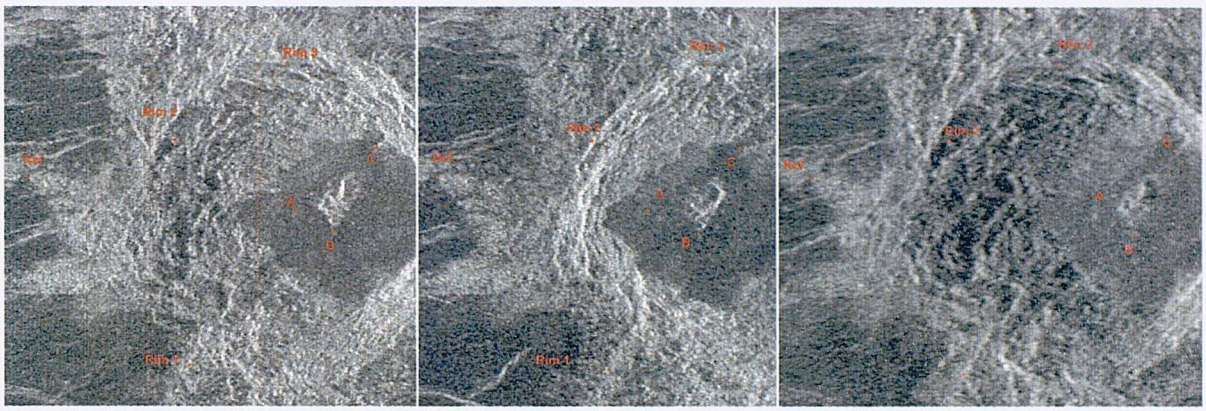


Figure 4.29: Samintang Rim Profile. There is a break in the rim to the North-northeast. Rim height variation is not un-typical.

Table 4.7 is the results spreadsheet for Samintang, based on the identifiable features marked in Fig 4.28. The deepest point, A, is a bright feature close to the centre of the floor area. The highest point on the rim is Rim 3, giving a "deepest" height difference of 1402 m. The mean is 1221 m. At the low incidence angles at Samintang (Cycle 1: 28.2^0; Cycle 3: 15.4^0), the standard deviation of height estimates may be as much as ~200 m. Hence, the mean rim-floor height from the DEM of 1586 m is inconsistent with these validation results.

Cycle 1			Cycle 3						Cycle 2							
Incidence		28.2		15.4										25.3		
Ref	69	413	1891	401	pixels	pixels	pixels	m	pixels	m	pixels	pixels	991	420		
							delta	delta	using d_1		using d_3		y_2 using		Actuals	
Point	x	y	x	y	d_1	d_3	ht	ht	offset	x_2	offset	x_2	d_1	d_2	x_2	y_2
A	366	451	2215	439	297	324	-15.3	-1147	-61	1227	-88	1227	458	458	1227	458
B	412	476	2256	464	343	365	-12.5	-935	-50	1284	-72	1284	483	483	1284	483
C	459	380	2303	370	390	412	-12.5	-935	-50	1331	-72	1331	387	389	1331	388
Rim 1	250	623	2067	620	181	176	2.8	212	11	1183	16	1183	630	639	1183	635
Rim 2	233	372	2051	360	164.3	160	2.4	181	10	1165	14	1165	379	379	1165	379
Rim 3	358	286	2174	275	289	283	3.4	255	14	1294	20	1294	293	294	1294	294

Table 4.7: Validation points for Samintang. The points are defined in Fig 4.30. Further explanation under Table 4.6 applies. In this case, all disparities are zero except for Rim 1. The maximum crater depth is the sum of the height of A below, and the height of Rim 3 above, the reference.



a. Cycle 1 b. Cycle 2 c. Cucle3

Figure 4.30: Validation points for Samintang Crater. These points were selected on the basis of inspection as the same features.

At such low incidences, radar shadowing occurred and may explin the discrepancy. As the West-East profile through the DEM in Fig. 4.31 shows, the western slope of this crater is steeper than the Cycle 3 incidence angle. Inspection of Fig. 4.30c confirms that there are a large number of dark areas on the western escarpment that may have exceeded MST's search limits during its matching processes. Where this happens, the depth of the floor is set by the first match after the radar shadow. At Samintang, the largely featureless floor may have given rise to a faulty initial match, especially until the matching found the central feature.

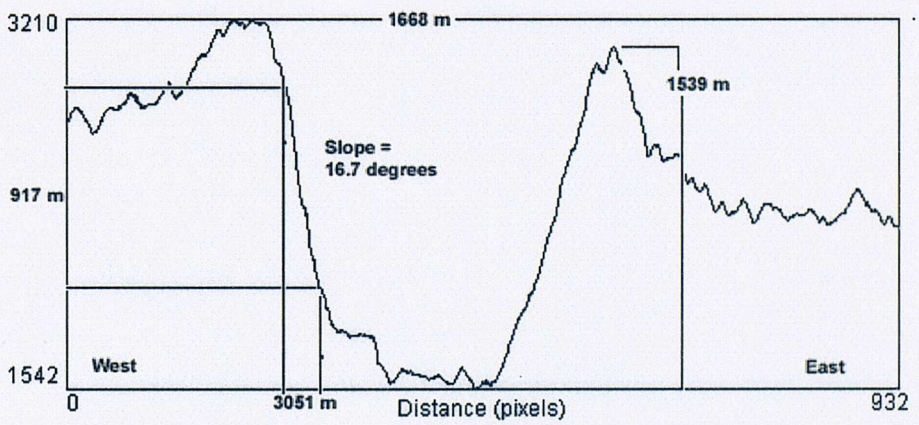


Figure 4.31: West-East profile of Samintang Crater. Each pixel on the horizontal axis is 75 metres. The western escarpment has a slope of 16.9^0 between the points marked, higher than the Cycle 3 Incidence Angle of 15.4^0.

The above analysis may be supported by the low rim height throughout its Northeastern quadrant, as shown in Fig 4.27. Hence, a floor-rim height determined from the eastern escarpment, viz 1538 m from Fig. 4.29, may be more reliable.

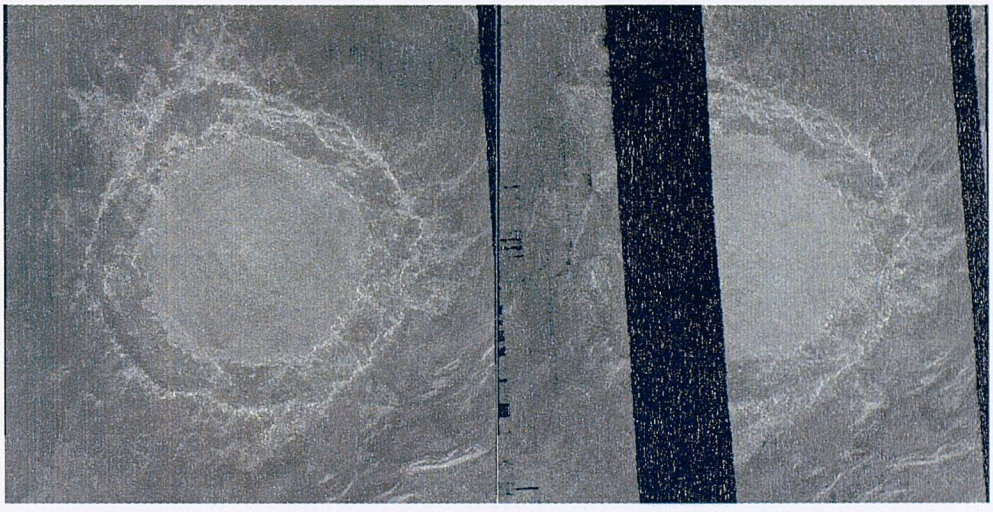
Overall, the validation tests indicate that Samintang may not be as deep as the 1586 m mean rim-floor depth found for from its DEM, and may be as much as 200 m too deep. However, these tests confirm that Samintang is one of the deepest craters.

4.3. Validation of the largest crater DEMs

Large craters, as defined in Chapter 3, are a particular problem for this study as none in the Sample is completely covered in both the Cycle 1 and 3 images, so many of their DEMs contain discontinuities. Also, because the chosen process used framelets of 1024 by 1024 pixels, and no means could be found to mosaic the resulting DEMs, the large craters had to be addressed as a series of sections.

4.3.1. Mead

The SAR coverage of Mead achieved by Magellan is illustrated in Fig. 4.32.



a. Cycle 1 b. Cycle 3

Figure 4.32: SAR Coverage of Mead. Mead was covered early in Cycle 1 when the radar was still being calibrated. Even so this image reveals more floor texture than in the Cycle 3 image. There was no Cycle 2 coverage of Mead.

Bierer produced 17 DEM mosaics of Mead (see Fig. 4.33) to the same procedure as Cochrane, who produced 3 to confirm consistency. The virtually featureless floor gave noisy MST results throughout the floor. Seven points on the Eastern rim provided a mean height of 540m above the outer terrace. A single measurement of the Western Rim provided a height of 580 m above the outer edge of its terrace. Measurement of the inner floor, as illustrated in Fig. 4.34, rests entirely on 2 cross-sections across Bierer's DEM "R12N057"; these show the outermost part of the inner floor is an average of 485m below the outer terrace. Hence, the composite crater depth of 1030 m validates the altimetry.

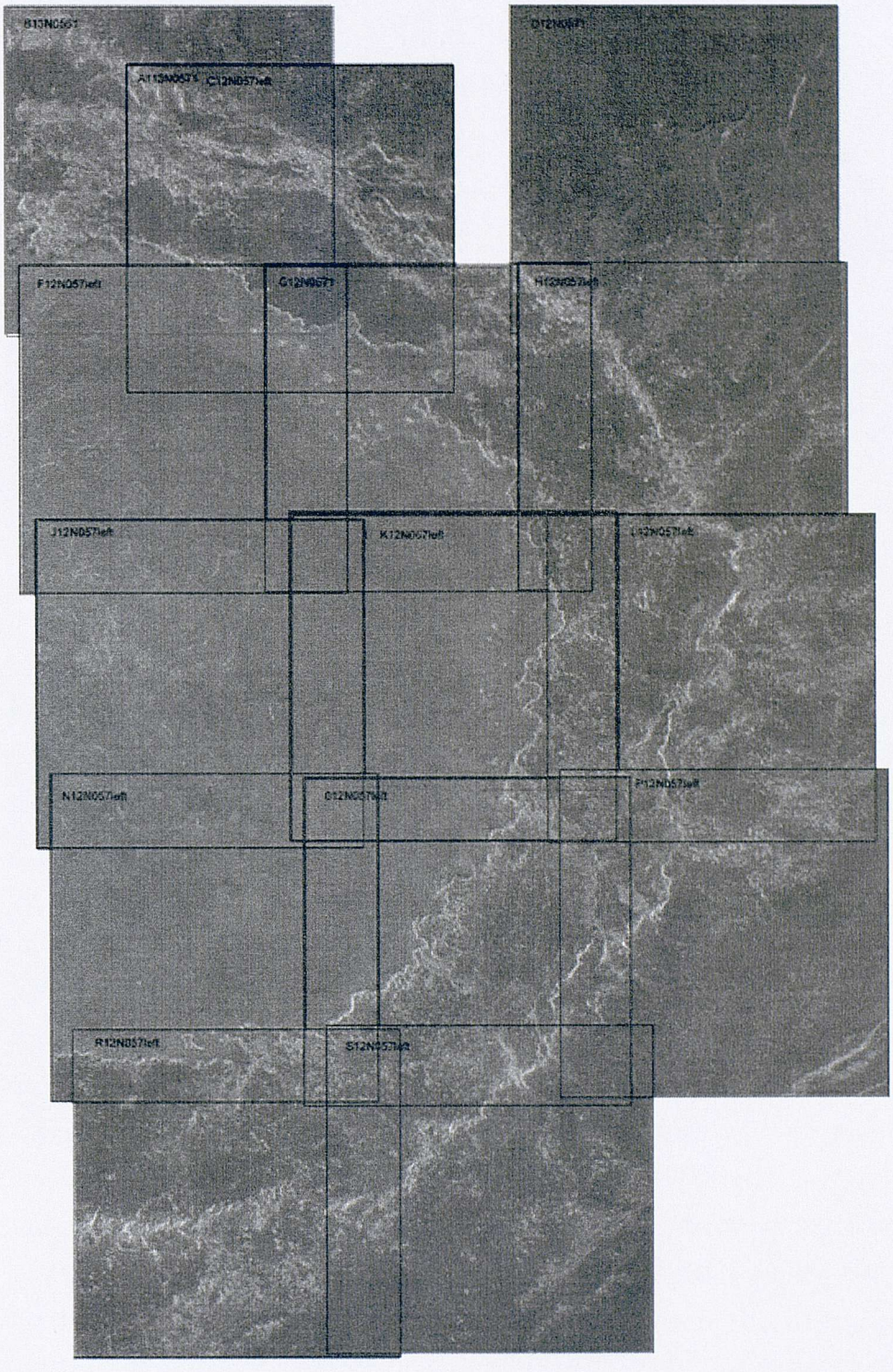


Figure 4.33: Mosaicking of the eastern half of Mead. Bierer produced 14 mosaics of the area of Mead to the east of the missing swaths, and 3 to the west. Each was a standard 75 x 75 km and contained generous overlaps. Many measurements of the Eastern rim give it a mean height of 540 m above the terrace. One measurement shows the Western Rim is 580m above what may be its terrace.

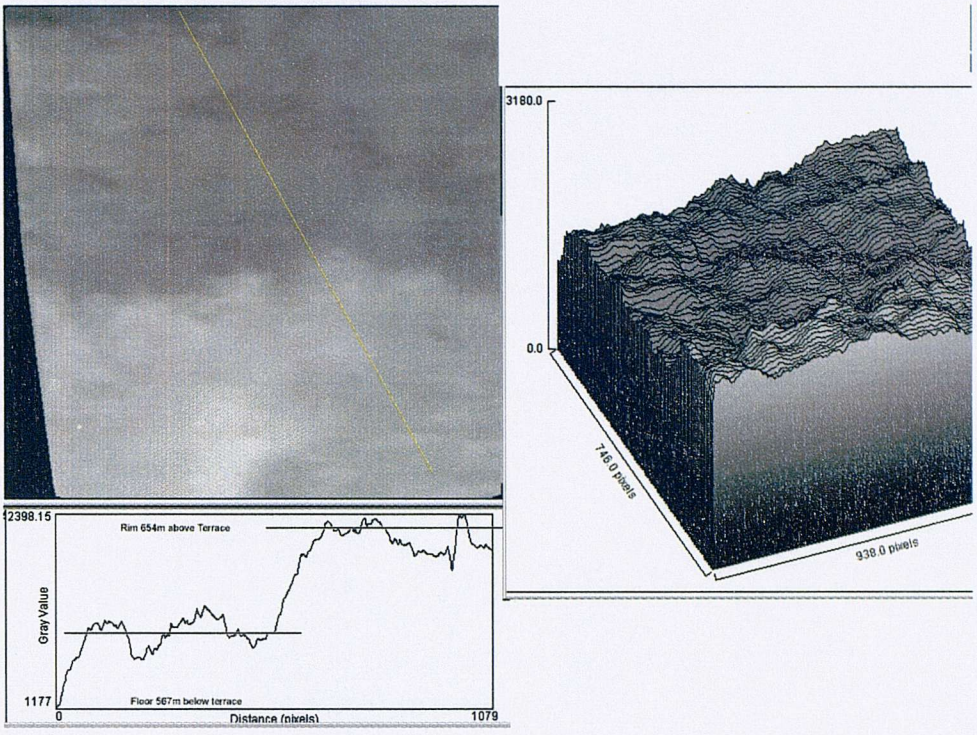


Figure 4.34: Checking the depth of the inner floor of Mead. These images record the second of 2 cross-sections across Bierer's DEM "R12N057" to measure the inner floor with respect to the outer terrace. The profile at bottom left is along the yellow line on the DEM greyscale; the other cross-section was close to the left hand edge of the surface plot at top right. The mean of the two tests shows that the outermost part of the inner floor is 485 m, below the terrace and 977m below this part of the south east rim.

Mead is 53% larger than any other crater on Venus and almost three times as large as the next largest DEM, Joliot-Curie. Hence, it is the most influential data point for D:d trend lines. Being so much larger, Mead is often omitted from crater population assessments, viz neither Ivanov *et al.* (1992) nor Sharpton (1994) address it. Alexopoulos & McKinnon (1994) provide a single altimeter profile indicating a depth of about 1300m. Herrick & Sharpton (1996) assess its geology and provide an averaged topography based on altimetry and stereo matching. Measuring their profiles, as in Fig. 4.35, gives a rim-floor depth rather less than 1 km and a diameter of about 320 km. However, their text says "the central area averages about 700 m below the surrounding plains and 1100 m below the elevated rim".

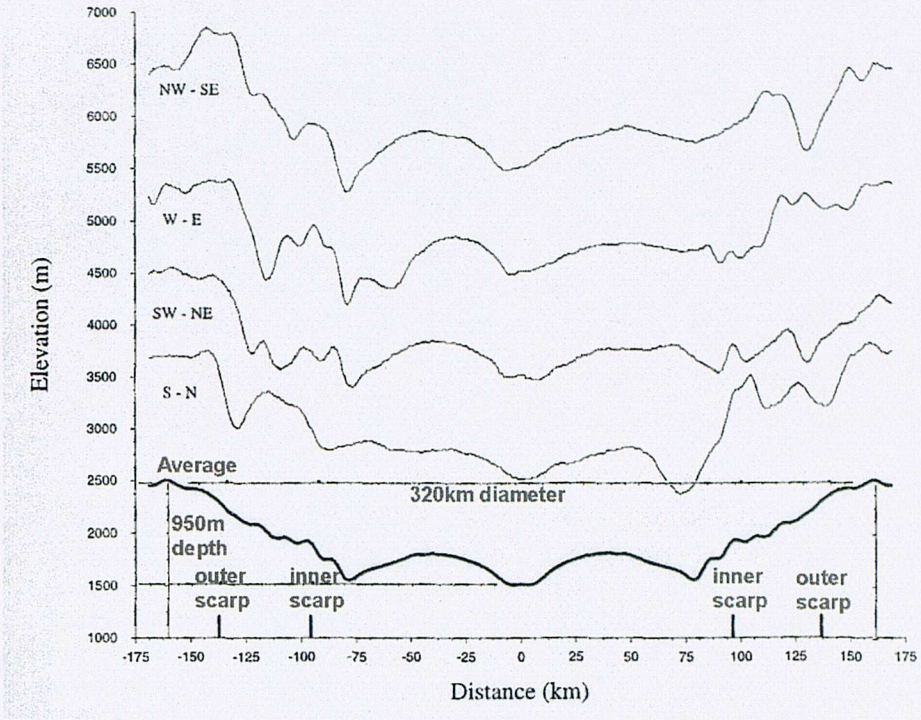
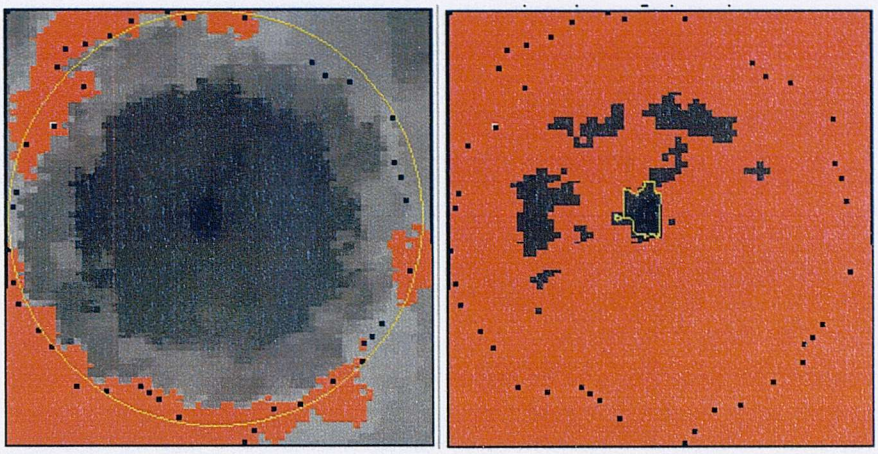


Figure 4.35: Altimetry profiles of Mead. Herrick & Sharpton (1996) provide these profiles across Mead, and an average of them, which indicates a diameter of 320 km and a rim-floor depth of 950 m. Their text reports a diameter of 269 km and a rim-floor depth of 1100 m. The floor is shown to be far from flat, which they attribute to viscous relaxation rather than simple up-doming.

This study used Image-J to measure GDTR altimetry of Mead in the same way as the DEMs were assessed. Fig. 4.36 illustrates a rim diameter of no more than 302.4 km and a mean rim-floor depth of 1066m. The details are described in the Notes on Mead on the CD, along with some further validation of crater depth using the one clearly identifiable feature in the middle of the floor in the Cycle 3 image. Overall, the foregoing discussion validates the altimetry profiles from Brown & Grimm (1996).

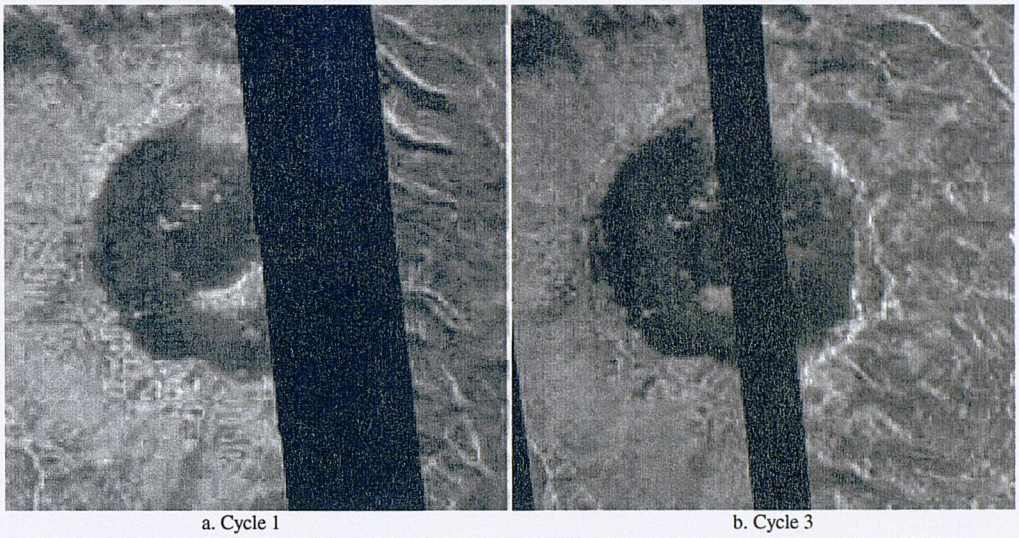


a. Cycle 1 b. Cycle 3

Figure 4.36: Image-J assessment of Mead. These images record the checks of the altimeter GTDR data using the same method as used to measure the DEMs. The yellow circle of 302.5 km diameter in Fig 4.34a is perhaps a little larger than the true rim, which, from the azimuthally averaged profile from Brown & Grimm (1996), is 296 km. The central floor area, marked in yellow in Fig 4.34b, was found to be 1066 m below the mean height of the 41 points marked on the rim. Compared to this mean depth, the height range of the 41 points about it is considerable: +567 m, – 433 m. Note that the outer semi-circle of dark patches in Fig 4.31b tends to confirm the finding in Herrick & Sharpton (1996) of annular up-doming.

4.3.2. Joliot-Curie

This crater was only imaged during Cycles 1 and 3, and that only partially as illustrated in Fig. 4.37.



a. Cycle 1 b. Cycle 3

Figure 4.37: Coverage of Joliot-Curie. Because of the missing swaths, it is only possible to produce DEMs of the western half of the crater, and 2 mosaics are required to cover a diameter of more than 100 km.

Silverthorne produced SFS DEMs of two different parts of the western half of Joliot-Curie; Fig. 4.38 is an ERDAS visualization of one of them, viewed from the South with 10-fold vertical exaggeration.

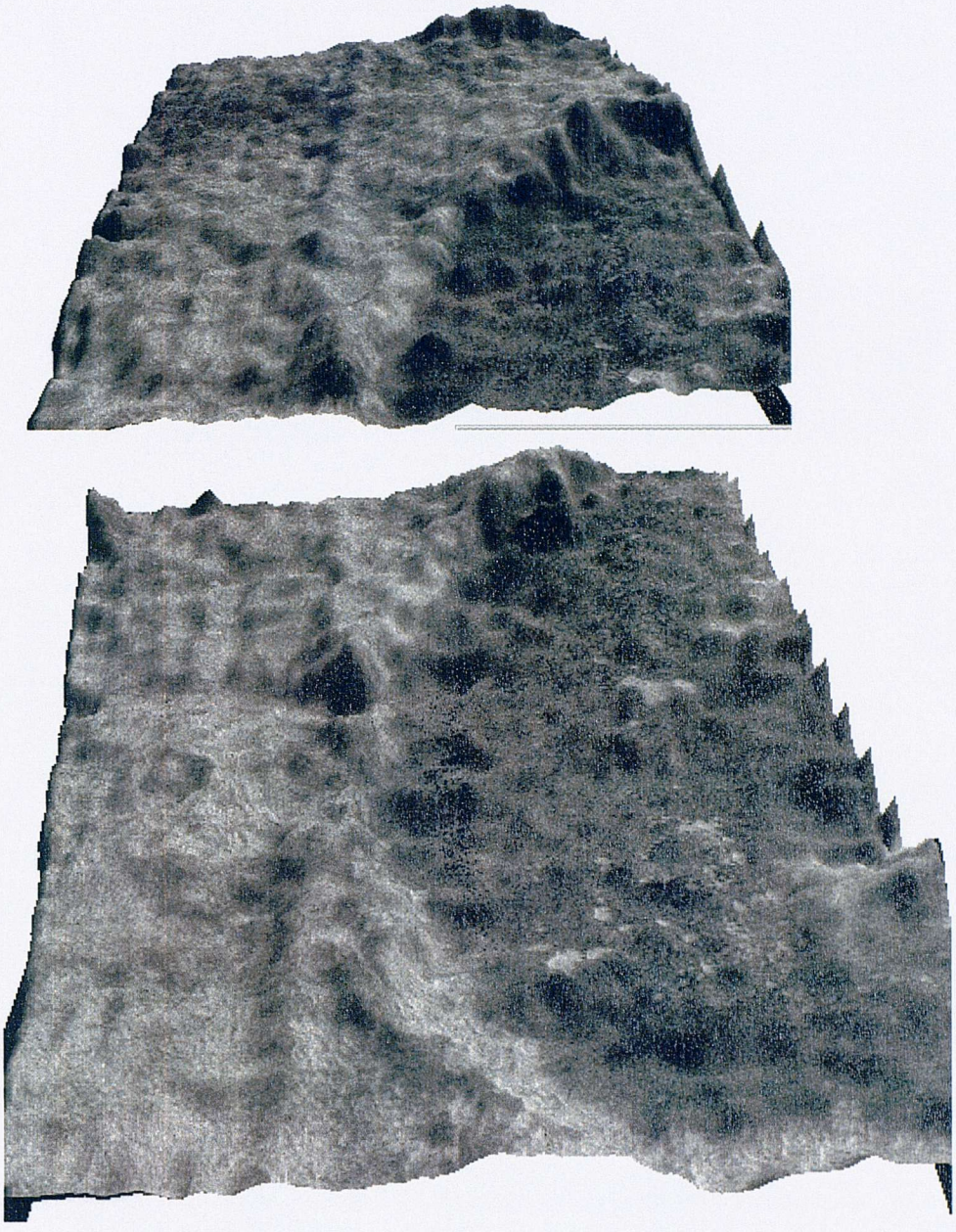


Figure 4.38: Visualization of the 2 DEM elements of Joliot-Curie. Silverthorne's DEMs of the western rim of Joliot Curie are viewed in ERDAS Imagine from the south, with 10-fold vertical exaggeration.

Depth measurements from North-South profiles of Silverthorne's DEMs required mosaicking and a correction for a pronounced slope due to the under lying topography, as illustrated in Fig. 4.39.

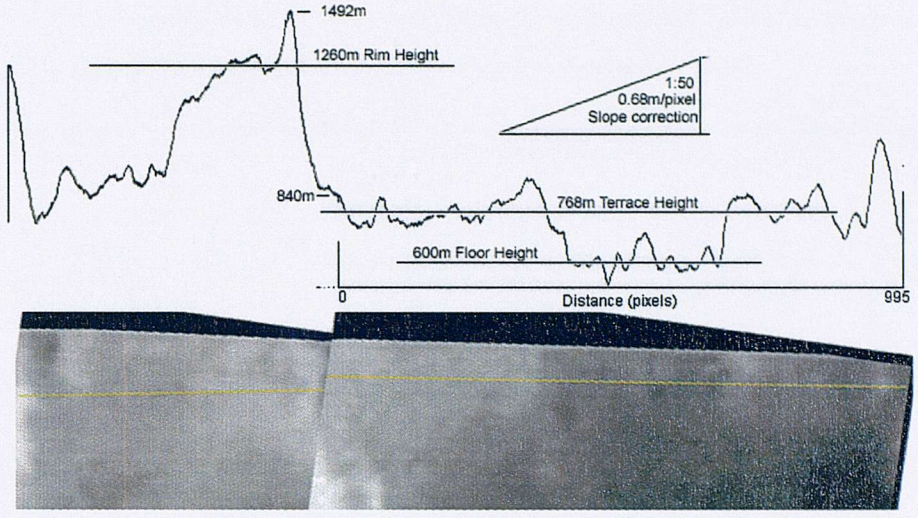


Figure 4.39: Cross-section across the western half of Joliot-Curie. The upper profile is along the yellow line in the lower grayscale image of the relevant part of Silverthorne's DEM. The marked slope of the crater floor and the surrounding terrain comes from Pioneer topographic data used as a reference for all Magellan SAR data. This can give rise to a gross underestimate of the crater diameter since, as marked on the profile, local topographic highs can appear in the DEM above and inside the geological rim.

Early measurements of Silverthorne's DEMs, which cover less than half of the rim, show that the rim peaks lie very close to the escarpment so the rim diameter might be as little as 90 km. This appeared to endorse a diameter of 91.1 km in the USGS database. However, the LPI database gives 100.9 km, and averaged altimetry profiles from Brown & Grimm (1996) indicate a diameter of 120 km. It was noted that the slope across the crater north-south is just over 1°, ie the southern rim peak is on about the same level as the foot of the northern rim. It is not clear how Herrick & Sharpton (2000) corrected for this effect, if at all, in determining their depth of 540 m. Certainly, corrections for the West-East slopes in this DEM, as illustrated in Fig. 4.39, place the actual peaks of the rim further west by several km. Profiles across corrected versions of Silverthorne's DEM's, as illustrated in Fig. 4.39, show a depth of 605 m compared to the mean rim to floor bottom depth of 725 m from altimetry profiles in Brown & Grimm (1996). Since this is primarily a study of SAR imagery the former figure was preferred, and similar to the height of the mean peaks above the mean of 10 % of the floor. See also the Notes on this crater in the CD.

As can be seen in Figs. 4.38 and 4.40, there is a break in the western rim through which lava may have flooded to form the dark crater floor.

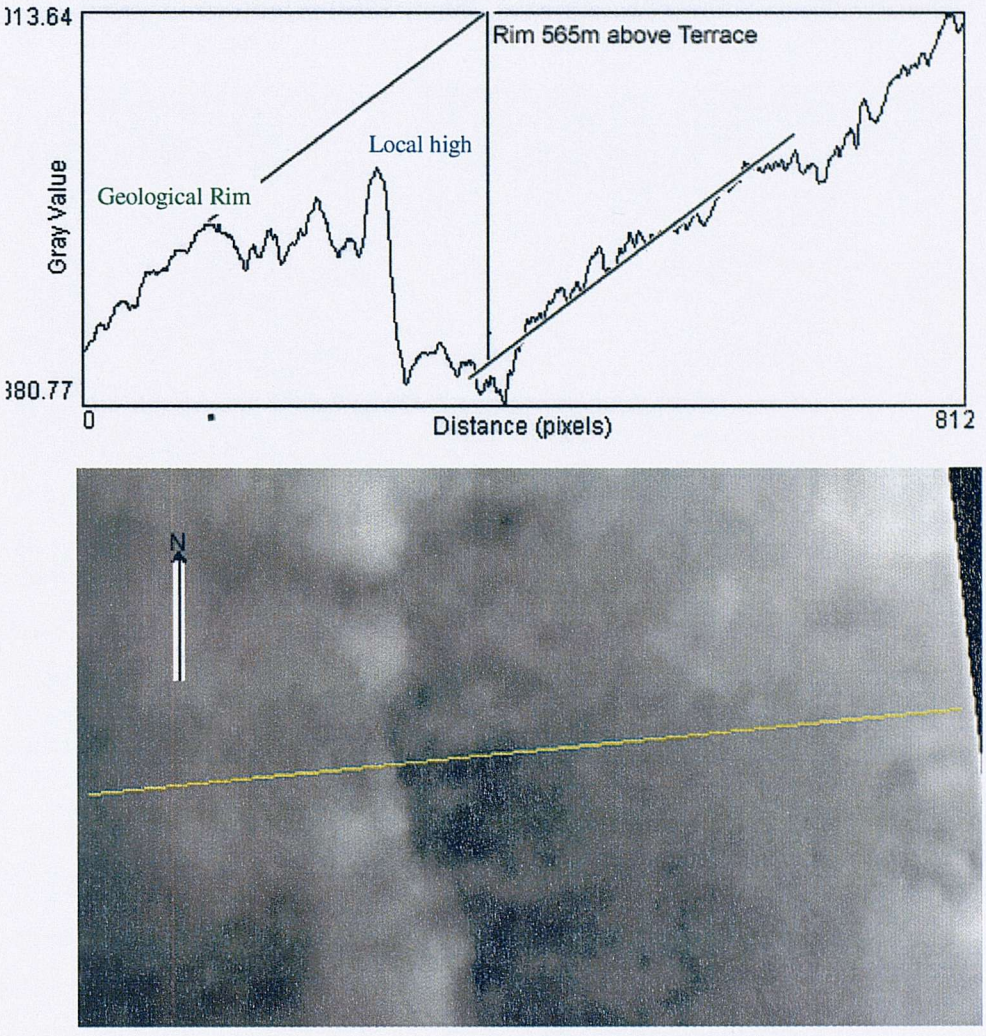
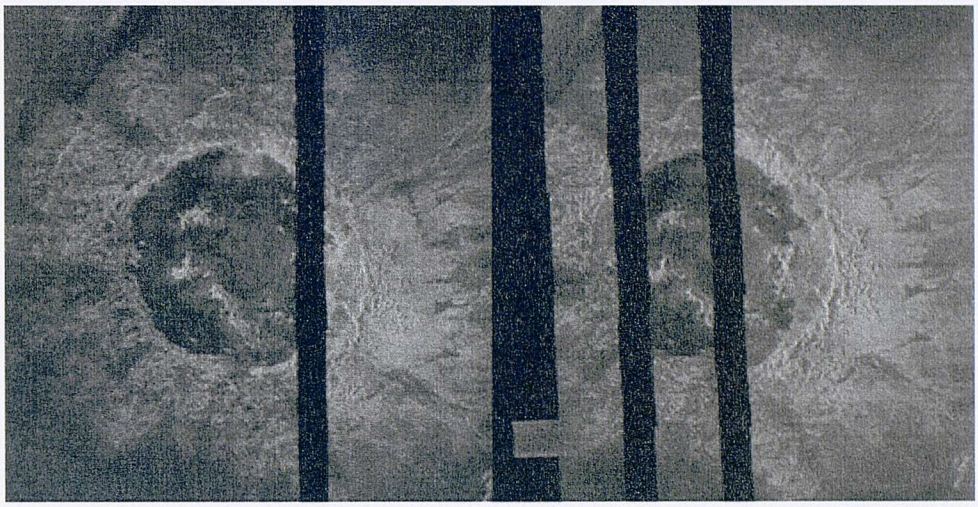


Figure 4.40: Cross-section across the western Rim of Joliot-Curie. The upper profile is along the yellow line in the lower grayscale image of the relevant part of Silverthorne's DEM. The marked slope of the crater floor and the surrounding terrain comes from Pioneer topographic data used as a reference for all Magellan SAR data. This can give rise to a gross underestimate of the crater diameter since, as marked on the profile, local topographic highs can appear in the DEM above and inside the geological rim.

4.3.3. Potanina

This crater was only imaged during Cycles 1 and 3, and that only partially as illustrated in Fig. 4.41.



a. Cycle 1 b. Cycle 3

Figure 4.41: Coverage of Potanina. Because of the missing swaths, it is only possible to produce DEMs of the western half of the crater, and "North" and "South" mosaics are required to cover a diameter of more than 100 km.

Four SFS DEM elements were made of Potanina and the results of mosaicking them are illustrated in Fig. 4.42. Mosaicking of the 2 western elements appears reasonably seamless to produce a composite north-south strip through the central region of the crater.

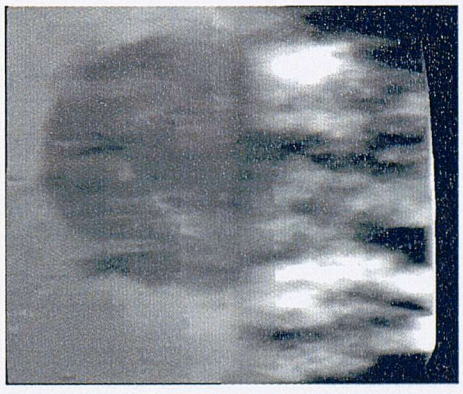


Figure 4.42: DEM mosaic of Potanina. Missing swaths make the eastern DEMs unreliable. It should be possible to produce a better DEM by flipping the images to start matching from the surrounding terrain to the east but mosaicking in the centre of the crater would then be even more difficult. The 2 western mosaics appear to match each other well.

The 2 DEM elements of the eastern side of the crater were made by matching from their top left corner near one missing swath. Fig. 4.43 shows the selected points in Image-J of the altimetry grayscale of Potanina. These gave a rim-floor depth of 925 m, which was used in the in the analyses presented in this Thesis.

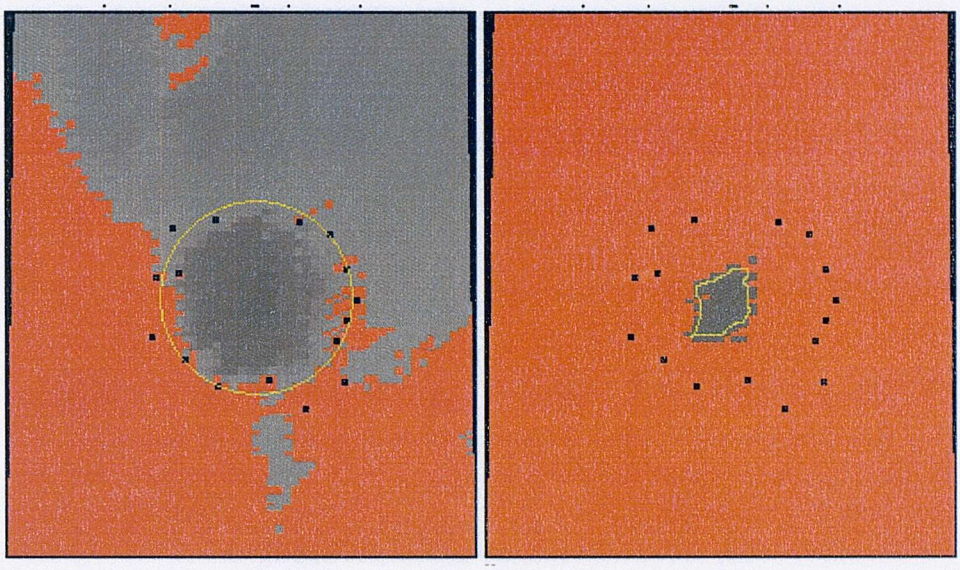


Figure 4.43: Points chosen to determine the depth of Potanina. The altimetry data for Potanina was measured in the same way as the DEMs of other craters. The mean height of the Rim peaks and saddles was found to be 925 m above the mean floor height. The yellow circle is 112.8 km diameter, and close fit to the rim features selected.

4.4. Chapter Summary

This Chapter has focussed on 9 craters at the extremes of the DEM Set of 62 craters, to validate not just that Set but also the strongest determinants of the trend lines proposed in Chapter 3.

Study of the 4 craters of < 10 km diameter that were also modelled for Herrick & Sharpton (2000) shows that a high matching point density reveals gently rounded shoulders of these craters. Hence that density is necessary to reliably establish rim diameter. Triangulation using a Cycle 2 image has validated all 4 DEMs produced for this study but only 2 in Herrick & Sharpton (2000), which are Nsele and Crater A. Both of the other 2 craters in Herrick & Sharpton (2000), which are Elma and Crater B, are shown to be too deep by approximately 100 m beyond the standard deviations quoted therein. The depth found in this study of all 4 small craters for which comparison is possible were validated as at least as deep as measured by Herrick & Sharpton (2000). Hence, the unusually shallow slope of the depth : Diameter trend line in Herrick & Sharpton (2000) has not been validated by this work.

The group of the 3 deepest craters has also been assessed. The DEM produced in this study of the shallowest and largest diameter crater, Deloria, has been validated by triangulation and shown to be about 70 m deeper than that produced for Herrick & Sharpton (2000), after allowing for the standard deviations quoted therein. There is no Cycle 2 image of the median member of this group, Recamier, and it has not been independently modelled. The third member, Samintang, is most probably not as deep as measured from the DEM produced in this study but there is no other model of it. Hence, the generic "Deepest Crater" of the DEM Set is an average of the 3, ie a mean rim diameter of 31.6 km and a mean rim-floor depth of 1408 m.

Validation of the 3 largest craters is restricted by the incomplete SAR imagery. The altimetry reported in several earlier studies has been reviewed. Considering the unusual floor cross-section of Mead, a mean rim height of 1066 km above the mean central floor, and a rim diameter of 296 km, were confirmed. Silverthorne's DEMs and altimetry evaluation converged on a rim-floor depth of

605 m for Joliot-Curie. Its diameter of 120 km comes from a very gentle rounding in the profiles in Brown & Grimm (1996) and constitutes a considerable increase over previously accepted figures. However, the available profiles through the DEMs produced for this study show a marked underlying slope across the crater, which may derive from Pioneer topography. Two of the DEM mosaics of Potanina produced for this study tended to validate 2 similar results from altimetry. These gave a rim-floor depth of 925 m and a diameter of 112.8 km.

All the large diameter craters are significantly shallower than the deepest craters. Hence, there is a valid case for more than one depth : Diameter trend line in the crater population of Venus.

Chapter 5

Errors and Artifacts in the Models

Initially, NASA had no declared intention to use Magellan for stereo imaging. Following an initial stereo trial reported in Leberl *et al.* (1992), NASA approved Magellan to attempt a third Cycle[38] for stereo mapping and to produce a Stereo Toolkit. Coverage limitations of the Cycle 3 data, as described in Ford *et al.* (1993) and Wall *et al.* (1995), and the lack of ground truth constrain the potential of stereo mapping using Magellan data. There are no published works on the systematic errors that affect DEMs of small features produced from Magellan data. Where authors need to address errors, they look no further than Leberl *et al.* (1992), e.g. Herrick & Sharpton (2000) take DEM errors to be in the order of 100m. In some cases, unquantified levels of subjectivity have been applied in the removal of "unexpected" height co-ordinates.

The DEMs produced for this study were generated fully automatically by MST, and rigorous assessment of these outputs is appropriate, as regards both quantifiable errors and recognisable artifacts.

[38] called Cycle 3

5.1. *DEM Error Analysis*

Leberl *et al.* (1992) identify 3 error factors in topographic elevations derived from stereo radar images, as follows:

1. a mismatch between stereo images expressed in pixels, and assumed to occur only during matching;
2. the limitation of range accuracy due to limited range resolution;
3. propagation into the stereo solution of errors in spacecraft position and velocity parameters.

Leberl *et al.* (1992) state that errors of Types 1and 2 are random at each pixel leading to noise in the elevation measurement, whereas errors of type 3 are systematic and slowly varying.

Certainly, Type 3 errors appear to have largely been removed by mosaicking F-BIDRs to closure round the planet. Howington-Kraus *et al.* (unpublished) present detailed corrections to the F-Maps for a part of central Ovda Regio measuring 0.5^0 East-West by 2^0 North-South, and the derivation of a DEM on a 675m grid across it. They report it compared well to an earlier DEM produced by Arvidson *et al.* on a 1200m grid (mean difference of 0.3m and standard deviation of 128.3m). This standard deviation was in part explained by a systematic, north-south tilt of the 2 DEMs of 10^{-3}. This type of error is not thought to dominate the topography of craters of, typically, a few 10s of km diameter and is not considered further in this Thesis.

Type 1 errors are considered further in Section 5.4.

Leberl *et al.* (1992) note that the Type 2 error is " expected to be less than half the slant range resolution, which is reported at 66 m". This figure comes from a fundamental radar theory that the best attainable resolution is inversely proportional to the transmitted modulation bandwidth of 2.26 MHz, eg see Elachi (1988). No other author in the bibliography defines a figure for Magellan's slant range resolution. Ford *et al* (1992) do define an *effective* slant range resolution as 88 m. Oliver & Quegan (1998) make clear that quoted resolutions are usually not

as good as expected from theory because of the effects of side-lobe suppression and multi-looking (discussed further in Section 5.3). Practical experience of image matching suggests that it is extremely difficult to match reliably to within half a pixel. For all these reasons, a slant range error of half the figure from Ford *et al.* (1992), ie 44m, is assumed to be the minimum mean Type 2 error in this Thesis.

Leberl *et al.* (1992) also give Fig 4.2 as a diagram to explain the following equation for elevation uncertainty, σ_h, as a function of range uncertainty, σ_r:

$$\sigma_h = \frac{(\sin^2 \Omega' + \sin^2 \Omega'')^{1/2}\Omega_r}{\sin(\Omega' - \Omega'')} .\sigma_r \quad \text{.....(24)}$$

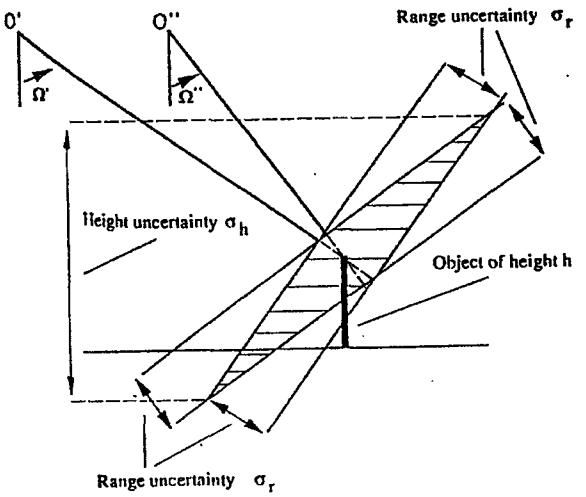


Figure 5.1: Effect of limited range resolution on surface terrain accuracy. The spacecraft is assumed to image the target at different look angles, Ω' & Ω'', during Cycles 1 and 3. This diagram defines Ω as a look angle but makes the satellite nadir direction parallel to the vertical at the target object, ie it is also the incidence angle. Furthermore, no dimensions for satellite altitude or stand-off range are included in the accompanying text. Hence, Ω is taken here as equal to θ, the incidence angle at the target.

This approach addresses one practical difficulty: that stereo imaging inherently converts the slant range resolution cell into ground resolution cells of different sizes. It does not address another: re-sampling at a standard 75 m per pixel. Taking the incidence angle, θ, equal to Ω and replacing σ by the more conventional δ, Table 5.1 gives some figures from Eqn 18 for some representative craters. The spreadsheet "Venus_Sample_Craters2.xls" in the accompanying CD

gives a value for the minimum mean type 2 height error, δ_h , for all 62 DEMs in the Sample area.

Crater	Latitude (degrees)	Longitude (degrees)	θ_{C1} (degrees)	θ_{C3} (degrees)	δ_r (m)	δ_h (m)
Florence	-15.3	85.0	40.4	21.2	44	100
Georgina	-20.4	58.8	38.2	20	44	100
Helvi	12.4	82.7	45.8	25.6	44	107
Kastusha	-28.6	60.0	33.9	17.8	44	101
Teumere	-38.3	88.1	28.5	15.5	44	107
Crater B	6.4	83.4	26.8	14.9	44	111

Table 5.1: Elevation (height) error due to finite range resolution. Using Eqn. 15 from Leberl *et al.* (1992) at the craters named shows that a slant range error of 44 m will give rise to Type 2 height errors in the DEM of between 100 and 111 m, depending on the Incidence Angles, θ, for Cycles 1 and 3. A full tabulation is provided in the spreadsheet "Venus_Sample_Craters2.xls" in the accompanying CD.

5.2. *Errors due to Block Adaptive Quantization*

Block Adaptive Quantization (BAQ) coding was provided on the Magellan downlink to reduce data corruption due to radio signal noise. The small effect of the narrower bandwidth on SAR signal dynamics was traded for more reliable downlink performance. However, the BAQ thresholding also significantly affects pixel-by-pixel comparison of processed imagery, eg during stereo matching. Fig. 5.2 illustrates that the quantizer will shift the same bright greyscale transition to one or other edge of the SAR resolution cell in which it occurs. When these modified positions in both Cycle 1 and Cycle 3 are matched, 1 of 4 possible altitudes will be computed for the original transition. None of them will be correct unless the Cycle 1 and Cycle 3 resolution cells both happened to begin exactly at the transition point.

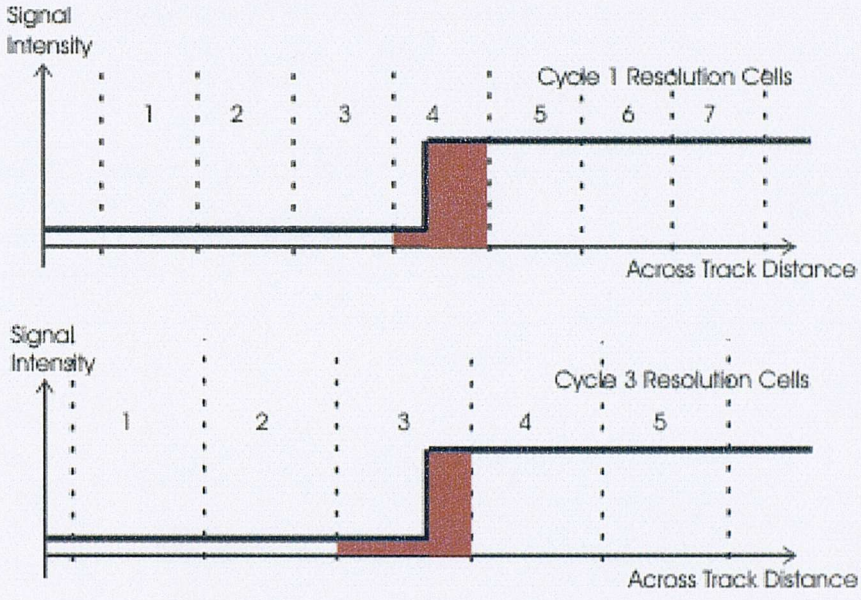


Figure 5.2: Effect of BAQ threshold on detected image transition position. In this example there is step increase in signal intensity to a uniformly bright feature after a uniformly dark area. Either the total signal power in the range bin (the pink area) is larger than the threshold for that cell, and the transition appears at the leading edge of that cell, or it is not and the transition is delayed until the start of the next cell. In either case, the threshold causes a translation error up- or down- range. Note that the lengths of the resolution cells are different in each cycle, so any transition is translated to subtly different places in the 2 images. The precise position of these transitions with respect to each other is fundamental to DEM generation, and the combination of the 2 threshold conditions in the 2 images may place the same original transition at any 1 of 4 possible altitudes in the DEM.

For example, at Teumere, a 4.7 km diameter crater at 38.3^0S, 88.1^0E, the resolution cells were 186 m and 345 m long in Cycles 1 and 3 respectively. Fig. 5.3 shows the pattern of altitude errors, calculated at every 5m across track, at Teumere for transitions, I, that were just large enough to trip the threshold if they occurred precisely at the start of a range resolution cell. Otherwise, such a transition would not contain sufficient energy to trip the cell in which it occurred, and was effectively delayed to the start of the subsequent cell.

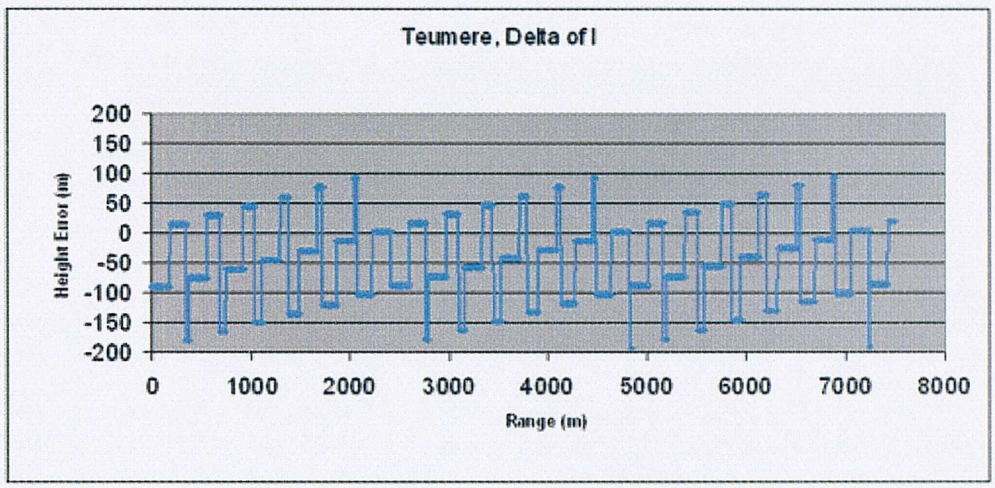


Figure 5.3: Errors on a DEM of Teumere, for transitions equal to I. Because the threshold tracks the long-term mean signal level, a transition of I, defined as just sufficient to trigger a transition of the quantizer output, is most likely given normally distributed signal characteristics. Smaller changes will not change the quantizer output.

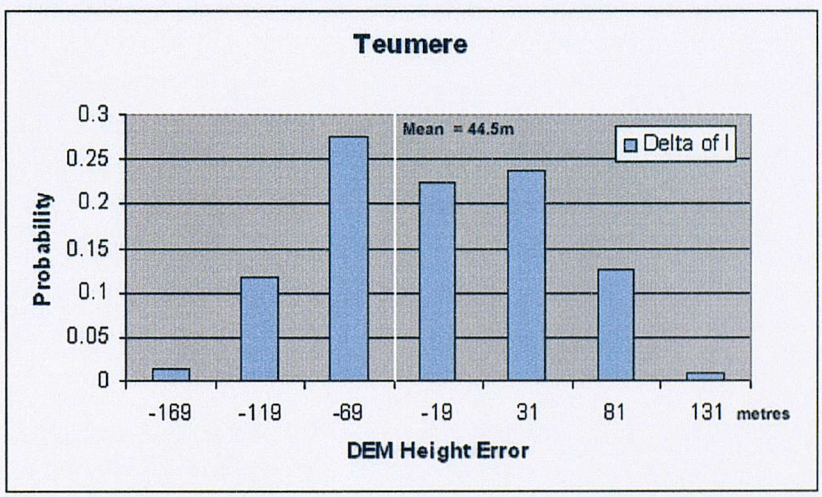


Figure 5.4: Histogram of Height Errors in a DEM of Teumere. Analysis of the data points , for transitions equal to I in Fig 5.2, shows they will give rise to a mean height error of – 44.5 m, with a standard deviation of 63.5 m.

The pattern for a Delta of I at Teumere gives a mean height error of -44.5 m throughout the DEM, a standard deviation of 63.5 m and a histogram as in Fig 5.4. Larger transitions will, increasingly, tend to shift the detected transitions up range in spite of occurring later (ie further across track) in the SAR resolution cell. Fig. 5.5 shows the patterns for transitions for deltas of I, twice that level (2I) and four times it (4I). Note that the profile of errors at Teumere due to 2I transitions is almost equally distributed about zero error. For normally distributed signal conditions, larger transitions are increasingly unlikely.

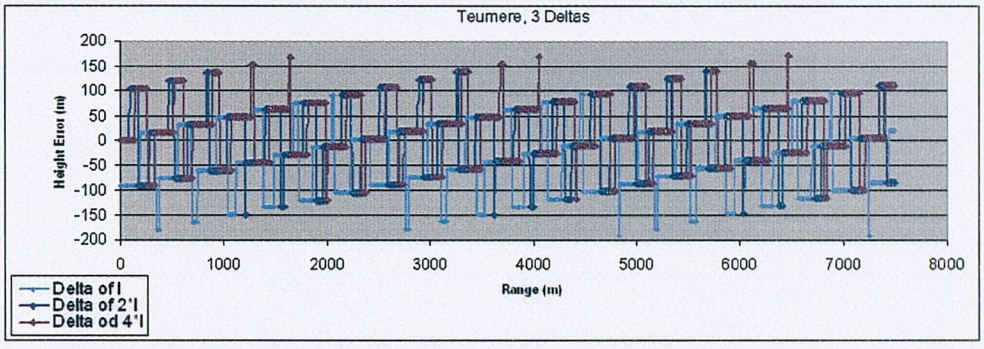


Figure 5.5: Errors on a DEM of Teumere, for transitions of I, 2I & 4I. The error profile due to 2I transitions is almost equally distributed about zero ie: similar numbers of transitions are moved up range as are moved down range. In this case, the mean DEM error is –1 m, with a standard deviation of 64.7 m. Larger transitions are increasingly likely to be moved up range: the mean for a delta of 4I is +25 m, with a standard deviation of 64.2 m.

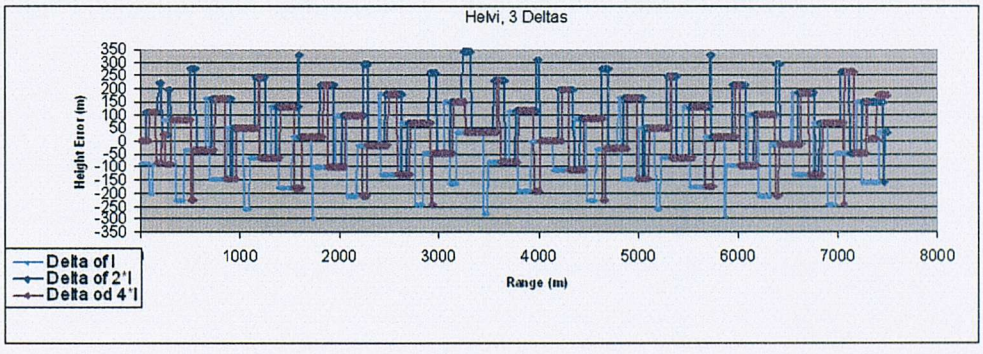


Figure 5.6: Errors on a DEM of Helvi, for transitions of I, 2I & 4I. The mean error for a Delta of I at Helvi is -43.4 m, and the standard deviation is 65 m Again, the error profile due to 2I transitions is almost equally distributed about zero, ie a mean DEM error of -1.8 m, with a standard deviation of 64.7 m. For a delta of 4I, the mean is +20 m, with a standard deviation of 64.7 m.

Teumere is close to the southern edge of the sample area, ie: it is one of the craters furthest from perigee. Fig. 5.6 shows these patterns for Helvi, a crater close to perigee. The mean error for a Delta of I is -43.4 m, and the standard deviation is 65m; for 2I the mean error is -1.8 m, with standard deviation of 64.7m; for 4I the mean error is +20 m, with standard deviation 64.7 m. So, as the spacecraft approached perigee, the Incidence angles got larger, so did the errors, and so did the standard deviation of those errors.

Several other cases, as indicated in Fig. 5.7, were investigated and all were found to lie within a continuum that starts with a Delta of I and extends to radar receiver saturation, the larger Deltas becoming progressively less likely.

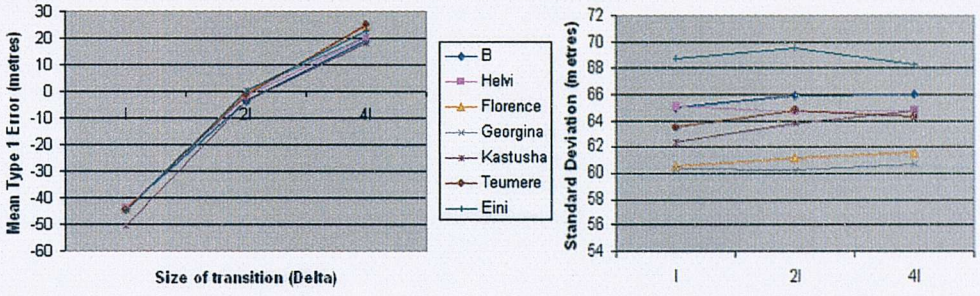


Figure 5.7: Type 1 Errors on DEMs. All signal transitions, I, that are just large enough to trigger the BAQ threshold do not register until the next range resolution cell, typically 45 m further down range. Increasingly more significant transitions have an increasing chance of triggering the resolution cell in which they occur. For signal transitions of 2I the net effect is near zero; very large transitions, like those of size 4I, tend to move towards the radar but these are very rare. The standard deviation of such errors is more significant, and averages 63m.

To characterise the errors with summary statistics, this continuum should be weighted by the probability of occurrence of its elements. Any such analysis should be based on recalling that the BAQ quantizer adjusted the threshold to minimise the mean-square-error of the reconstituted signals using weightings of 0.52 and 1.73. Kwok & Johnson (1989) show that the probability of a signal magnitude bit of 1, ie above the threshold, is 0.242. Such an analysis must also rest on assumptions about the signal characteristics that are valid near craters. However, the original single-look data records are not available from which accurate signal statistics might be recovered.

Fortuitously perhaps, that the mean error for 2I is always near zero. Also, as Section 5.3 will show, multi-looking will suppress marginal transitions (ie those close to I). Finally, large transitions are rare for most signal characterisations. This Thesis therefore assumes that the average effect of these errors is zero. However, their effect in any particular case may be significant, a risk that can be characterised by a standard deviation of 63.6 m.

To obtain a single error figure, Σ_{tot} , at one sigma confidence, this BAQ coding error, Σ_{BAQ} , may be added to the minimum Type 2 error, Σ_{T2} , at one sigma confidence on a root sum square basis as:

$$\Sigma_{1\sigma}{}^2 = (\Sigma_{T2} + \sigma_{T2})^2 + (\Sigma_{BAQ} + \sigma_{BAQ})^2 \quad \text{.....(22)}$$

where, in all these cases: $\sigma_{T2} = 0$, assuming MST will find the best match.

$\Sigma_{BAQ} = 0$, as justified in the preceding paragraph.

$\sigma_{BAQ} = 63.6$ m, as per the preceding paragraph.

A column in the spreadsheet "Venus_Sample_Craters2.xls" in the accompanying CD derives this one sigma value on the basis of Eqn (22). The values of $\Sigma_{1\sigma}$, for the DEMs of the 62 craters in the Sample then fall in the range of 118 to 128 m.

This is more than Herrick & Sharpton (2000), who state: "vertical resolution is potentially a few tens of meters but realistically is ~ 100 m" (p 20,247). However, Herrick & Sharpton (2000) also tabulate rim-floor standard deviations given by MST for specific DEMs in the range 41 to 660 m.

5.3. *Effects of Multi-looking*

Multi-looking, as summarised by Pettengill et al in Table 5.2, was used during image product generation in order to reduce the speckle. Although it also tended to average the magnitude (brightness or darkness) of features placed improperly by BAQ coding offsets, it did not remove them.

Altitude	Latitude	Incidence	CI Range resolution	Number of Looks	Number of displacements
km	Deg	Deg	m	N	n
290	10N	47	120	5	3
400	23N, 3S	43	130	6	3
600	46N, 26S	37	135	7	4
1000	62N, 42S	29	175	10	5
1750	83N, 63S	19	250	15	8
2100	90N, 67S	17	280	17	9

Table 5.2: Multi-looking parameters. Multi-looking, used primarily to compensate for additional speckle as the slant range increased from periapsis at 10^0N, also reduced the effect of BAQ coding offsets. The range walk shifted each look with respect to any given feature but, because of antenna beam symmetry, only to n positions. If the number of looks, N, is even, n = N/2 and, if odd, n = (N+1)/2 . In the Sample Area, the number of looks varied only between 5 and 10, so that the multi-looking had little effect in reducing the significance of BAQ coding offsets.

As the spacecraft moved past a feature close to periapsis, eg Helvi, the range resolution cells migrated up range and back again due to the spherical wave front within the 2.1^0 antenna beam width. To illustrate the imaging geometry, during Cycle 1 Magellan first approached Helvi on 29 Nov 90 just after 22.28 hrs GMT, travelling at 8.77 km/sec horizontally, and descending at 0.03 km/sec towards periapsis. It was at an altitude of 290 km, imaging at 45.8^0 Incidence down a slant range of 406 km, and the eastern swath edge lay across the centre of the crater. The SAR antenna beam subtended 14.9 km along the ground track, so any particular part of Helvi was imaged over a maximum of 1.7 secs. To compensate for the reducing altitude, the Incidence Angle was being increased at an average rate of 0.00169 deg/sec, ie the "range walk" caused the resolution cells to migrate down range at an average rate of 0.5 m/sec. Command Sequence Number (CSN)s M0332B, 280 - 290 incremented spacecraft and radar parameters every 5.9 s. This

steadily varied the pattern of the range resolution cells so that the multi-look processing tended to average out feature offsets due to the BAQ coding.

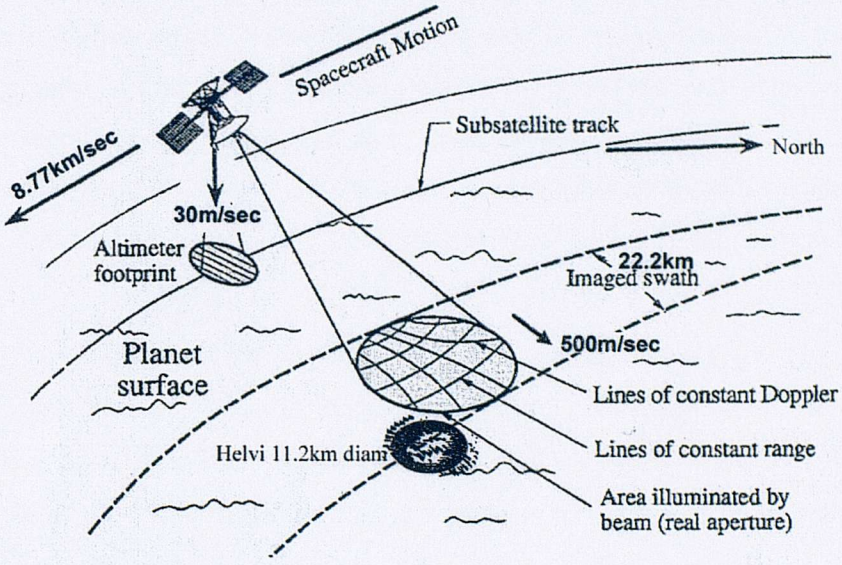


Figure 5.8: Spacecraft motion approaching Helvi during Cycle 1. The curved lines of constant range causes the range resolution cells to "walk" down range and then back again as they pass over any given feature. Ground processing correctly positions the cells but any BAQ coding offsets are smeared over the extent of the range walk.

Fig. 5.8 shows the range resolution cells were not aligned rectilinearly but around a curve where the spherical wave front intersects the planetary surface. Elachi (1988) gives an expression for this "range walk", r_w:

$$r_w = r_1 - r_0 = \frac{r_0 \theta_a^2}{8} \quad \text{.....(23)}$$

where: r_0 is the slant range perpendicular to the flight vector,

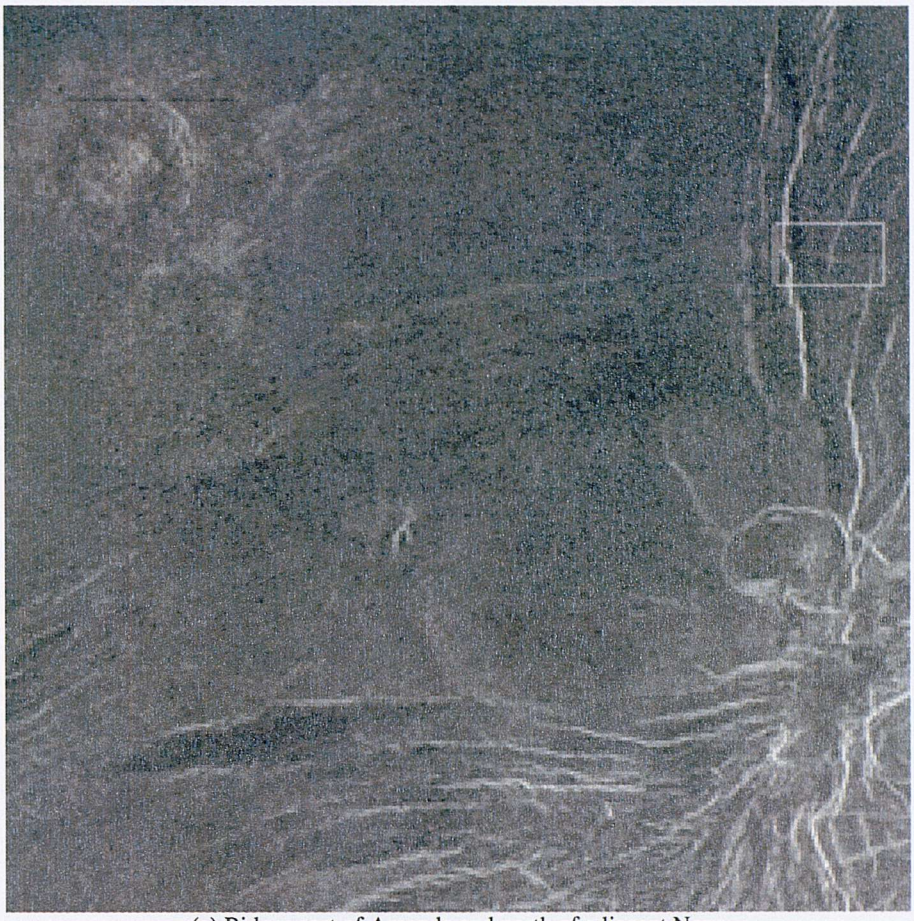
r_1 is the slant range when the target enters or exits the beam, and

θ_a is the azimuth beam width of the radar antenna.

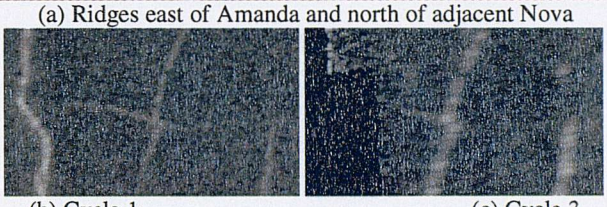
This equation was used in the ground processor to correctly geo-reference the individual images before they were overlaid and summed in the multi-looking process.

For Magellan, the azimuth beam width is 2.1^0 and, hence, the range walk is about 0.02% of the slant range resolution but the ground processor could not correct for its effect on the features misplaced due to BAQ coding. Furthermore, given the symmetry of the contour, the range resolution cells "walked" to the same position in 2 looks on each side of the beam centreline (except the middle look of an odd number of looks). In the case of Helvi, the first and last individual images, and the second and fourth, would have range resolution cell boundaries at the same ground range. This symmetry reduced the smearing due to multi-looking the shifted transitions, especially for the craters close to periapsis where there were few looks.

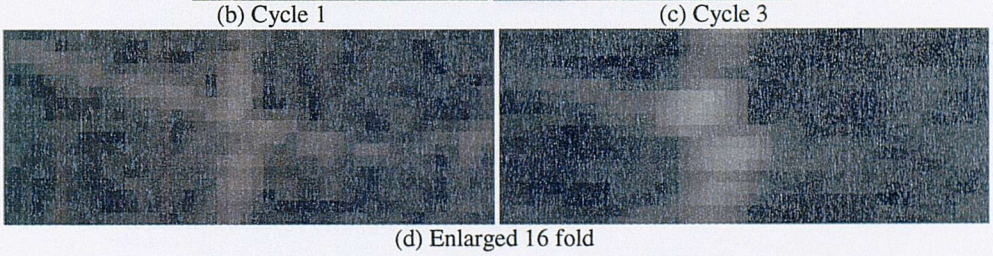
Fig 5.9 illustrates the extent of the smearing. Inspection at pixel level of many narrow linear features reveals the same characteristics. The azimuth and elevation beam widths are similar but note that this smearing over about 2 SAR resolution cells is in range, without a similar effect in azimuth. Hence the effect is due to the BAQ coding, and not the finite antenna beam width.



(a) Ridges east of Amanda and north of adjacent Nova



(b) Cycle 1 (c) Cycle 3



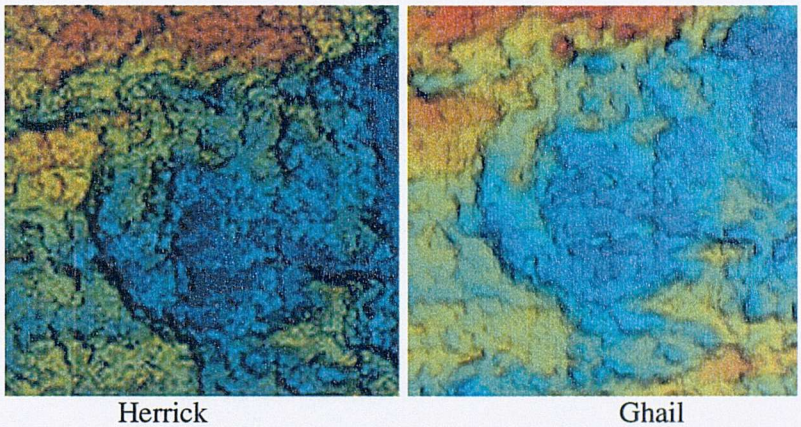
(d) Enlarged 16 fold

Figure 5.9: Ridges near Amanda. (a) is a 1024x1024 pixel raw F-Map Cycle 1 image of Amanda at 29.1^0S, (b) and (c) are cut outs, from Cycles 1 and 3 respectively, of the intersection of 2 narrow ridges, 80 km East of the crater. The North-South ridge emanates from a Nova to the South and is clearly more prominent than the East-West ridge. Enlarged 16-fold in (d), these features appear in "blocks" of 3 - 4 East-West pixels (ie 225 – 300m) in Cycle 1 and 6 - 7 East-West pixels (ie 600 – 675 m) in Cycle 3, in patterns that are repeated North-South. Ground range resolutions at Amanda are 161 m (Cycle 1) and 307 m (Cycle 3), and N is 7 or 8.

5.4. *Effects of Resampling and Mosaicking*

The multi-looked images were output by the Magellan SAR Processor as (F-BIDRs, consisting of approximately 350 pixels across track by 220,000 pixels along track, at 75m pitch in a greyscale of 250 values, and mosaicked into MIDRs, which consist of 7168 lines by 8192 samples. They were published on CDs and as prints called F-MIDRs, covering approximately 5^0 x 5^0. The F-BIDRs were later re-processed by USGS to produce the F-Map files, each measuring 2^0 latitude by 2^0 longitude. First, these were published on CDs. F-Maps are now available on the internet via http://pdsmaps.wr.usgs.gov/PDS/public/explorer/html/fmapadvc.htm.

BIDR production involved over-sampling the multi-looked images by a factor of at least 1.6, i.e. there was no information loss due to re-sampling. However, mosaicking was primarily for mapping and its effects are evident in the DEMs. For example, Fig. 5.10 shows DEMs of Langtry, a 50 km crater at 17^0S, 155^0E, produced by Herrick and Ghail using different versions of MST with different settings. Although the texture and colour scales are different, it is possible to see that both DEMs contain 2 linear, north-south ridges. Fig. 5.11 illustrates the actual pass numbers, and their geometry, over the crater for Cycles 1 and 3.



Herrick Ghail

Figure 5.10: DEMs of Langtry. Each author produced these DEMs with different versions of MST, and with different settings. Both exhibit 2 north-south ridges across the floor of the crater.

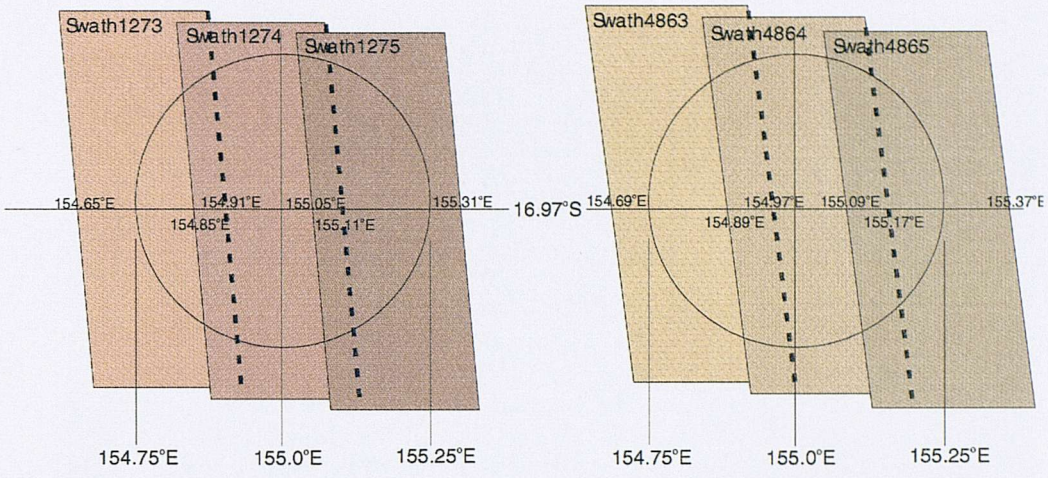


Figure 5.11: Parameters of the 3 swaths over Langtry during Cycles 1 and 3. The mosaicking process simply pasted one F-BIDR on its predecessor but at a slight angle to take account of local differences in ground track.

In Fig. 5.12, the swath overlaps are shown to coincide with the ridges in Ghail's DEM. The ridges are more prominent in Herrick's DEM, so the former appears the more robust method, at least in this regard.

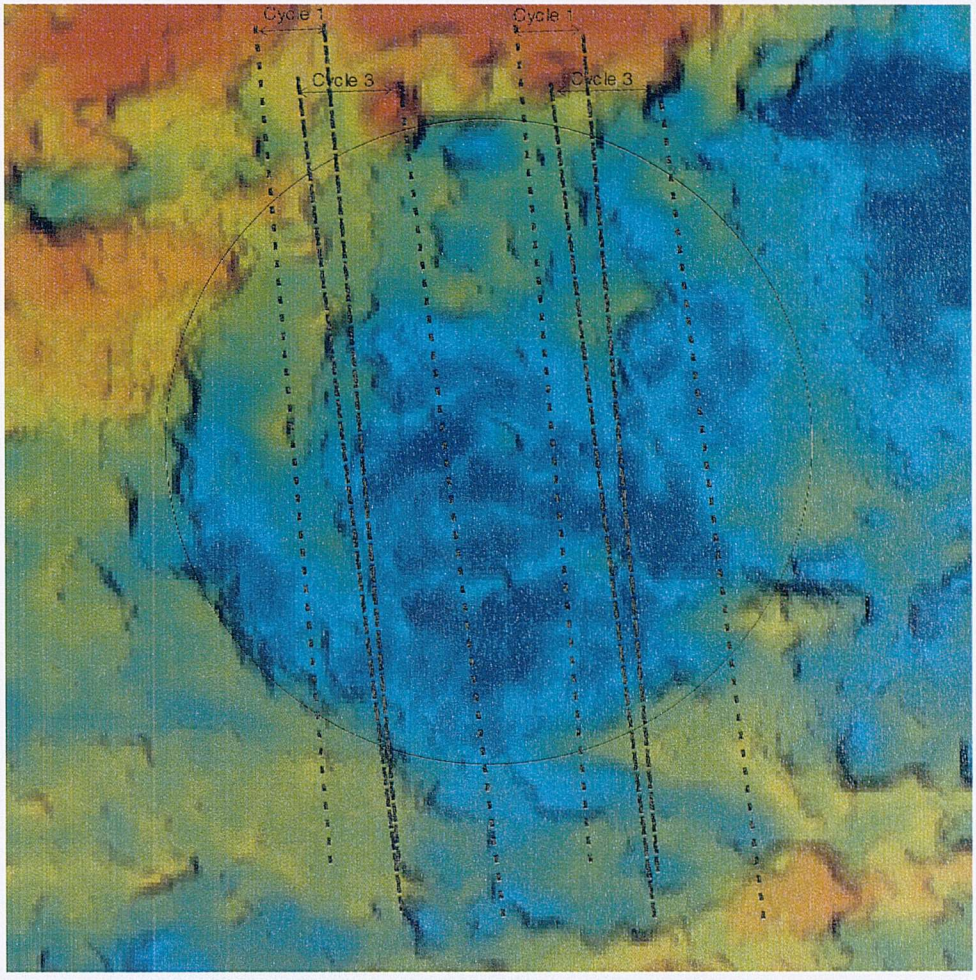


Figure 5.12: Ghail's DEM with swath overlaps superimposed. The mosaicking process produces ridges where there appears to have been insufficient image matching or smoothing.

5.5. *Effects of Subsurface Scattering*

Natural surfaces on Earth are inhomogeneous greater than some scale length, and their dielectric discontinuities give rise to volume scattering, so the SAR does not image only the surface. A considerable body of work has explored this effect for foliage penetration, ice sheet characterisation and subsurface aquafer topography. Figs. 5.13 and 5.14, provide examples of refraction in hyper-arid desert where the effect is especially noticeable.

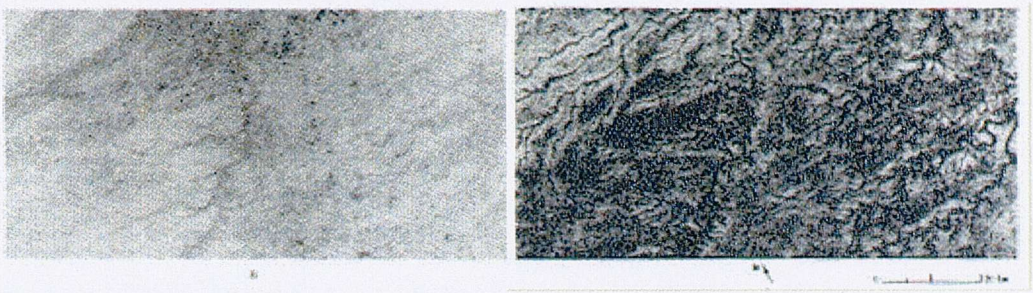


Figure 5.13: Comparison of Landsat and SIR-A images of hyper-arid desert. The Landsat image shows little detail whereas the SIR-A image of the same area shows details of drainage channels. Site inspection found sand (with a relative dielectric constant of $\varepsilon_r = 2.5$) about 2 m deep, above a subsurface layer of bedrock ($\varepsilon_r = 8$). At 12.6 cm, the Magellan wavelength is about half that of SIR-A, hence a similar difference of ε_r in only 1 m of regolith should cause similar effects. From Curlander & McDonough (1991).

Elachi (1988) also reports an experiment with SIR-B, at a wavelength, λ = 23.6 cm, and buried receivers which found 14dBm^{-1} loss in Nevada where the sediment moisture was 3%.

In their section on subsurface imaging, Ford *et al.* (1989) give a maximum depth of subsurface penetration on Earth of 6m at a wavelength, λ = 23.5 cm, and predicted Magellan would penetrate any homogenous layer of particles less than 8mm in diameter to image subsurface discontinuities. They provide no estimate for depth of penetration, x, for Venus but, since it is much dryer, perhaps 10m at λ = 12.6 cm, is likely. The relevant equations are:

Incidence angle after refraction, $\theta_r = \sin^{-1}(\sin\theta / (\varepsilon_r)^{0.5})$ .....(24)

Depth of penetration, $\delta = x \cos\theta_r$ .....(25)

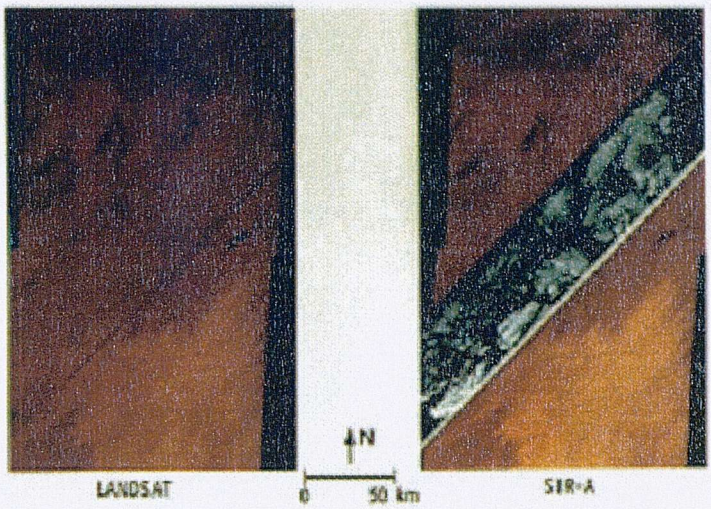


Figure 5.14: Landsat and SIR-A radar images of Egyptian Desert. The left hand image shows an optical image of the same area as in the right hand image, a SAR image with significant texture, over the bland Landsat image. Sediment moisture was less than 1%. The radar signal would be fully scattered in greater depths, so dark-floored craters may be covered in a few metres of fine, homogenous sediment not lava. From Elachi (1988).

Sharpton (1994), Herrick *et al. (1997)* and Herrick & Sharpton (2000) describe the dark crater floors as smooth, flat and probably due to lava rather than chemical weathering. It is not clear why they eliminate sediment. Phillips *et al* (1991 and 1992) attribute dark margins (not crater floors *per se*) to subdued surface roughness. McKinnon *et al.* (1997) endorse this view "because radar albedo reduces with incidence angle", which is not exclusive to lava surfaces.

Ford *et al.* (1993) do not return to subsurface imaging, but give a mean dielectric constant of 4.0 for smooth surfaces on Venus. The peak difference in Cycle 1 and 3 incidence angles (45.6 ^{0} & 25.2 ^{0} respectively, ie 4% maximum difference in the depth of penetration) occurs at 5 ^{0} latitude, and most craters in this study are near to equatorial.

Ulaby (1990) gives, empirically, $\varepsilon_r \sim 1.96^r$, where r = density in g/cm^2, for a variety of terrestrial rocks. Hence, ε_r might approach 2.7, causing a maximum difference in the depth of penetration of 7 %. Where the slope angle of a sediment wedge (e.g. in a crater bottom) is ~ 1^0 it will amplify the effect on dark return width ~ 60 fold. Along track, the SAR resolution was 120 m, so sediment layers of

10 m or more might be detectable in sediments wider than 600 m. Adjacent to the craters in the Sample Area, only one area of sediment was found.

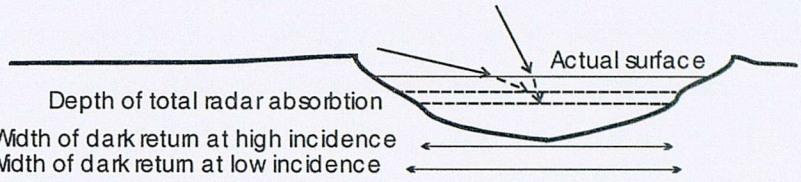
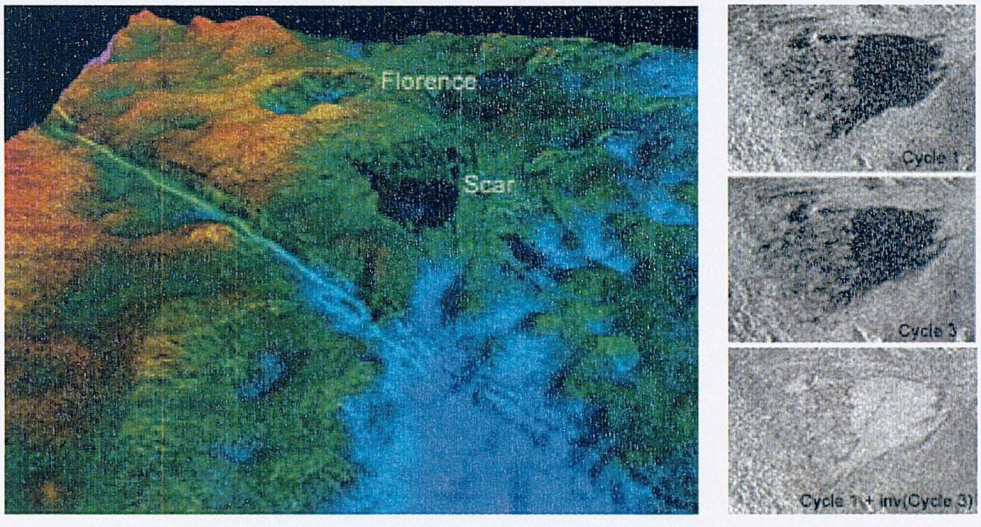


Figure 5.15: Radar penetration depths in fine sediment lying in a crater. A lower incidence signal is fully absorbed at a lower depth of sediment than the higher incidence signal. Since depressions are normally bowl-shaped the greater depth of penetration should be indicated by a narrower dark return in the SAR image.

Adjacent to Florence, an 11 km diameter crater at 15^0S and 85^0E, there is a very dark scar, the Cycle 1 image of which shown in Fig. 5.16(a). Perhaps this is debris, swept eastwards from the crater because the scar is larger in the Cycle 3 image.



(a) 3-D view (b) F-Map extracts

Figure 5.16: Scar adjacent to Florence. The dark scar is very much darker (DN = 68) than any other dark area in the scene. When the Cycle 3 is inverted and added to the Cycle 1 image, as in (b), there is a dark fringe around the scar indicating the difference in size is about 100m on all sides, which lifts East and West edges in the DEM by about the same distance vertically. The transport mechanism may not have terminated as abruptly as the sharp edge of the dark scar indicates, the scar being only that part of the overall deposit deep enough to fully absorb the radar signals. From Cochrane & Ghail (2002).

When a similar technique is used on 2 images of all the dark-floored craters in the Sample Area for which there are 2 images, there is no sign that the dimensions of the dark floor are different, ie no fringe is found around it. Fig. 5.17 illustrates the case of Lullin, with a typical floor darkness (e.g. 100 DN) for a "dark-floored" crater. Tinting the 2 images shows a slightly red-ish tinge around the floor edge but it is consistent with the Cycle 1 returns across the entire floor, i.e. the Cycle 1 image of the floor is generally a little brighter than the cyan-tinted Cycle 3 returns.

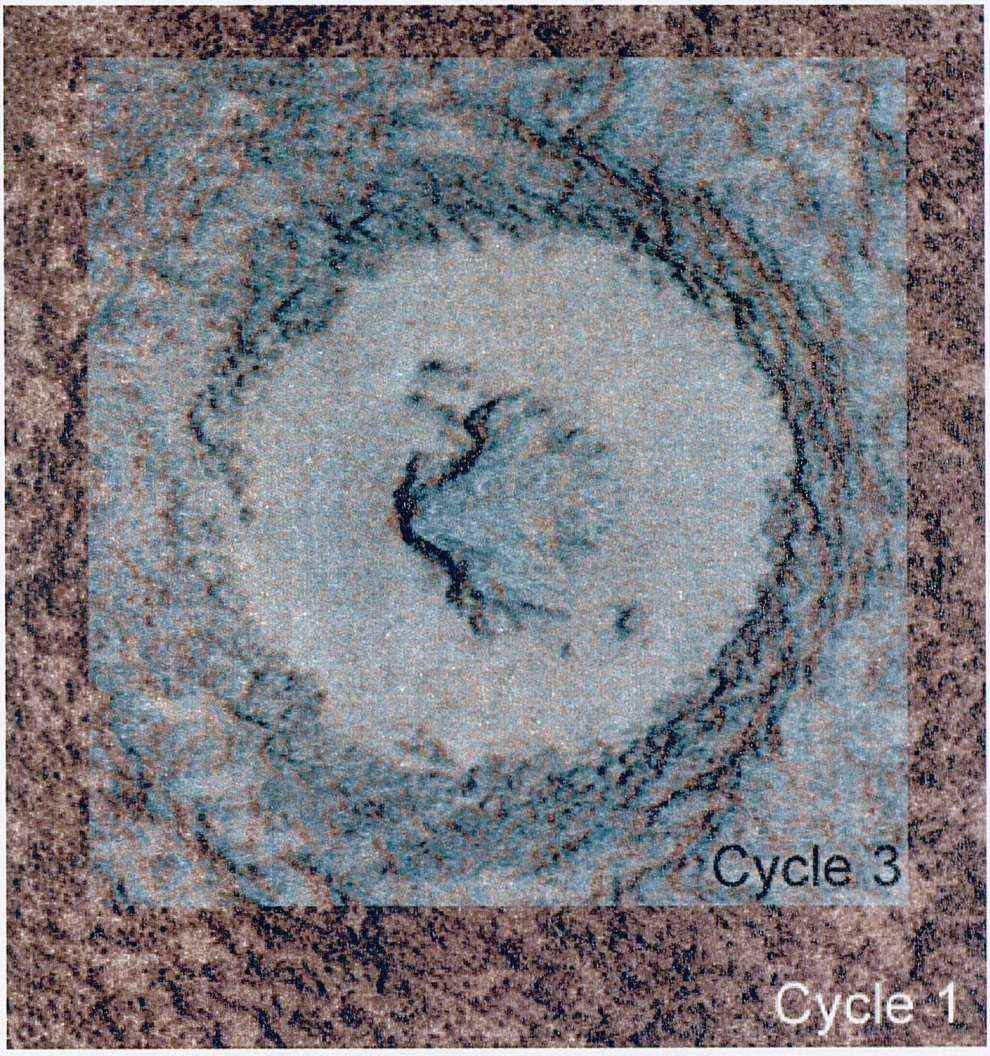


Figure 5.17: Overlaid images of Lullin. When Cycle 1 and Cycle 3 images are tinted and the latter lightened to 50% transparency, there is little evidence that the dark floor has different horizontal dimensions at different incidence angles.

Even in the particular case of Cori, where the dark material appears to be heaped up against the northern rim, as illustrated in Fig. 5.18, no sub-surface scattering was detected.



Figure 5.18: DEM of Cori crater showing dark material on the escarpment. The DEM is viewed from the East with x5 vertical eaggeration. The dark material appears to have been heaped against the northern rim escarpment. However, it is most probably the result of the MST matching process initially failing to track down the Northwestern rim.

5.6. *Effects of Radar Layover*

The Magellan design team chose relatively small Incidence angles to optimise the mapping function but at the price of more radar layover in rugged terrain. Radar layover arises because radar returns are mapped in time, ie according to their slant range. So, the crest of a radar-facing escarpment can appear to lie up range of its foot.

Fig. 5.19 is a Cycle 1 SAR image, coloured by altimetry, of the southwestern edge of Nistigri Corona. Fig. 5.20 shows the F-Map images from all 3 Cycles of 2 pits on the north shoulder of the middle dome, 38 km east of Ruit. Inflexion, in left and right images, of a channel between the pits suggests the surface outside the rim of the larger pit drops by as much as 100 m, and may then rise to the rim of the smaller pit. There are bright cusps on the downrange rim of left and right images and their width varies with incidence, so they must be laid over artifacts. The larger pit is 42 mapping pixels (3.2 km) wide, shown by the white bar above each image.

Each cusp cross-section is colour-coded by this convention in both Figs. 5.20 and 5.21. Fig. 5.21 is a triangulation of green and red artefacts to show the East rim of the large pit falls 700 m at an average angle of 48° to the pit floor. Projecting the blue cusp to that depth gives the West rim the same average angle. If the red cusp were partly or wholly due to normal imaging, it should be moved left and the pit would then be deeper than 700 m. Several pit profiles are consistent but, since cusp edges are brighter down-range than up-range, the rim is most probably sharp-edged and the lower part of the inner escarpment more nearly orthogonal to the radar, with a sharp transition to the floor.

The shape of the cusp flanks may indicate the profile of the inner rim there, if it is uniformly blocky. Altimetry shows the dome rises 367 ± 23 m above its surroundings, so the bottom of the larger pit is at least 300 m below the surrounding plain. We may conclude that the pits probably vented underlying material to form the dome, and may still be active. Any radar layover in the images of Ruit is much less pronounced so its rim escarpment is not as steep as the sides of the pits.

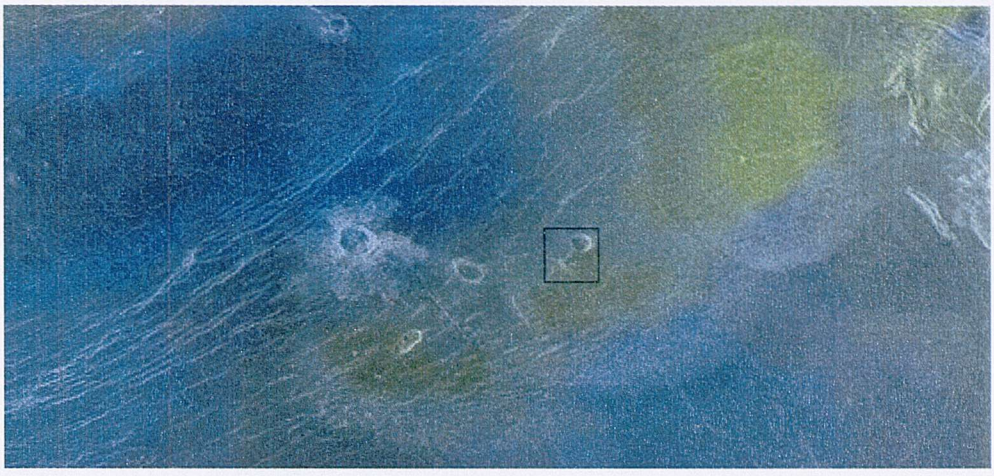
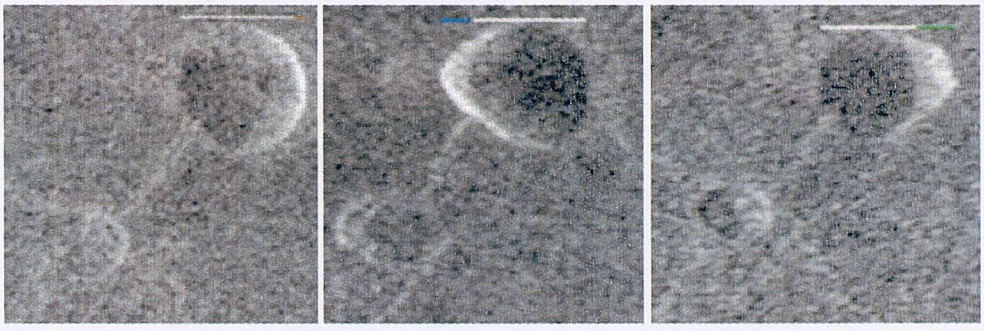


Figure 5.19: Domes with Pits near Ruit crater. The 3 domes form part of the rim of Nistigri Corona; the 6.4 km crater Ruit (26^0S, 73^0E) lies on the outer side of a deep valley or moat running around and inside the rim. Magellan Cycle 1 image colour coded according to altimetry data. The square denotes the context of Fig. 5.20a.



Cycle 1, Left, 35.5° Incidence Cycle 2, Right, 25.1 ° Incidence Cycle 3, Stereo, 18.7 ° Incidence

Figure 5.20: Radar layover artefacts in 3 images of Pits near Ruit crater. Images from all 3 Cycles of 2 pits on the north shoulder of the middle dome 38 km east of Ruit. The down-range cusps are artefacts, of different lengths denoted by the coloured bars at the top. Inflexion, in left and right looking images, of a channel between the pits suggests the surface outside the rims of the pits drops by ~ 100 m. F-Map extracts.

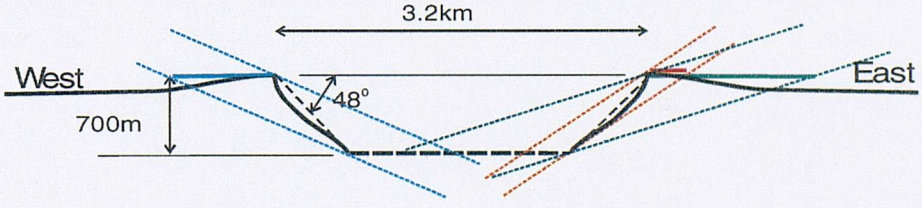


Figure 5.21: Probable cross-section of Larger Pit. Triangulation of the Cycle 1 and 3 artefacts (green and red) show the East rim of the large pit falls 700 m at an average angle of 48° to the pit floor. Projecting the Cycle 2 artefact (blue) gives the West rim the same average angle. Several pit profiles are consistent but, since cusp edges are brighter down-range than up-range, the rim is most probably sharp-edged and the lower part of the inner escarpment more nearly orthogonal to the radar, with a sharp transition to the floor.

In most craters studied for this Thesis, the effects of radar layover in escarpments are much less distinct, partly because of the ejecta field and, maybe, because crater rims are gently rounded.

However, these effects often allow recognition of the presence of a central peak. Fig. 5.22 illustrates the geometry of the layover of a steep central peak in a single image. Here only returns from inside the layover regions are depicted, with green being used to denote image intensity typical of the rest of the image.

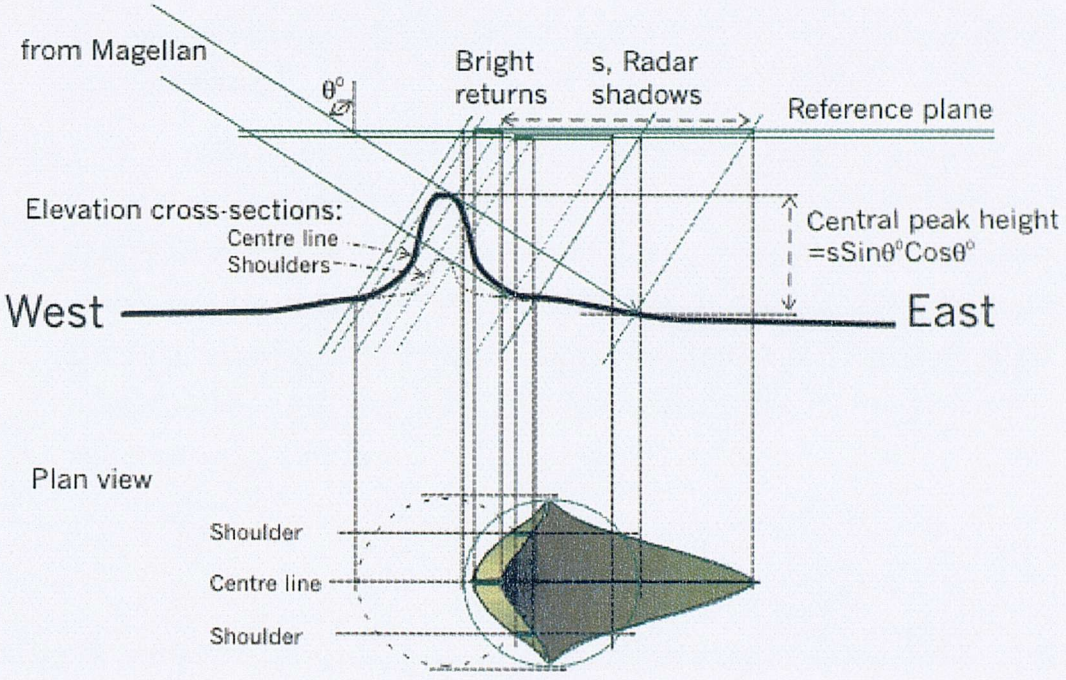


Figure 5.22: Projections of the layover of a Central Peak in a Cycle 1 image. Radar rays from Magellan strike the central peak first on the western face near its top, laying a return on top of that from the floor near its western base. Because the local incidence angle at the top is near zero, this causes a sudden brightness transition in the image. Later returns, from lower down on the western face of the central peak and its top, all appear together. The returns from the western face remain strong, because of the near zero local incidence angle, but those from the top of the peak diminish as the local incidence angle increases to 90° and cut off. In the case of a jagged peak, these latter returns quickly fall to zero, so a sharp brightness transition down range is a sign of such a peak. In general, the shape of the central peak is likely to cause both the elements of the composite signal to cut-off together.

Detailed geometrical analysis shows that, in the case illustrated in Fig. 5.22, the return from the summit of the central peak occurs exactly in the middle of such a bright feature for an incidence angle, θ, of 45^0, and at the leading (western) edge for θ of zero. Following Sharpton (1994), an approximation for the position of the peak, p_{cp}, from the leading edge of the bright return, as a fraction of its length, b, is given by:

$$p_{cp} = \frac{b \tan \theta}{2} \quad \text{.....(26)}$$

The position of this point in the bright return with reference to the rim and floor might be used to determine the height of the central peak but MST does not have the functionality to do so. Rather, it appears that MST may model all central peaks incorrectly.

If it is distinct enough, the down range radar shadow of the central peak could also be used to measure the height of the central peak above the crater floor more directly, as shown in Fig. 5.21. However the shadow is usually indistinct because of radar side lobe returns. A better way is to recognise the cusp shaped artifact in at least 2 images and use the floor offset method to estimate the depth of the summit of the central peak below the reference plane. The relevant geometry is illustrated in Fig. 5.23.

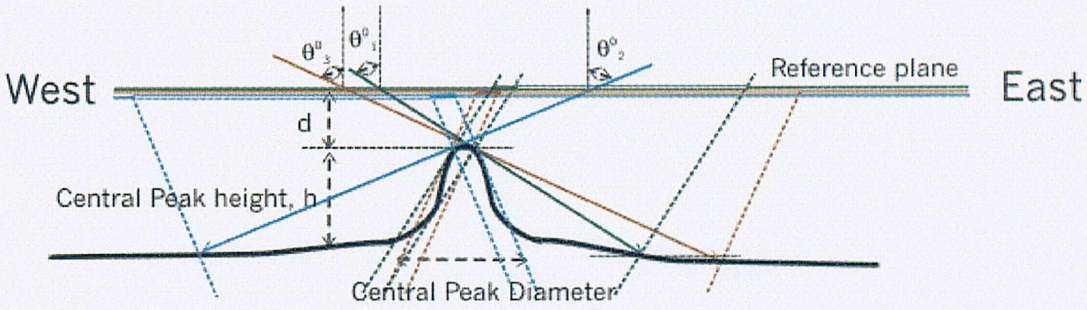
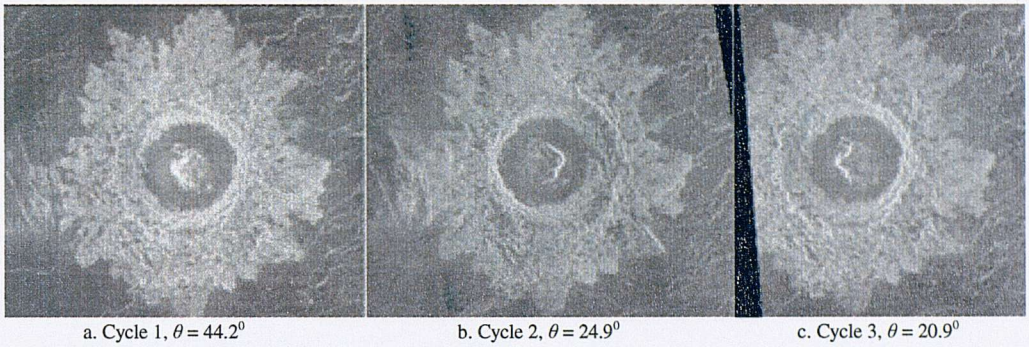


Figure 5.23: Projections of the layover of a Central Peak in 3 images. Similar returns occur from the northern and southern shoulders of the central peak but are displaced further and further down range the further they are from the centre. Such returns give rise to a cusp shaped artefact, with a north-south dimension across the extremes where the local slope presented to the radar is greater than its incidence angle referred to the reference plane. The height of the central peak above these extremes, i.e. its height above its local terrain, is given by the product of the east-west dimension of the cusp and the tangent of the Incidence angle.

In particular, it should be noted that Fig. 5.23 shows that a cusp due to radar layover will reversed in left- and right-looking images, e.g. Lullin, as in Fig. 5.24. This is a readily recognised characteristic, even in marginal cases like Elma, as discussed in Chapter 4. It may be that the ratio of crater diameter to central peak height is a characteristic that can be used to group craters due to single impacts and those due to multiple impacts. Hence, a tool to derive central peak height by this principle could be developed.



a. Cycle 1, $\theta = 44.2^0$ b. Cycle 2, $\theta = 24.9^0$ c. Cycle 3, $\theta = 20.9^0$

Figure 5.24: Examples of the layover of a Central Peak (Lullin). There is little if any layover of the central peak in the Cycle 1 image, indicating its overall slope is less than 44.9^0. In the Cycle 2 and 3 images, the bright cusp pointing towards the radar is a layover artefact.

5.7. *Chapter Summary*

This Chapter has shown that 2 of the 3 types of errors identified by Leberl *et al.* (1992) apply to the DEMs produced for this study. These are described as follows:

Type 1: image pixel mismatch, and

Type 2: finite range resolution.

The 2 types of error have been combined and found to fall within the range of ± 118 to 128 m, for 62 DEMs. This is more than some other authors have estimated. The errors given by MST for specific DEMs in Herrick & Sharpton (2000) are rather larger, so MST most probably suffers from other sources of error.

The effects of multi-looking have been shown to smear the effects of Type 1 errors due to the BAQ code. These increase uncertainty about DEM accuracy rather than the magnitude of its errors.

The effects of mosaicking and resampling on a DEM of Langtry have been illustrated. These can be recognised and ignored where they are found.

A means of identifying sub-surface scattering has been developed that allows an estimate of the minimum depth of sediment lying in a hollow near the crater Florence. All dark-floored craters in the Sample have been checked, and a null result is reported. Hence, it may be concluded that dark crater floor are either due to lava or shallow sediment, and not deep sediments.

Radar layover has been described and its effect on the modelling of central peaks discussed. A possible means of improving the measurement of Central Peaks has been outlined. Chapter 7 includes a proposal to carry such work forward.

Chapter 6

Geological Implications of the Models

The Sample Area definition allows the DEMs to be considered as broadly representative of the planetary crater population, and in their geological context. This Chapter examines the geological implications of the set of 62 DEMs produced in this study.

6.1. Crater Morphology

Chapter 5 estimated that vertical DEM errors are in the order of ± 125 m, at 1 sigma confidence. Three of the 62 DEMs produced for this study, listed in Table 6.1, are shallower than this error estimate.

Colour Key: Green = Cycles 1, 2&3 Blue = Cycles 1 & 3 Red = Cycles 1 & 2 Black = 1 Cycle only	Latitude	Longitude	Rim Diameter	Rim-Floor Ht	1 sigma Ht Error in DEM
Name	°Lat	°Long	m	m	m
Georgina	-20.4	58.8	7.3	74	118
Teumere	-38.3	88.1	7.0	83	124
CraterE	39.2	53.2	5.9	75	127

Table 6.1: Shallow Crater Parameters. The shallowest 3 DEMs all have a depth less than their 1 sigma height error. These DEMs are set aside in further trend analyses.

Crater E was excluded from Fig. 3.15 as it is not classed as Knobby Base. When Georgina and Teumere are also excluded, the measured depth:Diameter trends become as in Fig. 6.1. This difference does not significantly undermine the this Thesis which is that the largest morphological class of crater on Venus, called "Knobby Base" in the LPI database, has a Rim Diameter to Rim-floor depth trend that lies parallel to that for Simple craters.

Such a populous class merits more explanation that is currently provided in textbooks, eg Melosh (1989), Beatty et al (1999), de Pater & Lissauer (2001), and Norton (2002). This Thesis is that Knobby Base craters are the result of bolide disintegration and dispersion in the atmosphere, and possibly atmospheric entrainment. A simple formulation supports the suggestion that a "pancaked" bolide gives rise to a well-distributed set of "Simple" impacts, preserving the trend slope characteristic of Simple impacts until the impulse delivered exceeds the fluidization threashold for "Complex" crater formation at a final crater diameter of between 12 and 18 km.

Also, DEMs for larger craters (i.e. those classified by the LPI as Multiple Peak, Peak Ring, or Multi-ring) tend to a depth of about 1 km, irrespective of diameter. Herrick & Sharpton (1996) observe that the depth of Mead must have

been reduced, post-impact, by basin cooling and viscous relaxation of topography.

The diameters of all craters of other classes in the LPI taxonomy – "Bowl" and "Flat floored" - are small.

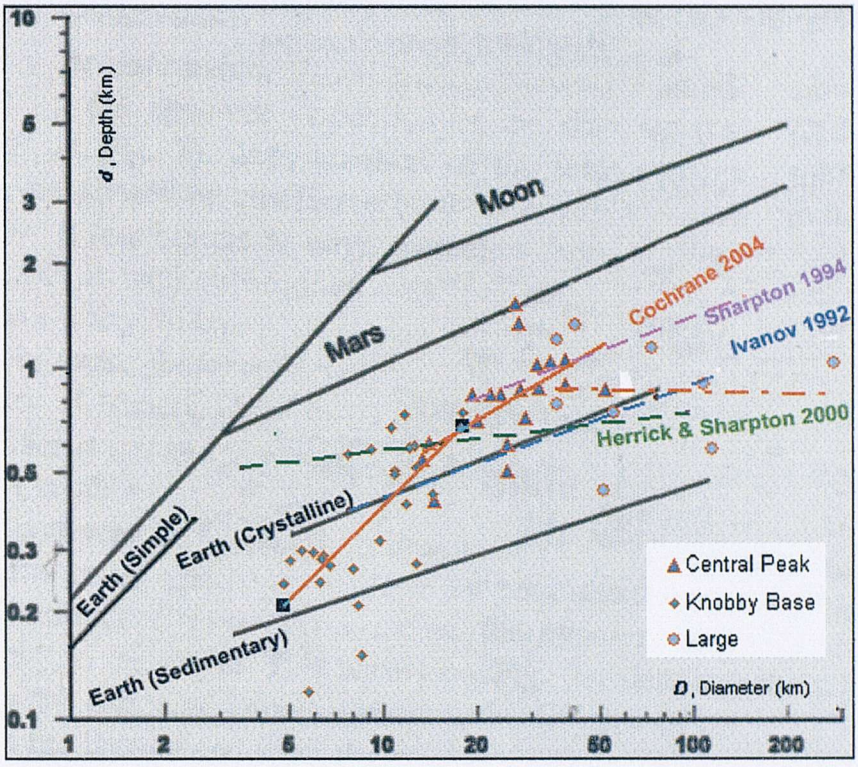


Figure 6.1: Depth/diameter trends for the 56 DEMs with significant depth. After removal of Georgina and Teumere, the trend for the 27 Knobby base craters is changed, from, $d_{KB} = 0.10D^{0.89}$ with $R^2 = 0.39$, as in Fig 3.15,to $d_{KB} = 0.11D^{0.89}$ with $R^2 = 0.47$. The trend for the 19 Central Peak craters remains: $d_{CP} = 3.8D^{0.53}$, with $R^2 = 0.34$.

The remaining topographical class, Central peak craters, might be expected to have escaped post-impact modification in sufficient numbers to preserve classical scaling and support reliable measurement. Here again, the slope of the trend is not in accord with theory perhaps because, at smaller diameters, this class merges into the Knobby Base class and, at larger diameters, whatever limits the depth of large craters begins to have effect. Such merging might reflect the fact that the underlying physics does not cause a sharp transition or because of poor recognition of the 2 classes when the LPI database was compiled. There is some evidence that both effects apply, so the Central peak craters with larger diameters

may demonstrate a more reliable depth:Diameter ratio. Here, the DEMs are as deep as found by Sharpton (1994), who identified the following 6 possible causes:

(i) Enhanced target strength on Venus, possibly related to low volatile content, reducing the efficiency of crater collapse;

(ii) More efficient or deeper excavation on Venus, possibly reflecting rheological effects of the hot Venusian environment;

(iii) More melting and efficient removal of melt from the crater cavity;

(iv) Enhanced ejection of material out of the cavity, possibly as a result of entrainment in an atmosphere set in motion by the passage of the projectile;

(v) Enhanced rim pile-up possibly due to atmospheric deceleration of ballistic ejecta; or

(vi) Atmospheric retardation of lateral growth of the excavation cavity, eg Shultz (1992).

The DEMs produced during this research will allow further investigation of these possible causes. In the meantime, if it can be concluded that sub-para (i) above applies to some extent, then the terrain around and across western Ovda Regio consists of stronger materials than are prevalent near the surfaces of other terrestrial planets. So far as the suggestion in Garvin (1990) is concerned, there appears to be no evidence of a megaregolith on Venus.

6.2. Age of the Cratered Surface

Chapter 3 shows a 10% underestimate of crater diameter. A typical DEM diameter rests on many measurements around the rim. Typically, crater rims on Venus have been found to have gently rounded mean profiles but with sufficiently jagged excursions to suggest an absence of rim weathering, even over 100s of Ma. These should be compared to the profiles of lunar craters to ensure the validity of crater age metrics.

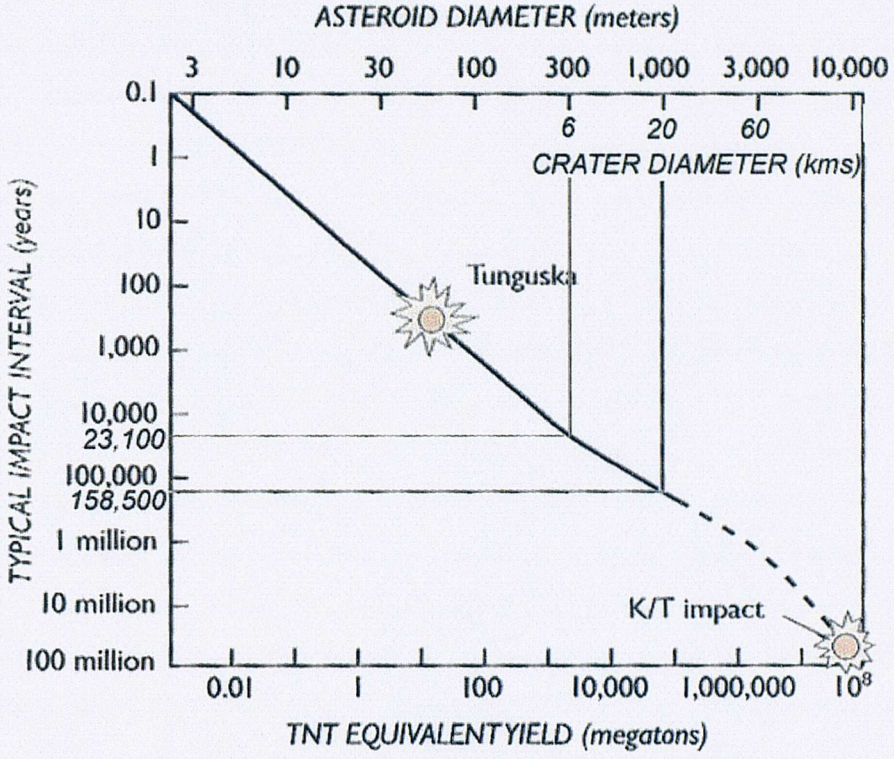


Figure 6.2: Trend for terrestrial impact frequency. Graph from Shoemaker & Shoemaker (1999). The data for impactors larger than 1 km is controversial. A constant ratio of 20 may be taken from French (1998) for impactor to crater diameter. Thus, a 3.3 fold increase in crater diameter from 6 to 20 is associated with a 6.9 fold increase in impact interval.

Fig. 6.2 is based on a graph of estimated impact intervals against impactor diameter provided by Shoemaker & Shoemaker (1999). French (1998) takes crater diameter to be 20 times the latter, and Fig 6.2 is marked up accordingly. It shows that a 10% increase in crater diameter is associated with a ~20% increase

in the estimated age of the cratered surface. MacKinnon *et al.* (1997), perhaps the most authoritative analysis of cratered surface age to date, estimated that the atmosphere of Venus had reduced the crater production population by a factor of ~ 3 at crater diameters of ~30km, and ~ 6 at ~ 20 km. They derived a nominal age for the cratered surface of ~700 to 800 Ma i.e. up to 3 times older than earlier estimates. Hence, the observed DEM diameters might increase the estimated surface age of Venus to 900 Ma.

However, MacKinnon *et al.* (1997) also accepted the crater depth/diameter ratios in Sharpton (1994) as "fitting comfortably" within the $1/g$ scaled populations of the Moon and Mercury. In concluding that "the dense atmosphere does not change the main morphologic relations for complex craters", they appear not to have considered the possibility that bolide fragments would separate far enough yet retain sufficient momentum that the impact area would become comparable to the final crater area. Hence it may be assumed that deficiencies of intermediate sized craters, noted to be associated with reduction not elimination of impacting comets, were modelled as resulting only from momentum loss rather than from both momentum loss and dispersion. Now, both the results presented here and in Herrick & Sharpton (2000) show shallower crater depth/diameter ratios than in Sharpton (1994). Therefore, MacKinnon *et al.* (1997) may have overestimated the nominal age for the cratered surface of Venus. Fig. 6.3 illustrates how the atmosphere might serve to increase the observed proportion of 3 – 5 km diameter craters, by spreading more than slowing the smallest bolides as well as slowing more than spreading mid-sized bolides. Only a small effect is necessary to improve the fit of their simulated profile to that observed. However, the effect might allow more extreme simulations to be fitted to the higher diameter curves yet also match the lower diameters, e.g. to give a younger surface age.

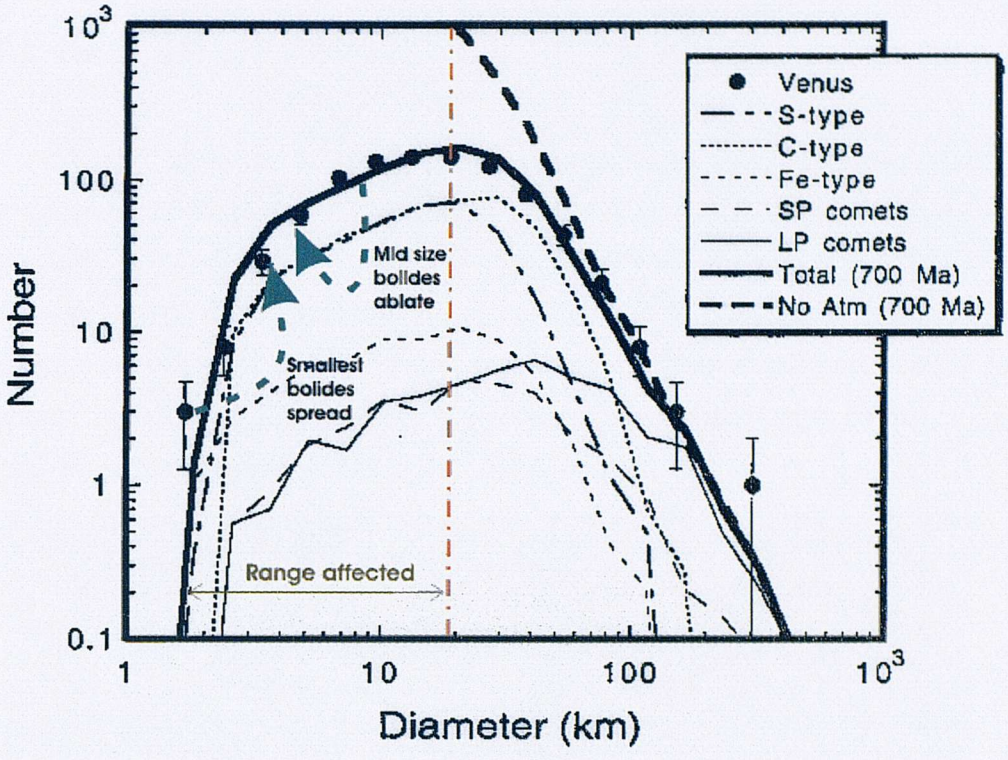


Figure 6.3: Effect of pancaking on the simulated age of the cratered surface of Venus. Results from MacKinnon *et al.* (1997) in black, concerning a population of 940 craters, a surface age of 700 Mr and using the impactor populations from Shoemaker *et al.* (1990, 1994). Pancaking may produce Knobby Base craters up to 18.5 km diameter (orange line), about 53.4% of the population. Pancaking of both the smallest and the mid-sized bolides may reduce the simulated excesses of the smallest and the mid-sized craters and produce the observed population of 3 – 5 km diameter craters.

6.3. The Shape of Manzolini

The LPI database describes Manzolini as a peak ring crater with a rim diameter of 43.7km. As illustrated in Fig. 6.3, it lies at 25.7°N and 91.3°E on the southern fringe of Shimti Tessera, perhaps where Niobe Planitia abuts Tellus Tessera. Eurynome Corona, immediately to the East of Manzolini, and Metra Corona beyond, suggests that the region is, or was, volcanically active. The terrain around Manzolini averages 170 m below the planetary mean radius, i.e. may have been affected by some sort of down-welling.

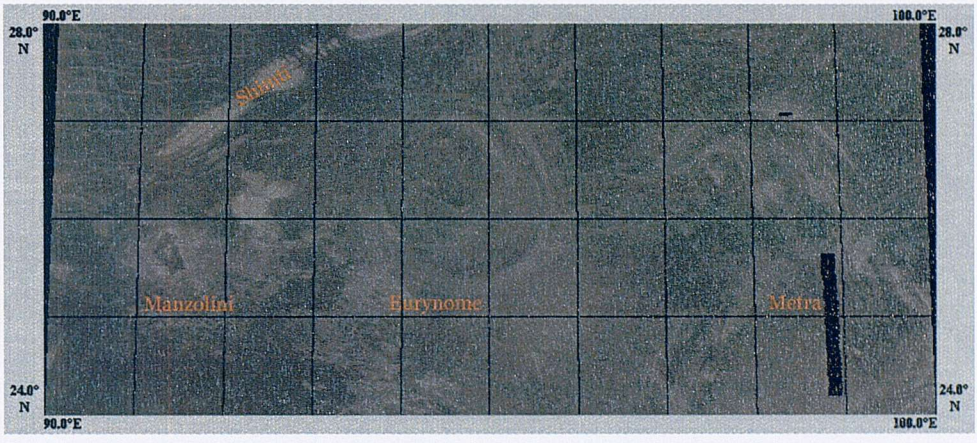


Figure 6.4: Vicinity of Manzolini. PDS download of Cycle 1 image mosaic, with latitude and longitude lines at 1^0 intervals, is 10^o of longitude (1055 km) by 4^o of latitude (388 km). Manzolini lies at the end of Shimti Tessera, which may be a major compression feature between Niobe Planitia to the south and east, and Tellus Tessera to the north and west. Manzolini lies 170 m below the planetary mean, possibly due to down-welling. Also, Euronome and Metra Coronas to the east denote some volcanic activity is or was involved. Manzolini has a very dark floor (DN: 74), which looks elliptical. It is surrounded by similar material (DN: 78). The LPI database shows it has a central peak of 9.6km diameter and a lava flow to the east and north of 139km length.

Fig. 6.5 shows the actual rim peaks picked out on an ortho-rectified image of Manzolini. A best fit circle shows that the rim is by no means as elliptical as the dark floor makes it look, and that the crater rim diameter is much larger (53.9 km) than listed by either LPI (43.7 km) or USGS (41.8 km). Fig. 6.6 provides a visualisation of the DEM.

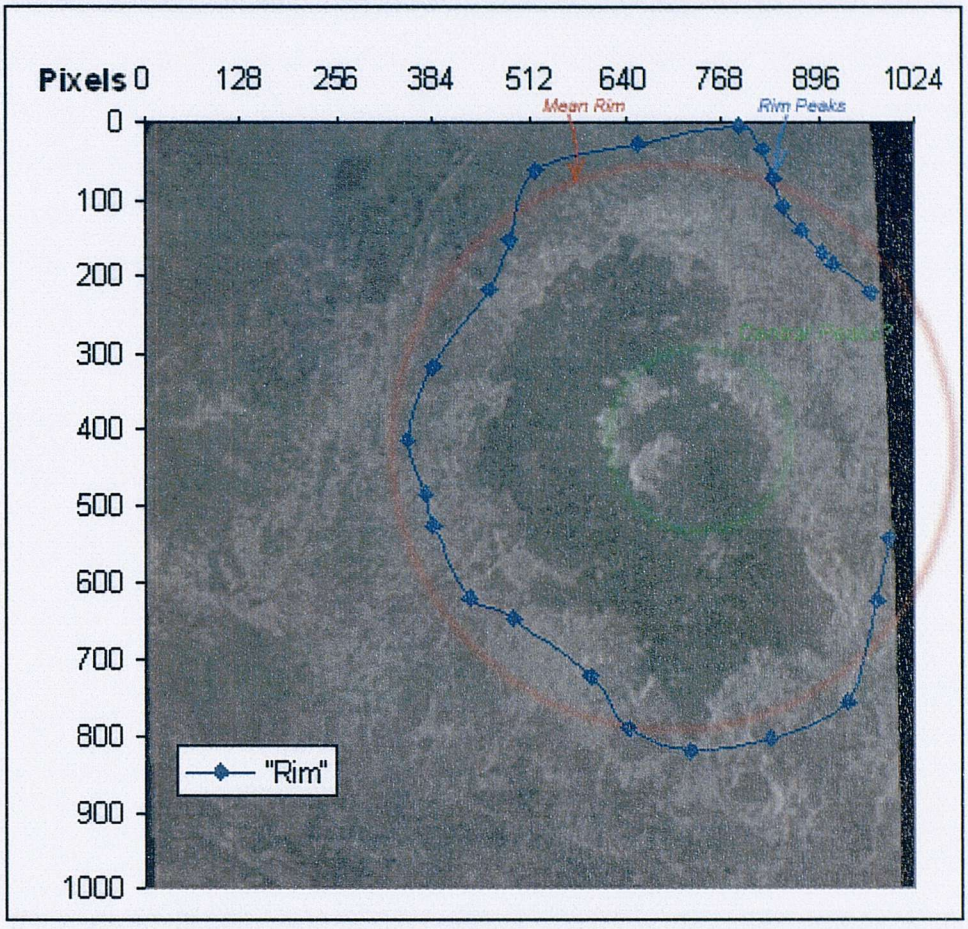


Figure 6.5: The Rim of Manzolini. The peaks on the rim of Manzolini are marked as blue squares; the blue line linking them is pinched in at 4 points. The rim diameter is taken to be the red circle. The rim is clearly much less distorted than the elliptical dark floor suggests. The central peaks lie close to the green circle but do not form a peak ring.

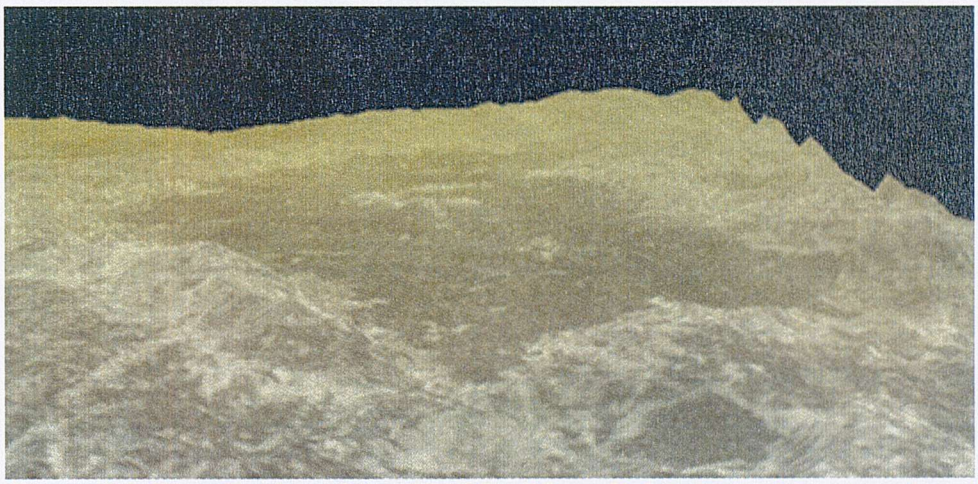
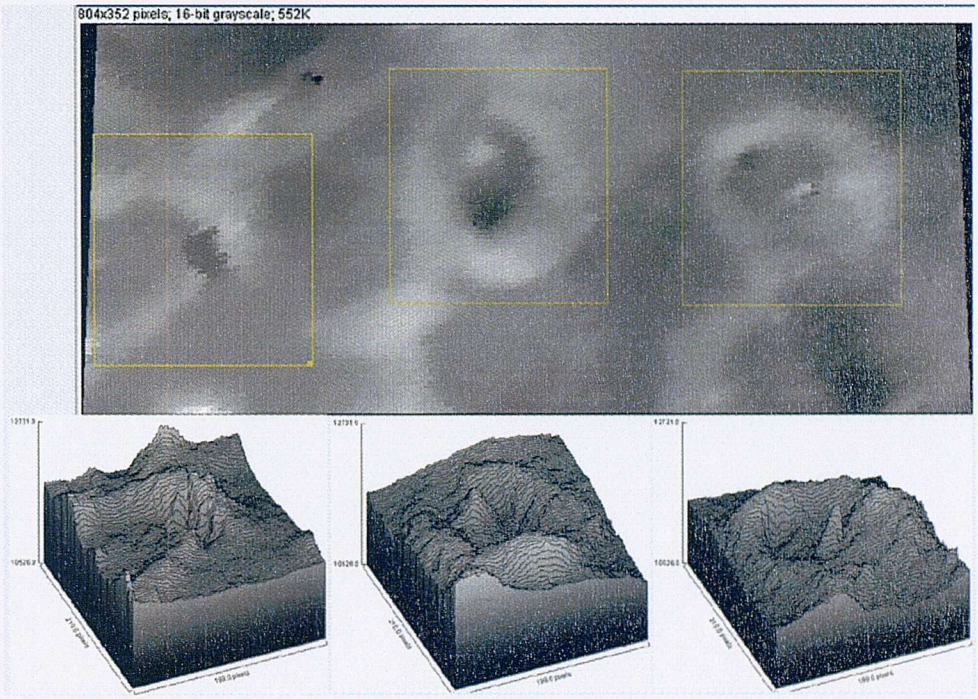


Figure 6.6: Visualisation of the DEM for Manzolini. In ERDAS Imagine, viewed from the south without vertical exaggeration. Yellow fog has been added to provide more sense of depth. The terrain rises steeply from the dark floor, especially to the East.

Fig. 6.7 shows the altimetry topographic surface in the region of Manzolini contains an extensive arcuate ridge feature as well as the crater. The crater lies on the inner edge of this ridge, and comparison of the sizes of the 2 features suggests that the impact occurred after the ridge formed. This arcuate feature is neither circular or complete but is otherwise not unlike the adjacent coronae to the East. If the arcuate ridge is an emergent corona, then the approximately even spacing of the 3 coronae suggests that there was steady movement of the crust over a hot spot in the mantle. Contrary to Stofan *et a.l* (1992), this may be evidence of systematic systematic variation of age along a chain of coronae.



a. Mazolini b. Eurynome c. Metra

Figure 6.7: Topography in the Region of Manzolini and adjacent Coronae. The region shown lies mainly east of Manzolini. Identical to that in Fig 6.4, it measures 10^{o} of longitude (1055 km) by 4^{o} of latitude (388 km). Yellow quadrilaterals on the upper altimetry grayscale show areas for which the altimetry is shown in wireframe models below. The darkest region of the altimetry greyscale is Manzolini's floor; the crater's shape suggests it formed after an arcuate ridge, not dissimilar to the outer features of adjacent coronae. The asymmetrical dark floor of the crater suggests that the arcuate ridge continued to evolve after crater formation.

Fig. 6.8, an East-West profile through the DEM, shows that the crater floor is inclined, with the dark floor in the western half about 300 m below the brighter floor on the other side of what might be a central peak ring. If the arcuate ridge is

of volcanic origin, it may have been the source of the unusually dark material on the floor of the crater and beyond its rim.

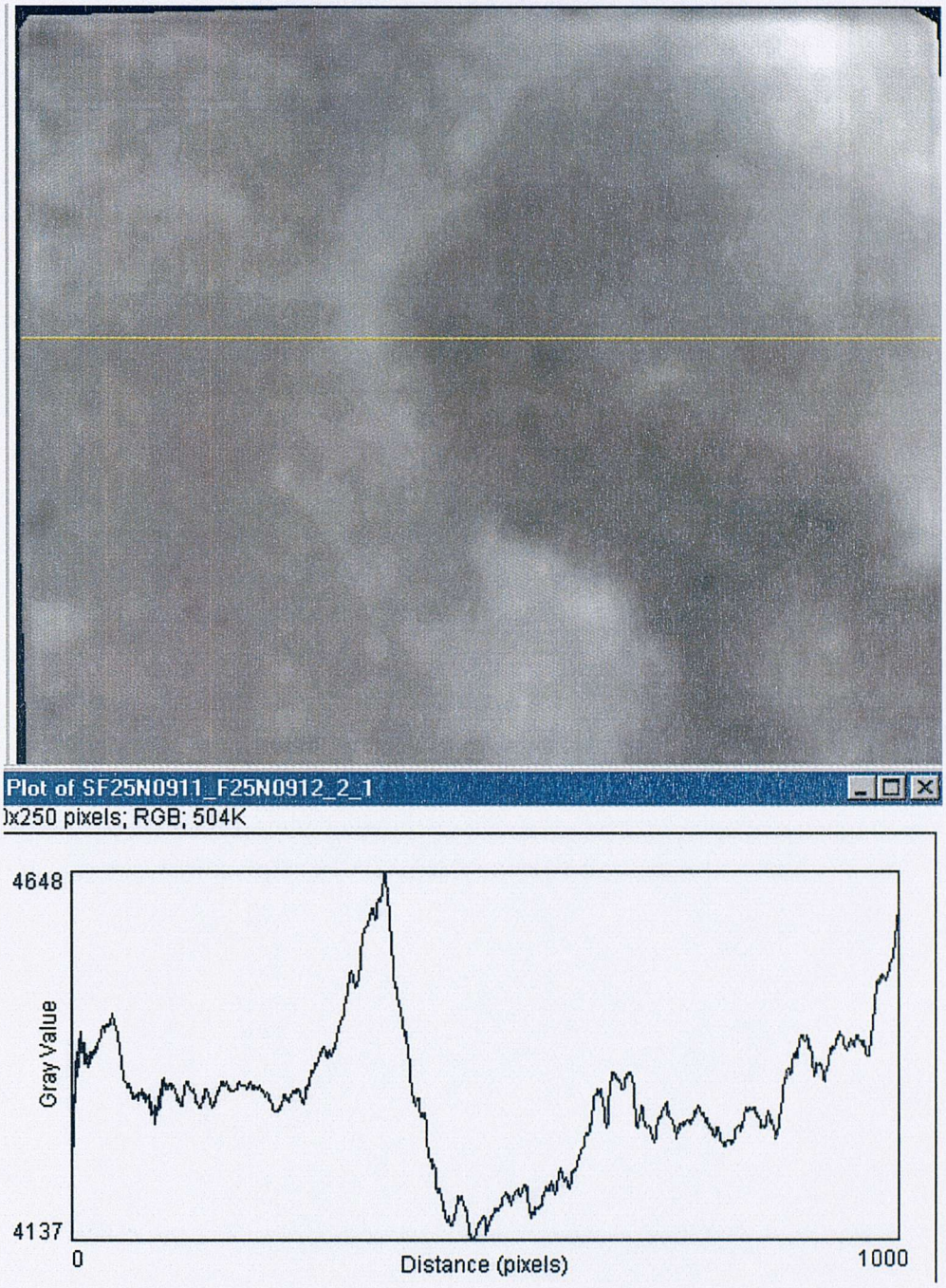


Figure 6.8: East-West profile through the DEM of Manzolini. A missing swath in the Cycle 3 image prevented modelling of the eastern crater rim and the high ground beyond. It is possible to pick out 2 prominences which may be part of a central peak ring. The western floor is perhaps 300m below that to the East, suggesting that the arcuate ridge formation may have tilted the crater since its formation and that the dark material remained relatively fluid for some time.

6.4. Radar-bright arc around Mead

Beyond the 510 km diameter dark halo around Mead lies a greyer surface, mainly to the south and west, with few sharp features. As shown in Fig 6.9, it is hard to recognise because it contains some geological features and is marred by the "venetian blind" radar artefact in the South and East. The nature of this grey surface may be revealed by the craters on it. Fig. 6.10 shows the 2 images of Kuro, compared to the equivalent images of its nearly identical twin, Florence, in Fig. 6.11. Florence has more features that are radar bright (i.e. jagged) than Kuro

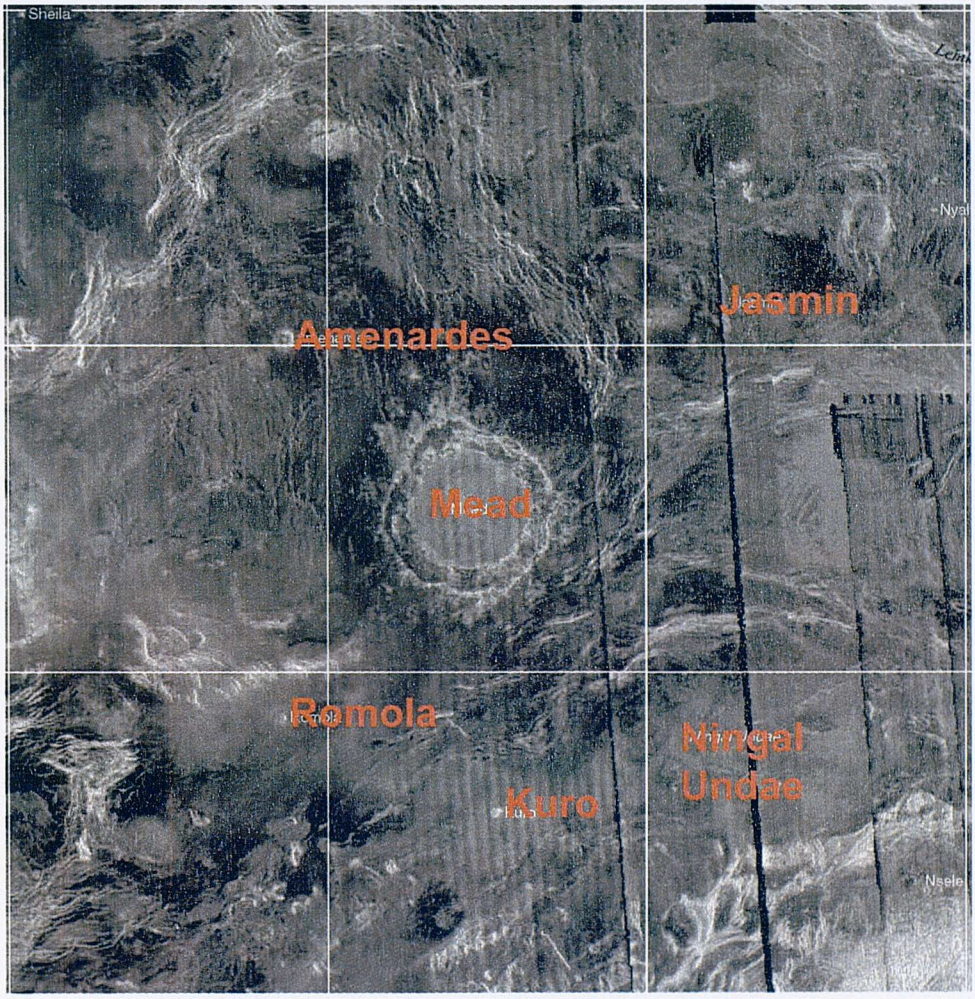
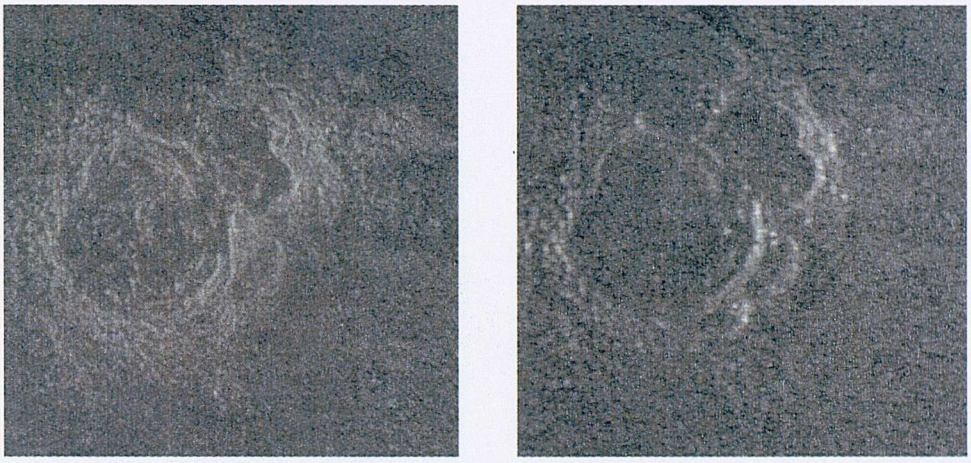


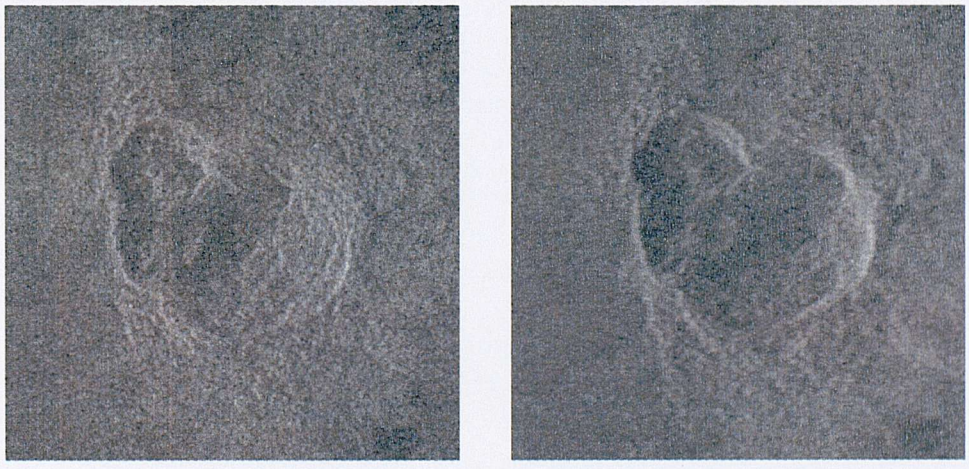
Figure 6.9: Radar-bright Arc southwest of Mead. The arc can be traced from Kuro through Romola but becomes more diffuse to the west of Mead. Amenardes has its own dark ring but may also have been emplaced on the bright arc. To the east of Kuro, the bright arc may terminate as Ningal Undae. Each square is 5° of longitude (528 km) by 5° of latitude (516 km). PDS download of Cycle 1 imagery.

even though it was imaged with about 15% greater resolution. Particularly in the Cycle 3 image, parts of Kuro's rim look unusually smooth albeit with higher contrast. Also, although both craters have similar sized ejecta blankets, that of Kuro has less contrast against its surroundings than that at Florence. This may suggest that the grey surface material south west of Mead is less brittle than the rock on which Florence lies, or that Kuro is the older and more weathered crater.



a. Cycle 1, $\theta = 45.9^0$ b. Cycle 3, $\theta = 25.4^0$

Figure 6.10: Images of Kuro. A 13 km diameter, 617 m deep multiple crater at 7.8^0N, 57.6^0E, 252 m below the planetary mean radius and, a continuous ejecta radius of 6.6 km from the rim. Kuro was imaged in Cycle 1 at a slant range of 412 km and 123 m ground range resolution; in Cycle 3 at a slant range of 295 km and 221 m resolution.



a. Cycle 1, $\theta = 40.4^0$ b. Cycle 3, $\theta = 21.3^0$

Figure 6.11: Images of Florence. A 13.3 km diameter, 621 m deep, multiple crater at 15.3^0S, 85^0E, and 1050 m above the planetary mean radius on the southern fringes of Ovda Regio. It has a continuous ejecta radius of 13.5 km from the rim. Florence was imaged in Cycle 1 at a slant range of 592 km and 137 m ground range resolution; in Cycle 3 at a slant range of 476 km and 259 m resolution.

As illustrated in Fig. 6.12, Romola lies on the brightest section of the grey arc, in the middle of a bland plain. Magellan provided only one image of Romola, and that is incomplete. Fig. 6.13 shows Romola to have no clear ejecta, rim, floor or central features and be less distinct than Kuro. Yet here, at the latitude of periapsis, the ground range resolution is at its finest. The LPI database classifies Romola as having a central peak, perhaps because there is a circular feature, which might be construed as a dark floor, around a bright prominence, which might be construed as a central peak. This study considers this feature to be too small and too far from the centre of the crater to be floor and peak. Instead, it considers Romola to be due to a multiple impact.

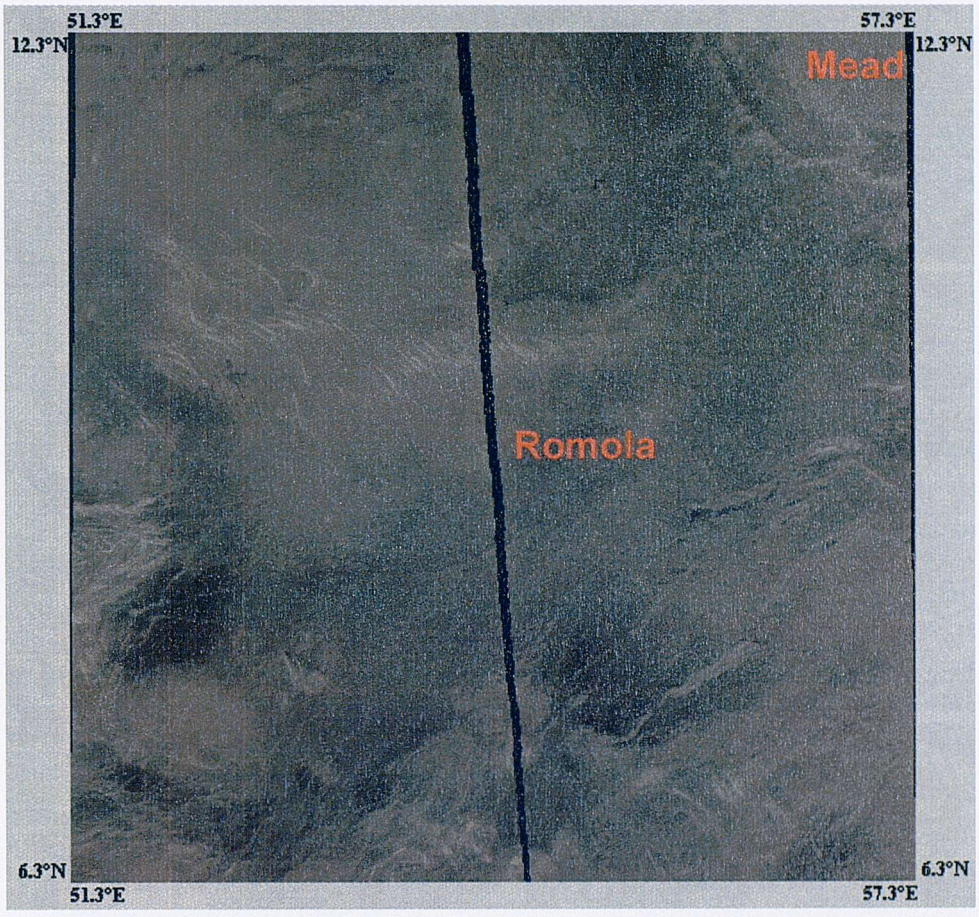


Figure 6.12: Region of Romola. The plain contains only one feature within 200km of Romola: a low ridge with many parallel striations which are approximately radial to Mead. PDS download of Cycle 1 mosaic.

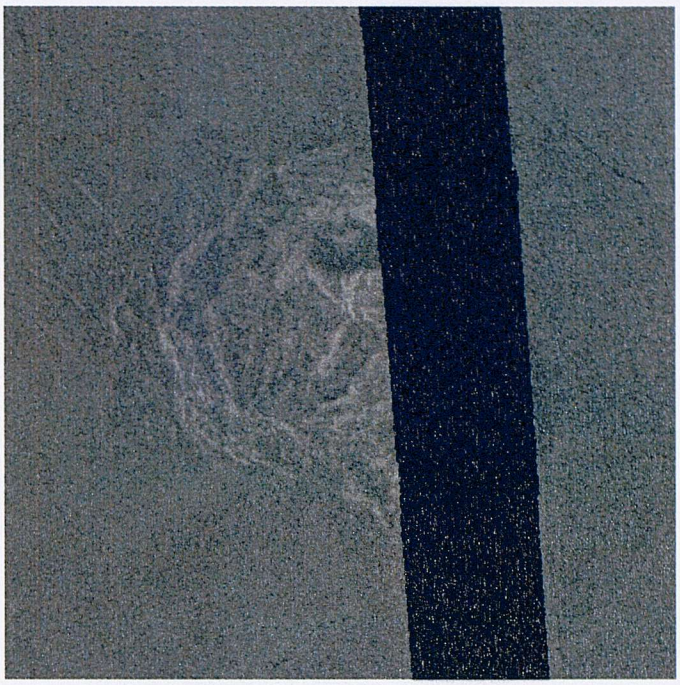


Figure 6.13: Image of Romola. A 19.1 km (LPI) or 17.5 km (USGS) diameter, multiple crater of uncertain depth at 9.3^{0}N, 54.3^{0}E, 126 m above the planetary mean radius and virtually no ejecta. Romola was imaged in Cycle 1 at 45.9^0 incidence and a slant range of 412 km.

There are 2 other candidates that lie as close to Mead as Kuro and Romola but do not lie on the grey arc: Jasmin and Amenardes.

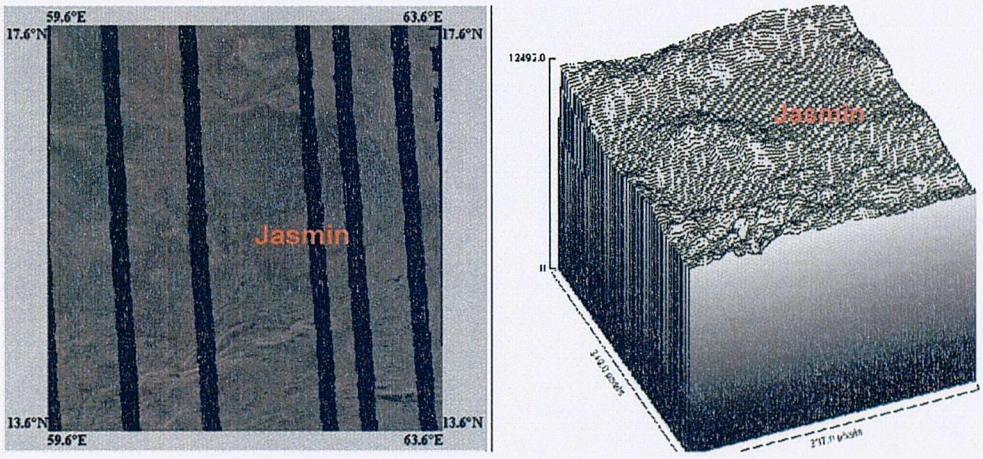


Figure 6.14: Region of Jasmin. On the left is a PDS mosaic of C3 images. On the right is a PDS download of altimetry of the same area as a surface plot, at 88 m per pixel. The SAR imagery shows Jasmin lies on an almost featureless plain but the altimetry shows it has 2 basins either side of it. The western basin is strikingly circular, and may be corona-like. Near Jasmin there are several, similar-sized pits, with sinuous channels. These may be evidences of vulcanism.

As Fig. 6.14 illustrates, Jasmin has no ejecta and lies on grainy-textured material, similar to that around Romola but with several wrinkle ridges. Our only image of Jasmin is Fig. 6.15, and captured during Cycle 3. It shows Jasmin is deep, circular and has what looks like a central peak. However, since there is evidence of vulcanism in the region, it might well be a caldera with an unusially shaped central pit. Being complete, this image does permit depth calculations by floor and peak offsets. These indicate that Jasmin, if symmetrical, is at least 2 km deep and very steep-sided. This is about twice as deep as other craters in the Sample of similar diameter, so the surface material here must be unusually volatile and tough, or Jasmin is a caldera. Whatever its true origin, parts of Jasmin's rim look unusually smooth, and like Kuro's in its Cycle 3 image.

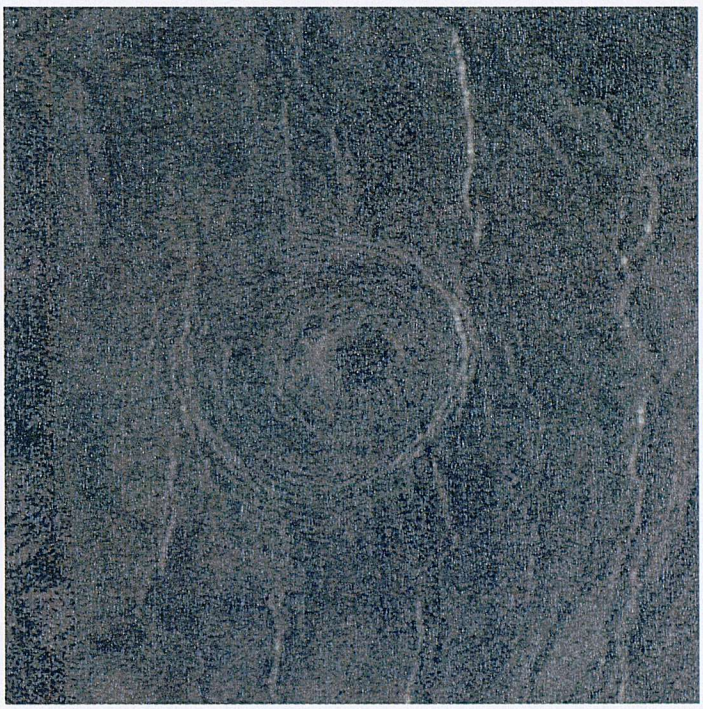
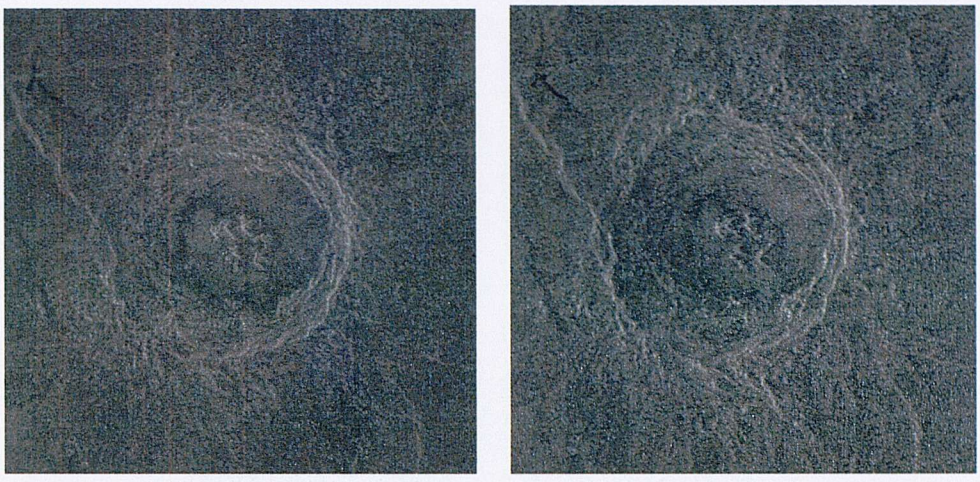


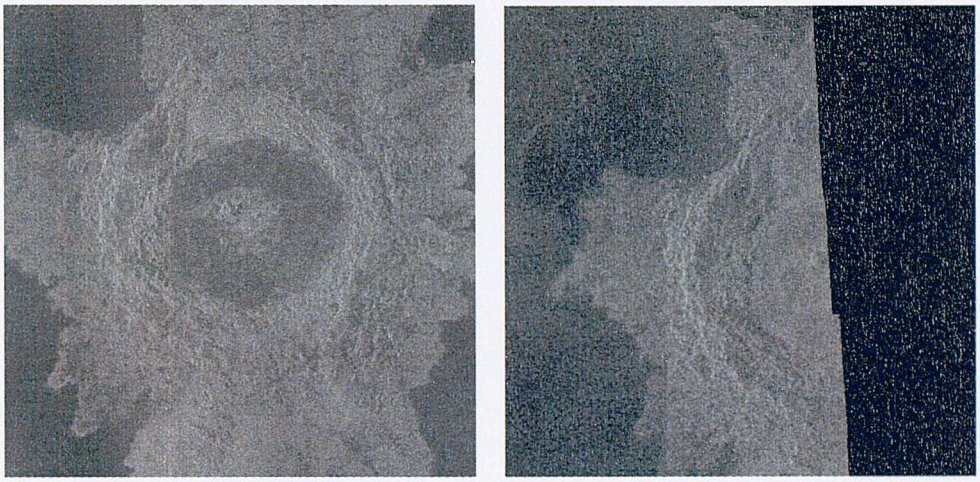
Figure 6.15: Image of Jasmin. A 15.6 km diameter feature of about 2 km depth at 15.6 ^{0}N, 61.6^{0}E, with virtually no ejecta. Jasmin was imaged in Cycle 3 at 25.6^{0} incidence, 217 m ground range resolution and a slant range of 300 km.

Fig. 6.16 shows 2 images of Amenardes for comparison to Adivar, in Fig. 6.17, which is similar in diameter, depth, altitude and imaging parameters. The western escarpment of Adivar has sharper features than the western escarpment of Amenardes, even though it is at the same resolution and distance from the radar. Also, Amenardes has much more ejecta than Adivar. It is concluded that the bright arc may be of softer material than Ahktamar Planitia where Adivar lies.



a. Cycle 1, $\theta = 45.6^0$ b. Cycle 3, $\theta = 25.6^0$

Figure 6.16: Images of Amenardes. A 29.8 km diameter, 743 m deep multiple crater at 15^0N, 54.3^0E, 323 m below the planetary mean radius and with a continuous ejecta radius of 19.4 km from the rim. Amenardes was imaged in Cycle 1 at 124 m ground range resolution and a slant range of 421 km, and in Cycle 3 and 217 m ground range resolution at a slant range of 300 km.

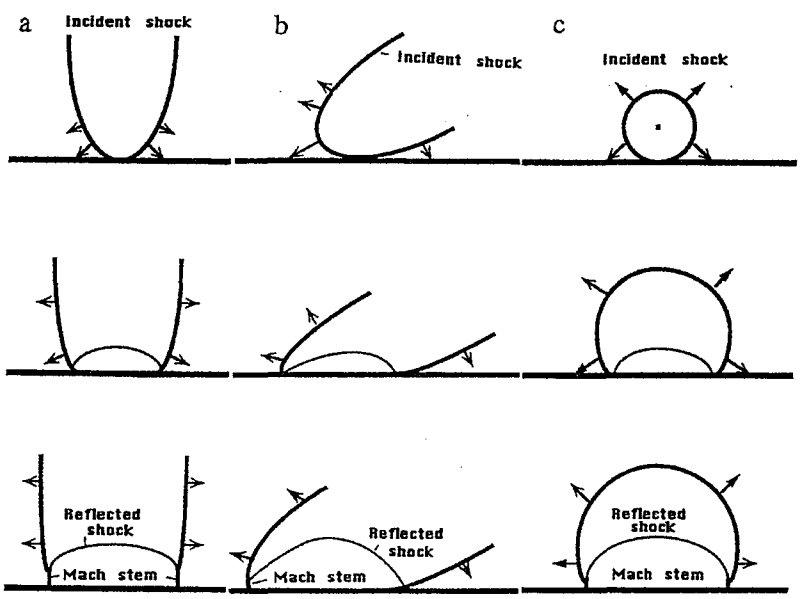


a. Cycle 1, $\theta = 45.9^0$ b. Cycle 3, $\theta = 25.5^0$

Figure 6.17: Images of Adivar. A 28.7 km diameter, 893 m deep multiple crater at 8.9^0N, 76.2^0E, 76 m below the planetary mean radius, with a continuous ejecta radius of 27.1 km from the rim. Adivar was imaged in Cycle 1 at 123 m ground range resolution and a slant range of 405 km, and in Cycle 3 at 220 m ground range resolution and a slant range of 293 km.

If Mead is assumed to be the most recent impact, these observations - that all 4 smaller craters are deficient of bright ejecta and 2 have unusually smooth rim features - support the descriptions of blast wave effects given in Zahnle (1992), Takata *et al.* (1995) and MacKinnon *et al.* (1997). The nature and position of the

grey arc to the south west further suggests that Mead was caused by an oblique impact from the north east. Essentially, Takata *et al.* (1995) propose that a Mach stem forms when the atmospheric shock front from an impact is reflected from the surface and merges with the direct shock. This Mach stem then relieves the surface shock and produces a supersonic wind that travels radially outward from the epicentre of the impact and parallel to the surface. This wind is considered powerful enough to sweep away fine material and rupture and overturn surface rocks. MacKinnon *et al.* (1997) presume all radar bright halos and penumbrae result when returns from decimeter-scale rubble predominate. Ghail [39] likened the effect to the pyroclastic gound flow of hot ash and molten rock erupted from a volcano. The flow of material ejected during the formation of Mead may have been very similar in appearance and effect, ie entrained by the atmosphere into a ground surge flow, which might be described as a "pyroclastic-like ejecta surge".



a. Normal Impact b. Oblique Impact c. Atmospheric Explosion

Figure 6.18: Sketch of bow shock propagation and interaction with the planetary surface. In all 3 cases, the atmospheric shock is reflected from the surface to form a Mach Stem curtain. This curtain is asymmetric for oblique impacts. NB. For strong explosions, the underground shock initially outruns the atmospheric shock, and preheats the atmosphere close to the surface. From Takata *et al.* (1995).

[39] Personal communication R Ghail, 6 Jun 2004.

6.5. Dark flow past Joliot-Curie

As illustrated in Fig. 6.19, Joliot-Curie has a dark region stretching several hundred kms from the bottom of its ejecta field to the northwest.

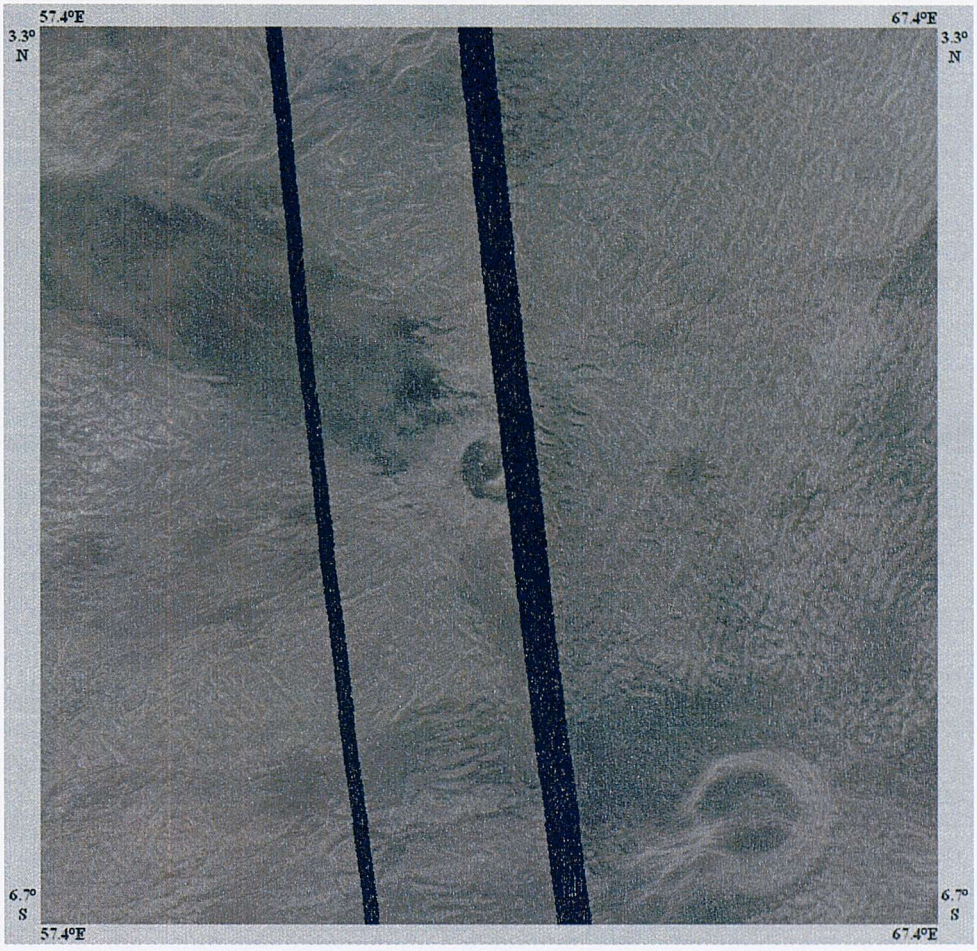


Figure 6.19: Region of Joliot-Curie. Both Joliot-Curie crater, in the centre of this image, and Verdandi Corona, in the bottom right, are associated with extensive, radar-dark areas. PDS download of a Cycle 1 image at 44.8^0 incidence and 455 km slant range.

There is also another, less dark region to the south, which local gradients suggest is lava from Verdandi Corona. In all, the flow stretches for about 1000 km down a height differential of 2.5 km, a slope of 1:400. During its progress, any lava from Verdandi had to progress through the ejecta field of Joliot-Curie, once formed. There is little trace of dark material amongst the radar-bright ejecta but this may be the result of the specular nature of the bright returns. As is the case in other craters, the radar-dark floor of Joliot-Curie is lower than the level of

the dark material skirting the ejecta field. Hence it would appear that the corona is older than the crater.

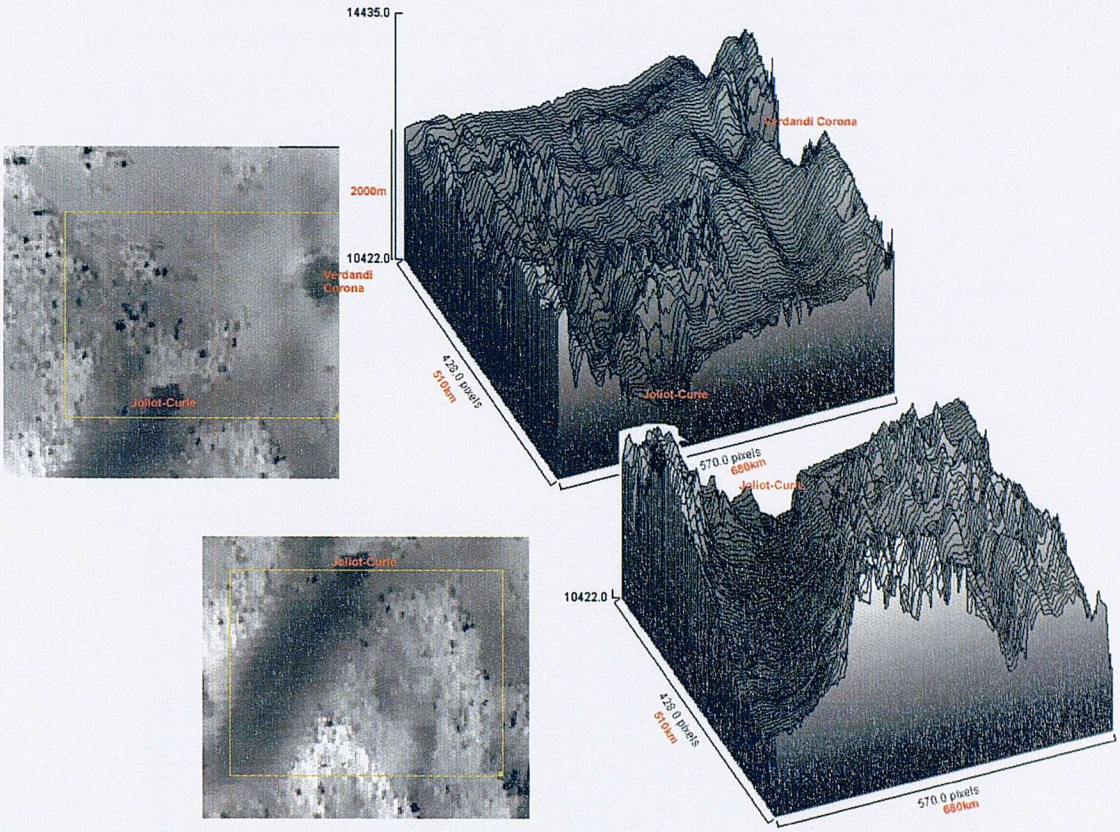


Figure 6.20: Altimetry near Joliot-Curie. The altimetry reveals a valley running down from a fissure through the wall of Verdandi Corona to Joliot-Curie, and then on to the northwest down a total height differential of 2.5 km. Dark material, extending 1000 km lies on the floor of that valley. Most probably, some lava emanated from Verdandi Corona but does not appear to have progressed through the ejecta field of Joliot-Curie. Hence, the impact most probably occurred after Verdandi Corona had discharged lava.

A more plausible explanation is that lava from Verdandi Corona formed a smooth, grey valley floor in a major fault in the northwest face of Ovda Regio. See Fig. 6.20. Then, an impact formed Joliot-Curie on that valley floor and produced material that was preferentially carried westwards by winds but only in sufficient quantity to change the radar signature of the valley floor and not the surrounding tessera. This observation may explain the relative absence, in tessera, of craters with dark halos, and argue for modification to the crater age estimates published in Basilevsky *et al.* (1987, 1993, 1997, 1998 and 2001).

6.6. New Crater Field

Although the bowl of Crater B may not be ellipsoid, as shown in Fig. 6.21, it is certainly elliptical in plan view. Both parts of Crater A lie only 110 - 120 km from Crater B, and near an extension of Crater B's major axis. The DEM of the westerly component of Crater A is ellipsoid, with an asymmetrical eject field. Both the major axis of the westerly Crater A rim and its ejecta field are aligned to the line through Craters A and B. The easterly component of Crater A may also be ellipsoid, and also appears to have an asymmetrical ejecta field. It is concluded that Crater B and the 2 elements of Crater A are a crater field due to the same impact.

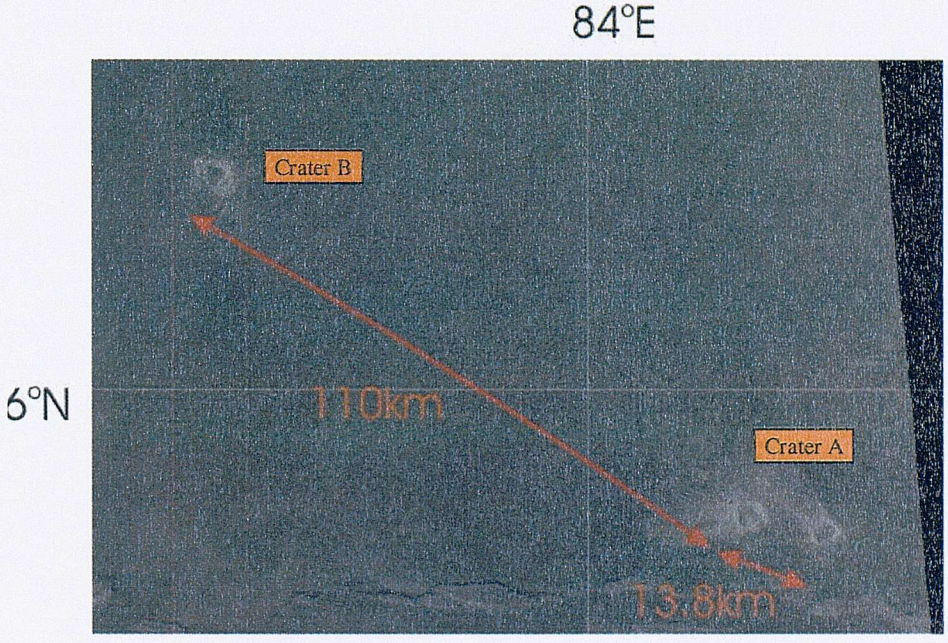


Figure 6.21: Map of the locality of Craters A and B. The LPI database lists Crater A as a crater field of 2 impacts, they are 13.8 km apart. Both craters are irregular, possibly elliptical. Crater B is only 110 km from the nearest of the Crater A impacts, and also a little elliptical. All 3 impact points are approximately in a line, which is parallel to the major axes of the ellipses.

Melosh (1989) does not specify what down range separation between bolide fragments is likely but does provide an equation for across track separation, which is said to reaches a maximum of 30 km on Venus for rock and iron bolides arriving vertically. In this particular case, Crater B appears to be more elliptical

in form, suggesting that its bolide arrived more obliquely than whatever caused Crater A. Ghail[40] has suggested that this might have occurred because the elements that formed Crater A arrived first and the shock fronts emanating from their impacts "bouyed up" the element that went on to form Crater B slightly later.

The fact that 3 craters, each of approximately 6 km diameter, are dispersed over more than 100 km tends to undermine the graph in McKinnon *et al.* (1997) and an update of Melosh & Passey (1980). This shows that the individual craters in a crater field on Venus will begin to overlap once they are 1 km in diameter, and coalesce into forming a single crater of less than 10 km diameter for all initial velocities up to about 40 km s^{-1}. However, the form of this crater field, on what appears to be a homogenous surface, supports a premise that bolides can break up into discrete, well-separated elements and any loose material in between is either never produced or is quickly removed by atmospheric effects.

[40] Personal communication: R Ghail, 6 Jun 2004.

6.7. Chapter Summary

The craters within the Sample Area have been shown to be broadly representative of all craters on the planet.

Three of the 62 DEMs produced during this study are shallower than twice their 1 sigma height error. These craters (Georgina, Teumere and Crater E) may be regaurded as a "shallow" set but their individual depth measurements should not be relied on.

If the crater profiles of the DEMs developed for this study are comparable to lunar analogs, the 10% increase in crater diameter established in Chapter 3 may be associated with a ~20% increase in age estimates for cratered surfaces, i.e. to ~900 Ma. Further work on bolide development during atmospheric descent, extended into contact, compression and excavation stages, may confirm the hypothesis that the large Knobby Base crater population of Venus was most probably produced by compound impacts, following bolide fragmentation in the atmosphere. A re-estimate the impactor population for Venus on this basis might, in turn, indicate that the surface age of Venus is rather younger than suggested in MacKinnon *et al.* (1997).

This study has also identified evidence of unusual or unexpected interaction between crater foramation and volcanism:

- Manzolini has not been severely distorted by lateral forces. It lies on the inner edge of an arcuate ridge feature. Its crater floor is inclined and its dark floor lies only in the western half of the crater.
- Beyond the 510 km diameter dark halo around Mead lies a grey arc to the south and west. Overlain by geological features and the "venetian blind" radar artifact, it is difficult to delineate. Close examination of 4 craters that lie on or close to this material suggest that they were modified by the supersonic winds emanating during the later formation of Mead. Furthermore, the grey arc is evidence of a "pyroclastic-like ejecta surge", the asymmetry of which indicates that Mead was formed by an oblique impact from the north east.

- Verdandi Corona produced some lava before Joliot-Curie was formed, which then darkened a valley floor to its north west. This scar extends for about 1000 km down a height differential of 2.5 km, so any lava released by Joliot-Curie had very low viscosity. Any significant amount of lava from Verdandi after Joliot-Curie formed had to progress past the crater but has left no discernible trace amongst radar-bright ejecta nor on the crater floor. A more plausible explanation is that Joliot-Curie ejected material that was preferentially carried westwards by winds but only in sufficient quantity to change the radar signature of the valley floor and not the surrounding tessera.
- Three craters, close to 6^0N, 84^0E and each about 6 km diameter most probably constitute a single crater field, dispersed over more than 100 km with little evidence if adjacent, smaller impacts. Hence, this field may be evidence that bolides can break up into discrete, well-spread elements and any loose material in between either is never produced or is quickly removed by atmospheric effects. This case may be evidence of interaction of the shock front propagating from the early elements affecting the terminal flight profiles of the later elements, and so extending the size of the resultant crater field.

Chapter 7

Proposals for Further Work

This study has demonstrated the value of DEMs of features on Venus produced with MST, and it has outlined a modelling tool to use radar layover in simple structures like central peaks on other planets besides Venus. Finally, it has produced some ideas about the geology on Venus that can only be established on the basis of more data, obtained by new spacecraft.

This Chapter outlines further work on each of these aspects.

7.1. *Reuse of MST and these Processes*

MST proved a useful tool for the generation of DEMs from SAR image files, and its accuracy has been estimated. MST and the processes developed for this study were used for 2 MSci projects that started in 2002. An F-Map CD library was copied from the archive at University College, and can now be supplemented with larger mosaicked files available over the PDS web-based service. However the licence for IDL necessary to run MST within the Ultra-F environment has now lapsed, as has that for the ERDAS Imagine suite used to visualise its DEM products. If these licences are renewed at a cost of a few thousand pounds, further studies of Venus topography could be undertaken. Two studies in particular stand out, and are described in the following paragraphs.

1. Completion of the Crater DEMs. An analysis of SAR imaging plans in Wall *et al.* (1995) shows that there are as many as 205 craters outside the Sample Area for which 2 same-side images may be available. Of these, as many as 89 may also have a right-looking image, which are particularly useful for the recognition of central peaks. These craters are listed in a spreadsheet called "Additional Craters for MST" within the workbook Venus_Sample_Craters1.9.xls. Such an additional modelling campaign should yield enough crater DEMs to make a 20% sample of the crater population of the planet, and refine understanding of the trends presented in this Thesis.

2. Topography of Ishtar Terra. MST. Ishtar Terra will be a major focus of interest for Venus Express. Its 24 hr, quasi-polar orbit has a pericentre at ~ 250 km altitude between 68 to 74^{0}N. Various details of the Venus Express experimental programme is given in ESA-SCI(2001)6 (2001). Although the VENSIS surface penetrating radar was not selected, this orbit will facilitate study of the geology of Ishtar Terra. A high resolution imaging spectrometer called PFS (High Resolution IR Fourier spectrometer) was selected, primarily for atmospheric composition analysis from weak night-side emissions. PFS will also be used to search for volcanic activity on the night-side surface of Venus through the 1.7 μm window. The spatial resolution of PFS is not known. Also, selected is VIRTIS (UV-visible-near IR imaging spectrometer) which will temperature map about 15% of the

surface of the planet. The spatial resolution of VIRTIS is 13 km from apoapsis and could be much better at periapsis except that scattering within the Venus atmosphere is expected to blur the thermal flux coming from the surface over a scale range comparable to the cloud height (30 km). These 2 instruments should start providing data from May 2006, and good maps would aid understanding of the geology of Venus. At 70^0N, the Magellan altimeter had an across-track resolution of 24 km and an along track resolution of 11 km. MST mapping could add topography with a vertical accuracy of ± 125 m to radar reflectivity maps with 100-fold better horizontal resolution than the altimetry. This would be a major undertaking: just to cover the area astride Maxwell Montes illustrated on the left hand side of Fig. 7.1 would require some 500 mosaics, each of which take about 2 hours to produce. A faster computer system than Ultra-F would reduce waiting time for the defined processes, possibly halving the overall processing time.

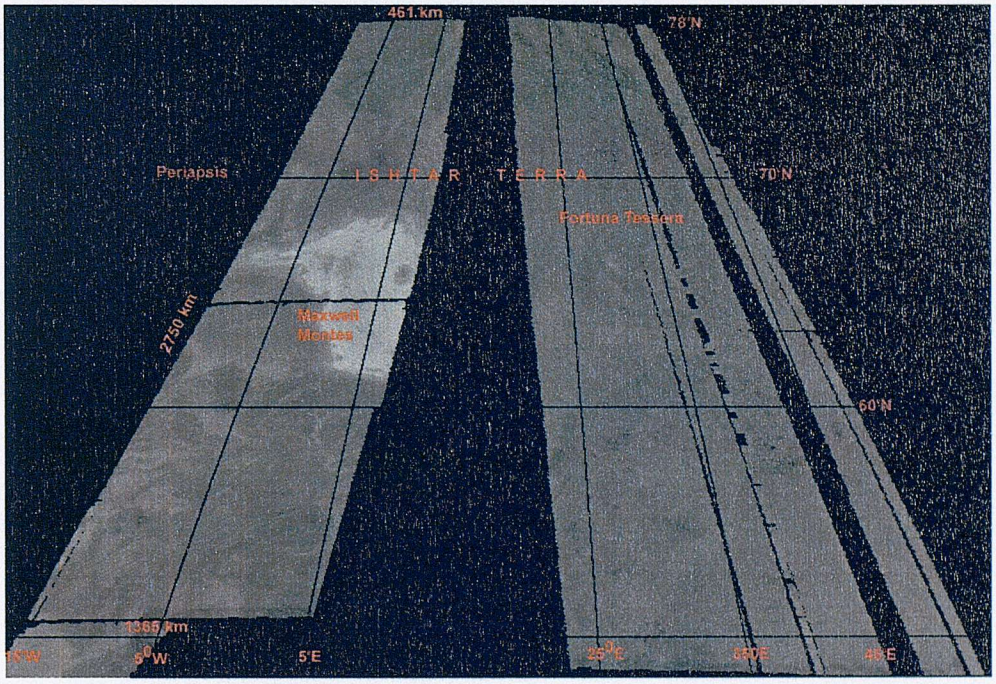


Figure 7.1: Cycle 3 coverage of Ishtar Terra. Magellan Cycle 3 coverage north of 50^0 latitude is restricted to 2 quadrilaterals over different parts of Ishtar Terra. The smaller of the 2 is likely to be the more interesting because it includes the western half of Maxwell Montes, the highest mountain range on Venus. The other, over parts of Fortuna Tessera may also be interesting. PDS download.

7.2. *Modelling Central Peaks*

Central peaks appear to be key features of medium sized craters, and are simpler shapes to model than crater rims. There are 195 candidate craters, in addition to those identified in Section 7.2, with opposite-side image pairs. They are listed in a spreadsheet called "Additional Opposite Side Pairs" within the workbook Venus_Sample_Craters1.9.xls. The principles for a new tool to measure the main features of central peaks were discussed in Chapter 5. These include recognition of radar layover and use of it to determine the shape of the peak.

An additional use for such a tool will arise on the Cassini mission; its SAR radar will return data on Titan as shown in Table 7.1.

Pass	Date(s)	Notes
T_A	Oct 04	Initial radar calibration
T_7	Sep 05	
T_8	Oct 05	
T_{12}	Mar 06	
T_{13}	Apr 06	
T_{16}	Jul 06	
$T_{19, 23, 25,}$ $T_{28, 29, 30}$	Oct 06 – May 07	Also T_{20} (TBC), decision expected post T_{10}.
$T_{39, 41, 43}$	Dec 07 – May 08	Also T_{44} (TBC), decision expected post T_{10}.

Table 7.1: SAR passes on Titan. Only 15 passes are planned; 2 more may be added. Personal communication Ralph Lorentz / Chris Cochrane 16 Apr 04.

Imaging will begin in a "Low Res" mode at about 4000 km slant range, switch to "Hi-Res" at an appropriate point for the closest approach of about 1000 km slant range, and then back to "Low Res" mode as the spacecraft climbs to about 4000 km slant range. Either left or right looking geometry will be used but it is not yet clear which geometry will be used on which pass. Each pass will image a swath width that varies from 400 km to 100 km and then back to 400 km. Each will cover about 1% of the planet, but many overlaps will occur. Fig. 7.2 illustrates which parts will be covered, and the extent of the overlaps.

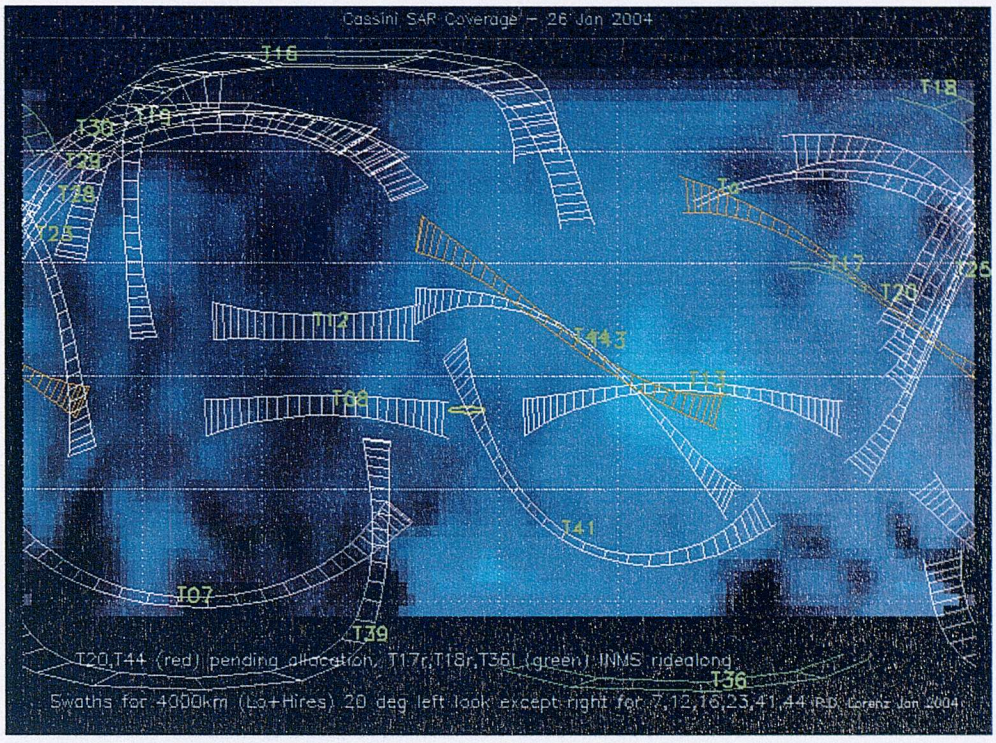


Figure 7.2: Ground traces for planned SAR passes over Titan. The background is a Hubble Space Telescope image in cylindrical projection described in Smith *et al.* (1996). The oval area in the centre of the chart at 40^0S is the target landing area for the Huygens probe. Personal communication: Ralph Lorentz, 16 Apr 04.

7.3. *Further Investigation of Venus*

The next mission to Venus is Europe's Venus Express; it is scheduled for launch into a 153 day transfer orbit to Venus from Baikonur during November 2005 on Soyuz-Fregat. The orbit geometry is favourable for data return to Earth over about 15 hours. Lavoisin of Moscow might provide an optical probe to descend through the atmosphere on a parachute and image the surface from the bottom of the lowest cloud layer, ie an altitude of just above 30km, down to a hard landing.

The three SAR imaging missions to Venus, are summarised in Table 7.2.

Mission	Units	Pioneer Venus	Venera 15 & 16	Magellan
Launch date		1978	1983	1990
Radar Frequency	GHz	1.75	3.75	2.38
Incidence Angle	deg	0.5	7-17	15-45
Antenna dimensions	m	0.38 x 0.38	6 x 1.4	3.7 x 3.7
Swath width	km	variable	~120	20-25
Range resolution	km	23	1	0.12 - 0.4
Azimuth resolution	km	70	1	0.12
Planet coverage	%	92	25	95

Table 7.2: Main parameters of Venus Surface Imaging Missions. Launched over 12 yrs, the resolution achieved by these spacecraft improved about 200-fold. All 3 radars operated in a narrow band of microwave frequencies.

Launch opportunities to Venus will continue to occur every 19 months, with the most favourable geometry approximately every 8 years (eg in Oct 2008).

Atmospheric absorption precludes radar imaging of Venus at wavelengths shorter than a few cm. If the Deep Space Network (DSN) is be used to downlink data (λ = 3.5cm), choice of an adjacent band (eg: 3.6cm) for the radar follows. SARs at such a wavelength, called X-band, have the following advantages:

- Detection of finer textured surface features, eg images more representative of optical imagery of the actual surface.
- Multispectral image comparisons with earlier Venus missions, e.g. different penetration of volumetric scatterers to measure their depth.

Such an instrument could be made using phased array technology, implying a smaller spacecraft, reduced mission mass and reduced launch costs. SAR Phased Array transmit modules each have a capacitor as a power source, so in downlink mode this assembly must burst the data at approximately the same duty cycle as in the SAR mode. The Magellan SAR operated with a typical duty cycle of 7, so a future mission might output data peaking at 50Mbps.

The following notes refer to a possible future European Imaging Radar mission, called Venus Orbiting Prospector (VOP). Its design would be dominated by an array, at least as big as that of Magellan (3.7m diameter), for SAR and downlink transmissions. The nominal azimuth resolution of a SAR will be half this width, provided other parameters, especially the PRF, are optimized. Horizontal beam steering of a SAR of this size in "Spotlight Mode" could achieve a best azimuth resolution given by Oliver & Quegan (1998) as:

$$\text{Azimuth resolution} = R_v.l_a /(2(R_v + H_s) \quad \ldots\ldots (27)$$

where: R_v = Radius of Venus

l_a = azimuth length of the SAR, in this case its diameter

H_s = altitude of the spacecraft

Hence, azimuth resolution could be less than 2 m. The other dimension of the array can be adjusted to trade instantaneous swath width against range resolution. Vertical beam steering could be used to target specific features at appropriate incidence. A rectangular array would simplify the layout of phased array modules; it might measure 3m x 4m, and achieve 1 m resolution. The orientation of the modules within the array could be alternated, so that V, H or circular polarization could be transmitted and V, H and circular polarization could be received. Current phased array technology weighs 5kg per m^2 and consumes an average power of 300 watts per m^2, ie this Phased Array would have a mass of 60kg and consume 3600 watts whilst imaging. The Array would contain most of the SAR avionics so it would have to be thermally insulated from direct radiation by the Sun and Venus, and cooled by louvres.

Allowing for other subsystems, the total payload mass might be 100-150 kg. To achieve Venus orbit, the total spacecraft mass might be 1 metric tonne. The

availability of launch vehicles to directly inject 1 tonne into Venus transfer orbit is a potential problem because Europe has no small launcher.

Spare Ariane 5 lift capacity to Geosynchronous Earth Orbit is often available at a reduced rate, ie perhaps $15 million per tonne. The array could be implemented with up to 2 folds to improve stowage, but a 1 tonne spacecraft must be mounted asymmetrically on the launch vehicle. The VOP might have to be mounted under, and support, another spacecraft of up to 5 tonnes. Hence, the VOP structure must be based on a central tube of the same diameter as the Ariane 5 attachment fitting, and carry it through to provide an upper attachment fitting for the main payload. This is like the original Cluster spacecraft, 4 of which were stacked on each other for launch by Ariane 5. After separation of the main payload, a flap of TR cells should fold over the central tube to complete the array.

Polar orbits are required for global mapping missions like Magellan but necessarily also provide excessive coverage of the polar regions. A lower inclination provides semi-orthogonal coverage of lower latitudes on ascending and descending passes. Stereo imaging of all 4 aspects of any feature can be achieved by combining semi-orthogonal coverage, rotation of a side-looking radar from left- to right-looking, and beam steering in elevation or azimuth. Many interesting geological structures lie on Venus between 60^0N and 60^0S. The ground traces of an orbit at 60^0 inclination cover 83% of the globe, with crossings inclined to each other at more than 50^0 between 45^0N and 45^0S, ie 77% of the globe. Thus, comprehensive coverage of features lying within three quarters of the globe could be achieved from 60^0 incidence. Against selection of this inclination angle, Maxwell Montes lies above 60^0N and, arguably, has the most interesting geology on Venus. Also, most of the Magellan coverage gaps are south of 60^0S.

The elliptical orbit of Magellan required complex trade-offs between the key radar system performance parameters, especially spatial resolution, amplitude resolution and incidence angle. A circular orbit is strongly favoured for VOP to avoid these complications since comparison of images from different angles will be fundamental to geological assessment of the features. The altitude should be low to minimise attenuation but high enough to provide adequate swath width. It may be necessary to make occasional small height adjustments to optimize the

orbit phase for maximum coverage of particular features. 150 ~ 200 km seems the right range.

The Cluster spacecraft each had a 150 Newton bi-propellant thruster and 600 kg of propellant to get to and then manoeuvre around the Earth's bow shock. The cost of the last of these spacecraft was quoted at the time as 45 million ECU, excluding payload and launch costs. VOP might require a higher fuel mass fraction to achieve an inclined, circular orbit around Venus. Ion Propulsion has been demonstrated on the SMART Mission, will minimize launch mass and make best use of the solar array required for the radar. Its location within the spacecraft should align it with the launch thrust cone and shield feedback of ions onto electrical surfaces, eg the SAR antenna.

To reduce perturbations, the spacecraft should be as symmetrical as possible to the solar flux during imaging. Twin, deployable, solar arrays with one degree of freedom once deployed is the simplest solution. They should be sized to meet the power requirement for radar imaging.

Circularization of the orbit round Venus, in order to achieve a constant radar range resolution in the imagery of the planet, will take time but will be relatively easy with Ion propulsion. Choice of an active phased array is likely, with a much larger aperture than Magellan's because it could be launched folded and because 8cm wavelength, phased array technology is now relatively cheap following its development for a number of military applications and is less massive than 12.6cm technology. Its distributed topology and low power devices make it more reliable than a centralised architecture with a few high-power devices. Hence such a mission can be planned to collect its data over a longer period of operations. Like Magellan, one antenna would be used for both imaging and data return but could provide higher resolution imagery for the reasons given above. Modern coding will preserve greater textual variation in the imagery with better data compression on the downlink to the Deep Space Network. Overall, a ten-fold improvement on the imaging performance of Magellan may be achievable.

7.4. *Chapter Summary*

This Chapter has proposed 2 programmes of work to use DEMs made with MST to study geological features on Venus.

It has outlined a way to use radar layover of simple structures like central peaks to model their main characteristics.

Finally, it has discussed how a new spacecraft might gather more data on key areas of the geology of Venus.

References

Alexopoulos, JS and WB McKinnon, 1994; **Large impact craters and basins on Venus, with implications for ring mechanics on the terrestrial planets.** *Spec. Pap. Geol. Soc.Am., 293*, pp 29 - 50.

Alvarez, L, W Alvarez, F Asaro and H Michel, 1980, **Extraterrestrial Cause for the Cretaceous-Tertiary Extinction**, *Science, June ed*, pp 1095-1108.

Alvarez, W, P Claeys & SW Keiffer, 1995, **Emplacement of cretaceous-Tertiary boundary shocked quartz from Chicxulub crater**, *Science, 269*, pp 930-935.

Arkani-Hamed, J, GG Schaber, and RG Strom, 1993, **Constraints on the thermal evolution of Venus inferred from Magellan data,** *J. Geophys. Res., Vol 98*, pp5309 – 5315.

Arvidson, RE, RA Brackett, MK Shepard, NR Izenburg and B Fegley, Jr, 1994, **Microwave Signatures and Surface Properties of Ovda Regio and Surroundings**, Icarus 112, pp 171-186.

Bakun-Czubarow, N, 1992, **Mineralogy and Petrology of the Terrestrial Planets** in Teisseyre, R (ed) "Evolution of the Earth and other Planetary Bodies", Chap 5, PWN-Polish Scientific Publishers and Elsevier.

Baldwin, RB, 1968**, Rille patterns in lunar crater Humboldt**, *J. Geophys. Res., Vol 73*, pp 3227-3229.

Basilevsky, AT, BA Ivanov, GA Burba, IM Chernaya, VP Kruchkov, OV Nikolaeva, DB Campbell and LB Ronca, 1987, **Impact craters on Venus: A continuation of the analysis of data from the Venera 15 and 16 spacecraft** , *J. Geophys. Res., Vol 92*, pp 12,869 – 12,901.

Basilevsky, AT, 1993, *Geophys. Res. Lett. Vol 20*, pp 883-886.

Basilevsky, Head, Schaber and Strom, 1997, **The resurfacing history of Venus;** *Venus II, Part VIII.* University of Arizona Press.

Basilevsky, AT and JW Head III, 1998, **The geologic history of Venus: A stratigraphic view,** *J. Geophys. Res. Vol 103, No E4*, pp 8531-8544, Apr edition.

Basilevsky, AT and JW Head III, 2001, **Venus: Crater-associated radar-dark deposits as a tool to estimate age,** Brown University-Vernadsky Institute Mirosypmosium, 34, MS009.

Beatty, JK, CC Petersen and A Chaikin, eds, 1999, **The New Solar System, Ed4**, Sky Publishing.

Ben-Menahem, A, 1975, **Source parameters of the siberian explosion of June 30, 1908, from analysis and synthesis of seismic signals at four stations,** *Physics of the Earth and Planetary Interiors, Vol 11, Iss 1*, pp 1 – 35.

Bierer, S, **Multi-ring Impact Basins on Venus and Earth,** MSci (Geological Sciences) Thesis, Univ. of London. Unpublished .

Brackett, RA and WB McKinnon, 1992, **Cratering Mechanics on Venus: Pressue enhancement by the atmospheric ocean,** *Geophys. Res. Lett., Vol 19, No 21*, pp 21158, Nov edition.

Brotchie, JF and R Silvester, 1969, **On Crustal Flexure**, *J. Geophys. Res., Vol 74*, pp 5240-5252

Brown, CD and R E Grimm, 1996, **Floor subsidence and rebound of large Venus craters**, *J. Geophys. Res., Vol 101, E11*, pp26.057-26,067.

Bryson, Bill, 2003, **A Short History of Nearly Everything**, Doubleday, London.

Campbell, BA, 1994, **Mering Magellan Emissivity and SAR Data for Analysis of Venus Surface Dielectric Properties**, *Icarus, No 112*, pp 187 – 203.

Cassen, P, and DS Woolum, 1999, **The Origin of the Solar System**, in The New Solar System, Ed4, edited by Beatty, JK, CC Petersen and A Chaikin, Sky Publishing.

Christiansen, EH and WK Hamblin, 1995, **Exploring the Planets**, Prentice Hall.

Chyba, CF, PJ Thomas and KJ Zahnle, **The 1908 Tunguska explosion: atmospheric distruption of a stony asteroid**, *Nature Vol 361*, 7 Jan, pp 40 – 44.

Cochrane, CG, 2001, **Venusian Impact Craters triangulated by Magellan**, *Lunar Plant. Sci., 32.*

Cochrane, CG, and R H Ghail, 2002, **How Much Sediment Is There On Venus?** *Lunar Plant. Sci., 33.*

Cochrane, CG, 2002, **Depth/Diameter Ratios Of Impact Craters On Venus,** Vernadsky-Brown Symposium, Moscow.

Cochrane, CG, 2003, **Crater Morphometry on Venus,** *Lunar Plant. Sci. 34.*

Connors, C, 1995, **Determining heights and slopes of fault scarps and other surfaces on Venus using magellan stereo radar**, *J. Geophys. Res., Vol 100, E7*, pp 14,361-14,381.

Connors, C, and J Suppe, 2001, **Constraints on magnitudes of extension on Venus from slope measurements**, *J. Geophys. Res.*, Vol 106, No 2, pp 3237 - 3260.

Crumper, LS, and JW Head, 1987, **Bilateral topographic symmetry across Aphrodite Terra, Venus**, *Geophys. Res. Lett.* 14, p 607.

Crumper, LS, JW Head, and JC Aubele, 1993, **Relation of major volcanic centre concentrations on Venus to global tectonic patterns**, *Science 261* (591-595)

Curlander, JC, and RN McDonough, 1991, **Synthetic Aperture Radar – Systems and Signal Processing**, John Wiley.

Czechowski, Z, Leliwa-Kopystynski and R Teisseyre,, 1992, **Rise of Plantary Bodies**, in Teisseyre, R (ed) "Evolution of the Earth and other Planetary Bodies", Chap 3, PWN-Polish Scientific Publishers and Elsevier.

De Laubenfels, M W, 1956, **Dinosaur Extinction: One more Hypothesis**, *Journal of Paleontology, Vol 30, No 1*, pp 207-218.

Davis, ME, and PG Rogers, 1991, **Improving the Ephemeris Solutions,** R/N No N-3437-JPL, pp 70 – 76, included in JPL D-9236, Dec 91, **Proceedings of the Magellan Project Science Review.**

Davis, M, P Hut and RA Muller, 1984, **Extinction of species by periodic comet showers**, *Nature 308, April.*

ESA-SCI(2001)6, 2001, **Venus Express Mission Definition Report**, European Space Agency available on http://solarsystem.estec.esa.nl/Flexi2005/.

Elachi, C, 1988, **Spaceborne Radar remote Sensing: Applications and Techniques**, IEEE Inc, New York.

French, B, 1998, **Traces of Catastrophe.** Lunar & Planetary Institute No 954.

Ford, JP, RG Blom, JA Crisp, C Elachi, TG Farr, RS Saunders, EE Theilig, SD Wall, SB Yewell, 1989, **Spaceborne Radar Observations: Guide for Magellan Radar-Image Analysis.** JPL 89-41.

Ford, JP, and GH Pettengill, 1992, **Venus Topography and Kilometer Scale Slopes**, *J. Geophys. Res., Vol 97, No E8,* pp13,103 – 13,114.

Ford, JP, JJ Plaut, CM Weitz, TG Farr, DA Senske, ER Stofan, G Michaels and TJ Parker, 1993, **Guide to Magellan Image Interpretation**, JPL 93-24.

Ford, JP, SL McConnell, CE Leff, RS Austin, KK Beratan and MJ Rokey, 1995, **User Guide to the Magellan Synthetic Aperture Radar Images.** JPL 1356.

Garvin,JB, 1990, **The Global Budget of Impact-Drived Sediments on Venus,** *Earth, Moon and Planets, 50/51*, pp175-190.

Gehrels, T. (ed.), 1994, **Hazards due to Comets and Asteroids**, University of Arizona Press, Tucson.

Grady, MM, R Hutchinson, GJ McCall, DA Rothery (eds), 1998, **Meteorites: Flux with Time and Impact Effects**, *Spec. Pap. Geol. Soc.Am.*, 140, 278 pp

Greeley, R, RE Arvison, C Elachi, MA Geringer, JJ Plaut, RS Saunders, G Scubert, ER Stofan, EJP Thouvenot, SD Wall, and CM Weitz, 1992, **Aeolian features on Venus: Preliminary Magellan results.** *J. Geophys. Res., No E8, Vol 97*, pp 13,319 – 13,346

Grieve, RAF, and PB Robertson, 1979, **The terrestrial cratering record I: Current status of observations**, *Icarus, Vol 38*, pp 212 – 229.

Grieve, RAF, PB Robertson and MR Dence, 1981, **Constraints on the formation of ring impact structures, based on terrestrial data**, in Shultz, PH, and RB Merrill, eds, **Multi-ring basins**, Pergamon Press, pp 37 – 57.

Grieve, RAF and MJ Cintala, 1999, **Planetary Impacts**, in The New Solar System, Ed4, edited by Beatty, JK, CC Petersen and A Chaikin, Sky Publishing.

Grigoryan, SS, 1979, Motion and Destruction of Meteors in Planetary Atmospheres, Kosmicheskie Issledovaniya, Vol 17, No 6, pp 875-893, translated in 1980 by Plenum Publishing Corp.

Hartmann, WK, 1972, **Interplanet Variations in Scale of Crater Morphology – Earth, Mars Moon**, *Icarus 17*, pp707-713.

Hartmann, WK, **Moons and Planets.** Wadsworth Publishing, 1999.

Hauck, SA II, RJ Phillips and MH Price, 1998, **Venus: Crater distribution and plains resurfacing models**, *J. Geophys. Res., Vol 103, E6*, 13,635-13,642.

Head, JW, and LS Crumper, 1987, **Evidence for divergent planet-boundary characteristics and crustal spreading on Venus**, *Science, 238*: 1380-1385.

Head, JW, LS Crumper, JC Aubele, JE Guest & RS Saunders, 1997, **Venus Volcanism: Classification of Volcanic Features and Structures, Associations, and Global Distribution from Magellan Data**, *J. Geophys. Res., No E8, Vol 97*, pp 13,153-13,198.

Head, JW, & AT Basilevsky, 1999, **Venus: Surface and Interior**, in The New Solar System, Ed4, edited by Beatty, JK, CC Petersen and A Chaikin, Sky Publishing.

Herrick, RR, & RJ Phillips, 1994a, **Implications of a Global Survey of Venusian Impact Craters,** *Icarus 111*, pp 387-416.

Herrick, RR, & RJ Phillips, 1994b, **Effects of the Venusian Atmosphere on Incoming Meteoroids and the Impact Crater Population,** *Icarus 112*, pp 253-281.

Herrick, RR, N Izenburg and RJ Phillips, 1995, **Comment on "Strom, Schaber and Dawson; The global resurfacing of Venus. JGR, Vol 99"**, *J. Geophys. Res., Vol 100.*

Herrick, RR and VL Sharpton, 1996, **Geologic history of the Mead impact basin, Venus**, *Geology, v24*, pp11-14.

Herrick, RR, VL Sharpton, MC Malin, SN Lyons and K Feely, 1997, **Morphology and Morphometry of Impact Craters.** *Venus II, Part VIII.* University of Arizona Press.

Herrick, RR and VL Sharpton, 2000, **Implications from stereo-derived topography of Venusian craters**, *J. Geophys. Res., Vol 105*; pp 20245-20262.

Holsapple, KA, and RM Schmitt, 1982, **On the Scaling of Crater Dimensions 2. Impact Processes**, *J. Geophys. Res., Vol 87*, No B3, pp 1849 – 1870, March 10 Edition.

Holsapple, KA, 1993, **The Scaling of Impact Processes in Planetary Sciences,** AREPS, 21, pp 333 – 373.

Howington-Kraus, E, R Kirk, D Galuska, T Hare and B Redding, 2002, **Validation of the USGS Sensor Model for topographic mapping of Venus using Magellan Stereoimagery**, *Lunar Plant. Sci.* 33.

Hills, JG, & MP Goda, 1993, **The fragmentation of small asteroids in the atmosphere**, *Astronomical Journal, Vol 105, No 3*, pp1114-1144.

Ivanov, B A, 1989, **Morphometry of impact craters of Venus** Ivanov, B A, 1989, **Morphometry of impact craters of Venus** (in Russian), *Astron. Vestn, 23*, pp 39 – 49.

Ivanov, BA and O Yu, 1991(a), **On the break-up Diameter of Meteoroids in the Venusian Atmosphere**, pp 533-534, *Lunar Plant. Sci.,* X1X.

Ivanov, BA and O Yu, 1991(b), **Simple Hydrodynamic model of atmospheric break-up of hypervelocity projectiles**, pp 535-536, *Lunar Plant. Sci.* X1X.

Ivanov, B A, IV Nemchinov, VA Svetsov, AA Provalov, VM Khazins, and RJ Phillips, 1992, **Impact Cratering on Venus: Physical and Mechanical Models**, *J. Geophys. Res., Vol 97, E10*, pp 16,167-16,181.

Jetsu, K and Pelt, 2000, **Spurious periods in the terrestrial impact crater record**, Astron. Astrophys. 353, pp409-428.

Johnson, WTK and AT Edgerton, 1985, **Venus Radar Mapper (VRM) Multimode radar system design,** *Soc. Photo. Ins. Ex., Vol 589*, pp 158-164.

Johnson, WTK, **Magellan Radar Mission to Venus**, 1991, *IEEE Proceedings*, V79, No6, pp777 - 790.

Jones, AP, GD Price, NJ Price, PS DeCarli and RA Clegg, 2002, **Impact induced melting and the development of large igneous provinces,** *Earth & Planetary Science Letters 202,* pp551-561.

JPL Publication 90-24, 1990, **Magellan Venus Explorer's Guide,** (available on-line on http://pds.jpl.nasa.gov/mveg/guide.html).

JPL Publication D-2300, 1991, **Magellan Planetary Constants and Models,** Rev D.

Kaula, WM, 1990, **Venus: a contrast in evolution to Earth,** *Science, Vol 247*, pp 1191-1196, Mar.

Klose, KB, JA Wood and A Hashimoto, 1992, **Mineral Equilibria and the high radar reflectivity of Venus moutain tops,** *J. Geophys. Res., Vol 97, No E8*, pp 16,353 – 16, 370.

Korycansky, DG, KJ Zahnle & M-M MacLaw, 2000, **High Resolution Calculations of Asteroid Impacts into the Venusian Atmosphere,** *Icarus 146*, pp387-403.

Korycansky, DG, KJ Zahnle & M-M MacLaw, 2002, **High Resolution Simulations of the Impacts of Asteroid into the Venusian Atmosphere II: 3D Models,** *Icarus 146,* pp387-403.

Krotikov, VD, 1962, **Certain electrical characteristics of terrestrial rock and their comparison with the lunar surface layer**. *Izvestiya vuzov, Radiofizika 5 (No 6)*, pp 1057 – 1061

Kwok, R, and WTK Johnson, 1989, **Block Adaptive Quantization of Magellan SAR Data,** *IEEE Transactions in Geoscience and Remote Sensing, Vol 27, No 4*, pp 375 – 383.

Kuzmin and Marov, 1974, **Physics of the planet Venus,** Moscow: Nauka. Trans. Leo Kannet Associates, NASA-TT-F-16226, Washington DC.

Leberl, FW, KE Maurice, JK Thomas and W Kober, 1991, **Radargrammetric measurement from the initial Magellan coverage of planet Venus,** *Photogrammetric Engineering Remote Sensing, 57(12)*, pp 1561 – 1270.

Leberl, FW, JK Thomas and KE Maurice, 1992, **Initial results from the Magellan Stereo Experiment.** *J. Geophys. Res.*, Vol 97, No 8, p13675-13,689.

Lee, H, JV Morgan and MR Warner, 2003, **Radargrammetry of Opposite-Side Stereo Magellan Synthetic Aperture radar on Venus,** Unpublished – copy in CD.

McKinnon, WB, KJ Zahnle, BA Ivanov and HJ Melosh, 1997; **Cratering on Venus: Models and Observations.** *Venus II, Part VIII.* University of Arizona Press, p969-1014.
McKinnon, WB, and PM Schenk, 1985, **Crater Scaling**, *Lunar Plant. Sci. 26*, pp 544 – 545.

McKinnon, WB, PM Schenk and JM Moore, 2003, **Goldilocks and the three complex crater scaling laws**; LPI Workshop on Impact Cratering.

McNab, D and J Younger, 1999, **The Planets**, BBC Worldwide, London W12 OTT.

Matsui, T, F Imamura, E Tajika, Y Nakano and Y Fujisawa, 2000, **Catastrophic Global Tsunami induced by K/T Impact**, Catastrophic Events Conference, 3104 pdf.

Marov, MY, and DH Grinspoon, 1998, **Venus,** Yale University Press, New Haven & London

Maurice, KE, 1997, **User Notes for Magellan Stereo Toolkit (MST) Release V2.0**, Vexcel Image Information Engineering, pp 2.

Melosh, HJ and QR Passey, 1980, **Effects of atmospheric breakup on crater field formation**, *Icarus 42*, pp 211-233.

Melosh, HJ, 1981, **Atmospheric break-up of Terrestrial Impactors**. Pp 29-35, LPSC 12,

Melosh, HJ, 1989, **Impact Cratering,** Oxford University Press Inc, New York.

Melosh, HJ, & BA Ivanov, 1999, **Impact Crater Collapse**, *Annual Review of Earth Planetary Science, Vol 27*, pp385-415.

Moores, EM and RJ Twiss, **Tectonics**, 1995, WH Freeman and Company, New York.

Muhleman, DO, 1964, **Radar scattering from Venus and the Moon**, *Astronomy Journal, Vol 69*, pp 34 – 41.

Namiki, N, & SC Solomon, 1994, **Impact Crater Densities on Volcanoes and Coronae on Venus: Implications for Volcanic Resurfacing.** *Science, Vol 265*, pp929-933.

NASA Planetary Data System, files separately dated, **Magellan Experimenter's Notebook**, available via the anonymous ftp server on wufs.wustl.edu, in the directory pub/magellan/database Geosciences Node.

Norton, OR, 2002, **The Cambridge Encyclopedia of Meteorites**, Cambridge Univ. Press.

Oliver, C, and S Quegan, 1998, **Understanding Synthetic Aperture Radar Images**, ARTECH Huse, Inc, Norwood, Boston, MA 02062.

O'Keefe, JD, and TJ Ahrens, 1982, **The interaction of the Cretaceous/Tertiary Extinction Bolide with the atmosphere, ocean and solid Earth.** In *Global Implications of impacts of large Asteroids and Comets on Earth*, TL Silver and PH Shultz eds), *Spec. Pap. Geol. Soc.Am., 190*, pp 103-120..

Passey, QR, 1980, Effects of atmospheric breakup on crater field formation, *Lunar Plant. Sci.* XVI, pp 629-630.

Palmentier, EM, and PC Hess, 1992, **Chemical Differentiation of a convecting interior: Consequences for a one-plate planet such as Venus**, *Geophys. Res. Lett. 19*, pp 2015 – 2018.

Palmer, T, 1994, **Catastrophism, Neocatastrophism and Evolution**, Society for Interdisciplinary Studies.

de Pater, I, and JJ Lissauer, 2001, **Planetary Sciences**, Cambridge University Press.

Pettengill, GH, PG Ford and S Noisette, 1982, Venus: **Global surface radar reflectivity**, *Science 217*, pp 640-642.

Pettengill, GH, PG Ford and BD Chaoman, 1988, **Venus surface electromagnetic properties**, *J. Geophys. Res., Vol* 93 No B12, pp 881-892.

Pettengill, GH, et al, 1991, **Magellan: Radar Performance and Data Products**, *Science Vol 252*, pp260-265.

Phillips, RJ, et al, 1991, **Initial analysis of Venus impact craters with Magellan data**, *Science 252*, pp288-297.

Phillips, RJ, et al, **Impact Craters and Venus Resurfacing History**, 1992, *J. Geophys. Res., Vol 97, No E10*, pp15923-15948, Oct edition..

Pike, RJ, 1974, **Depth/diameter relations for fresh lunar craters: Revision from spacecraft data**, *Geophys. Res. Lett. Vol 1*, p 291 – 294.

Pike, RJ, 1980, **Control of crater morphology by gravity and target type,** *Lunar Plant. Sci.* XI, Pergamon Press, P2159-2189.

Pike, RJ, 1988, **Geomorphology of impact craters on Mercury**, in Vilas, F, CR Chapman and MS Matthews, eds, **Mercury**, Univ. of Arizona Press, pp 165 – 273.

Price, M & J Suppe, 1994, **Mean age of rifting and volcanism on Venus deduced from impact crater densities.** *Science, Vol 372* pp 756-759.

Rampino, MR and RB Stothers, 1984, **Terrestrial mass extinctions, cometary impacts and the Sun's motion perpendicular to the galactic plane**, *Nature 308*, April edition, pp712-713.

Raup, DM, **The Nemesis Affair**, 1986, W W Norton & Co.

Ringwood, AE and DL Anderson, 1977, **Earth and Venus: a comparative study**, *Icarus, 30*, 243-253.

Saunders, RS, GH Pettengill, RE Arvidsen, WL Sjogen, WTK Johnson and L Pieri, 1990, **The Magellan Venus Radar Mapping Mission**, *J. Geophys. Res. Vol 95, No B6*, pp 8339 – 8355.

Saunders, RS, and GH Pettengill, 1991, **Magellan Mission Summary**, *Science, Vol 252*, pp 247 – 249.

Saunders, RS, AJ Spear, PC Allen, RS Austin, AL Berman, RC Chandler, J Clark, AV DeCharon, EM de Jong, DG Griffith, JM Gunn, S Hensley, WTK Johnson, CE Kirby, KS Leung, DT Lyons, GA Michaels, J Miller, RB Morris, AD Morricon, RG Pierson, JF Scott, SJ Shaffer, JP Slonski, ER Stofan, TW Thompson and SD Wall, 1992, **Magellan Mission Summary**, *J. Geophys. Res., Vol 97, No E8*, pp 13,067 – 13,090.

Saunders, RS, 1999, **Venus**, in *The New Solar System*, Ed4, edited by Beatty, JK, CC Petersen and A Chaikin, Sky Publishing.

Schaber, GG, RG Strom, HJ Moore, LA Soderblom, RL Kirk, DJ Chadwick, DD Dawson, LR Gaddis, JM Boyce, and J Russell, 1992, **Geology and distribution of impact craters on Venus: What are they telling us?** *J. Geophys. Res. Vol 97, No E8*, pp 13257-13302.

Sharpton, VL 1994, **Evidence from Magellan for unexpectedly deep complex craters on Venus.** *Spec. Pap. Geol. Soc.Am., 293*, pp19-27.

Shoemaker, EM, 1977, **Why study impact craters?** in Impact and Explosion Cratering, Pergamon Press (New York), eds Roddy, DJ, RO Pepin and RB Merrill, p 1-10.

Shoemaker, EM, RF Wolfe & CS Shoemaker, 1990, **Asteroid flux and impact cratering rate on Venus**, in Global Catastrophes in earth History, eds Sharpton, VL & PD Ward, GSA SP-247, pp 155 – 170.

Shoemaker, EM, PR Weissman & CS Shoemaker, 1994, **The flux of periodic comets near Earth**, in *Hazards Due to Comets and Asteroids*, ed T Gehrels (Tuson: Univ. of Arizona), pp 313 – 335.

Shoemaker, EM, & CS Shoemaker, 1999, **The Role of Collisions**, in The New Solar System, Ed4, edited by Beatty, JK, CC Petersen and A Chaikin, Sky Publishing.

Shultz, PH, 1992, **Atmospheric effects on ejecta emplacement and crater formation on Venus from Magellan,** *J. Geophys. Res., Vol 97, No 8,*, pp16,183-16,248.

Silverthorn, S, **The Topographic Modelling of Impact Craters on Venus using Radar Stereoscopy,** MSci (Geological Sciences) Thesis, Univ. of London. Unpublished .

Sjorgren, WL, BG Bills, PW Birkland and RN Wimberley, 1980, **Gravity anomalies on Venus**, *J. Geophys. Res., Vol* 85, pp 8295-8302.

Smith, PH, MT Lemmon,, RD Lorentz, LA Sromovsky, JJ Caldwell and MD Allison, 1996, **Titan's Surface, Revealed by HST Imaging**, *Icarus 119*, 339-349.
Solomon, SC, and JW Head, 1982, **Mechanisms for lithospheric heat transport on Venus: Implications for tectonic style and volcanism**, *J. Geophys. Res., Vol* 87, pp 9239 – 9246.

Steel, D, 1995, **Rogue Asteroids and Doomsday Comets**, Wiley, New York.

Stofan, ER, VL Sharpton, G Schubert, G Baer, DL Bindschadler, DM James, and SW Squyers, 1992, **Global distribution and characteristics of Coronae and related features on Venus: Implications for origin and relation to mantle processes.** *J. Geophys. Res., Vol* 97, No E8, pp 13347-13380.

Strom, RG, GG Schaber and DD Dawson, 1994, **The global resurfacing of Venus.** *J. Geophys. Res., Vol* 99, E5, pp 10,899-10,926.

Strom, Schaber and Dawson, 1995, **Reply to "Herrick, Izenburg and Phillips; Comment on "Strom, Schaber and Dawson; The global resurfacing of Venus. JGR, Vol 99", May 94 in JGR Vol 100, Nov 95"** also in *J. Geophys. Res., Vol* 100.

Svetsov, VV, 1996, **Total ablation of the debris from the 1908 Tunguska explosion**, *Letters to Nature, Vol 383*, 24 Oct, pp 697 – 699.

Takata, T, TJ Ahrens & RJ Phillips, 1995, **Atmospheric effects on cratering on Venus**, *J. Geophys. Res., Vol* 10, No E11, pp 23,329-23,348.

Turekian, KK & JM Luck, 1983, **Osmium-187/Osmium-186 in manganese nodules and the Cretaceous-Tertiary boundary**, *Science 236*, pp 613-615.

Turcotte, DL, 1993, **An episodic hypothesis for Venusian tectonics**, *J. Geophys. Res., Vol* 98: 17061-17068.

Ulaby, FT, TH Bengal, MC Dobson, JR East, JB Garvin, DL Evans, 1990, **Microwave Dielectric properties of dry rocks**, *IEEE Trans. Geosci. Rem. Sens. Vol 28*, pp 325-336.

Urey, H, 1973, **Cometary Collisions and Geological Periods,** *Nature 242*, p32.

Wall, SD, SL McConnell, CE Leff, RS Austin, KK Beratan and MJ Rokey, 1995, **User Guide to the Magellan Synthetic Aperture Radar Images**, NASA Publication 1356.

Whitmire, DP & AA Jackson IV, 1984, **Are periodic mass extinctions driven by a distant solar companion?** *Nature 308*, pp 713-715.

Whitmire, DP & JJ Matese, 1985, **Periodic comet shaowers and planet X**, *Nature 313*, April edition, pp 36-38.

Wichman, RW, and PH Shultz, 1993, **Large Floor-fractured Craters and Isostatic Crater Modification: Implications for Lithospheric Thickness of Venus**, *Lunar Plant. Sci.* 24, pp 1495-6, 1995.

Wichman, RW, 1996, **Internal Crater Modification on Venus: Implications of Interior Crater Morphometry**, *Lunar Plant. Sci.* 27, pp 1495-6.

Wichman, RW, **Internal crater modification on Venus: Recognizing crater-centred volcanism by changes in floor morphometry and floor brightness**, *J. Geophys. Res., Vol 104, No E9*, pp 21,957-21,977.

Wood, JA, 1999, **Origin of the Solar System**, in The New Solar System, Ed4, edited by Beatty, JK, CC Petersen and A Chaikin, Sky Publishing.

Young, C, 1990, **The Magellan Venus Explorer's Guide**, JPL Publication, 90 – 24.

Zahnle, K J, 1992, **Airburst origin of dark shadows**, *J. Geophys. Res.*, Vol 97, pp 10,243-10.256.

Acronyms used in this Thesis

Acronym	Meaning
BAQ	Block Adaptive Quantization
C1-MIDR	Compressed once Mosaicked Image Data Record
C2-MIDR	Compressed twice Mosaicked Image Data Record
C3-MIDR	Compressed 3 times Mosaicked Image Data Record
CRM	Catastrophic Resurfacing Model
CSN	Command Sequence Number
DEM	Digital Elevation Model
DMAT	Data Management and Archive Team
DN	Digital Number, the greyscale code value in the image
DSCC	Deep Space Control Center
EDR	Experiment Data Record
ERM	Equilibrium Resurfacing Model
ERS	Earth Resources Satellite
ESA	European Space Agency
F-BIDR	Full-Resolution Basic Image Data Record
F-Map	Full Resolution Map
F-MIDR	Full-Resolution Mosaicked Image Data Record
IDL	Image Display Language, and an output of MST
IDPS	Image Data Processing Subsystem
JPL	Jet Propulsion Laboratory, Pasadena, CA
LPI	Lunar and Planetary Institute
MHRP	Magellan High-Rate Processor
MIDR	Mosaicked Image Data Records
MPR	Mean Planetary Radius
MST	Magellan Stereo Toolkit
NASA	National Aeronautics and Space Administration
ODR	Original Data Record
PDS	Planetary Data System
PIF	Planetary Information Facility
QC	Quality Control, a function of MST
RADAR	Radar Detection and Ranging
SAR	Synthetic Aperture RADAR
SDPS	SAR Data Processing Subsystem
SFOC	Space Flight Operations Center at JPL
SFS	Shape from Shading, a function of MST
SPH	Smooth Particle Hydrodynamic
USGS	United States Geological Survey
VOI	Venus Orbit Insertion
VOIR	Venus Orbiting Imaging Radar
VRM	Venus Radar Mapper

Contents of the Accompanying CD

Crater Notes

Andreanova

Bernhardt

Joliot-Curie

Mead

Potanina

Magellan Experimenters Notebook

Interpolation13.xls

Orbptin0376.xls

Orbptin1538.xls

Orbptin2820.xls

Orbptin4801.xls

Ptinfotab.xls

MST Programme Listings

CorrelateOptimise.doc

MST automatch.doc

Procedures developed for this Thesis

Procedure for generating DEMs7.doc

Procedure for generatng colour-coded DEMs in ERDAS Imagine.doc

Procedure for transferring MST Files to ERDAS Imagine2.doc

Procedure for validating DEM from right-looking image.doc

Spreadsheets developed for this Thesis

CraterA c1c3parallaxht calculatorMarkedv2.xls

D~d of MST DEMs in sample6d.xls

Topographic Offsets at B due to BAQ.xls

Topographic Offsets at Eini due to BAQ.xls

Topographic Offsets at Georgina due to BAQ.xls

Topographic Offsets at Helvi due to BAQ.xls

Topographic Offsets at Florence due to BAQ.xls

Venus_Sample_Craters2.xls